

AD A 020530

2

**THE TURBULENT BOUNDARY LAYER ON A ROUGH,
POROUS PLATE: EXPERIMENTAL HEAT TRANSFER
WITH UNIFORM BLOWING**

By

J. M. Healy, R. J. Moffat and W. M. Kays

Report No. HMT-18

Prepared with Support from

The Department of the Navy
N00123-71-C-0372

and

The Office of Naval Research
N00014-67-A-0112-0072



Thermosciences Division
Department of Mechanical Engineering
Stanford University
Stanford, California

May 1974

9-1-74
A

1
release;
classified

August 1974

ERRATA

HMT-18 (Heizer, Moffat & Kays)

<u>Page</u>	<u>Line</u>	<u>Mistake</u>	<u>Should Read</u>
211	9	$y^+ = \dots$	$u^+ = \dots$
30	30	on	of
35	4	$St = \dots$	$\Delta St = \dots$
38	1	x	x_0
46	Fig. 2.9		Add (ft/sec) to vertical scale
49	Fig. 2.13		Add $\times 10^{-4}$ to all ΔSt
55	22	$Re_T = u_T k_s / \mu$	$Re_T = u_T k_s / \nu$
63	15	Fig. 3.10	Fig. 3.9
11	1	of stream	of free stream
150	23	agent	agent
197	4	photograph	photograph

6
THE TURBULENT BOUNDARY LAYER ON A ROUGH, POROUS PLATE:
EXPERIMENTAL HEAT TRANSFER WITH UNIFORM BLOWING,

10 By
J. M. Alcalzer, R. J. Moffat and W. M. Kays

14
Report No. HMT-18

Prepared with Support from

C
The Department of the Navy

12
N00123-71-G-0372,

and

~~The Office of Naval Research~~

N00014-67-A-0112-0072

Thermosciences Division
Department of Mechanical Engineering
Stanford University
Stanford, California

11
May 1974

12 178p.

401 973 ✓

15

ACKNOWLEDGMENTS

The heat transfer portion of this research program and the construction of the heat transfer apparatus was supported by the Department of the Navy, Research Contract N00123-71-G-0372. The authors wish to express their appreciation to Dr. W. H. Thielbahr of the China Lake Naval Weapons Center, for his interest and assistance in completing this study. The hydrodynamic portion of the program and much of the rig instrumentation was funded by the Office of Naval Research, research contract N00014-67-A0112-0072. The authors thank Mr. James Patton and Dr. Ralph Roberts for their support.

The authors also wish to thank Mr. Robert Bosenburg and Dr. J. V. Labacqz for providing us with the facilities needed to fabricate the porous plates used in these experiments. Also to George Yoshida, Tots Ikebe and particularly to Robin Birch for their ingenuity and craftsmanship in constructing the wind tunnel, Mr. Marcos Pimenta who assisted in both the construction of the apparatus and in the data taking, Mr. T. R. Mogel who designed the power supply system and R. H. Niegel who, along with Ted Mogel helped build and shake-down the power supply system.

Last but not least, we appreciate the excellent typing of Ruth Korb, Helen Healzer and Jan Moffat who also coordinated the publication of this report.

Letter on file

A
|

10 TO THE 7th Power
OK

ABSTRACT

Stanton number measurements have been made for a transpired turbulent boundary layer on a rough surface. Tests were conducted at uniform blowing fractions from 0 to .008, with uniform surface temperature and uniform free-stream velocity. The x-Reynolds number range of these tests was from 10^5 to 10^7 and the roughness Reynolds number range from 20 to 200. The data are believed to be accurate to within ± 0.001 Stanton number units over most of this range. At each test condition, several velocity profiles were taken to measure the boundary layer growth. The boundary layer momentum thickness variation along the test surface has been used to estimate rough-plate skin friction.

The data indicate the expected increase in both skin friction and heat transfer due to roughness. The data display some unusual features when plotted against boundary layer size. For any given value of F , for all free-stream velocities, the Stanton number data fall on a single curve when plotted against enthalpy thickness, and the skin friction data collapse (but less well) to a single curve when plotted against momentum thickness. This behavior might have been expected for a "fully rough" plate but was not expected at the lower end of the roughness Reynolds number range of these tests. The blowing data indicate that within the uncertainty of the experiment, a form of the Couette flow model used for smooth surface boundary layers can also be used for rough surfaces to predict the effects of blowing on Stanton number.

Predictions of the experimental boundary layers have been carried out using a finite-difference boundary layer prediction method which employs the Patanker-Spalding finite-difference formulation and a mean field closure with a mixing-length model employing van Driest type damping. The effects of roughness have been incorporated into this prediction program by modification of the mixing-length model used for smooth-surface turbulent boundary layers.

The apparatus constructed for these tests is a closed-loop wind tunnel using air at essentially ambient condition as both the transpired and free-stream fluid. The rough surface consists of 24 porous plates

forming an eight foot long test section. The individual plates were fabricated by brazing together 50-mil OFHC copper balls stacked in their most dense array. In the test section assembly each plate is individually controlled with its own electric heater, transpiration air supply and instrumentation. The construction of the test section is such that blowing, no blowing, and suction cases can be tested.

...

TABLE OF CONTENTS

	Page
Acknowledgments	iii
Abstract	iv
Table of Contents	vi
List of Figures	viii
Nomenclature	xiii
Chapter 1. INTRODUCTION AND BACKGROUND	1
A. General Background	1
B. Previous Heat Transfer Experimental Work	3
C. Rough Surface Flow Models	5
D. Objectives of Present Research	6
E. General Features of the Program	6
Chapter 2. THE EXPERIMENTAL APPARATUS	10
A. Description of the Apparatus	10
B. The Test Plate Assembly	18
C. Porous Plates	20
D. Rig Instrumentation	26
E. Rig Qualification Tests	30
F. Data Reduction Program	37
G. Experimental Uncertainty	39
Chapter 3. THE EXPERIMENTAL RESULTS	53
A. Rough Surface Boundary Layer Data Without Blowing	53
B. The Effects of Blowing	60
C. Roughness and Blowing Effects on Transition	62
D. Comparison with Other Rough Surface Experiments	64
Chapter 4. PREDICTION OF THE ROUGH SURFACE DATA	89
A. Hydrodynamic Predictions of the Rough Surface Boundary Layer	89
B. Heat Transfer Predictions for the Rough Surface Boundary Layer	93
Chapter 5. SUMMARY AND CONCLUSIONS	110
References	113

	Page
Appendices	
A. Main Air Supply System Components	118
B. Transpiration Flow Metering System	123
C. Plate Power Control Circuit	130
D. Porous Plate Fabrication	135
E. Tabulation of Experimental Results	142
F. Listing of Data Reduction Program	158

LIST OF FIGURES

Figure		Page
1.1	Heat transfer increase ratio, rough-to-smooth Nusselt number versus rough-to-smooth friction factor	8
1.2	Friction factor ratio exponent	8
1.3	Roughness Rig operating map, x-Reynolds number versus roughness size Reynolds number	9
2.1	Rough surface wind tunnel flow schematic	42
2.2	Photograph of Roughness Rig	42
2.3	Photograph of aluminum casting	43
2.4	Cross section view of typical compartment	43
2.5	Photograph of clamping arrangement used for gluing the plate and casting assembly	44
2.6	Photograph of the back of the casting assembly	44
2.7	Photograph of the top of the casting assembly	45
2.8	Photograph of the rough surface, close-up	45
2.9	Velocity distribution above the Roughness Rig surface	46
2.10	Roughness Rig thermocouple schematic	47
2.11	Photograph of the Pitot probe	48
2.12	Momentum thickness distribution across the tunnel at plate 23	48
2.13	Non-blown and blowing energy balances	49
2.14	Stanton number versus x-Reynolds number for $u_{\infty} = 239$ fps, $F = 0.002$ (standard) and for $u_{\infty} = 226$ fps, $F = 0.002$ (with an insert in the diffuser)	50
2.15	Comparison of skin friction predictions to data by Andersen [8] and Simpson [2]	50
2.16	Data reduction program flow chart	51
2.17	Stanton number error due to experimental uncertainties	52

Figure		Page
3.1	Rough surface skin friction and Stanton number versus x-Reynolds number	67
3.2	Rough surface skin friction and Stanton number versus momentum and enthalpy thickness Reynolds number	68
3.3	Velocity profiles at different test section velocities. .	69
3.4	Velocity profiles at $u_{\infty} = 139$ fps at different stations along the test section	70
3.5	Rough surface momentum thickness versus distance from the boundary layer virtual origin	71
3.6	Rough surface skin friction versus (momentum thickness)/(ball radius) and rough surface Stanton number versus (enthalpy thickness)/(ball radius)	72
3.7	Rough surface Stanton number versus (enthalpy thickness)/(ball radius) at $u_{\infty} = 18.8$ fps and $u_{\infty} = 90$ fps	73
3.8	Rough surface skin friction versus x-Reynolds number at $u_{\infty} = 32$ fps	74
3.9	Rough surface Stanton number versus x-Reynolds number at $u_{\infty} = 32$ fps	74
3.10	Rough surface skin friction versus x-Reynolds number at $u_{\infty} = 90$ fps	75
3.11	Rough surface Stanton number versus x-Reynolds number at $u_{\infty} = 90$ fps	75
3.12	Rough surface skin friction versus x-Reynolds number at $u_{\infty} = 139$ fps	76
3.13	Rough surface Stanton number versus x-Reynolds number at $u_{\infty} = 139$ fps	76
3.14	Rough surface skin friction versus x-Reynolds number at $u_{\infty} = 190$ fps	77
3.15	Rough surface Stanton number versus x-Reynolds number at $u_{\infty} = 190$ fps	77
3.16	Rough surface skin friction versus x-Reynolds number at $u_{\infty} = 242$ fps	78

Figure		Page
3.17	Rough surface Stanton number versus x-Reynolds number at $u_{\infty} = 242$ fps	78
3.18	Stanton number versus (enthalpy thickness)/(ball radius) for all boundary layers	79
3.19	Stanton number versus (enthalpy thickness)/(ball radius) at $u_{\infty} = 32$ fps	80
3.20	Stanton number versus (enthalpy thickness)/(ball radius) at $u_{\infty} = 90$ fps	81
3.21	Stanton number versus (enthalpy thickness)/(ball radius) at $u_{\infty} = 139$ fps	82
3.22	Stanton number versus (enthalpy thickness)/(ball radius) at $u_{\infty} = 190$ fps	83
3.23	Stanton number versus (enthalpy thickness)/(ball radius) at $u_{\infty} = 242$ fps	84
3.24	Momentum thickness versus distance from virtual origin for all boundary layers	85
3.25	Comparison of rough surface transition Stanton number to smooth plate transition data by Reynolds [53]	86
3.26	Comparison of skin friction data with Prandtl-Schlichting correlation	86
3.27	Comparison of skin friction data in E versus Re_x coordinates	87
3.28	Comparison of heat transfer data to correlations by Dipprey and Sabersky [24] and Owen and Thompson [25]	87
3.29	Comparison of heat transfer data to correlations by Nunner [23] and Norris [30]	88
4.1	Rough surface damping constant, A^+ , versus roughness Reynolds number	98
4.2	Mixing-length wall value, Δz_0^+ , versus roughness Reynolds number	99
4.3	Rough surface mixing-length, l^+ , versus y^+	100
4.4	Prediction of rough pipe friction factor data	101

Figure		Page
4.5	Predicted and measured rough surface velocity profiles at $u_{\infty} = 32$ fps and $u_{\infty} = 139$ fps with no blowing	102
4.6	Predicted and measured rough surface velocity profiles at $u_{\infty} = 32$ fps and $u_{\infty} = 139$ fps with $F = .004$	103
4.7	Prediction of rough surface skin friction data	104
4.8	Smooth surface turbulent Prandtl number model	105
4.9	Rough pipe heat transfer predictions with smooth surface turbulent Prandtl number model	105
4.10	Prediction of Dipprey and Sabersky [24] data for smooth tube and $k_s/d = .0024$	106
4.11	Prediction of Dipprey and Sabersky [24] data for $k_s/d =$.0138 and $k_s/d = .0448$	107
4.12	Rough surface thermal mixing-length factor, C_H , versus roughness Reynolds number	108
4.13	Prediction of rough surface Stanton number data with blowing	109
A.1	Heat exchanger oblique header and screen box	120
A.2	Photograph of the screen box, heat exchanger and header assembly	120
A.3	Nozzle wall shape	121
A.4	Photograph of the nozzle halves and mold before assembly. .	121
A.5	Multistage, vaned diffuser	122
A.6	Photograph of the diffuser before installation in the wind tunnel	122
B.1	Schematic of the constant current, hot wire type flow meter	128
B.2	Photograph of the flow meter heater element	129
B.3	Typical flow meter calibration curve	129
C.1	Plate power control circuit schematic	132

Figure		Page
C.2	Plate power control protection circuit schematic	133
C.3	Photograph of the rear of the plate power control panel. .	134
C.4	Photograph of the bus bar box	134
D.1	Photograph of ball assembly in mold, almost complete . . .	139
D.2	Photograph of balls being arranged in the molds	139
D.3	Photograph of the molds on the furnace pedestal before firing	140
D.4	Photograph of furnace being raised after brazing the ball assembly	140
D.5	Photograph of the brazed ball-plate with mold after firing	141
D.6	Photograph of an end view of the plate after firing . . .	141

NOMENCLATURE

- A van Driest damping function for a smooth surface.
- A_R van Driest damping function for a rough surface.
- B Blowing parameter, F/St .
- C_H Defined by Equation (4-9).
- c Specific heat of fluid, $Btu/lb_m \cdot ^\circ F$.
- c_f Skin friction coefficient, $\tau_o / (\rho u_\infty^2 / 2)$
- d Pipe diameter, ft.
- E Parameter defined by the equation $y^+ = \frac{1}{\kappa} \ln(Ey^+)$
- F Blowing fraction, $\rho_o v_o / \rho_\infty u_\infty$.
- g_c Proportionality factor in Newton's Second Law, $lb_m \text{ ft} / lb_f \text{ sec}^2$.
- G Free-stream mass velocity = $\rho_\infty u_\infty$, $lb_m / \text{sec ft}^2$.
- k Roughness particle size, ft.
- k_s Equivalent sand grain roughness size, ft.
- l mixing length, ft.
- Δl_o Mixing length at wall, ft.
- \dot{m}'' Mass flux through the plate surface, $lb_m / \text{sec ft}^2$.
- n Exponent in equation (1-1).
- r Ball radius, ft.
- T Temperature, $^\circ F$.
- u_∞ Boundary layer free-stream velocity, ft/sec.
- u_τ Shear velocity = $\sqrt{\tau_o g_c / \rho_o}$, ft/sec.
- v Velocity normal to the test surface, ft/sec.
- \bar{v} Average velocity in a pipe flow, ft/sec.
- x Distance measured downstream from test section inlet, ft.
- x_o Distance measured downstream from test section inlet to virtual origin, ft.
- y Distance normal to the surface, ft.

Nomenclature (cont.)

Greek

α	Thermal diffusivity, ft^2/sec .
ν	Kinematic viscosity, ft^2/sec .
τ_o	Wall shear stress, lb_f/ft^2 .
δ	Boundary layer displacement thickness, ft.
δ_{99}	99% thickness of the momentum boundary layer, ft.
λ	Proportionality constant used in outer region mixing-length formulation ($l = \lambda \delta_{99}$).
κ	Mixing-length constant, $l = \kappa y$.
θ	Boundary layer momentum thickness, ft.
Δ	Boundary layer enthalpy thickness, ft.
ρ	Density, lb_m/ft^3 .
μ	Viscosity, $\text{lb}_m/\text{sec ft}$.
ω	Humidity, $\text{lb}_m \text{ water vapor}/\text{lb}_m \text{ dry air}$

Dimensionless Groups

Re_d	Pipe Reynolds number = $d\bar{v}/\nu$.
Re_k	Roughness size Reynolds number = ku_∞/ν .
Re_τ	Roughness Reynolds number = $k_s u_\tau/\nu$.
Re_x	x-Reynolds number = xu_∞/ν .
Re_θ	Momentum thickness Reynolds number = $\theta u_\infty/\nu$.
Re_Δ	Enthalpy thickness Reynolds number = $\Delta u_\infty/\nu$.
St	Stanton number = h/Gc
ΔSt	Stanton number error, see Equation (2-2).
St_o	Stanton number without blowing = h/Gc .
Pr	Prandtl number = ν/α .
Pr_t	Turbulent Prandtl number.

Nomenclature (cont.)

Subscripts

- ∞ Refers to free-stream conditions.
- w Refers to value on fluid side of wall - fluid interface.
- T Refers to condition of transpiration flow beneath porous plate.
- H Thermal (used as mixing-length subscript).
- m Momentum (used as mixing-length subscript).
- s Smooth surface value.

Superscripts

- + Refers to variables non-dimensionalized in wall coordinates;
 $y^+ = yu_\tau/\nu$.

CHAPTER I

INTRODUCTION AND BACKGROUND

Heat transfer between a surface and a fluid stream is affected by the surface condition, the fluid properties, the velocity field, and the thermal boundary conditions. Studies of this complex interaction are generally conducted by fixing all but one of these descriptors and varying the remaining one to determine its effect. Most prior studies of boundary layer heat transfer have been concerned with the effects of fluid properties, temperature boundary conditions, or main stream velocity distribution. Current interest in protecting surfaces by transpiration or ablation has introduced a class of problems in which surface roughness is an unavoidable feature.¹

A. General Background

Much of what we know about rough surface hydrodynamics is based on ideas and results of the pipe flow experiments by Nikuradse [9].² To avoid the difficulties of defining an arbitrary rough surface with an uncertain distribution of roughness elements, he investigated the flow through sand-grain roughened tubes. Roughness elements for these experiments consisted of selected sand, carefully sieved and attached in maximum density to the tube walls. The roughness in these experiments was described by a single parameter, k_s , the size of the sand-grain elements. This 'sand-grain' measure of roughness has become a standard in skin friction studies. It is still common practice to express the effect of an arbitrary roughness in terms of an 'equivalent sand-grain roughness', k_s .

¹ This introductory paragraph was first used by Professor Moffat in the original proposal to the Navy for the rough surface research contract that supported these tests. This same introduction was repeated again in each of the 12 quarterly reports describing our progress on the project. It seems appropriate that it be used again to introduce the final reporting of this phase of the roughness work.

² Numbers in brackets refer to references listed at the end of this report.

The pipe flow experiments showed three domains of behavior in terms of the roughness Reynolds number, $Re_T = u_T k_s / \nu$. For values of roughness Reynolds number less than 5 the flow behaved as though the surface were smooth. For values of roughness Reynolds number greater than 70, the pipe friction factor became independent of Reynolds number, $Re_d = \bar{v} d / \nu$. This state was described as 'fully rough'. Values of roughness Reynolds number between 5 and 70 defined a region of 'transitional roughness'.

Prandtl [10] and von Karman [11] used Nikuradse's results (in 1934) to predict the behavior of the rough surface boundary layer. These predictions indicated that the boundary layer would attain a 'fully rough' state such that the skin friction would be a function only of x/k_s . Early rough surface boundary layer experimental studies were carried out by Moore [12] and Hanna [13]. Moore looked at air flowing over a flat plate roughened by regular arrays of square bars attached to its surface. Hanna's experiment was carried out with air flowing over surfaces roughened by screens attached to them. Several other experimenters looked at the rough surface boundary layer, but most notable among these were two studies by Perry et al. [14,15] and Liu et al. [16]. The experiments by Perry and his co-workers were carried out with lateral rectangular bars on a flat plate and with zero and adverse pressure gradients. They found that pressure gradient did not alter the roughness effects on the boundary layer. They also attempted to simulate a change in effective sand-grain roughness by changing the spacing between the array of bars used to roughen the plate. They found that changing the bar spacing did not change the effective sand-grain roughness of the surface as had been expected. This led them to define a second type of roughness whose behavior, unlike sand-grain roughness, could not be correlated in terms of an external length scale, but scaled on the 'logarithmic asymptote'. This is the distance between the top of the roughness elements and the apparent surface of the plate, the plane where the velocity profiles extrapolate to zero.

The experiment by Liu was conducted in water using an array of rectangular bars to roughen the otherwise smooth surface. Liu also varied his bar spacing to change the roughness of his surface and determined

equivalent sand-grain roughnesses for all surface roughness that he tested. He was not able, however, to correlate his skin friction data from different surface roughnesses with a single x -Reynolds number expression. Liu's report also contains a very complete table of both the experimental and analytical work that had been done till then (1966) for both rough pipe and boundary layer type flows.

More recent rough surface hydrodynamic studies have been made by Grass [17], who used a hydrogen bubble technique to measure instantaneous velocity distributions in a water tunnel above a sand-grain roughness. His study documented details of the turbulent structure near the wall. Wu [18] used a floating element balance to measure skin friction in an air tunnel with a sand-grain roughened surface. These tests showed 'fully rough' behavior and agreed well with the Prandtl-Schlichting prediction. Tsuji and Iida [19] examined velocity profiles over rough surfaces and showed that they could be predicted using a modified mixing-length approach, maintaining a non-zero value of the mixing length at the wall. In a related study, Antonia and Luxton [20] investigated the effect of an abrupt change from a smooth to a rough surface. In this study the rough surface was constructed from parallel square bars like many earlier studies, but one of the bars was instrumented with static pressure taps to provide a direct measure of form drag. The method of measuring form drag on individual roughness elements was also used by Perry [14]. Townes et al. [21,22] have studied the structure of turbulent flow in sand-grain roughened pipes.

B. Previous Heat-Transfer Experimental Work

Much less has been done in the field of heat transfer. One of the first systematic rough surface experimental studies was carried out by Nunner [23]. These experiments used air flowing through rough pipes. The results were used to establish a simple empirical relationship between the increase in Nusselt number due to roughness and the increase in the skin friction. Several important heat transfer studies followed, notably by Dipprey and Sabersky [24], Owen and Thompson [25] and Gowen and Smith [26].

Dipprey and Sabersky looked at the flow of four fluids of different Prandtl numbers through one smooth pipe and three rough pipes. These studies demonstrated that rough wall heat transfer varied with the Prandtl number, even in the fully rough regime where molecular viscosity effects seem not important.

Owen and Thompson proposed a flow model near the rough surface which explains why increasing surface roughness can increase the heat transfer. Based on their ideas, they developed an expression for a sublayer Stanton number which was able to correlate a large block of the rough pipe heat transfer data.

Gowen and Smith studied flow in several rough pipes using fluids of three different Prandtl numbers. In one of their pipes they were able to make temperature profile measurements in the flow over the rough wall. Like earlier investigators, they developed an expression for rough wall Stanton number based on the rough wall skin friction, but in this case they were able to include information obtained from their temperature profiles.

There were, of course, other rough wall heat transfer studies, mostly confined to internal flow applications. Two papers which summarize this work are by Sood and Johnson [29] and more recently by Norris [30]. The survey by Norris points out that of the many forms of rough wall heat transfer correlations that have been proposed, none is simpler or has had a great deal more success in correlating the data than the simple expression by Nunner,

$$\frac{Nu}{Nu_s} = \left(\frac{f}{f_s} \right)^n, \quad (1-1)$$

where the exponent n can be expressed as a function of Prandtl number. The general form of this relationship is shown in Fig. 1.1, and Norris's recommended Prandtl variation is shown in Fig. 1.2. An approximate expression for the exponent is:

$$n = .68(Pr)^{0.215}. \quad (1-2)$$

An interesting feature of all the pipe experiments is that there is a 'ceiling' which corresponds to a rough-to-smooth skin friction ratio of about 4.0. This ceiling seems to vary with the type of roughness, with sand-grain roughness producing lower heat transfer than surfaces roughened with wires and square ribs. This range in the heat transfer ceiling is shaded in Fig. 1.1. For increases in skin friction above this ceiling, there is not a corresponding increase in the heat transfer.

There continues to be current interest in rough wall heat transfer. Much of it is specifically related to heat transfer to nose cones and other re-entry vehicles. Unfortunately, much of the work done is not in the open literature. Two related studies by Reshotko [27] and Boldman and Graham [28] examine heat transfer to a nozzle with a rough surface.

C. Rough-Surface Heat-Transfer Models

Several authors have presented prediction methods for rough wall boundary layer heat transfer. Integral boundary layer prediction schemes which include roughness effects have been described by Dvorak [32,33] and by Chen [31]. Nestler [34] has proposed a scheme using a correlation by Owen and Thompson to relate the increase in Stanton number due to roughness to the increase in the skin friction and other boundary layer parameters. Finite-difference turbulent boundary layer prediction schemes which include roughness effects have been described by Lumsdaine et al. [35] and by McDonald and Fish [36]. Each of these studies has modified the mixing-length distribution to introduce roughness effects. The Lumsdaine paper discusses a prediction program for skin friction only. It employs a van Driest type damped mixing-length model near the wall. To account for roughness, they follow the recommendation of van Driest [39] and add an additional term to the mixing-length damping expression which includes a roughness parameter.

The McDonald and Fish method includes both skin friction and heat transfer calculations. Roughness effects are entered through the mixing-length damping by defining an incremental damping due to roughness which is added to the normal boundary layer damping. This damping effect is the sole means of including roughness effects into both the hydrodynamic and heat-transfer predictions in this method.

D. Objectives of the Present Research

The first objective of this study was to find a suitable rough surface to test. We sought a surface which was at the same time repeatable, describable, and also porous.

The second objective was to measure the heat transfer from the rough surface to a turbulent boundary layer over a wide range of free-stream velocities. As a secondary part of this objective, the overall hydrodynamic performance of the rough surface was to be determined in terms of boundary layer growth and skin friction.

The third objective was to study the effect of blowing on the rough surface heat transfer to determine whether or not transpiration changed the effective roughness.

A final objective was adopted after the apparatus had been completed and testing had begun: to study the effects of roughness and blowing on heat transfer in the transition region. At the lowest test section velocity, it was discovered that a fully developed, laminar boundary layer existed over the first quarter of the test section. It was decided that instead of tripping the boundary layer at the test section inlet to immediately establish a turbulent layer, that we would examine the effects of blowing and test section velocity in the transition region as these data would be of considerable interest and could be obtained at minimal cost.

E. General Features of the Program

Spherical roughness elements were selected for this study. The test surface was constructed from 0.050 inch diameter O.F.H.C. copper balls arranged such that the surface formed a regular array of hemispherical caps. This surface was more regular than sand grains, being geometrically describable, but more like sand-grain roughness than the transverse-bar roughness elements used in other tests.

High-conductivity copper balls were used in fabrication of the surface to ensure a high thermal conductivity of the porous plates. With a high-conductivity surface, heaters can be embedded into the plate and yield a uniform surface temperature, independent of whether the transpiration is "on" or "off". This allows us to use the same surface to test

both the unblown as well as the blown boundary layers. This is a necessary requirement if we are to determine if blowing changes the effects of surface roughness.

The apparatus constructed to test this rough surface has the capability of operating over a wide range of free-stream conditions selected to optimize the usefulness of the data. Fig. 1.3 shows an operating map of the rough surface heat transfer apparatus. The coordinates used for this map describe the performances in terms of a roughness particle-size Reynolds number and an x-Reynolds number. The range of test section velocities of the rig was selected such that at a given particle-size Reynolds number, the x-Reynolds number could be varied by a factor of 10^3 . In these coordinates, it's possible to overlap operating conditions with the existing smooth surface boundary layer apparatus. The rig operating parameters were also restricted to ensure an essentially constant property boundary layer to minimize the effects of variable fluid properties.

The following chapters describe the heat transfer apparatus and its qualification tests, the data which have been obtained in these tests, and, finally, the attempts to predict the data with a finite-difference boundary layer prediction program.

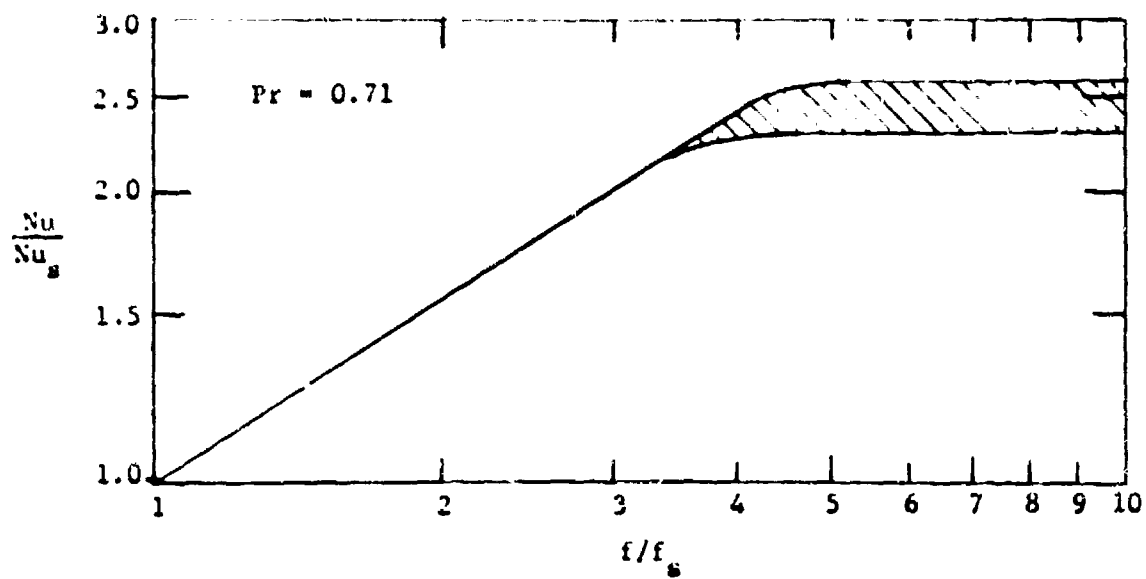


Fig. 1.1 Heat transfer increase ratio, rough-to-smooth Nusselt number versus rough-to-smooth friction factor

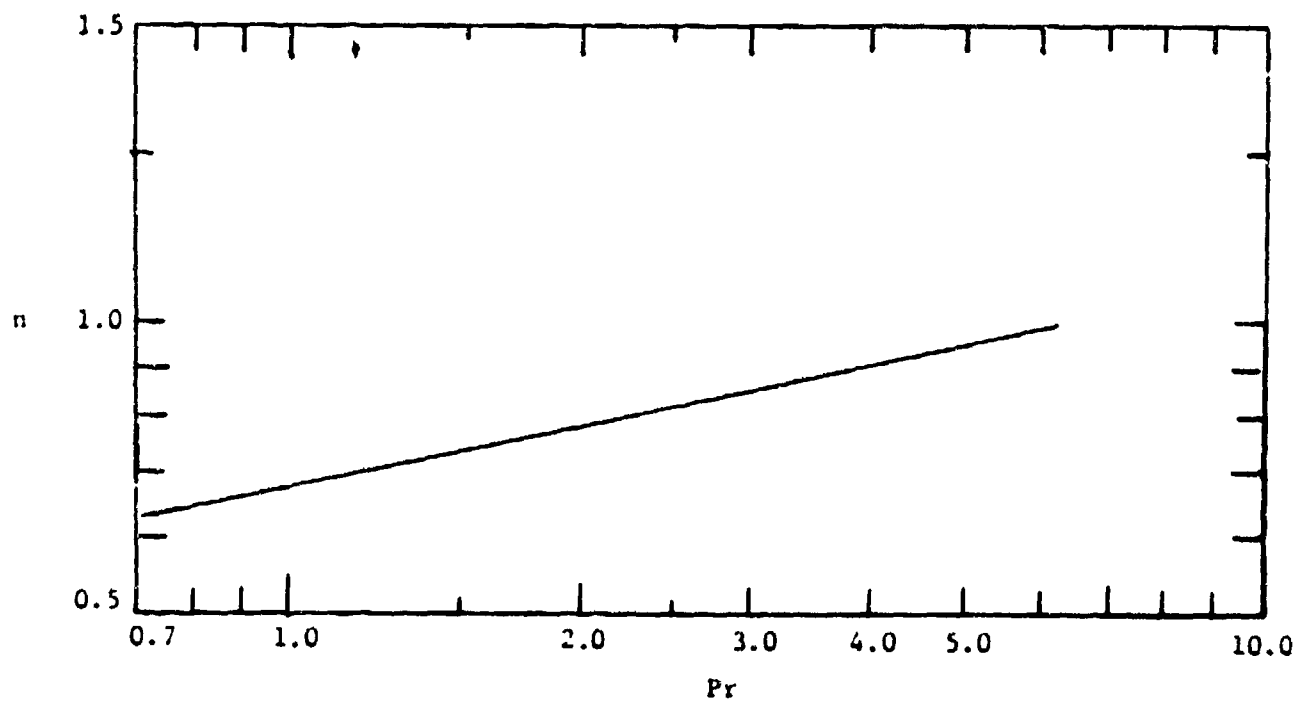


Fig. 1.2 Friction factor ratio exponent

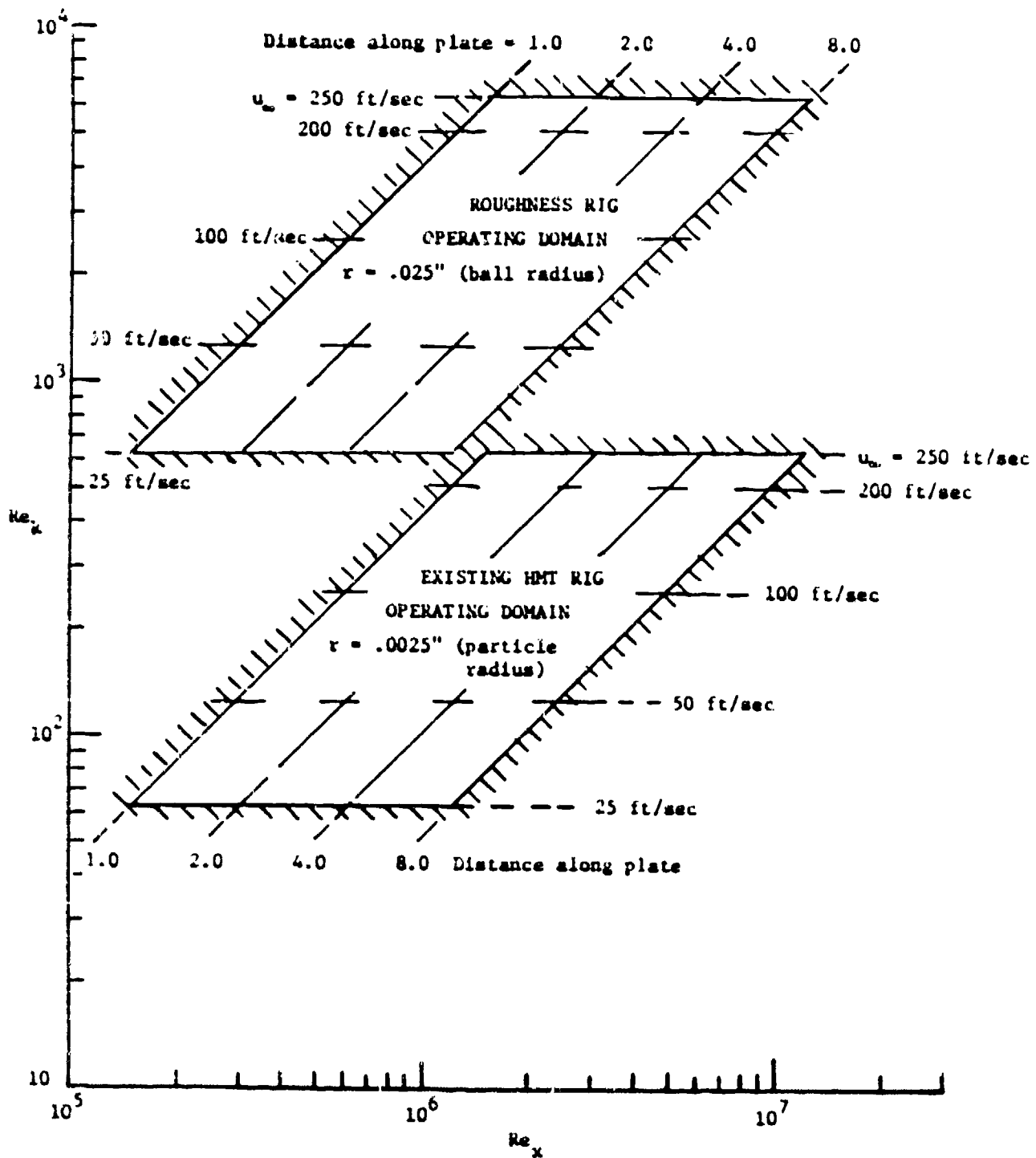


Fig. 1.3 Roughness Rig operating map, x-Reynolds number versus roughness size Reynolds number

CHAPTER II

THE EXPERIMENTAL APPARATUS

The apparatus used in these experiments was constructed especially for this study and in the discussion that follows, it will be referred to as the Roughness Rig. The Roughness Rig is located in the Thermosciences Laboratory on the second floor of the Mechanical Engineering Building at Stanford. Its basic design was copied after an existing heat transfer facility which the Heat and Mass Transfer Group at Stanford has used over the past six years to investigate the transpired turbulent boundary layer on a smooth surface. This heat and mass transfer apparatus was described first by Moffat [1]. References [2 - 8] describe modifications that have been made since Moffat's original experiments. This existing HMT Rig is still very much in use and continues to play an important role in the Heat and Mass Transfer Group's research activities.

A. Description of the Apparatus

The Roughness Rig is a closed loop wind tunnel using air at essentially ambient conditions. Its test surface consists of a 24-segment porous plate, 18 inches wide and 8 feet long. Figure 2.1 shows a flow schematic of the four main rig systems: main air supply, transpiration air supply, plate heater electrical power system, and the heat exchanger cooling water system. A photograph of the Roughness Rig is shown in Figure 2.2. The following is a description of the four main rig systems.

A.1 The Main Air Supply System

The flow path of the main air system is as follows: (1) main air blower, (2) overhead ducting to an oblique header, (3) main-stream heat exchanger, (4) screen box, (5) nozzle to test section inlet, (6) 8 foot long test section and (7) a multistage diffuser which returns the main-stream air back to the blower.

The Roughness Rig main air supply blower is a 445-BL Class 3 Buffalo Blower with a 20 horsepower belt drive. At rated conditions, this blower delivers 8300 cfm and develops a head of 12 inches of water. The blower and drive are mounted on a 900 lb seismic base to minimize vibration. Flexible boots connect the blower to the remainder of the tunnel. The main air stream velocity in the test section is varied by changing the pulleys and belts on the blower and drive. The range of blower speeds attainable with this drive arrangement is from the blower rated speed of 2400 rpm down to 372 rpm.

From the main blower discharge, air is delivered through a 24" diameter overhead duct to an oblique inlet header on the main-stream heat exchanger. Ducting construction is from galvanized sheet metal with gasketed joints and sealed internally at all seams with a silastic gasket sealer material. The oblique inlet header to the heat exchanger was designed based on recommendations by Wolf [40]. The header shape is specified for uniform flow distribution and minimum pressure loss.

The header supplies air to a 5 row, 33" x 48" heat exchanger used for main air stream temperature control. The heat exchanger cooling water is continuously pumped from a holding tank through both the main-stream heat exchanger and the transpiration air heat exchanger. In operation, the cooling water temperature is adjusted until the main-stream air at the test section inlet is at ambient temperature. This avoids the formation of a thermal boundary layer prior to the test section inlet.

The heat exchanger is followed by a screen box containing four stainless steel, #40 mesh, 0.0065" dia. wire screens. The screens were sized to minimize the mean field velocity disturbances as well as reduce the main air stream turbulence level. Based on the work of Schubauer et al [41], this screen pack should reduce mean velocity disturbances by a factor of 600 and turbulent fluctuations by a factor of 10. The screen pack combined with the large area contraction nozzle provides a uniform and well damped inlet velocity field to the test section. Details of the inlet velocity field measurements are reported in Section F.

The nozzle accelerates the flow from the screen box to the test section inlet, a 19.8 to 1 area contraction. The nozzle wall design is based on a polynomial shape as recommended by Rouse and Hassan [42]. This conforms with experience in designing similar nozzles at Stanford. The wall shape, which is a two-dimensional contraction, has been chosen such that both the first and second derivatives of flow area are zero at the nozzle exit. There is a slight acceleration in the inlet flow to avoid possible separation in this region. This was accomplished by designing the nozzle length for 40" and cutting off the first inch when the nozzle was actually built. A teledeltos model of each of the nozzle walls was used to insure that the nozzle smoothly accelerated the flow and there was not separation at inlet or exit.

The test section consists of the test plate assembly, two side walls and a movable upper surface. At the inlet, the test section is 20 inches wide and 4 inches high. The upper surface is pivoted at the inlet so that it can be adjusted to give either an increasing or decreasing flow area in the flow direction. The top and side walls are constructed from continuous sheets of 1/2 inch thick plexiglass. The top is sufficiently flexible so that it can be warped to accommodate the nonlinear growth of the test section boundary layers. The side walls contain two sets of static pressure taps, on 2 and 12 inch centers in the flow direction. The pressure taps on 12 inch centers in the flow direction are used to position the top to achieve the desired free stream velocity distribution. The tests described here were conducted with uniform free stream velocity. To obtain this test condition, the top wall is set, experimentally, for each run by adjusting it until there is no measurable change in static pressure along the test section centerline. In practice, local deviations of ± 0.001 inches of water were accepted. A probe sled, which spans the test section, locks onto the side walls in fixed positions over the center of each of the 24 individual test plates. Probes, supported from this sled extend down through access holes in the movable top. In addition to the access holes along the test section centerline the second, eleventh and twenty-third (of twenty-four) of the individual test plates are pro-

vided with a full set of access holes extending across the width of the test section on one inch centers. These are primarily to examine boundary layer uniformity in the transverse direction.

Flow from the test section exits into a multistage vaned diffuser. The diffuser inlet has a movable top to allow alignment with the test section top. The inlet section is followed by three separate vaned two-dimensional diffusion sections finally emptying into a plenum box. The diffuser area ratio between test section and plenum box is in excess of 7:1. The plenum box is connected to the main blower inlet through a flexible boot. Each of the individual diffuser sections were designed based on the experimental work of Cocharan and Kline [43] and the total diffuser recovers approximately 40% of the kinetic energy head in the flow leaving the test section. A small charging blower is attached to the plenum box to make up air leakage from the tunnel. This blower is used to ensure that the test section static pressure is equal to the ambient pressure in the laboratory. This avoids any leakage of air into or out of the test section which might disturb the two-dimensionality of the flow.

Appendix A contains a brief description of the construction details of the screen box, nozzle and diffuser.

A.2 The Transpiration Air Supply System

The flow path of the transpiration air system is as follows: (1) inlet air filter box, (2) transpiration blower, (3) transpiration heat exchanger, (4) transpiration flow header box, (5) individual delivery tubes to each of the porous plate sections.

The purpose of the inlet filter box is to prevent clogging and contamination of the porous plates. It is constructed using 5 micron retention filter felt material and is sized to have 60 square feet of filter area.

The filter box is connected to a Buffalo type V, size 25 blower. This blower is driven by a 15 horsepower, 3600 RPM motor, connected directly to the blower. In this configuration, the blower runs at one speed and transpiration flow is controlled by ball valves in the individ-

ual delivery lines. This particular blower was designed for a higher volumetric flow than is required at low transpiration rates. In order to avoid off-design operation, the blower was equipped with dump valves so that a part of its discharge air could be dumped back into the lab. It was found, however, that the blower performance was stable over the entire flow range of interest in these experiments without venting its discharge.

Transpiration air from the blower is delivered through a 10 inch flexible duct to a large box containing the transpiration air heat exchanger and bypass system which allows partial or total heat exchanger by-pass. A 5 row, 18 x 24 inch heat exchanger is used in the transpiration system. The heat exchanger receives its cooling water from the same recirculating water system which supplies the main air heat exchanger. From the heat exchanger enclosure, the transpiration air is passed through several mixing turns, then dumped into a header box. In operation, the heat exchanger and its by-pass system are used to insure that the transpiration air is delivered to the header at ambient temperature. This avoids the formation of temperature gradients in the delivery system which acts itself like a heat exchanger between the transpiration air and the laboratory.

The transpiration header box is physically located under the test section. Individual supply lines, one for each porous plate, are connected to the side of the header box. The first section of each supply line is a 3 foot long riser reaching from the header box to a ball valve used to control the flow to each plate. In each riser section, upstream of the valve, is a hot-wire type flowmeter. Details concerning the fabrication and calibration of these flowmeters are described in Appendix B. The hot-wire flowmeter was chosen because of its wide sensitivity range. The range of flows which must be accurately metered to cover the operating range of the Roughness Rig is from less than 1 cfm to over 50 cfm. To cover this range with a loss-based metering system such as an orifice or rotameter would require two or more parallel meters in each line. To complete the supply line from the control valve to the test plate assembly, 1 inch flexible tubing was used. This final link in the supply line makes the Roughness Rig transpiration system compatible

with the existing HMT Rig plate assemblies. It would be possible to install the existing smooth plate assemblies on the Roughness Rig and they would be completely compatible with the transpiration system. To minimize the interaction between the transpiration air and the surroundings, the header box and supply lines have been insulated. The header box is covered with a layer of aluminum foil backed, rock wool insulation and the supply lines have been encased in a cardboard and masonite zone box to insure a thermally uniform environment for the system. Thermocouples in the individual supply lines indicate temperature differences on the order of one degree Fahrenheit from end to end of the 8 foot header box, the hotter end being nearest the transpiration blower.

When a blown boundary layer is established in the test section, the transpiration system operates in an open loop mode. Transpiration air is drawn in through the filter box and delivered to the test section. It is then dumped, downstream at the diffuser plenum box. The small charging blower which is used to control test section pressure is disconnected and air is bled from the diffuser plenum box through a control slide valve. Test section static pressure can easily be balanced to match the ambient pressure by controlling the flow of air through the control valve.

When boundary layer suction is required the flexible duct connection is moved to the suction side of the blower and the blower discharge is used to charge the diffuser plenum to provide test section static pressure control.

A.3 The Plate Header Electrical Power System

The plate heater power supply is a 750 amp, 24 kilowatt Lincoln Arc Welder. The field resistance of the welder has been modified to fix its output at 22 volts D.C. Power connections are made to the ground and 'high point' taps on the welder to minimize line voltage droop with increasing load. Power is delivered to a bus bar box mounted on the side of the Roughness Rig through overhead copper bus bar system. Each individual plate has its own heater which consists of a single piece of #26 AWG stranded copper wire with irradiated PVC insulation. This wire

is laced back and forth in eight grooves in the back of the plate. Ends of the heater wire are connected to #12 AWG stranded copper leads which pass through the side of the aluminum support casting. One heater lead is connected to a precision ammeter shunt, one for each plate, and then to the ground bus bar in the box. The other lead is connected to a power transistor mounted on the other bus bar in the box. The power transistor is part of the power control circuit for each plate heater. Plate power is controlled by individual amplifier circuits, one for each plate, which can adjust heater voltage. All of the control circuit elements except the power transistors on the bus bar have been reduced to a printed circuit assembly, 6 channels per board and are mounted in a card box behind a control panel in the instrument console located on the left of the rig, see Fig. 2.2. On this control panel are potentiometers with digital read out faces and small edge voltmeters which indicate heater voltage for each channel. The plate voltage and therefore the power is proportional to the potentiometer setting for that channel. By recording pot settings from a particular run, test conditions can be very nearly repeated by resetting the pots to their former setting. A detailed description of the power control circuits is given in Appendix C. The bus bar on which the power transistors are mounted acts as a heat sink for the power transistors. Under certain conditions these transistors reject a substantial heat load and it is necessary to provide water cooling of the bus bar. This was accomplished by soft soldering 1/2 x 1 inch rectangular copper wave guide into two parallel grooves milled lengthwise in the surface of the 8 foot long, 3 x 3/8 inch copper bus bar. The wave guide is used as a cooling water passage to reduce transistor temperatures. A magnetic valve wired into the starter switch circuit for the welder power supply automatically turns the bus bar cooling water on when the welder is started. A time delay relay set for a one minute delay insures that the bus bar cooling continues until after the welder has coasted down once it has been stopped.

Heater power measurements are made by measuring the voltage drop across the heater and across a precision shunt in the heater circuit. Heater voltage and shunt voltage leads are carried in shielded pairs to

selector switch read-out stations. These selector switches are 'zone boxed' to prevent any thermally induced, stray signals which could introduce errors in power readings.

These read-out stations are also equipped with VIDAR plug connections which will allow automatic data acquisition at a later date. The ammeter shunts used for power read-out were individually calibrated, in place, against a high precision shunt from the Thermo Sciences Measurements Center. In addition to individual shunt calibration, the shunt connections were potted with RTV compound to insulate them against possible external thermal effects and each of the 24 shunts were provided with an air cooling system to insure that there would be no stray thermally induced EMF signals.

A.3 The Heat Exchanger Cooling Water System

Cooling water for both the main air and transpiration air heat exchangers is supplied from a single loop which continuously circulates cooling water through both heat exchangers from an insulated holding tank. By maintaining a high water circulation rate, in excess of 20 GPM, temperature gradients across the heat exchangers are minimized. This ensures uniform temperature in the air being cooled. The main air heat exchanger is sized to remove the heat load from the main blower as well as the heater power added in the test section. The transpiration air heat exchanger removes the heat load due to the transpiration blower. Temperature control of the cooling water is achieved by dumping a portion of the heat exchanger return water and making it back up from the water supply main. The make-up water is mixed in the holding tank to provide a buffer against temperature fluctuations in the supply water. It was found that the cooling water temperature dominated the exit air temperature from both the main and transpiration air heat exchangers. This was not unexpected for an air-water system with high effectiveness heat exchangers such as are used here. By holding the circulating water temperature just below the ambient temperature, the exit air temperature from both heat exchangers can be held at the laboratory ambient temperature.

B. The Test Plate Assembly

The test plate assembly forms the bottom surface of the Roughness Rig test section. Its design has been copied after the test plate assembly used in the existing HMT Rig. It is 22 inches wide, 2 inches wider than the inside dimension of the test section, and 96 inches long in the flow direction. It is made up of four subassemblies, bolted to a common support structure. Each subassembly consists of an aluminum casting in which are mounted 6 individual porous plates, each 4 inches wide and 18 inches long. The porous region of the test surface thus is 96 inches long and 18 inches wide. A photograph of a machined casting is shown in Fig. 2.3. A cross section through one of the plates and the compartment in the aluminum casting beneath it is shown in Fig. 2.4.

Transpiration air enters through the air delivery tube from the flow control valve. Like the smooth plate HMT Rig, a one inch delivery tube is used for each compartment. The air jet entering the lower compartment is diverted by a baffle plate to avoid direct impingement on the pre-plate. The air flow in this first inlet plenum may be poorly distributed and may have significant eddies. To protect the working plate, the upper surface of the inlet plenum is a porous bronze pre-plate which provides a pressure drop type damping of the maldistribution. Air passing through the pre-plate is distributed no worse than the variation in permeability of the commercially available pre-plates.

Directly above the pre-plate is the thermocouple location for measuring the temperature of the air delivered to the porous plates. A layer of honeycomb material is fastened to the bottom surface of the porous plates. This honeycomb has hexagonal cells, $3/16$ inch in diameter and is $3/8$ inch thick. The honeycomb acts as a 'flow straightener' for the flow from the pre-plates. It also eliminates eddies or jets which could cause both flow and temperature maldistributions. The honeycomb not only isolates the plate from contact with eddies in the underbody region, it significantly reduces the radiation view factor between the back of the plate and the underbody. Essentially all that the back of the plate can 'see' through the honeycomb is the pre-plate directly below it.

Thermocouples for measuring the plate temperatures are set into the porous plate with their junctions located .068 inches from the ball crests which form the rough surface. The surface and air temperature thermocouples are 0.010 inch diameter iron-constantan thermocouples.

The electric heater wires are stranded, 26 AWG copper wire. Irradiated polyvinyl chloride insulation for the wire was chosen for the temperature tolerance of this material and a series of glue bond tests. The heater wires are glued into grooves spaced 0.43 inches apart on the back of the porous plates with a thin bead of Armstrong A-31 epoxy. Each plate is supported along its long edges by a 1/32 inch thick linen-reinforced phenolic stand-off. These strips serve to thermally isolate the plates from the castings and minimize heat losses. The phenolic strips are glued to the sides of adjoining plates and inserted into slots milled into the web dividing two adjacent compartments in the casting. Care was taken to provide an air tight seal entirely around each compartment to prevent leakage between adjacent compartments.

Assembly of the plates into the casting is a hand operation since adjacent plates must fit together with a minimum disturbance to the surface roughness pattern. Small irregularities between plates were corrected by hand-finishing and matching each group of six plates. The first step in the assembly was to glue the hand fitted group of six plates together to form a continuous sheet, 18 x 24 inches. Between each pair of plates, the phenolic stand-offs are also glued in place. This gluing assembly is made by clamping the plates together on a precision surface table, under a high clamping load. The next step was installation of the heater wires in each of the plates. The casting and plates were next assembled together, again on a surface table, clamped together. Figure 2.5 shows a photograph of the clamping arrangement used for gluing the casting and plate assembly together. The final step was the installation of the honeycomb, thermocouples, pre-plates and the bottom plates on the castings. On the top surface, balsa filler strips were used to fill the gap between the plate edges and the top surfaces of the casting side rails. Figure 2.6 is a photograph of the back of the plate assembly showing the honeycomb, thermocouples and pre-

plates. A photograph of the top surface of the casting assembly in place on the support structure is shown in Fig. 2.7.

Five surface temperature thermocouples are installed in each plate. One is in the geometric center of the plate. The remaining four are arranged 1 1/3 inch upstream and downstream and three inches to the right and left of the central thermocouple. This array can sense temperature gradients both in the flow direction and in the transverse direction. The area enclosed by this thermocouple pattern is considered to be the measuring area, the rest of the plate acts as a 'guard' to minimize thermal and hydrodynamic edge effects.

Casting temperatures are measured by thermocouples installed in every other web of each casting at the test section center line. Temperature control of the casting is provided by cooling water tubes in the casting webs. To maintain casting temperature as close as possible to the transpiration air temperature, the casting cooling water is first circulated through a copper tube heat exchanger inside the transpiration header box. The purpose of holding the casting temperature at the transpiration air temperature is to minimize heat transfer between the transpiration air and the casting. Any heat exchange after the temperature of the gas stream has been measured in the casting underbody would introduce an energy balance error. Casting temperature control is also useful to evaluate conduction losses from the plates as will be discussed in Section E of this chapter.

C. Porous Plates

When construction was begun on the Roughness Rig, considerable effort went into the problem of plate fabrication. The porous plates used in the smooth plate HMT rig were made by sintering carefully screened bronze particles whose average diameter was .005 inches in a stainless steel mold, under Stanford supervision. This was necessary because commercially sintered plates exhibited permeability variations of 20 to 30%. The decision to use 0.050 spherical particles on the Roughness Rig virtually eliminated sintering as a possibility.

C.1 Plate Fabrication

When construction of the Roughness Rig began, several west coast vendors were contacted and asked to submit samples of sintered porous plates for porosity testing. Only one vendor, the Commercial Filter Corporation of Los Angeles, submitted a sample. This was constructed using bits of a .030 inch bronze wire sintered into an 8 inch square, 1/2 inch thick plate. Tests revealed that the porosity of this sample was highly non-uniform and it was not acceptable. At this same time, the decision was made to fabricate the plates by assembling particles, rather than by a bulk process, and O.F.H.C. copper balls were chosen as ideal elements. The problem then became one of joining the balls together. Brazing seemed most likely to succeed, providing the braze material could be uniformly applied. Discussions with brazing specialists revealed that a nickel-phosphorus brazing alloy could be deposited on the copper balls. This established the technique which was used to fabricate the porous plates used for the Roughness Rig. The plates are constructed from O.F.H.C. copper balls, .050 inches in diameter. The braze material was provided by plating each ball with .0005 inches of electroless nickel. The balls were then arranged by hand into rows and layers inside copper molds in their most dense array and fired in an inert atmosphere furnace to just above the melting temperature of the nickel plating. This resulted in a brazing together of the ball pack into a uniformly porous plate. The plating material, as it melted, formed small fillets between adjacent balls at each contact point. A close-up photograph of the surface of the porous plate is shown in Fig. 2.8. The final dimensions of each plate were 18.0 x 4.0 x 0.5 inches. This method of plate fabrication, although tedious, provided a well defined surface roughness pattern and uniformly porous plate for the transpiration experiments. A more detailed description of the plate fabrication technique is given in Appendix D.

C.2 Plate Heaters

Eight heater grooves were formed in the back surface of each plate by omitting eight of the rows of balls. The allowable heater wire spacing

is governed by the requirement that the temperature of the top surface of the plate remain uniform. The uniformity of temperature across the top plate surface is determined by the wire spacing, the thermal conductivity, the plate thickness and the transpiration flow rate. An analysis of this problem was carried out by Moffat [1] when the original HMT Rig was designed. Using parameters from his analysis, the temperature non-uniformity in the Roughness Rig plates have been estimated to be on the order of 0.01°F . A key parameter in this analysis is the thermal conductivity of the porous plate. In order to estimate the thermal conductivity of the Roughness Rig plates, the ball pack was thermally modeled by a series of resistances representing the ball layers and nickel connecting spots. Several brazed samples were examined under a microscope to estimate the size of the braze connections between adjacent balls. These varied somewhat but a conservative size for the connecting 'spot' diameter was .008 inches. Using this as an average spot size, the conductivity of the ball pack becomes 30 BTU/hr ft $^{\circ}\text{F}$. This is the value used for the estimate of surface temperature uniformity. It can be argued that this is a somewhat conservative estimate since the arrangement of the balls in the pack are such that a given ball is in contact with 6 surrounding balls on the same layer, but with only 3 balls each in the balls layers above and below. Since the conductivity of the ball pack is controlled by the size and number of contact spots, the ball pack used for the Roughness Rig has a higher apparent thermal conductive across a given ball layer than it does between ball layers.

C.3 Thermocouple Installation

Plate thermocouples were imbedded to a depth that located their junctions at the center of the ball layer below the surface ball layer. Several braze samples were drilled for thermocouple holes and then sectioned to examine the condition of the ball pack around the hole. The brazing process apparently removes all the temper from the OHFC copper balls and they become very soft. It proved difficult to drill the ball pack and the technicians had to carefully prepare the drill bit used for this operation to achieve clean holes. The soft copper

actually wiped itself at the hole surface. The holes appeared to be through solid material when examined in cross section. Upon closer examination, it appeared as if the interstitial regions between ball layers were covered with a very thin layer of copper at the hole surface so the hole appeared to have a solid wall. Further, by drilling the holes on a milling machine, it was possible to locate the bottom of the hole at a ball center in the ball layer below the surface. In this location, the thermocouple junction was .068 inches below the top of the surface layer of balls. Because of the high conductivity of the ball pack, the temperatures recorded by these thermocouples were taken to be the plate surface temperatures. The thermocouples were installed by partially filling the holes with epoxy using a hypodermic needle, then inserting the thermocouple into the hole until it was felt to bottom out. This resulted in a small collar of epoxy squeezing up around the thermocouple at the plate back surface. Every installation was examined from the front surface and there were no cases where bleeding through of the epoxy around the thermocouple holes could be detected.

C.4 Plate Permeability

Uniformity of plate permeability is an important requirement for any transpired boundary layer experiment. Non-uniformities can result in variations in both surface temperature as well as local transpiration rate. Permeability measurements on the plates used in the smooth plate HMT rig were made before their installation. An instrument was developed which sealed off both faces of the plate except for a 3/4 inch diameter spot, and then forced a metered flow of air through that spot. The pressure drop across the plate provide the measure of the resistance to flow through the test area. With this device, porosity maps were constructed by making measurements on one inch centers over the surface of each plate.

Porosity variation measurements on the Roughness Rig plates were made after the plates were in place in the sub-assembly castings, with thermocouples and heater wires installed, using the actual rig transpiration air supply system. After assembly of each casting was complete, it

was installed on the rig support structure, with the transpiration air supply connected and test section sidewalls but not the test section top in place. A constant current hot-wire anemometer was supported on a traversing mechanism mounted on the sidewalls. It was adjusted to a height of about 1/8 inch above the plate surface. Output from the anemometer was run directly into an X-Y plotter. A resistance bridge built into the traversing mechanism drove the plotter such that the pen movement across the graph corresponding approximately to probe movement over the plate. This set-up was used to map the surface velocity of the air delivered through each plate.

Initial results from these tests yielded velocity traces which appeared very lumpy at high blowing rates. The non-uniformity in velocity was several percent and the spanwise period of the velocity disturbances appeared to be several ball diameters. A literature survey into the subject of flow through porous media uncovered several interesting papers which seem to explain the phenomena that had been observed. Two of particular interest are by Bradshaw [44] and Morgan [45], both of whom studied the flow through screens. Both of these studies showed the existence of a critical velocity in the flow through the porous material. Above this velocity, the flow emerges from the porous media as a pattern of jets. These jets coalesce into random groups because they can only entrain fluid from each other. The velocity field investigated by Morgan was behind a two dimensional grid. It showed the same onset of a lumpy structure with a period that was two or three times the grid spacing. To confirm that the "lumpy" surface velocity measurements were the result of the coalescence of the jets leaving the plate surface, the tests were repeated over a wide range of surface velocities. Results from these traces are shown in Fig. 2.9. Here the surface velocity traverses have been superimposed in a single graph. The top graph shows the results obtained by starting at a high surface velocity and reducing it. The top curve is for a surface velocity of 0.39 ft/sec. It shows the lumpy appearance which was observed over all the plates. The magnitude of the non-uniformities is reduced as the surface velocity is reduced but they are still clearly present at 0.21 ft/sec. The velocity

is much smoother at 0.18 ft/sec and at lower surface velocities. This indicates there is a critical velocity at or near 0.18 ft/sec. The lower graph in the figure shows results obtained when the surface velocities are increased beginning from a low value. Here smooth traces are obtained up to 0.24 ft/sec. Above this, the lumpy traces reappear and persist to higher velocities. Apparently the onset of the flow instabilities have a hysteresis-like response to velocity changes. The jets continue to coalesce to much lower surface velocities as the surface velocity is reduced than the surface velocity at which coalescence begins when the surface velocity is being increased.

As a final step to confirm the mechanism, these same tests were repeated over the porous plates in the existing HMT rig. Again the flow showed the same lumpy structure, but the velocity traces appeared much finer grained than had been observed over the rough surface. This was expected since the jet pattern over the smooth surface porous plates should be much finer to start with. It was also noted that the onset of flow instabilities occur at surface velocities above the normal operating range of the rig.

The next step was to investigate the possible effects of this jetting action on the heat transfer experiments. It was feared that the jetting action might artificially enhance boundary layer heat transfer. To evaluate this possible effect, a series of eight Stanton number runs with blowing were made at a test section velocity of 90 ft/sec. At this velocity, it was possible to run several blowing fractions above and below the critical surface velocity observed in the permeability mapping. If there was an effect on heat transfer due to the onset of a surface jetting, it should clearly be seen in the heat transfer data. The data was taken and reduced without corrections for radiation or conduction losses. Although it showed some scatter, it clearly indicated that there was no abrupt change in the surface heat transfer. Apparently, the presence of the boundary flow on the porous surface stabilized the transpiration flow and there was no onset of instability or any similar effect that can be seen in the heat transfer data.

The porosity maps for the plates were completed but the flow striations could be eliminated only by reducing the transpiration

velocity to low values. At these low levels, the width of the recorded line was equal to about 5% of the velocity signal. This prevented the careful resolution of non-uniformities that had been hoped for. With that reservation, the plate porosity appeared entirely uniform: the recorded traces contained no discernible evidence of non-uniformities.

D. Rig Instrumentation

D.1 Temperature Instrumentation

All temperature measurements on the Roughness Rig are made using iron-constantan (ISA type J) thermocouples. Many precautions have been taken to reduce the spurious EMF's frequently encountered in thermocouple circuits. The thermocouples are all brought together at a common test console zone box where they are connected to rotary thermocouple switches for read-out. A diagram of the thermocouple circuit is shown in Fig. 2.10. The thermocouples were made sufficiently long so that the thermocouple wire itself could be used for the test console lead wires. To avoid introducing sharp temperature gradients in any of the thermocouples, all plate, transpiration air, and casting thermocouples were thermally guarded with Polyflo tubing. The test console zone box is constructed from 1/2 inch plywood, lined inside with 1/16 inch aluminum plate and insulated outside with aluminum foil backed, rock wool insulation. All entry ports are gasketed and all busing of wire connections within the zone box is done with thermocouple wire. These precautions were taken to reduce temperature stratification within the zone box and to minimize its effect. Thermocouples are mounted at opposite ends of the zone box to provide a direct measurement of the zone box temperature gradient. In its present configuration, temperature gradients greater than 1/10°F have never been observed. The entire thermocouple circuit uses a single ice-bath reference junction which is also thermally guarded in Polyflo tubing to stretch its thermal gradients. Thermocouple output is measured with a Hewlett-Packard Integrating Digital Voltmeter, Model 2401C.

The most difficult temperature measurement problem in this system is the plate surface temperature. These thermocouples are glued into

close-fitting holes in the bottom of the plate. The wire extending from the bottom surface is exposed to the transpiration air which is at a different temperature than the plate. This tends to introduce an error in the measurement of the plate temperature. To estimate this error on the smooth plate HMT Rig, Moffat [1] developed a thermal model of the thermocouple treating it like a cylindrical fin, partly exposed to the plate and partly exposed to the transpiration air. The problem is complicated by the fact that the thermocouple may not be perfectly bonded in the hole. This problem is modeled by introducing a 'bond factor' between the plate and thermocouple. Because of the small thermocouple wire diameter and relatively deep immersion into the plate, bonding factors can be taken as low as 0.5 and still have conduction errors less than 0.1°F for a 20°F temperature difference across the plate. Subsequent qualification tests on the plate indicated that the thermocouple error due to imperfect bonding and to other sources are acceptably small. These tests are discussed in Section E of this chapter.

None of the temperature measuring locations on the Roughness Rig are so restrictive in space that conduction error becomes a problem. Ample immersion depth is available everywhere.

As noted earlier, each plate contains five thermocouples arranged in a cross pattern. In the tests performed here, these thermocouples were wired in parallel in the instrument console zone box so that an average of their collective readings were taken. Care was taken to size all the thermocouple lengths the same for each casting so if they were ganged together, they would give a true average reading.

D.2 Pressure

Pressures were measured on a variety of manometers and transducers. A 3 inch inclined Merriam Manometer was used to measure tunnel static pressures and to set the top for zero pressure gradient conditions. This same manometer was used to record mainstream total pressure when test section velocities were below 100 ft/sec. At higher mainstream velocities, total pressures were read out with a transducer. Two

Statham unbonded strain gauge differential pressure transducers were used for velocity profile measurements; a PM5 (pressure range 0 to 0.5 psi) and a PM97 (pressure range 0 to 0.05 psi). Both units were equipped with zeroing bridges and individually calibrated in the Thermosciences Measurements Center against a precision 30" Merriam Micromanometer. The H-P 2401 IDVM equipped with an external quartz crystal oscillator clock was used to read the pressure transducers.

D.3 Flow Rate

Transpiration flow rates for each of the porous plates are measured using hot-wire type flow meters which are discussed in Appendix B. The flow signal from these meters is from a differential thermocouple which is read out with the H-P 2401 IDVM using the external clock to extend signal integration time. Before each flow meter reading is taken, the flow meter heater circuit current is checked to insure it is set exactly at the calibration value. This is done by reading the voltage drop across a precision Weston 1 amp shunt, again with the IDVM.

In addition to the flow meter signal, transpiration air temperature for each supply line is measured so the appropriate temperature corrections can be made.

D.4 Electric Power Measurement

One advantage of the D.C. power supply system used in the Roughness Rig is that power measurements are relatively simple. The heater voltage is measured directly with leads which are attached to the heater wires just as they leave the castings. The heater ground connection is made through individual shunts which are mounted beneath the bus bar box. Measurement leads from the shunt and heater are taken in shielded pairs to the same instrument console where the thermocouples are read, but are connected in a separate 'zoned' selector switch station for read out. The heater and shunt voltage are read separately, using the IDVM, and plate power calculations are made in the data reduction program using the individual shunt resistances obtained from an in-place calibration of each shunt. The plate heater power supply voltages have been

carefully scoped to insure that a constant voltage level is applied to each plate over the entire power range. This insures that the selective sampling of the IDVM will yield a truly representative average measurement for the voltage across the heater and shunt.

D.5 Mainstream Conditions

For all runs, mainstream temperature and total-to-static pressure were measured. In addition, mean velocity profiles were taken at several positions along the test section length. Mainstream temperature was measured through the circuitry already described with a probe constructed using .004 inch iron-constantan thermocouple wire. This probe is a fixed position version of the traversing probe described by Kearney [6]. The mainstream total pressures were measured with a Kiel-type probe located in the center of the potential flow region and the static pressures were taken from the adjacent wall tap. All static wall taps were .040 diameter at the wall plane with 0.125 inch diameter tubing connections outside the test section.

Mean velocity profiles were taken using a small diameter boundary layer probe mounted in a micrometer driven traversing probe holder. The probe holder is supported from an instrument sled which is aligned with the instrument ports in the test section top using locating pins and is attached with hold down bolts to the side walls. A photograph of the probe itself is shown in Fig. 2.11. The probe stem is made from 1/8 inch diameter brass tubing. Into the brass stem is soldered a .030 inch stainless steel hypodermic needle which has been bent into a C-shape. The probe mouth has been flattened down to a thickness of .022 inches.

In use, the probe was lowered until it was in visible contact with the rough surface. This could be confirmed with a resistance reading from a VOM attached to the probe and to a thermocouple in the plate the probe was centered over. As the probe was traversed away from the surface, the circuit was broken when the probe lifted from the surface. This method was used to locate the first reading with respect to the crest of the surface balls. The traversing probe was checked at least

once during each run by comparing it with a Kiel probe to insure it was not clogged with dirt particles which would result in erroneous readings. Care was also taken to align the probe before every set of readings to avoid error introduced by probe yaw.

E. Rig Qualification Tests

The Roughness Rig was tested in detail for reliability before being approved for use. There were three types of qualification tests performed: tests of the mainstream condition, instrument system qualification tests and energy balance tests to determine validity of the data reduction program.

E.1 Mainstream Conditions

Extensive uniformity and stability tests were conducted on the test section inlet flow by M. Crawford, another member of the HMT group. The purpose of these tests was to measure mainstream uniformity and local free stream turbulence intensity. The importance of a uniform free stream inlet condition is to insure a two-dimensional flow in the test section. Boundary layer skin friction and enthalpy thickness are inferred from momentum thickness and Stanton Number measurements and the integral momentum and energy equations. A two-dimensional boundary layer is necessary if these techniques are to be used in reducing the experimental data.

To test mainstream uniformity, velocity profiles across the test section inlet were taken using a differential Kiel probe technique. The differential traversing employs two identical probes connected to a differential measuring instrument. This technique allows separation of space-wise and time-wise variation in flow, to a first order at least. If the velocity field can be represented as a product of two functions; one varying slightly in space, the other varying in time, then differential traversing (using probes of the same time constant) will display only space-wise variations on the flow field. Two test section velocities were examined; the lowest velocity, 32 ft/sec and maximum test section velocity, 242 ft/sec. Measurements were taken at 135 positions in the

test section inlet plane at each of the two velocities. The study showed velocity defects no greater $\pm 0.16\%$ at the low test section velocity and $\pm 0.10\%$ at the higher test section velocity.

Free stream turbulence intensity measurement was also made with a DISA 55D05 constant temperature anemometer read through a DISA 55D15 linearizer. The velocity fluctuations about the mean velocity were measured on a Thermosystems RMS voltmeter, Model 1060. Measurements were made at the same two test section velocities and at a total of 120 positions in the test section inlet plane. These results showed a very uniform turbulence intensity over the entire inlet plane with an intensity level of about 0.4% at both test section velocities. This was higher than expected but still below levels measured in the existing HMT Rig. The design objective for the screen pack was a free stream turbulence intensity level of 0.1% to 0.2%. This higher than expected level does not limit the rig's performance.

An additional check on the two-dimensionality of the test section boundary layer was made by measuring its uniformity in the lateral direction at the end of the test section. Lateral holes are provided for this purpose in the test section top over plate 23. Velocity profiles were taken at the test section center and at two positions on either side of the center for a tunnel velocity at 90 ft/sec. Momentum thicknesses from these profiles are plotted in Fig. 2.12, the variation can be seen to be no more than $\pm 3\%$.

E.2 Instrument System Qualification Tests

To qualify the plate temperature measuring system a scheme was used that had been developed for use on the smooth plate HMT Rig. Rather than calibrate the individual thermocouples, they were calibrated in place for each plate. This was accomplished using a plenum box which could be placed over each test plate in such a way as to collect all the air passing through the center 6-inch span. The plenum box was surrounded by four similar guard chambers and was equipped with a guard heater system so that the walls of the box could be maintained at the same temperature as the air. The entire unit was lined with

aluminized Mylar and insulated with 1/2 inch felt. A mixing section was installed in the plenum box so that the air entering from the test plate would be mixed thoroughly before its temperature was measured with two independent thermocouples. The guard chamber surrounding the plenum box was equipped with adjustable area vent holes so all chambers had the same static pressure to prevent cross flows. The bottom surfaces of the box, where it contacts the plates are covered with closed cell foam rubber to further prevent cross flow between chambers. In operation, the guard heater system power is adjusted until thermocouples in the box walls indicate that the box is at the same temperature as the mean mixed air temperature, as measured by the mixing chamber thermocouples. This temperature is then compared to the average of the five thermocouples in the plate beneath the plenum box. These tests were conducted over a range of blowing rates from 5 to 20 CFM and over a range of air temperature differences from zero (no plate power) to 20°F. Over this wide range of temperature and flow conditions none of the plate average thermocouple readings differed from the mixing chamber thermocouple readings by more than 0.2°F (6 microvolts). From these tests it was concluded that the plate temperature measurements as recorded by the five plate thermocouples was satisfactory and errors due to imperfect bonding of the thermocouples and other sources are acceptably small.

While these tests were in progress, thermocouple traverses were made under the plates, just below the honeycomb using a special probe installed through fittings in the side of the castings in the center of each plate. These traverses showed a nearly uniform temperature distribution beneath the plate. Typically these profiles showed higher readings at the plate center by 2 or 3 microvolts than at 3 inches to either side of center.

A final series of tests were performed using the transpiration air system with the top removed, but without plate power. These tests were run with both hot and cold transpiration air, by either by-passing or using maximum cooling in the transpiration air heat exchanger. In addition, either maximum or no casting cooling water was used. The

purpose of these tests was to provide a maximum amount of thermal distortion, without plate power, to insure that the temperature measuring system could properly record these unusual conditions. Operating in this mode, the plate thermocouples can be used to check the single, centrally located air thermocouple located just below the plate. Without plate power, the five plate thermocouples read the average temperature of the transpiration air. In cases where there is a temperature mismatch between the casting and transpiration air, the air thermocouple is subject to error. It was discovered that the casting temperature had a much more dominant effect on the transpiration air temperature than had been thought. When the casting inlet air was colder than the casting, the five plate thermocouples indicated a higher reading than the single air thermocouple behind the plate. The opposite was true when air entering the casting was hotter than the casting. Apparently the air next to the casting is heated or cooled by the casting and enters the plates with a temperature gradient. This gradient was not observed in the traverses taken beneath the plates since these were taken in the longitudinal direction. The measurement error due to the inlet temperature gradient is related to the mismatch between the casting temperature and the temperature of the transpiration air as it enters the casting.

The temperature of the transpiration air is measured at the header box, just upstream of the flow meters to provide the temperature corrections for the flow meter readings but not at the inlet to the casting. To estimate the air temperature at the casting inlet, the transpiration system was modeled as a heat exchanger between the air and the laboratory. Thermocouples were installed at the casting inlet of four plates to check this model and good agreement was obtained. Using the casting inlet temperatures estimated with this model, a correction term was formulated for the air thermocouples. The error was assumed to vary linearly with the inlet air-to-casting temperature difference. This correction, while relatively small aided in closure of system energy balance.

E.3 Energy Balance Tests

Energy balance tests were conducted to establish the validity of

the experimental system. The system includes not only the Roughness Rig and its measuring system but the procedure used to reduce data from the rig. Experimental Stanton numbers are obtained by taking plate power, subtracting off the losses and the energy carried away by the transpiration air, and dividing by the plate-to-free stream temperature difference. In equation form this is given by:

$$St = \frac{(\text{plate power}) - \dot{m}''c (T_w - T_t) - (\text{losses})}{G c (T_w - T_\infty)} \quad (2-1)$$

A key part of the data reduction program is the modeling used to evaluate energy losses. Depending on blowing fractions and plate temperatures, these losses represent from 1% to 10% of the total power supplied. The loss mechanisms modeled are: radiation from the top and bottom surfaces of the plates, conduction between the plates and the casting through the phenolic support webs and conduction through the stagnant air beneath the plates when there is no transpiration. The purpose of the energy balance tests was to evaluate the modeling used for energy losses.

Two kinds of energy balance tests were conducted on the Roughness Rig. Each of these tests provided a direct measure of the ability of the rig's measuring system to produce zero values of measured heat transfer when test conditions were such that there was zero heat transfer.

In the first energy balance mode, the wind tunnel was operated without transpiration and without main stream cooling. In this mode, the free stream temperature equilibrated near 100°F. Plate power was adjusted to match the plate temperature to the free-stream temperature. In this operating condition, the plate power exactly equaled plate losses. These losses were due to radiation from the back of the plate and conduction to the casting and to the air beneath the plate. These tests were run with no casting cooling, to minimize conduction losses, and then again with maximum casting cooling to magnify conduction losses. Since the plate and free-stream temperatures were the same, there was no heat transfer between the plate and the free-stream. The difference between measured plate power and calculated losses for the observed conditions represent a potential Stanton number error. Data taken from this energy

balance run were reduced with the data reduction program and the net Stanton number error was evaluated using the energy balance difference and a typical plate-to-free stream temperature difference:

$$St = \frac{(\text{plate power}) - (\text{calculated losses})}{G c (T_w - T_\infty)_{typ}} \quad (2-2)$$

The typical temperature difference used was 25°F which is representative of the Roughness Rig test conditions. Figure 2.13 shows a plot of Stanton number error versus distance along the test section. There was some difficulty in closing the energy balance in the first few plates, attributed to an inlet thermal boundary layer. With the tunnel operating hotter than ambient, a thin thermal boundary layer of cool air next to the duct walls was unavoidable. Since the plate and free-stream temperatures were equal, the first few plates removed the inlet thermal boundary layer and acted as guard heaters for the rest of the test section.

In the second energy balance mode, the tunnel was operated with transpiration flow only and with the test section top removed so that the transpiration flow moved directly upwards. In this operating condition, there was, again, no surface heat transfer. All the plate power was taken up either in losses or by the transpiration flow. These blowing energy balances were conducted over a wide range of transpiration rates and air-to-plate temperature differences, again to demonstrate the adequacy of the data reduction program to predict the losses and achieve energy balance closure at all operating conditions. For this case the potential Stanton number error was given by:

$$\Delta St = \frac{(\text{plate power}) - \dot{m}'' c (T_w - T_t) - (\text{calculated losses})}{G_{typ} c (T_w - T_\infty)_{typ}} \quad (2-3)$$

Blowing energy balance runs were made at 2, 8, 15 and 22 CFM which covers the range over which the Roughness Rig experiments were conducted. As before, the typical temperature difference, $(T_w - T_\infty)_{typ}$, was taken at 25°F. The typical mass flow, G_{typ} , was chosen so that the combination of it with the transpiration rate would give a blowing fraction of .008,

the maximum tested. This was done for all but the lowest transpiration rate. The value of G_{typ} used for both 2 CFM and 8 CFM corresponded to the minimum test section velocity. A plot of the Stanton number error from these tests versus distance along the test section is shown in Fig. 2.13. As can be noted, the Stanton number error was, in almost every case, within ± 0.0001 Stanton number units. In those few cases where the error exceeds this value, subsequent energy balance tests did close to within ± 0.0001 level. This has led us to believe that the Stanton number data are reliable to within ± 0.0001 Stanton number units over the range of conditions tested.

E.4 Verification of the Data from Plate 24

Despite the excellent closure that was obtained in the energy balance tests, an anomaly was noticed in the heat transfer data from plate 24. At conditions of high blowing and high test section velocity, plate 24 exhibited a much lower Stanton number than its neighbor, plate 23. This behavior was entirely repeatable and in fact was visible in earlier data taken when the rig was first being shaken down, but was not as apparent then. After carefully confirming the flow meter calibration and the temperature measuring system it was concluded that the reduced Stanton number was real and not the result of trouble in the measuring system. A review of the possible sources of this problem led to the conclusion that it was related to the diffuser, directly downstream of plate 24. It seemed likely that at high blowing rates, when there was injection of low momentum fluid into the boundary layer, the exit diffuser experienced stall. This stall probably began right at the diffuser inlet but may have propagated upstream to plate 24 itself. The presence of the 'stall bubble' could disturb the flow in the region near plate 24 enough to reduce the plate heat transfer. The exit diffuser was designed to operate without stall, however it is known that the inlet velocity profile has an important effect on diffuser performance. A thickened boundary layer due to blowing could result in stall that would otherwise not have been there. To confirm this possibility a temporary extension of the test section surface was installed in the first stage of the diffuser. This

extension produced a step in the flow path at the inlet to the second stage of the diffuser and reduced the overall performance of the diffuser, but did remove the influence of the diffuser from plate 24. The tunnel was then run at 240 ft/sec with a blowing fraction of .002, without the step. After reaching equilibrium, data were recorded and then the diffuser insert was installed and the run repeated. The insert reduced diffuser performance so that the test section velocity only reached 226 ft/sec. Since the flow meter settings were unchanged, a slightly higher blowing fraction resulted. This reduced the Stanton number slightly below the previous data, but the plate 24 Stanton number was significantly increased. It was still slightly low (.0001 Stanton number units) but much improved over the Stanton number without the insert. Figure 2.14 shows the Stanton number data from these two tests.

Because of this difficulty, the plate 24 data has not been shown for data runs at high velocity and blowing fraction but is listed with the tabulation of experimental results in Appendix E, for completeness.

F. Data Reduction Program

In reducing data taken from the Roughness Rig experiments, three separate data reduction programs were used, two for the hydrodynamic data and one for the heat transfer data.

The first data reduction program was used for the boundary layer mean velocity profiles and converted the pitot tube pressure readings to velocity. It then executed a simple trapezoidal rule numerical integration to get momentum and displacement thicknesses and finally shape factor. The second data reduction program used a least square curve fit to the momentum thickness data for the entire plate length to determine the skin friction, using the integral momentum equation for the two-dimensional boundary layer. It was assumed that over the relatively small momentum thickness range of a single run, the momentum thickness varied as a simple power law with distance along the test section. The equation which was curve fit was:

$$\theta = a(x-x_0)^b \quad (2-4)$$

where x_0 is the boundary layer virtual origin and a , b and x are determined by the curve fit. The procedure used was that of 'weighted residuals' as described in Chapter 18 of Scarborough [46]. Since no trip was used in the Roughness Rig experiments both laminar and turbulent regions existed inside the test section. Only momentum thickness measurements taken in the fully turbulent boundary layer were used in the fit. The Stanton number data was then examined to ensure that each of the velocity profiles used had been in the fully turbulent boundary layer. To qualify this procedure for predicting skin friction, the momentum thickness measurements taken by Andersen [8] and by Simpson [2] were used as a trial data set. The skin friction data reported by Simpson were based on his 'best estimate' using several evaluation methods. Skin friction predictions by Andersen were made using turbulent shear measurements taken in the boundary layer, then extrapolated to the wall. Figure 2.15 compares skin friction predictions made by the present curve fitting method to the values originally reported. For both data sets the curve fitting method yields a reasonably good check of the skin friction values that Simpson and Andersen found by independent means. Since both of these data reduction programs are straightforward applications of well known principals, listings of the programs are not given.

The data reduction program for the heat transfer data is more complicated since it must convert data from the Roughness Rig into Stanton numbers. A flow diagram for the data reduction program is shown in Fig. 2.16 and a Fortran listing is given in Appendix F. The program has several features. It contains the individual calibrations for each flow meter and performs a logarithmic interpolation to obtain the flow from each flow meter reading, based on the calibration data points. Thermocouple readings are converted into temperatures by interpolating in tables taken from National Bureau of Standards Circular #561. Plate voltage and shunt voltages are converted into power using calibrated resistance values for each shunt and correcting for excess heat release due to the turnaround wrappings of the heater wires at the plate ends. It also estimates conduction and radiation losses from each plate based on plate, casting and other rig temperatures. The program also converts manometer readings

to pressure levels and the free-stream thermocouple reading into the free-stream total temperature using a 0.96 recovery factor for the thermocouple probe. The program has two output options: the summary output shown in Appendix E and a more detailed output with additional diagnostic information.

G. Experimental Uncertainties

To investigate the possible effects of measurement uncertainty on the experimental Stanton number, the following procedure was used. The data reduction program was used to calculate the derivative of each experimental variable with respect to the Stanton number. This was done by sequentially varying each variable by the amount of its uncertainty as input to the data reduction program and calculating the change in Stanton number which resulted. Assuming that these uncertainties are all independent they can be combined by the procedure of Kline and McClintock [47].

The results of this uncertainty analysis is shown in Fig. 2.17 for all test section velocities, over the range of blowing in these experiments. As can be seen, the lowest test section velocity, at high blowing is the most affected by the propagation of uncertainties in these experiments. The following basic uncertainty intervals were assumed for the input values:

Plate Voltage	1 millivolt
Shunt Voltage	10 microvolts
All Temperatures	10 microvolts
Stagnation Pressure	.002 inches of water
Flow Meter Readings	25 microvolts

It can be concluded from this study that except at high blowing the uncertainty in Stanton numbers due to random errors is less than the $\pm .0001$ Stanton number units cited earlier based on the energy balance tests.

Another area of experimental uncertainty associated with these experiments is associated with the velocity profile measurements. A problem which is common to all rough surface boundary layers is the location of the origin of the velocity profile. Profile measurements begin with the probe resting on top of the rough surface. The location of this data

point with respect to the surface is known, but examination of the profile data indicates that the origin of the profile is somewhere below the ball crests. Several authors have discussed systematic procedures for determining 'origin error'. What has been done in the present work is to examine each profile on an individual basis and extrapolate to what appears to be a reasonable choice for its velocity origin. Generally this turned out to be .010 inches below the ball crests. The bounds on this number would be from zero (the profile origin at the ball crests) to a maximum of .025 inches, the profile origin at half of the ball diameter. With these bounds, it seems unlikely that the experimental uncertainty of the profile origin could exceed $\pm .010$ inches. To investigate the sensitivity of the integral boundary layer parameters to an uncertainty in the profile origin of $\pm .010$ inches, the velocity profile data reduction program was used. A portion of the profile data was reduced again with a .010 inch shift in the profile origin. It was not surprising to find that the displacement thickness was very sensitive to the shift while the momentum thickness was not sensitive. There was no detectable effect of test section velocity: this is not surprising since the boundary layers were all very similar at all test section velocities. A more important parameter was the thickness of the boundary layer. Near the front of the test section where the probe could not penetrate as deeply into the thin boundary layer, an origin error of .010 inches produced errors on the order of 10% in the boundary layer displacement thickness and 1% in the momentum thickness. At the end of the test section, where the boundary layer was thicker, the uncertainty in profile origin produced errors of 7% to 8% in displacement thickness and again, 1% in momentum thickness. From these results, we have concluded that the experimental uncertainty in the profile virtual origin results in uncertainties on the order of 10% in the boundary layer displacement thickness and 1% in the momentum thickness.

Some additional work has been done to translate the momentum thickness uncertainty into uncertainty in the skin friction prediction. This can be done by varying the inputs to the program which uses a fit to the momentum thickness data to predict skin friction. The results from

study have been inconclusive. The effect of the momentum thickness uncertainty depends on how many other points used by the curve fit remain unchanged and even on which point is perturbed. Another very important parameter is the blowing fraction, since it is subtracted from the momentum thickness before the skin friction fit is made. A general result which was obtained is that a 1% variation in momentum thickness, for the non-blown boundary layer could produce a variation of 8% to 10% in skin friction in a boundary layer with 5 or more velocity profiles as basis for its least square fit. In many cases, the variation was less and in cases with high blowing the variation was greater. Because of the many difficulties inherent in taking the derivative of experimental data points, it is felt that no further claims about the accuracy of the skin friction data generated by fitting the momentum thickness measurements was justified. Experimental work now in progress on the Roughness Rig should produce much better skin friction data, with much less experimental uncertainty.

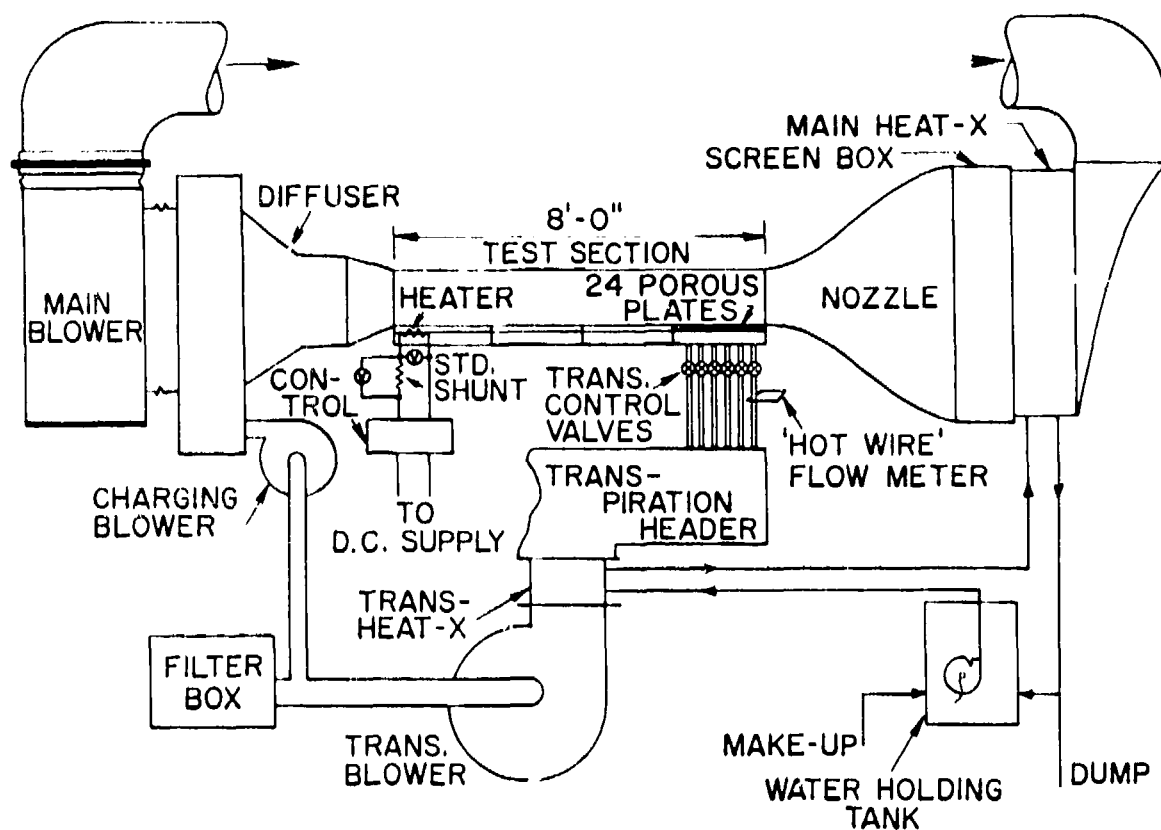


Fig. 2.1 Rough surface wind tunnel flow schematic

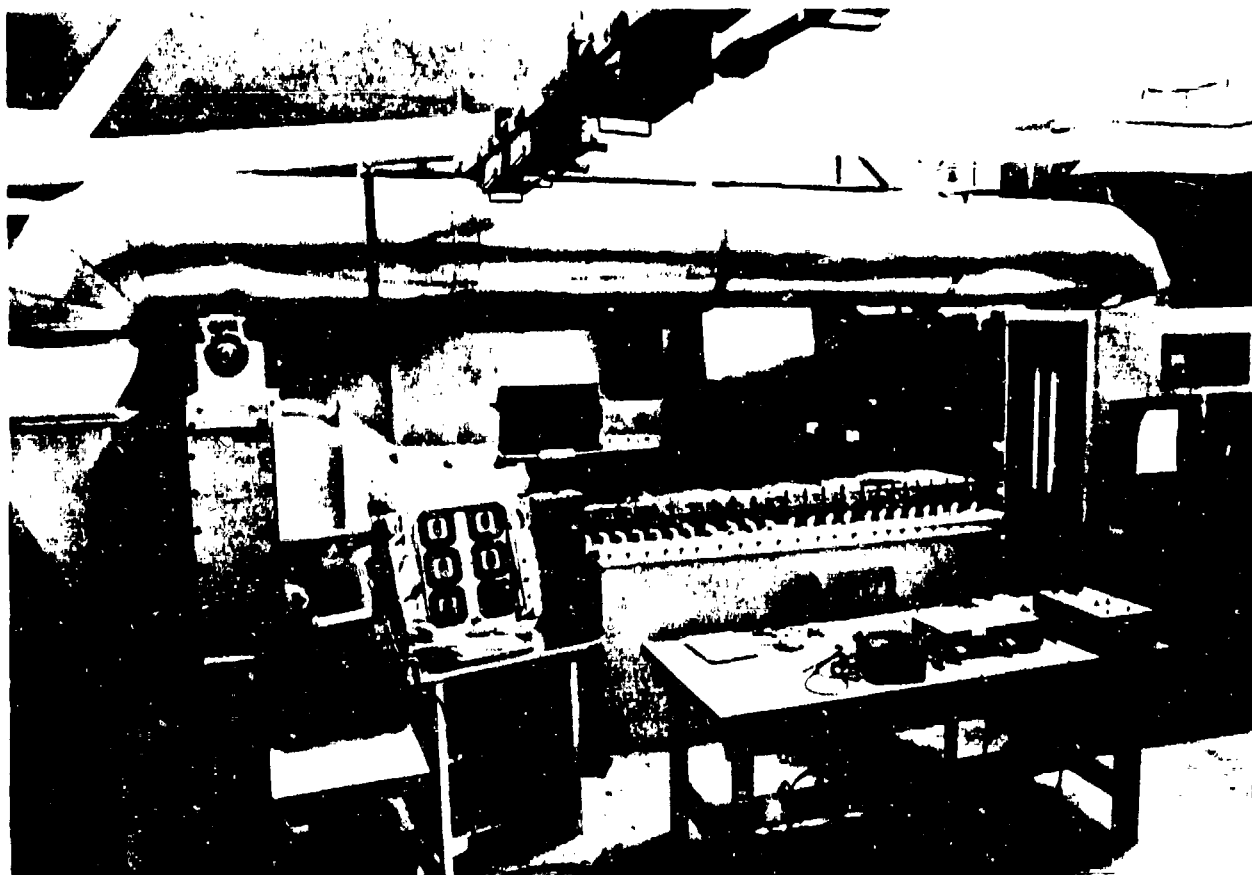


Fig. 2.2 Photograph of Roughness Rig

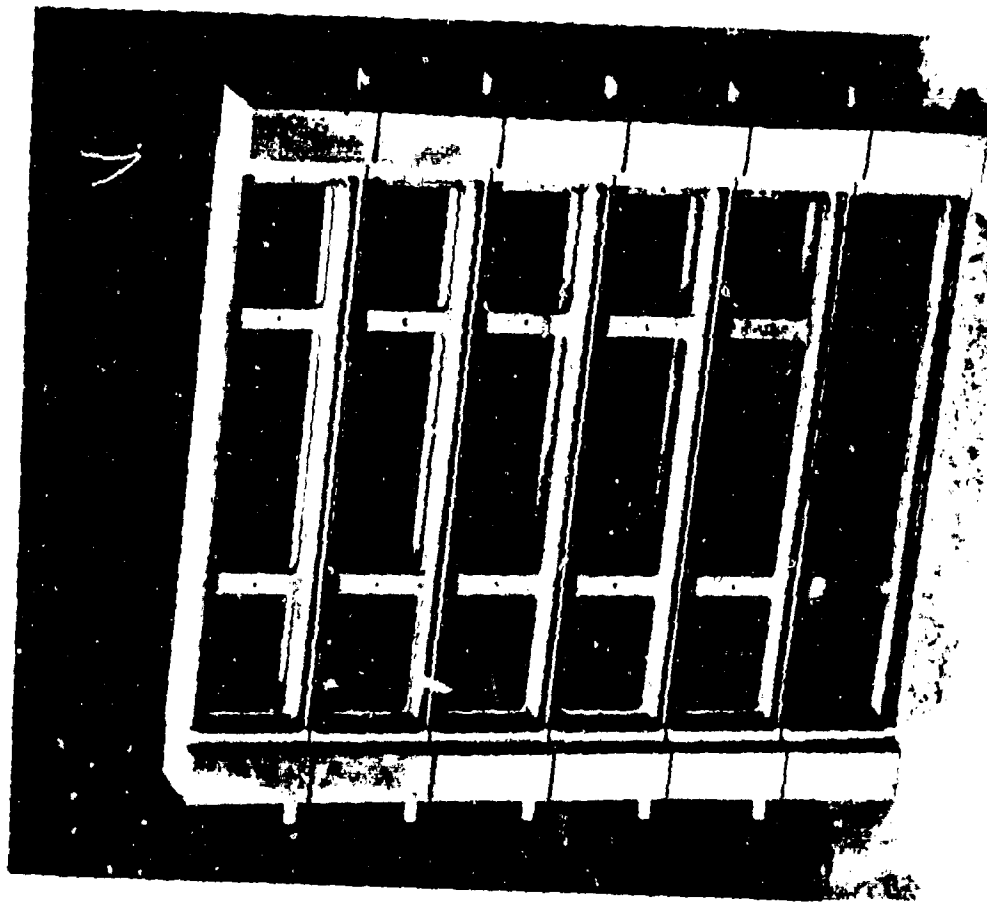


Fig. 2.3 Photograph of aluminum casting

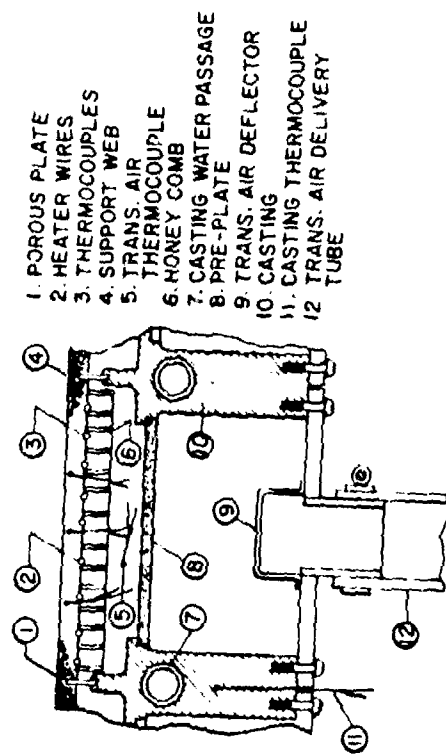


Fig. 2.4 Cross section view of typical compartment

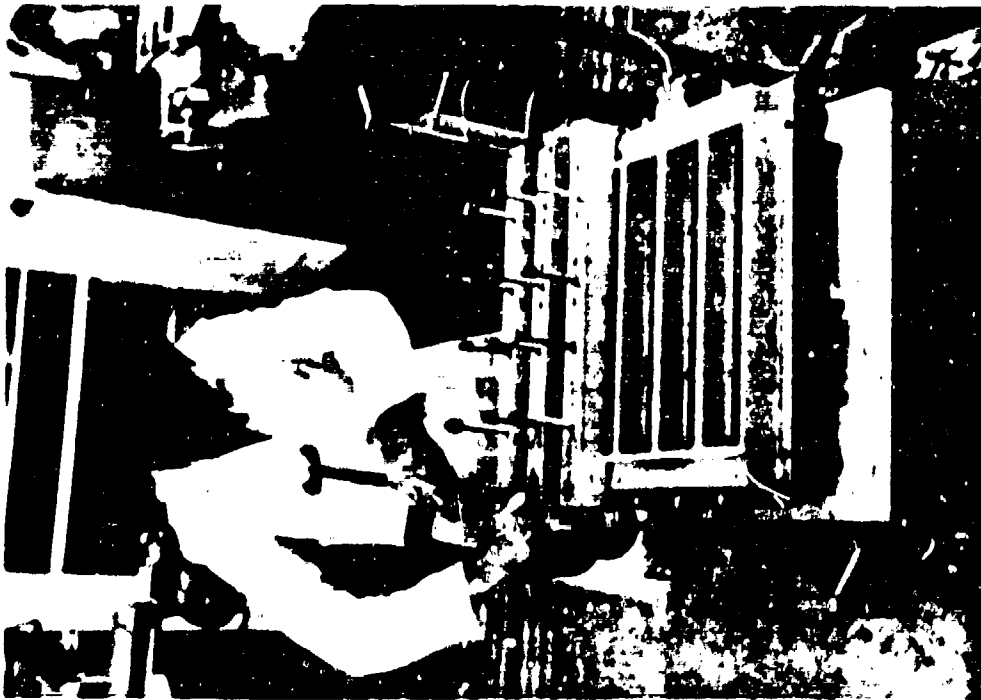


Fig. 2.5 Photograph of clamping arrangement
used for gluing the plate and casting
assembly



Fig. 2.6 Photograph of the back of the casting
assembly

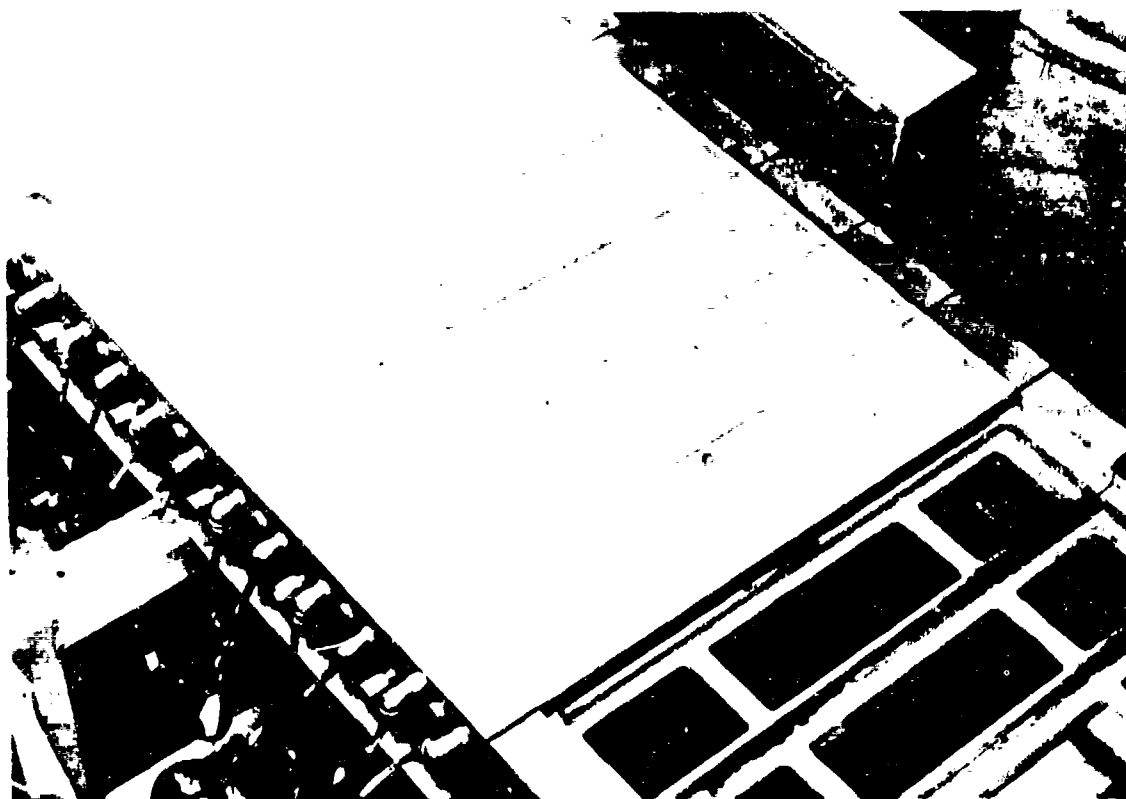


Fig. 2.7 Photograph of the top of the casting assembly

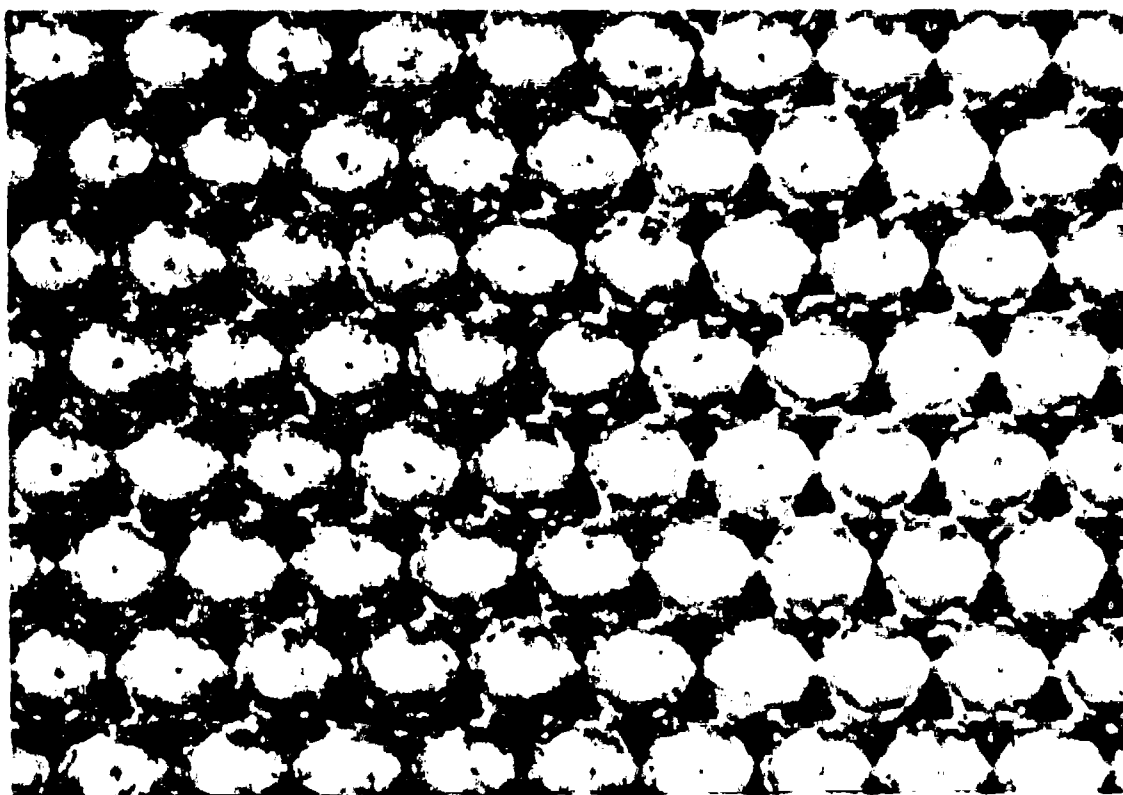


Fig. 2.8 Photograph of the rough surface, close-up

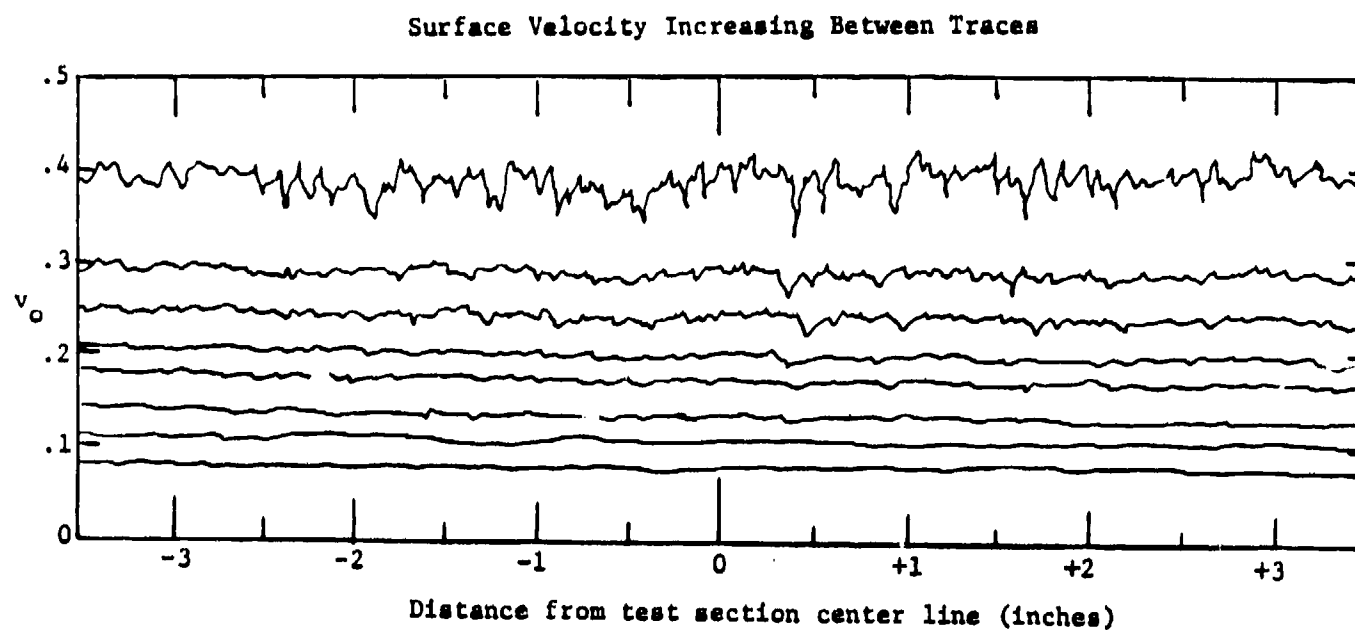
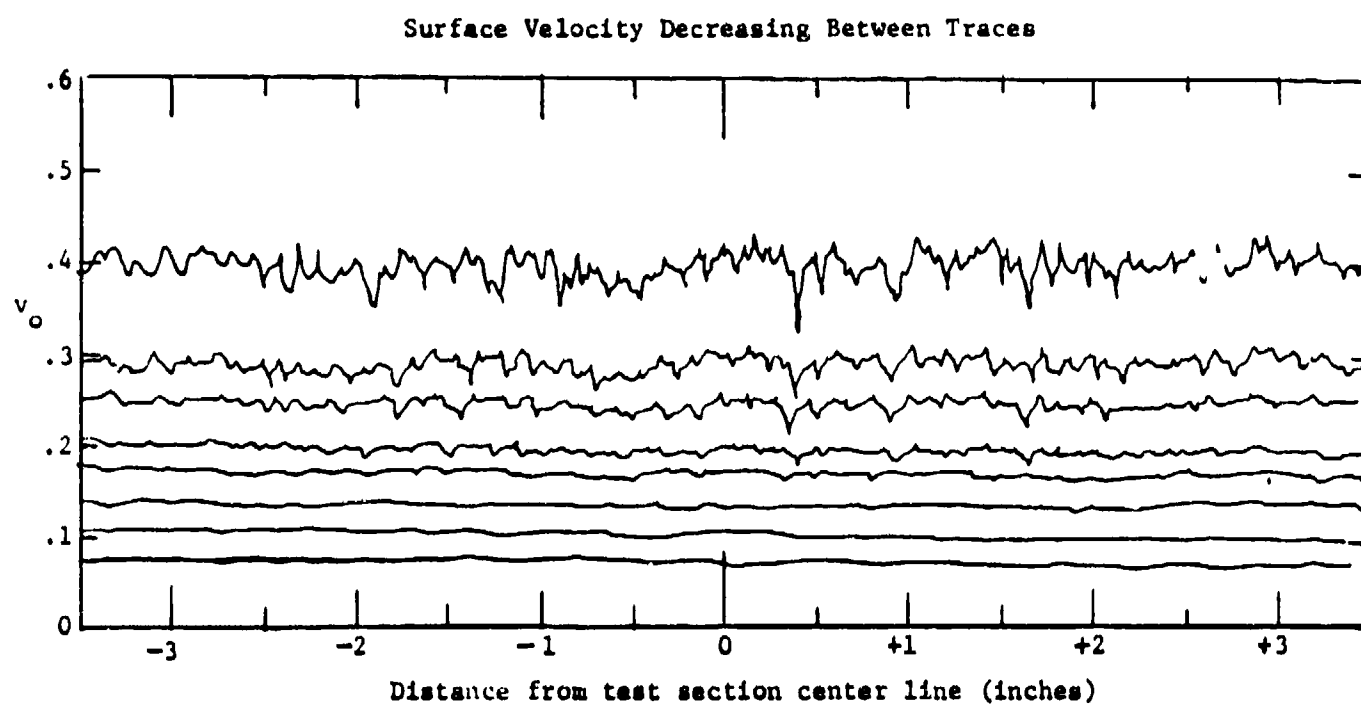


Fig. 2.9 Velocity distribution above the Roughness Rig surface

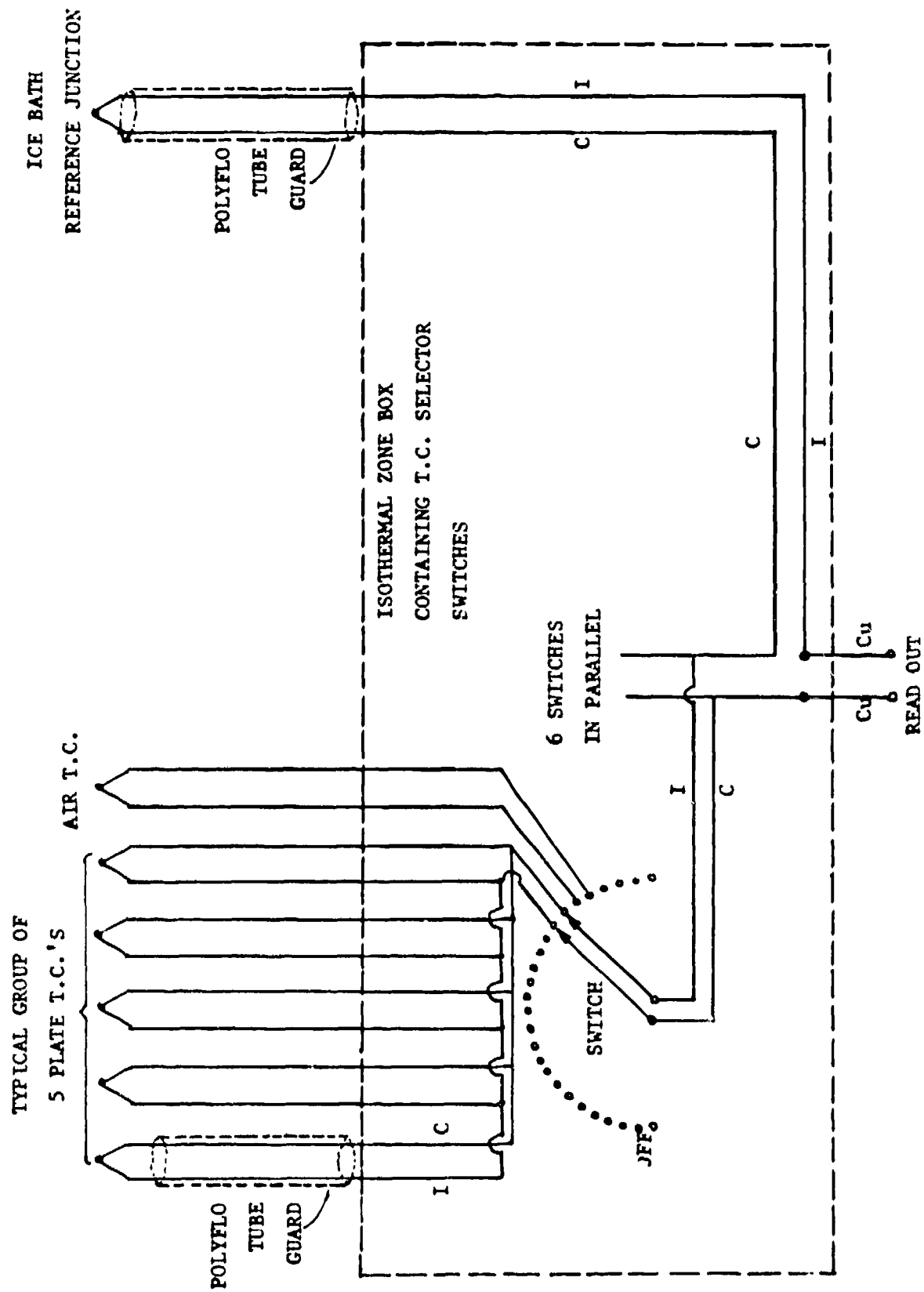


Fig. 2.10 Roughness Rig thermocouple schematic



Fig. 2.11 Photograph of the Pitot probe

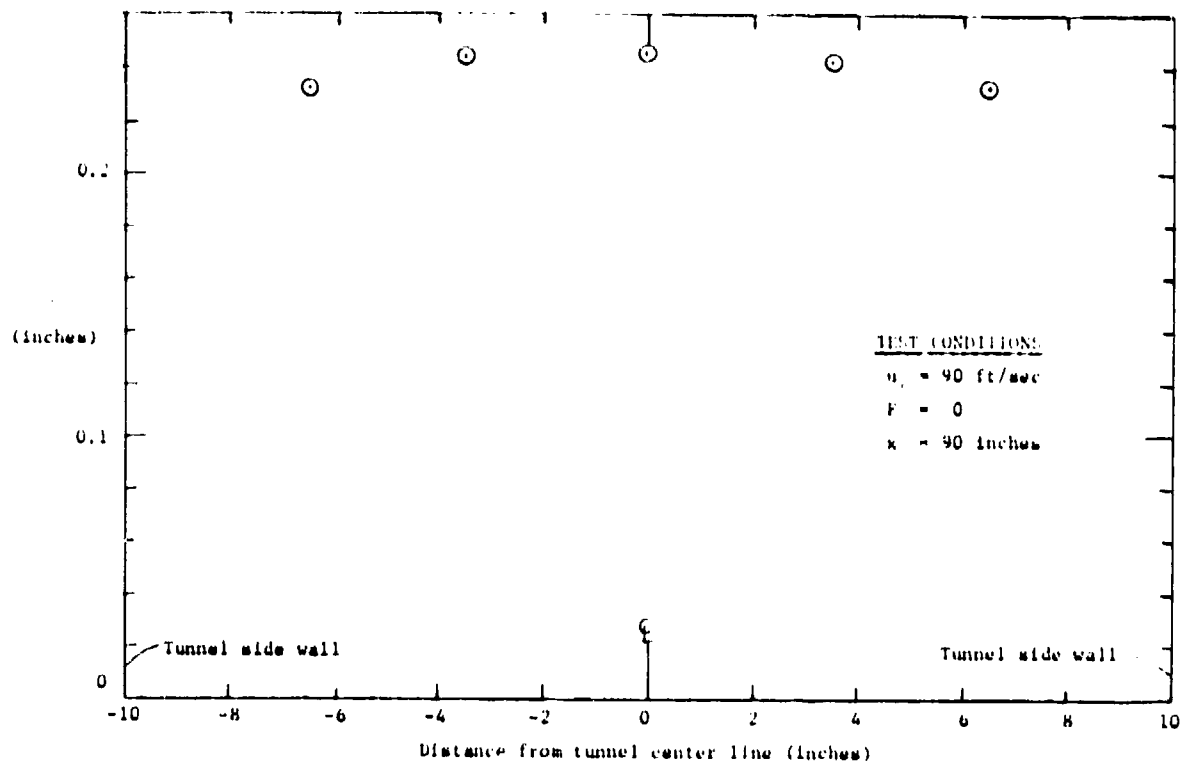


Fig. 2.12 Momentum thickness distribution across the tunnel at plate 23

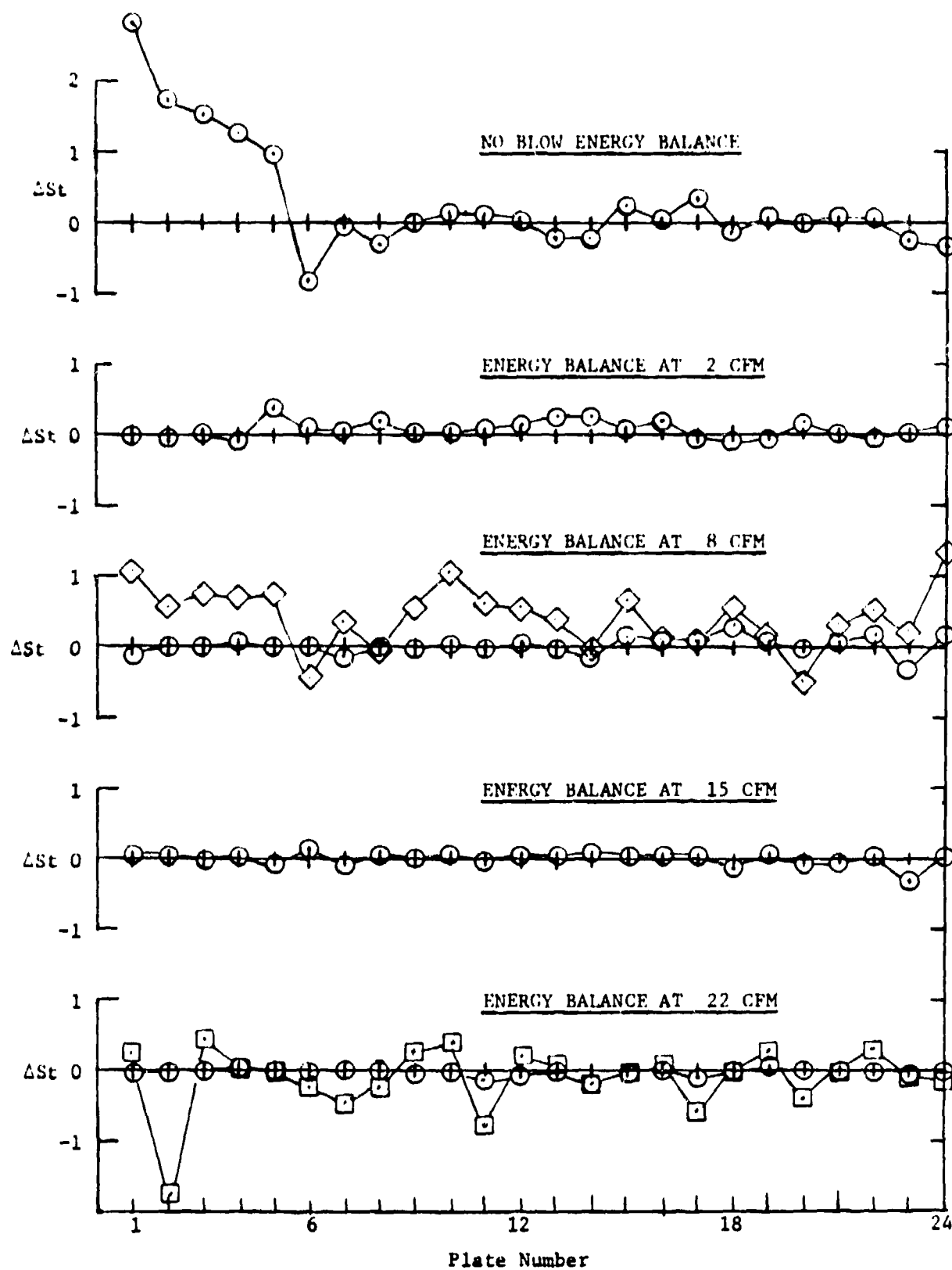


Fig. 2.13 Non-blown and blowing energy balances

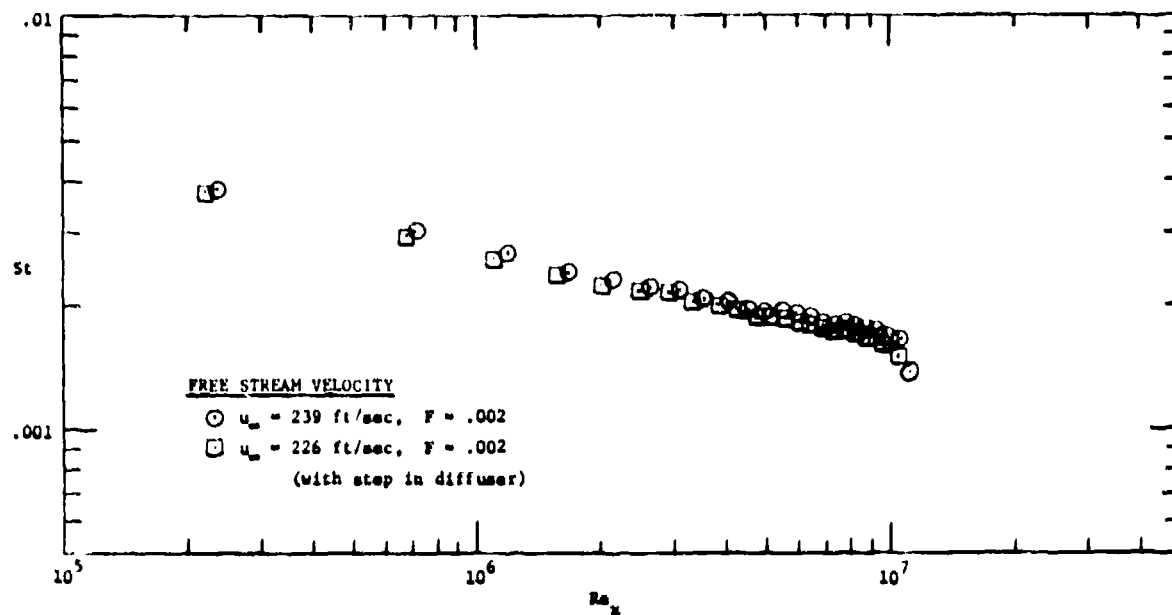


Fig. 2.14 Stanton number versus x -Reynolds number for $u_{\infty} = 239$ fps, $F = 0.002$ (standard) and for $u_{\infty} = 226$ fps, $F = 0.002$ (with an insert in the diffuser)

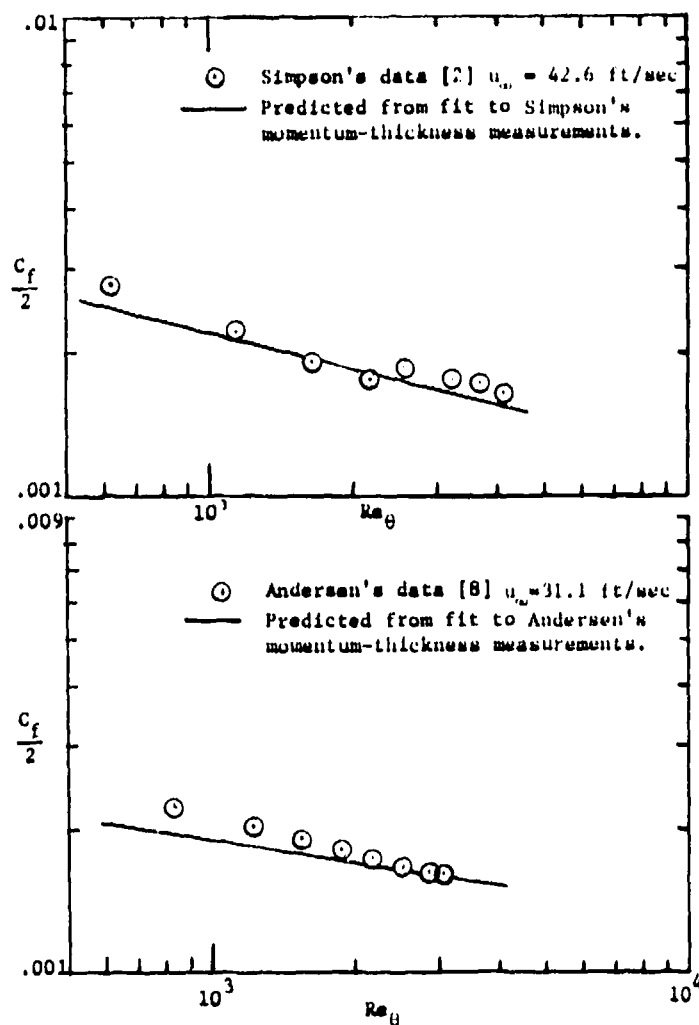


Fig. 2.15 Comparison of skin friction predictions to data by Andersen [8] and Simpson [2]

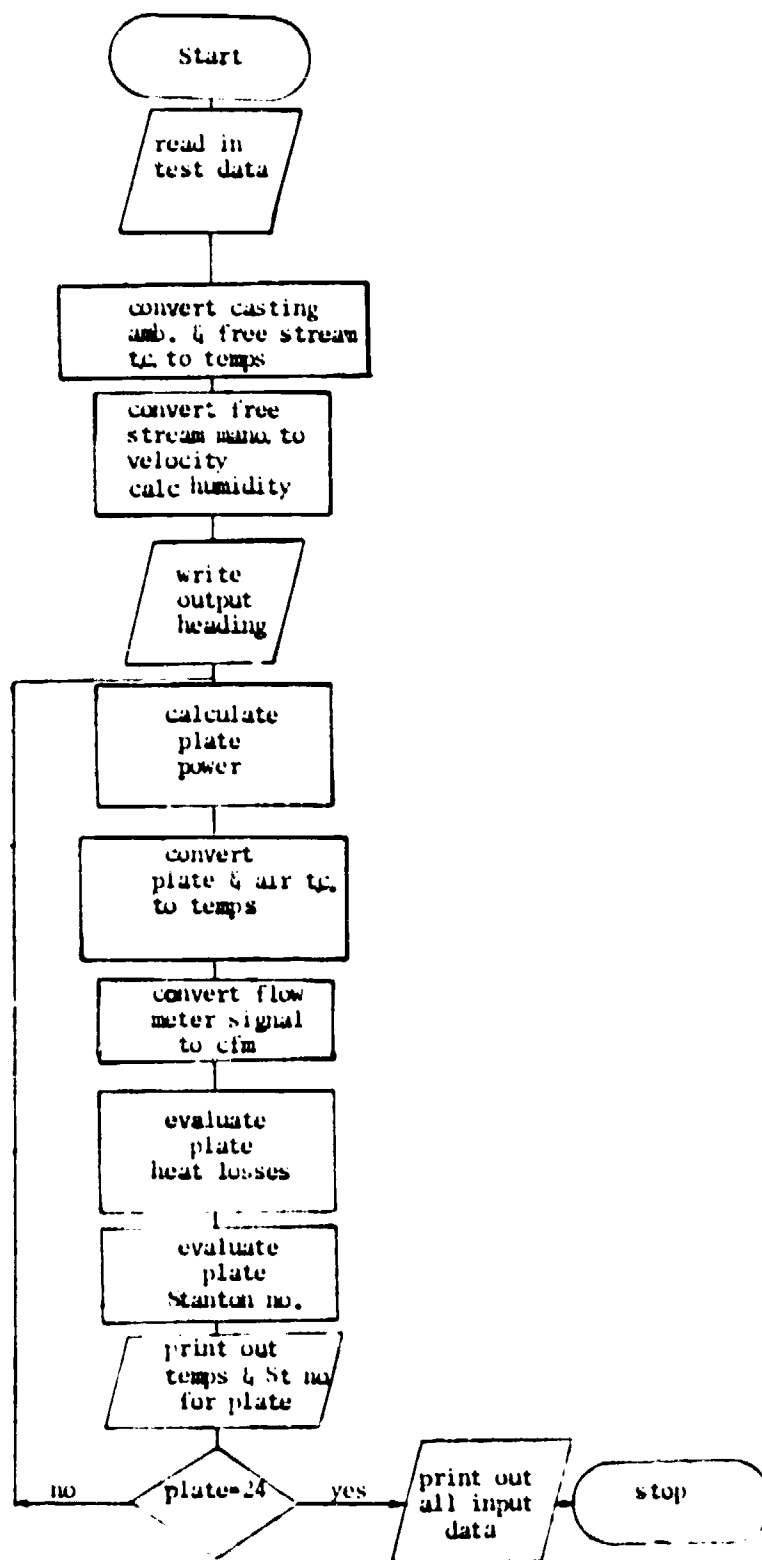


Fig. 2.16 Data reduction program flow chart

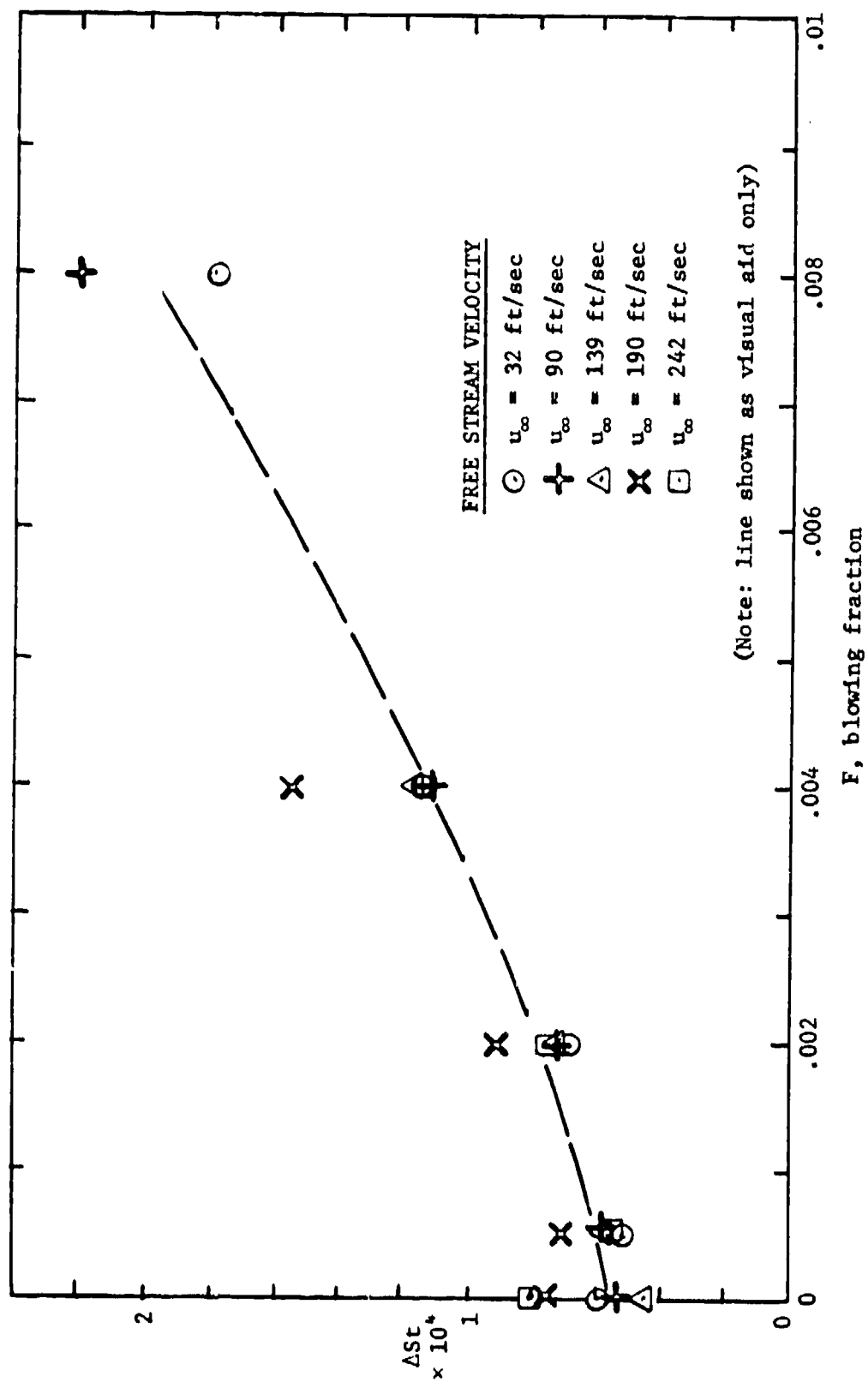


Fig. 2.17 Stanton number error due to experimental uncertainties

CHAPTER III

EXPERIMENTAL RESULTS

Measurements taken in these experiments can be divided into two types -- Stanton number data and mean-velocity profile data which were used to infer boundary layer momentum thickness and skin friction.

The range of conditions for the Roughness Rig tests can be summarized as in Table 3-1. The data taken can be organized into the following blocks: fully developed turbulent boundary layer skin friction and Stanton number without blowing, the effects of blowing on rough surface Stanton number and friction factor, and rough surface transition with and without blowing. The presentation of the data will be organized in the same manner.

A. Rough Surface Boundary Layer Data without Blowing

Rough surface boundary layer friction factors and Stanton numbers are plotted against x -Reynolds number in Fig. 3.1 for each of the five test-section velocities used. It is apparent that there is a roughness effect and that, in these coordinates, the friction factor and the Stanton number increase with test section velocity. This is an important difference from smooth plate data, which do not show a velocity effect in these coordinates. Smooth plate data for air in this range of x -Reynolds number would correlate, for all test-section velocities, with equations of the form:

$$\text{Smooth} \quad c_f/2 = .0295 Re_x^{-0.2}, \quad (3-1)$$

$$\text{Smooth} \quad St = .0295 Pr^{-0.4} Re_x^{-0.2} = .034 Re_x^{-0.2}. \quad (3-2)$$

For comparison, these two correlations are shown in Fig. 3.1. Only the 32 fps data seem to be approaching the smooth plate correlations.

With transition occurring at different locations for each velocity, it might be argued that the failure to correlate is due to different locations of the boundary layer 'virtual origin'. To avoid this problem,

Table 3-1

Roughness Rig Test Conditions

Nominal Test Section Velocity (ft/sec)	32	90	135	190	242
Blowing Range (m"/G)	0 to .008	0 to .008	0 to .004	0 to .004	0 to .002
x-Reynolds Number $\times 10^{-6}$ (measured from test section inlet)	.03 to 1.63	.09 to 4.23	.19 to 6.60	.44 to 9.11	.49 to 11.23
Momentum Thickness Reynolds Number $\times 10^{-3}$ (for no blowing)	.24 to 3.1	.41 to 10.6	.84 to 17.0	1.41 to 23.9	1.52 to 30.5
Roughness Reynolds Number (for no blowing)	24 to 29	64 to 79	101 to 124	142 to 160	178 to 200

boundary layer data are frequently presented in local coordinates. Fig. 3.2 shows friction factor and Stanton number as functions of local momentum thickness Reynolds number and enthalpy thickness Reynolds number, respectively. In these coordinates, too, the effect of the rough surface has been to separate the data taken at different test section velocities. Also shown are typical correlations for a smooth plate in local coordinates:

$$\text{Smooth} \quad c_f/2 = .0128 Re_\theta^{-.25} \quad (3-3)$$

$$\text{Smooth} \quad St = .0128 Pr^{-0.5} Re_\Delta^{-0.25} = .0153 Re_\Delta^{-.25} \quad (3-4)$$

It is apparent that boundary layer thickness Reynolds number is not a sufficient descriptor for the rough surface data. At any boundary layer thickness Reynolds number, higher velocities yield higher values of friction factor and Stanton number. While the data at 32 fps lie close to the smooth correlations, at the highest test section velocity the friction factor is nearly twice the expected smooth plate value. At that velocity the Stanton number is up by about one and one-half times. This behavior is similar to that reported by Nunner [23] for rough pipes. His results, given by Eqn. (1-1), show the increase in heat transfer due to roughness approximately equal to the square root of the increase in skin friction.

The present data are clearly affected by the surface roughness. As already noted in Chapter I, the roughness Reynolds number, $Re_\tau = u_\tau k_s / \mu$, is often used to categorize the behavior of rough surfaces. Values less than 5 to 10 define 'smooth' behavior, while between 10 and 70 the surface is described as 'transitionally rough', and above 70 it is referred to as 'fully rough'. The roughness Reynolds number range for these tests is shown in Table 3-1. The 32 fps data lie between 24 and 29, in the 'transitionally rough' range, while all other velocities have 'fully rough' roughness Reynolds numbers. For these calculations, k_s , the equivalent sand-grain roughness was taken as 0.625 times the ball diameter, yielding an equivalent sand grain roughness of .031 inches. This multiplier is the value recommended by Schlichting [51] for densely packed spheres.

The effects of roughness are also evident in the rough surface velocity profiles. Fig. 3.3 shows velocity profiles from these experiments at different test section velocities. In Fig. 3.4, velocity profiles are shown for one velocity and several different stations along the test section, along with a typical velocity profile for a smooth surface. The rough surface velocity profiles show the characteristic offset or depression when plotted in wall coordinates. The amount of the depression, Δu^+ , can be used to determine the equivalent sand grain roughness of the surface, as described by Schlichting. Applying this method to the non-blown velocity profiles from these experiments, the ratio of the equivalent sand grain roughness to the ball diameter is found to be very nearly the same for all the velocity profiles lying between 0.60 and 0.63. This confirms the value recommended by Schlichting for a similar surface, but tested in duct flow instead of boundary layer type flow.

One difficulty in interpreting rough surface velocity profiles arises in determining the profile origin. Typically, the apparent surface of the rough plate lies below the tops of the roughness elements. Different investigators have handled this problem in different ways. Tsuji and Iida [19] measured velocity profiles from the crests of the roughness elements. Others, such as Moore [12], Perry [14,15] and Liu [16], place the profile origin below the crests of the roughness elements. Perry has argued that the distance below the rough element crests should be adjusted until the velocity profile plotted in semi-log coordinates exhibits the familiar 'log' region. This approach establishes both the wall shear and the 'logarithmic asymptote', which is the distance below the roughness element crests to the profile origin. All of the methods which have been suggested require some judgment by the individual examining the data. In the present work, still another method was used: origins for the velocity profiles taken in these experiments were determined by extrapolating the data to zero in cartesian coordinates, by eye. Typically, the origins for the turbulent velocity profiles fell about .010 inches below the crests of the balls. Laminar and transitional profiles were depressed less. Using the origins determined

in this manner, the profiles were integrated to obtain momentum thicknesses which were then used to evaluate skin friction. This approach provides a convenient basis for determining origins for all the profiles and yield results similar to what would have been obtained using Perry's method for the fully turbulent profiles.

One interesting result obtained from the velocity profile data is that the apparent roughness of the plate seems independent of both distance along the plate (boundary layer thickness) and of free-stream velocity (viscosity effects). Thus the roughness effects seem to scale on roughness particle size, not on 'relative particle size'. This is different from rough pipe data, where roughness effects scale on (k_s/d) , the ratio of the roughness size to the pipe diameter.

Early rough surface boundary layer experiments demonstrated that the skin friction becomes a function of x/k_s alone. It follows from this that the momentum thickness also must be a function of x/k_s alone for the zero-pressure gradient flow if the surface roughness is not changing. Fig. 3.5 shows measured values of θ versus $(x-x_0)$ for each of the test section velocities, x_0 being the appropriate virtual origin. The growth curves of all the boundary layers are substantially the same. Also shown is the expected behavior of a smooth plate at the same test-section velocities. Although the 32 fps data are somewhat low and the 190 and 242 fps data show a slight shift at the downstream end, the coherence is good compared to the smooth plate curves. The two-dimensional integral boundary layer equation for flat plate unblown flows is:

$$\frac{c_f}{2} = \frac{d\theta}{dx} \quad (3-5)$$

From Fig. 3.5 it can be seen that $d\theta/dx$ is substantially independent of velocity, above 32 fps, being the same function of θ for all velocities. From this observation $c_f/2$ is mainly a function of θ alone. This might have been anticipated from early data which showed $c_f/2$ was only a function of x/k_s and independent of velocity.

Skin friction, deduced by differentiating the individual curves of θ versus x , is shown in Fig. 3.6 plotted against the ratio of momentum thickness to ball radius. The 32 fps data are clearly low, and there

remains a small velocity dependence in the other data. At the two highest velocities, the skin friction lies 10% to 15% above the other data at the downstream end of the plate. It's difficult to assess the significance of this, based on the present data. An error in measurement of θ of only 3% to 5% could produce the differences observed in the friction factors. Further, smooth surface data, if plotted in these same coordinates would place the low-velocity skin friction above high-velocity values. This suggests that the velocity dependence observed here is probably not an approach to the 'fully rough state'. Finally, the Stanton number data show no such tendency, and they are less sensitive to errors which may be present in the skin friction data.

Figure 3.6 also shows the Stanton number data for all five velocities used, plotted versus Δ/r , where Δ is the enthalpy thickness of the boundary layer. The data are coherent for all velocities in the turbulent region, including the data for 32 fps. After an initial overshoot of a few percent, the 32 fps Stanton number data fall on top of the data for all higher velocities. The turbulent data show no velocity dependence; the Stanton number is a function only of Δ/r , for all velocities. It is interesting to compare the values of Stanton number and friction factor at the same boundary layer thicknesses (i.e., $\Delta/r = \theta/r$). Friction factors for 90 and 140 fps tend to lie about 5% above the Stanton number values all along the plate, rather than 15% low, as in the smooth plate case. The agreement between the 32 fps data and those for higher velocities was surprising, in view of the friction factor results. Furthermore, the roughness Reynolds number for that velocity lies between 22 and 30, hardly 'fully rough'.

To further investigate the Stanton number behavior at low roughness Reynolds numbers, a special test was conducted at a free-stream velocity of 18.8 fps. The boundary layer was augmented by blowing at $F = .004$ over the first two feet of the test section. The boundary layer was then allowed to relax into its natural state. Stanton number data for the unblown plates are shown in Fig. 3.7, along with the mean of the 90 fps data. It is notable that the low velocity Stanton number data form a natural extension of the unblown 90 fps data. The roughness Reynolds

number at the end of the test section for the 18.8 fps run was only 14, as determined from hot wire measurements of the shear stress near the surface. This is far below the 'fully rough' condition and nearly 'smooth' by the usual criteria. It seems clear that 'fully rough' behavior of the heat transfer data persists to much lower roughness Reynolds numbers, for the present surface geometry, than had been expected. The classification of 'rough' or 'smooth' based on roughness Reynolds number does not seem to be a reliable indicator for the heat transfer performance of rough surface tested here.

In the turbulent range, the present data fit the following correlation:

$$\text{Rough} \quad St = .0043 \left(\frac{\Delta}{r} \right)^{-0.25} \quad (3-6)$$

The usual smooth-plate correlation in terms of enthalpy thickness Reynolds number can be cast in a similar form:

$$\text{Smooth} \quad St = \frac{0.0153}{\left(\frac{u_{\infty} r}{\nu} \right)^{.25}} \left(\frac{\Delta}{r} \right)^{-0.25} \quad (3-7)$$

In this form the Stanton number for both rough and smooth behavior is substantially the same at 32 fps. At 18.8 fps, the smooth plate correlation predicts a value nearly 50% higher than the rough. This is because of the inverse dependence of the smooth correlation on free-stream velocity. Clearly, the smooth plate correlation in this form does not provide a suitable limit for the rough surface behavior.

In summary, the unblown data in Figs. 3.5, 3.6 and 3.7 seem nearly independent of free-stream velocity. Stanton number appears entirely independent of velocity, being only a function of enthalpy thickness. Skin friction may be independent and at most has a small dependence. Skin friction, when θ/r is fixed, is only about 5% higher than Stanton number at the same value of Δ/r . The effective value of the Reynolds analogy factor is about 0.95, instead of 1.15, which is typical of a smooth plate. The boundary layer seems to be completely turbulent, with no discernible molecular effect. The effective value of the turbulent

Prandtl number seems near unity. Roughness effects on heat transfer persists to very low values of the roughness Reynolds number, with no evidence of the 'transitional roughness range' in the Stanton number data. Momentum thickness and friction factor data do, however, seem to show a transitional effect.

B. The Effects of Blowing

Blowing diminishes the Stanton number and skin friction for a rough plate, just as it does for a smooth plate. Roughness Rig skin friction and Stanton number data at each of the five test section velocities are shown in Fig. 3.8 through 3.17. These data exhibit very similar trends to the smooth plate skin friction and heat transfer data presented by Moffat [1] and Simpson [2].

An important feature of the unblown turbulent boundary layer Stanton-number data is its lack of dependence on free-stream velocity. This independence is preserved with blowing. Fig. 3.18 shows Stanton number data for all the blown boundary layers at all velocities plotted versus Δ/r parametric in F . Although the scatter is increased, the fully rough blown turbulent boundary layer exhibits the same independence of velocity as does the unblown boundary layer.

In view of this agreement, it is of interest to examine the roughness Reynolds number range of the data, since this is so often used as the measure of the rough surface behavior. At 32 fps and $F = 0.002$, the roughness Reynolds number is about 17 at the point farthest downstream. For all higher velocities or lower blowing fractions, Re_τ is greater. Higher blowing reduces the wall shear still further, and, for 32 fps, takes the roughness Reynolds number down to 10 ($F = 0.004$ at the 20th plate). No reliable friction data are available for $F = 0.008$ at 32 fps, but Stanton number data for $F = 0.008$ are shown in Fig. 3.18. The 32 fps Stanton number data at both $F = 0.004$ and 0.008 are higher than the remaining data, and it is felt that they may represent a different state of the boundary layer than the higher velocities. The scatter in these data sometimes (though not often) exceeds ± 0.0001 Stanton-number units. No cause has been assigned.

Values of Stanton number with blowing are predictable from the unblown values by a Couette relationship used for smooth plate flows, with proper interpretation:

$$\frac{St}{St_o} \bigg|_{\Delta} = \left[\frac{\ln(1+B)}{B} \right]^{1.25} (1+B)^{.25} \quad (3-8)$$

The fully rough prediction is to be made at constant Δ , whereas the smooth plate prediction is made at constant Re_{Δ} . Predictions based on this equation are shown as solid lines in Figs. 3.19 through 3.23. The agreement is excellent for all data more than about 30 boundary layer thicknesses past the peak of the transition hump. Data points more than 30 boundary layer thicknesses past transition are accented in Figs. 3.19 through 3.23. The application of the Couette flow estimator based on enthalpy thickness instead of enthalpy thickness Reynolds number is very reasonable in view of the success of this coordinate in organizing the Stanton number data.

The skin friction data with blowing show a high degree of scatter and like the unblown data it is difficult to draw any definitive conclusions from them. It is interesting, however, to examine the momentum thicknesses of the blown boundary layer. These measurements are less prone to uncertainties and provide a better basis for interpreting the rough surface behavior. Fig. 3.24 shows all of the momentum thicknesses, plotted against distance from the virtual origin, parametric in F . It is clear that in these coordinates, the boundary layers for all velocities are substantially the same. This leads one to suspect that in terms of local thickness coordinates the skin friction should be the same. There is so much scatter in the blown skin friction data that this cannot be confirmed. It does seem likely, however, that the skin friction has only a small dependence on free-stream velocity, since that was observed in the unblown data. More accurate skin friction measurements will be taken in the continuing experimental program on the rough surface boundary layer, and this question will undoubtedly be answered in the future.

The curve fitting technique used to determine skin friction did not work well at blowing fractions greater than .004. The skin friction is

so small at these high blowing rates that even small uncertainties in the momentum thickness measurement result in differences in skin friction that are percentage-wise large. Because of this, skin friction predictions for the .008 blowing fraction runs have not been included in the figures. The skin friction at 90 fps and $F = .002$ was accorded some special treatment. The curve fit technique predicted a virtual origin for the boundary layer that was inconsistent with the other data at that velocity. In this one particular data set, the virtual origin was selected by extrapolating the boundary layer momentum thicknesses to zero in cartesian coordinates. The skin friction was then evaluated with the same curve fit routine but with fixed virtual origin. In all other data sets, the curve fitting routine was allowed to select both the virtual origin and the curve from which the skin friction data were determined.

The effects of blowing on heat transfer and skin friction to a 'fully rough' turbulent boundary layer can be summarized as follows. Stanton number is a function of Δ and F only, and the blown value can be predicted from the customary predictive equation, but evaluated at constant Δ instead of constant Re_Δ . The effects of blowing on skin friction are less well defined, but boundary layer thickness measurements indicate that the growth of the momentum boundary layer is substantially independent of velocity and a function only of the blowing fraction. Based on this and the behavior of the unblown skin friction data, it seems likely that the rough surface blown skin friction has at most small dependence of free-stream velocity. In view of the data scatter, more definitive conclusions are not possible.

C. Roughness and Blowing Effects on Transition

All boundary layers in these experiments were allowed natural transitions without a boundary layer trip. There are two advantages of 'tripping' the boundary layer and having the virtual origin at the test-section inlet: the momentum boundary layer origin is matched to the thermal boundary layer, and it makes maximum use of the test section length. However, when the well-defined laminar boundary layer and transition region were found at the 32 fps test section velocity, it was decided

that the opportunity to observe the effects of roughness and blowing on transition more than offset any advantages offered by tripping the boundary layer. There is very little experimental information in the literature about transition of the blown boundary layer on a rough wall. The present experimental program was not specifically designed to study transition, but some interesting observations could be made from the data concerning rough surface boundary layer transition.

The effect of the laminar boundary layer on Stanton number can clearly be seen in the non-blowing data in Fig. 3.1. Increasing the free-stream velocity moves the transition upstream. It is interesting to note, however, from Fig. 3.2 that the transition is well correlated by momentum thickness Reynolds number. Transition occurs at a momentum thickness (and enthalpy thickness) Reynolds number of about 400.

The effects of blowing on transition can be seen using the data for 32 fps in Fig. 3.10. Shown on this figure are momentum thickness Reynolds numbers at the onset of transition. The data clearly show that blowing moves the transition upstream but does not much affect the momentum thickness Reynolds number (about 400) at which the transition occurs. It is important to note that the thermal protection offered by blowing does not offset the effect of an early transition. Blowing through a region which would otherwise have remained laminar can result in a much higher heat load than no blowing at all.

The present data indicate that, like pipe flow data, below a certain critical Reynolds number the rough surface boundary layer remains laminar. For these experiments, transition occurs at or near the same Reynolds number that would be expected for a smooth surface transition. There are signs of transition in all of Stanton number data, even at the higher test section velocities.

A final remark that can be made about the laminar-to-turbulent transition observed in these tests is that once initiated, it occurs in a relatively short distance. Smooth plate boundary layer transition is often spread over a larger Reynolds number range. Fig. 3.25 compares smooth plate transition data by Reynolds [53] to the present experiment. The smooth plate Stanton number after transition approaches the asymptotic turbulent value slower than the rough surface data from these

experiments. A possible explanation of this is that the surface roughness elements may aid the transition process once initiated and help bring it to completion over a shorter section of the plate.

D. Comparison with Other Rough Surface Experiments

Direct comparison of skin friction and heat transfer data to similar rough surface experiments is useful because it demonstrates that the present results are similar to what has been found in other rough surface experiments. Several investigators have compared their rough surface skin friction to the 'fully rough' skin friction correlation suggested by Prandtl and Schlichting [10].

$$c_f = (2.87 + 1.58 \log x/k_s)^{-2.5} \quad (3-9)$$

Moore's [12] data compare reasonably well with this equation, but he found different size roughness elements were not organized in these coordinates. The data by Liu [16] were reasonably well organized, but the predicted skin friction was about 20% higher than the data. Wu [18] measured average skin friction over a 10 x 21 inch test plate which agrees well with the Prandtl-Schlichting equation for the average skin friction. Skin friction measurements from these experiments are shown in Fig. 3.26. Like Liu's, the present data lie about 20% lower than the Prandtl-Schlichting curve.

In a more recent and extensive study, Lakshman and Jayatilke [52] examine nearly every available set of rough surface skin friction data from both pipes and plates. They correlate the data in E and Re_τ coordinates, where E is defined by the equation:

$$u^+ = \frac{1}{\kappa} \ln(Ey^+) \quad (3-10)$$

Data from these experiments are shown in Fig. 3.27 in E versus Re_τ coordinates. Also shown is the line for sand-grain roughness. Although the data lie above the sand-grain roughness line in the transition roughness Reynolds number range, it is reasonably well organized in these coordinates and agree well at 'fully rough' roughness Reynolds numbers.

A direct comparison of the heat transfer results with other rough surface experiments is more difficult because previous rough surface heat transfer experiments have been performed in pipe geometries. The data correlations of these tests typically include pipe dimensions or have their roughness scaled by pipe diameters. The heat transfer data by Dipprey and Sabersky [24] were correlated by the following expression:

$$\frac{1}{\sqrt{c_f/2}} \left[\frac{c_f/2}{St} - 1 \right] = g(Re_\tau, Pr) - A(Re_\tau) \quad (3-11)$$

For fully rough flow, the g and A functions are simplified to give:

$$\frac{1}{\sqrt{c_f/2}} \left[\frac{c_f/2}{St} - 1 \right] + 8.48 = 5.19 Re_\tau^{0.2} Pr^{0.44} = g_{fr}(Re_\tau, Pr) \quad (3-12)$$

Dipprey and Sabersky were able to correlate all of their fully rough data in g_{fr} and Re_τ coordinates. Owen and Thompson [25] recommend the following expression for heat transfer from a flat plate:

$$\frac{1}{St} = \frac{u_\infty}{u_\tau} \left(\frac{u_\infty}{u_\tau} + \frac{1}{B^*} \right) \quad (3-13)$$

where B^* is the sublayer Stanton number. Based on their experiments and data by others, the following correlation was recommended for the sublayer Stanton number:

$$B^* = \frac{1}{\alpha} Re_\tau^{-0.45} Pr^{0.8} \quad (3-14)$$

with α lying between 0.45 and 0.7 but represented best by 0.52. The Owen-Thompson expression can be cast into a form similar to the Dipprey-Sabersky correlation:

$$\frac{1}{\sqrt{c_f/2}} \left[\frac{c_f/2}{St} - 1 \right] + 8.48 = 0.52 Re_\tau^{0.45} Pr^{0.8} + 8.48 \quad (3-15)$$

These two models for rough surface heat transfer are plotted in Fig. 3.28 along with data from the present experiments. Both correlations agree reasonably well for roughness Reynolds numbers greater than 70. The data from the present experiments fall below these predictions.

Both of these correlations employ a skin friction-to-Stanton number ratio, minus one. The correlation in this form emphasizes experimental uncertainties of the present data by looking at differences between nearly equal experimentally determined values.

Another useful data comparison can be made using the correlation suggested by Nunner [23]. This correlation compares the increase in rough surface skin friction to the increase in heat transfer. Data from these experiments is shown in Figure 3.29. Also shown is Nunner's correlation and the more recent correlation recommended by Norris [30]. The data from these experiments is best organized by Nunner's original correlation.

Based on these comparisons, it appears that the rough surface skin friction and heat transfer data from the present experiments are comparable with other similar experiments.

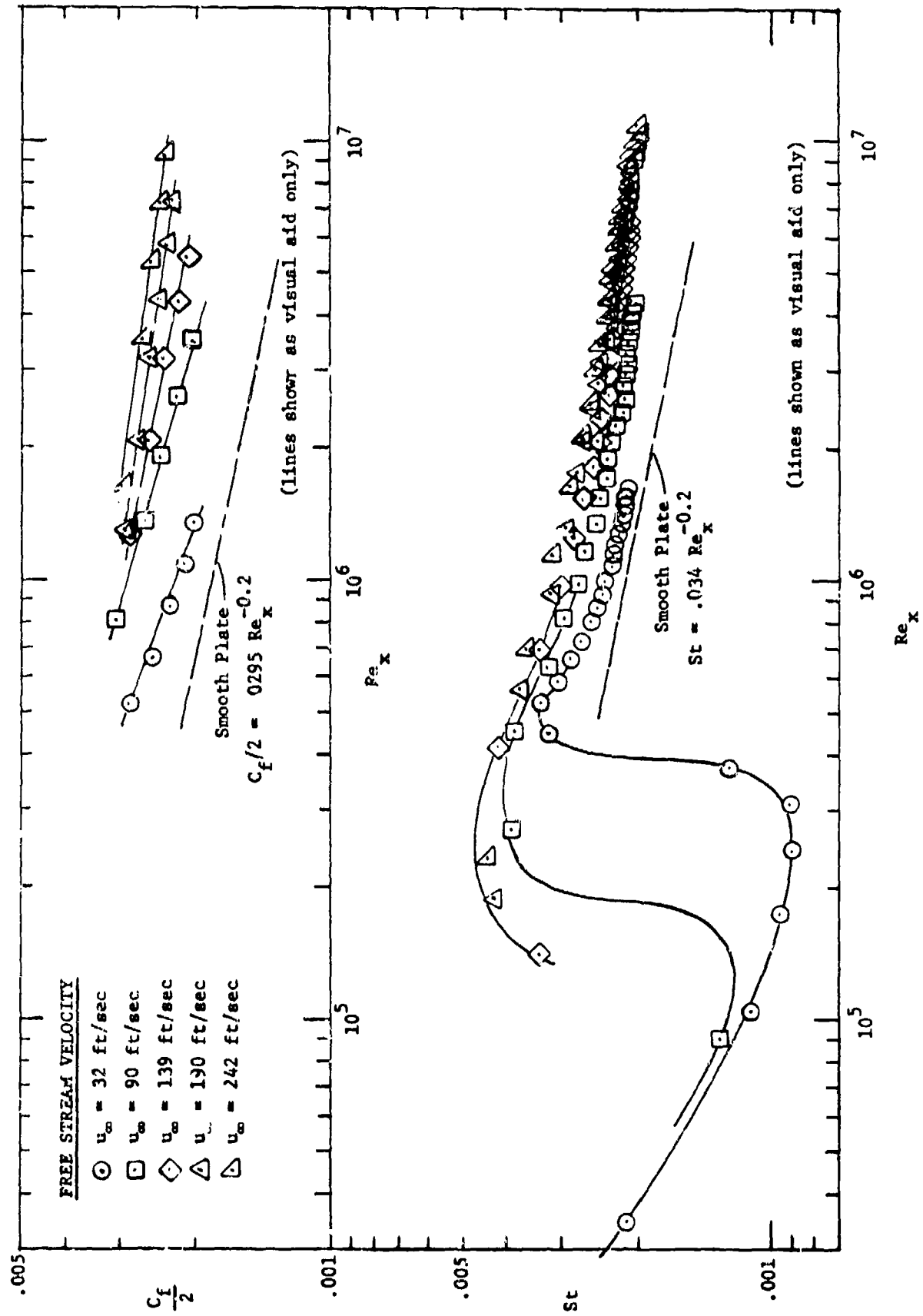


Fig. 3.1 Rough surface skin friction and Stanton number versus x -Reynolds number

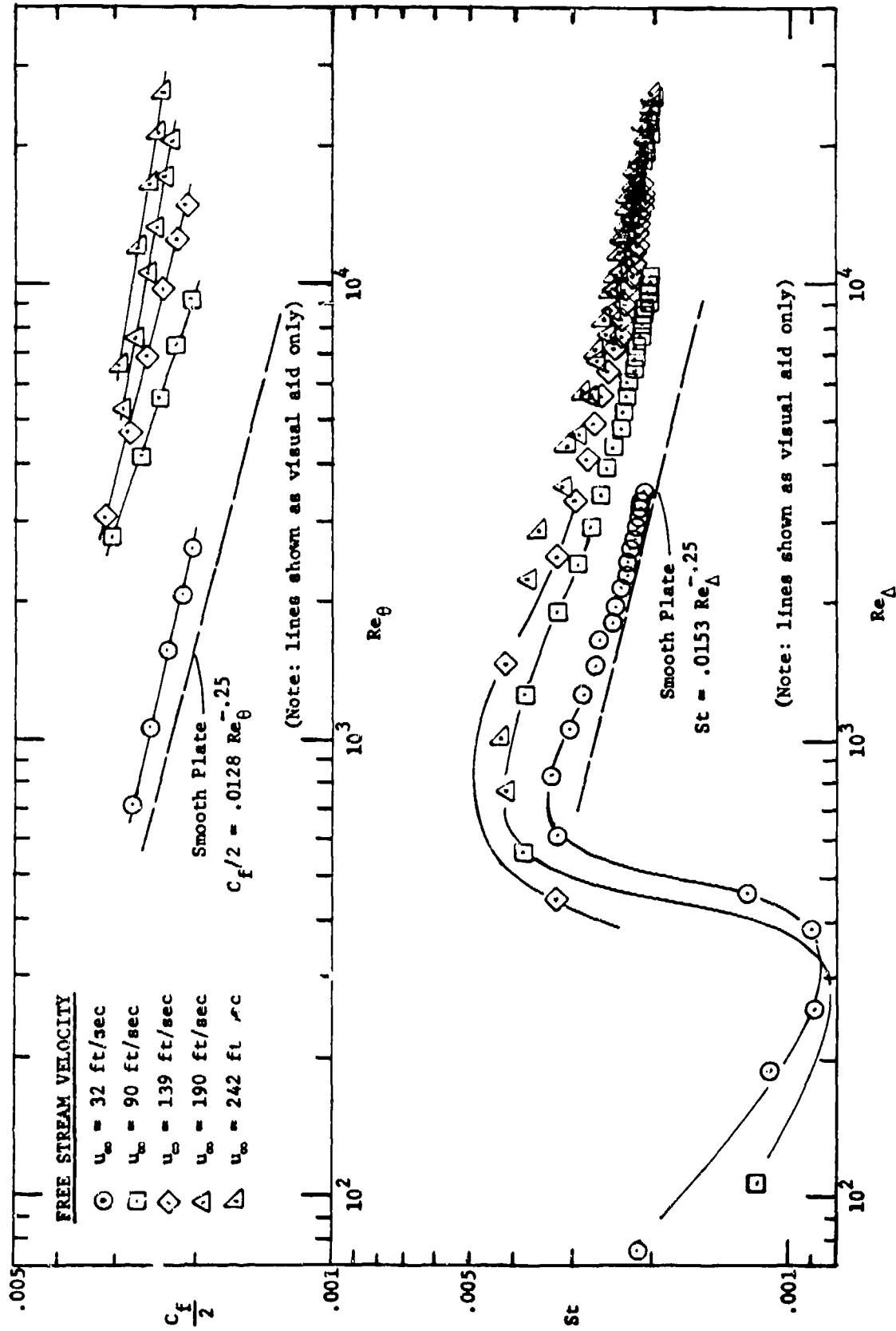


Fig. 3.2 Rough surface skin friction and Stanton number versus momentum and enthalpy thickness Reynolds number

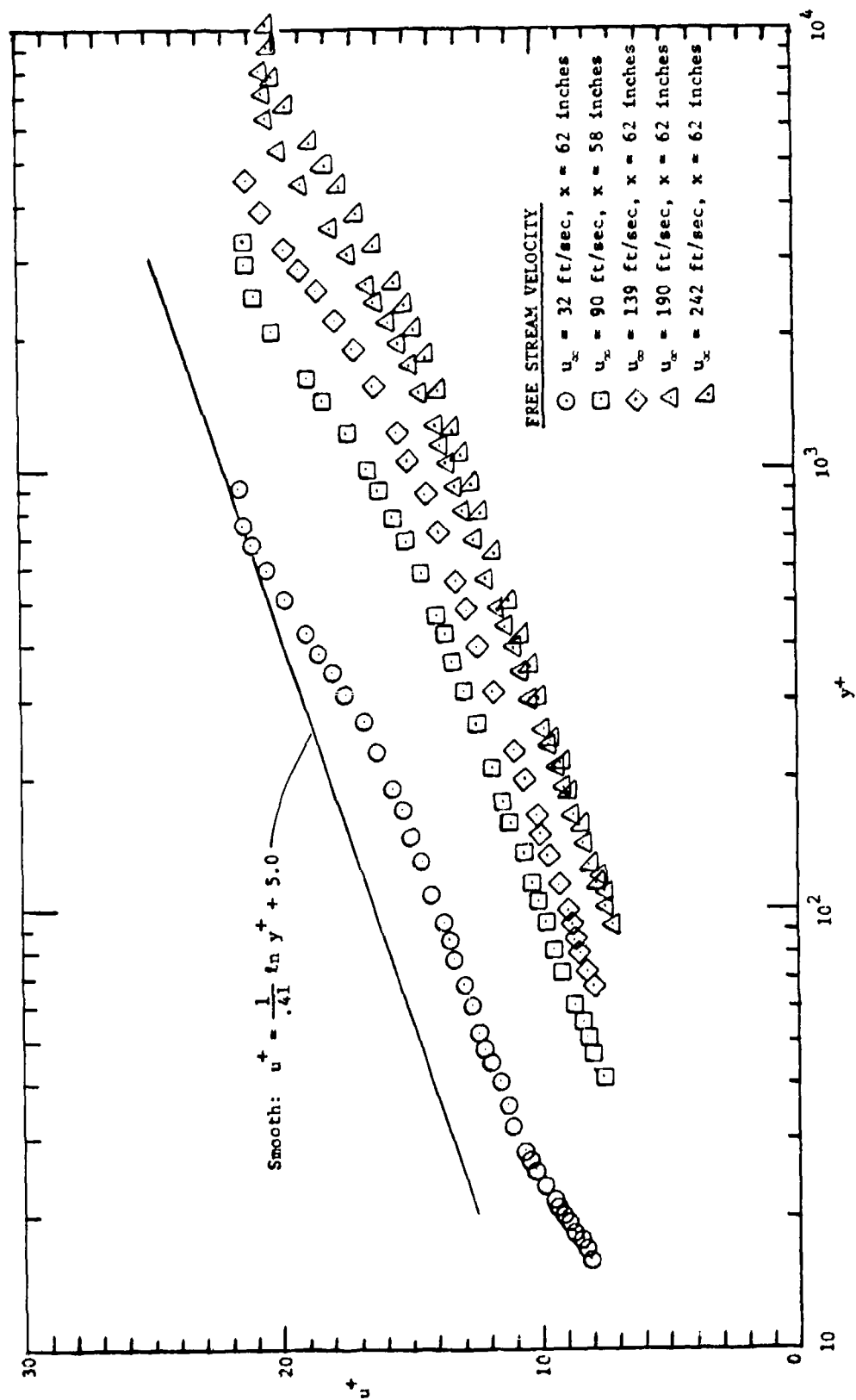


Fig. 3.3 Velocity profiles at different test section velocities

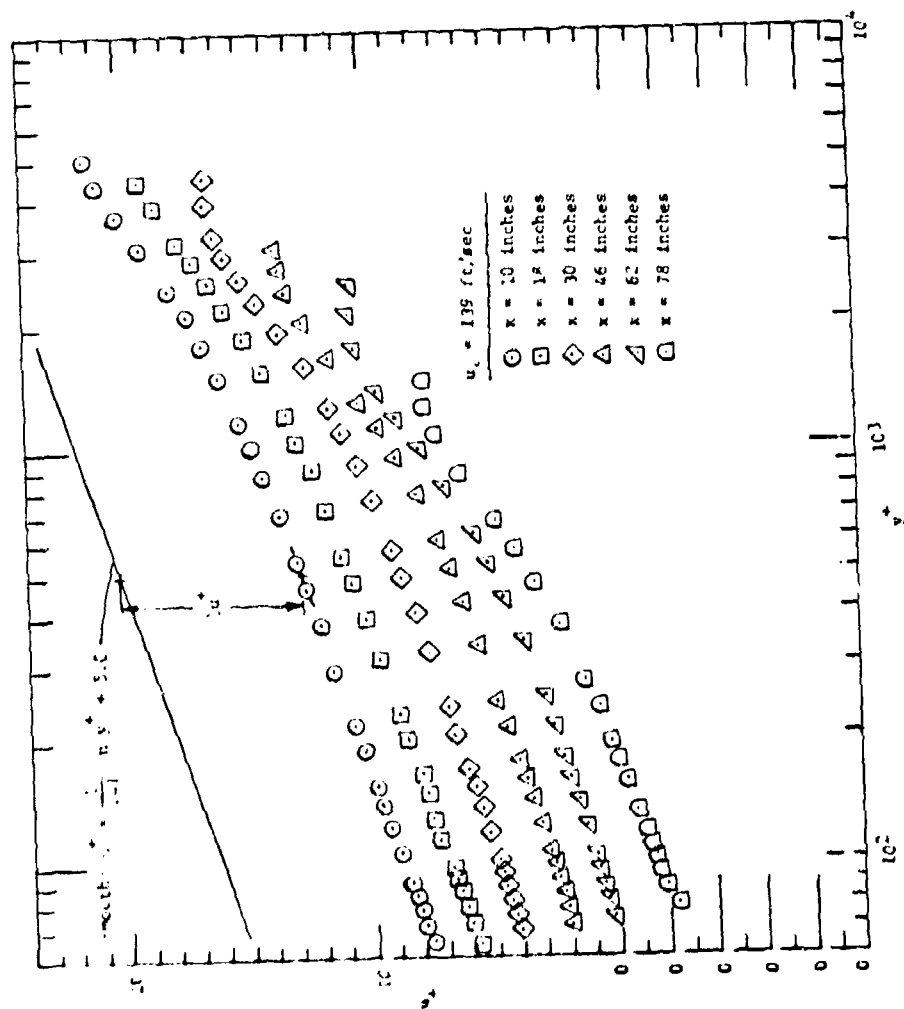


Fig. 3.4 Velocity profiles at $u_\infty = 139 \text{ fps}$ at different stations along the test section

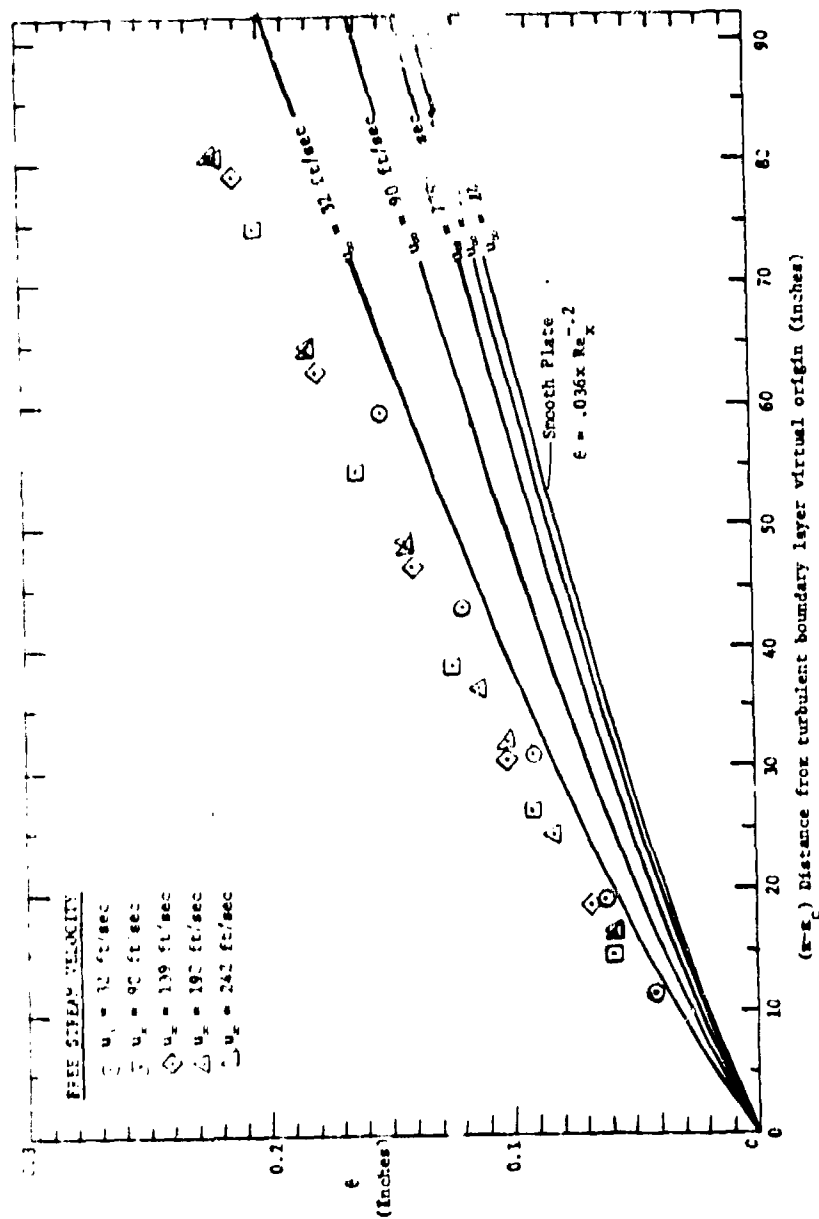


Fig. 3.5 Rough surface momentum thickness versus distance from the boundary layer virtual origin

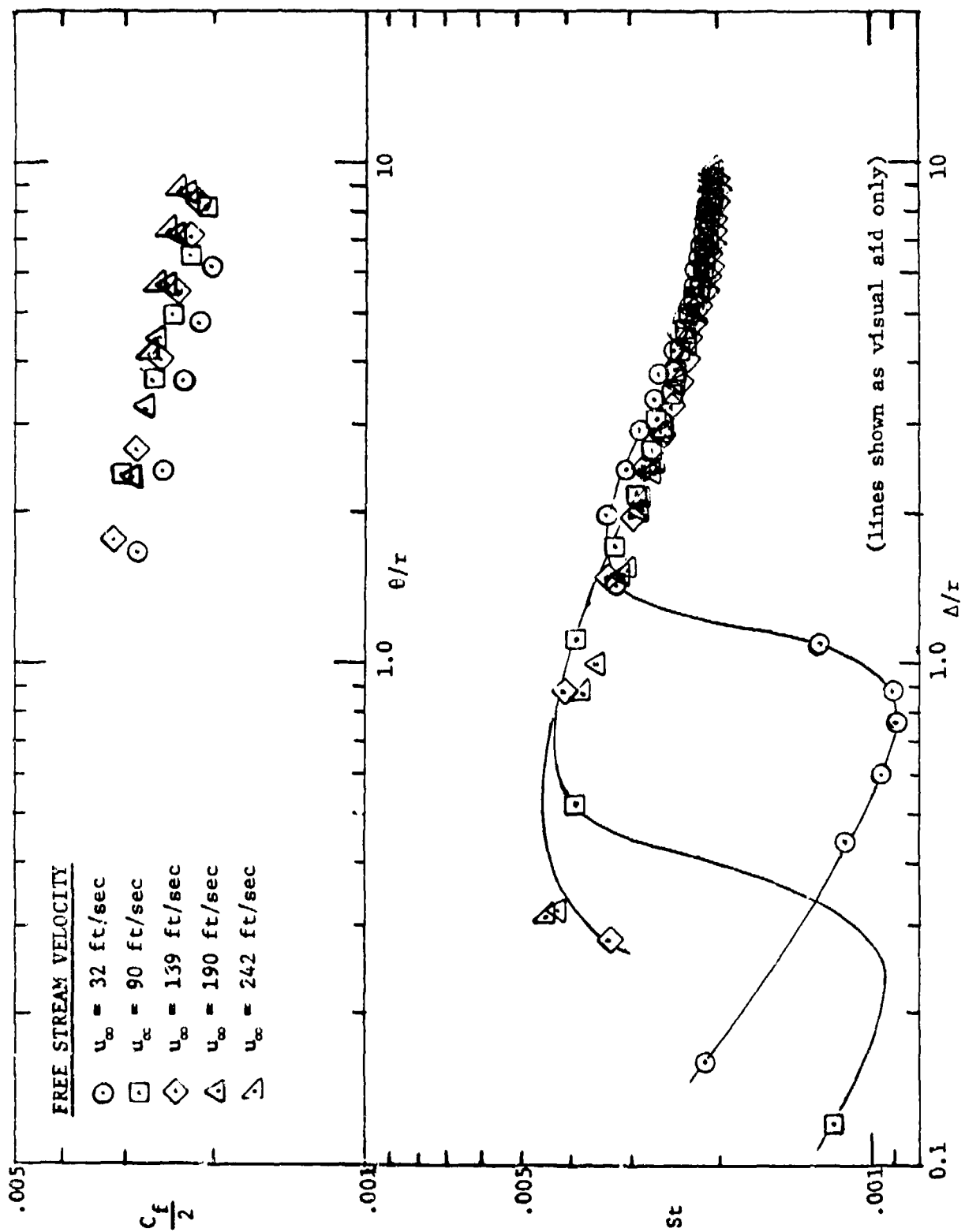


Fig. 3.6 Rough surface skin friction versus (momentum thickness)/(ball radius) and rough surface Stanton number versus (enthalpy thickness)/(ball radius)

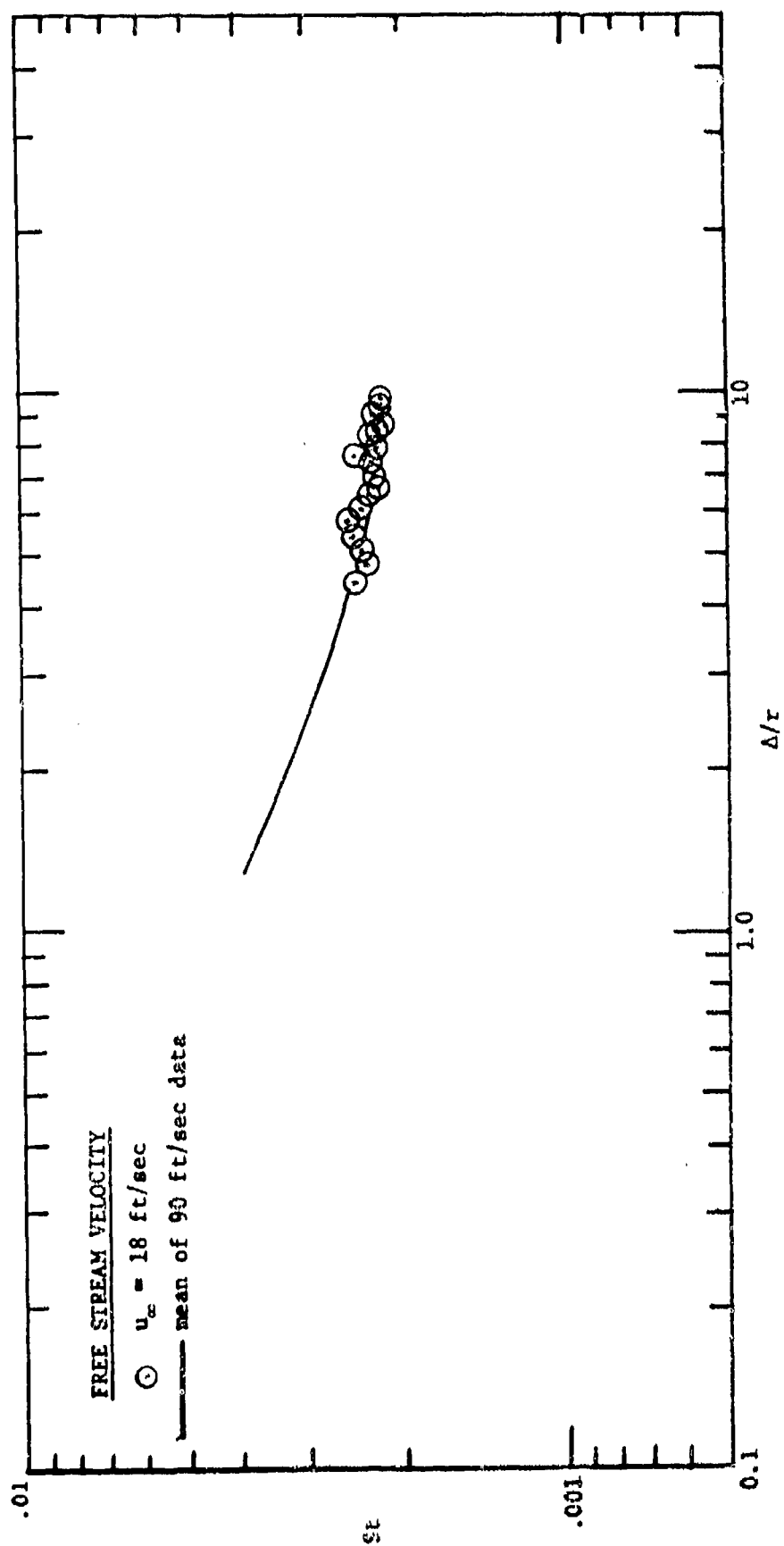


Fig. 3.7 Rough surface Stanton number versus (enthalpy thickness)/(ball radius) at $u_{\infty} = 18.8 \text{ fps}$ and $u_{\infty} = 90 \text{ fps}$

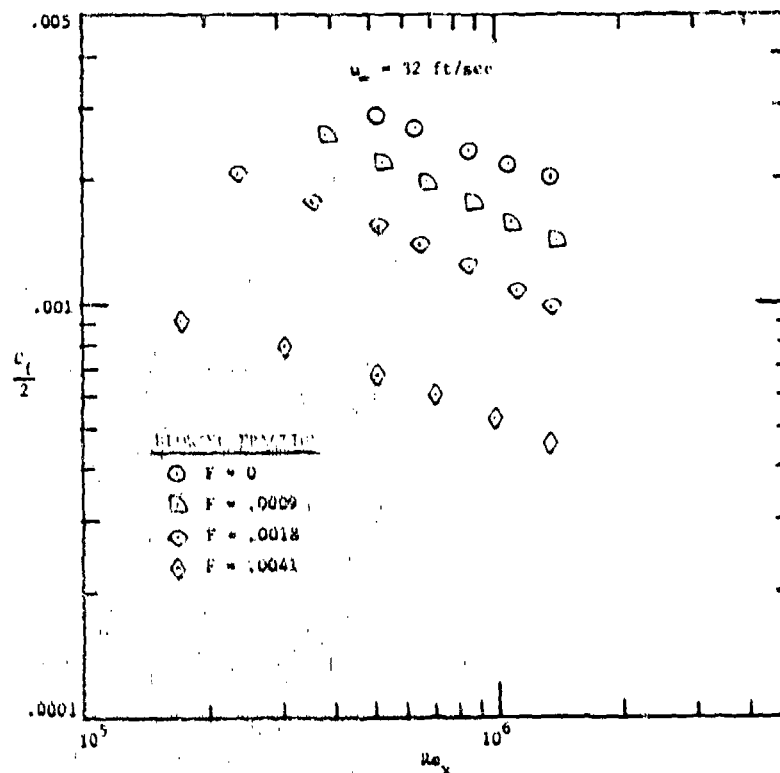


Fig. 3.8 Rough surface skin friction versus x-Reynolds number at $u_{\infty} = 32 \text{ fps}$

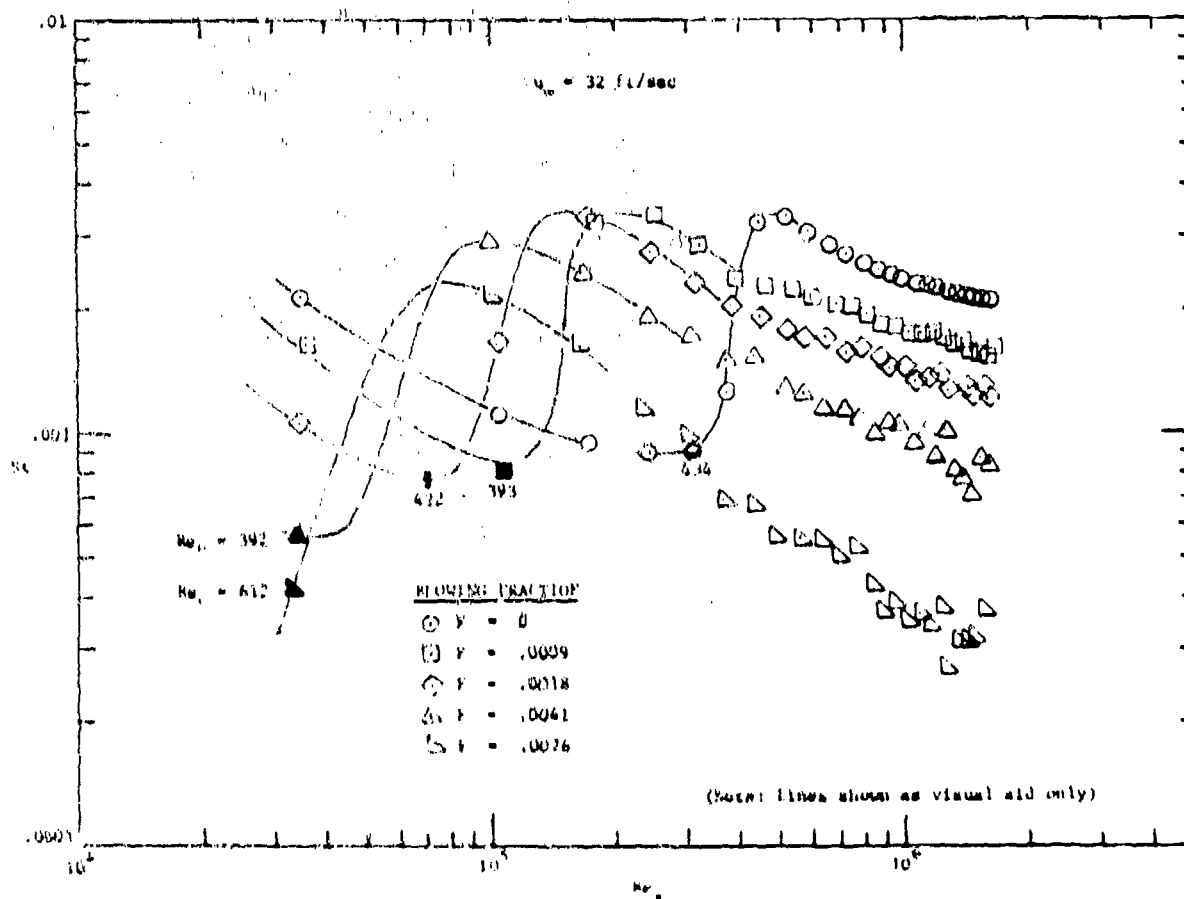


Fig. 3.9 Rough surface Stanton number versus x-Reynolds number at $u_{\infty} = 32 \text{ fps}$

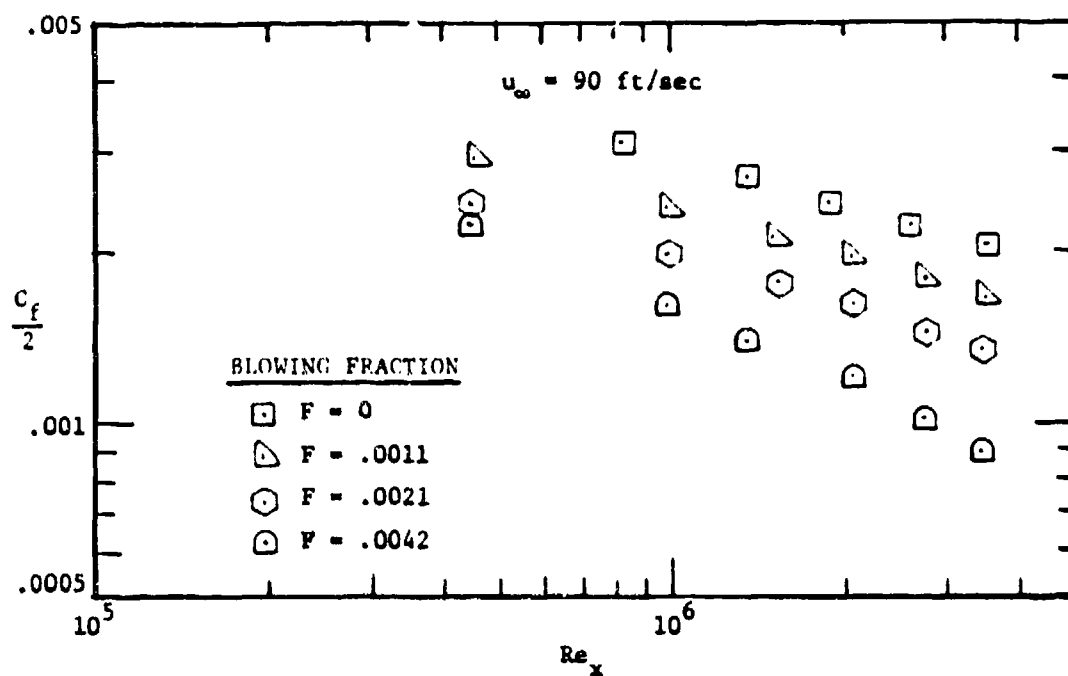


Fig. 3.10 Rough surface skin friction versus x-Reynolds number at $u_\infty = 90$ fps

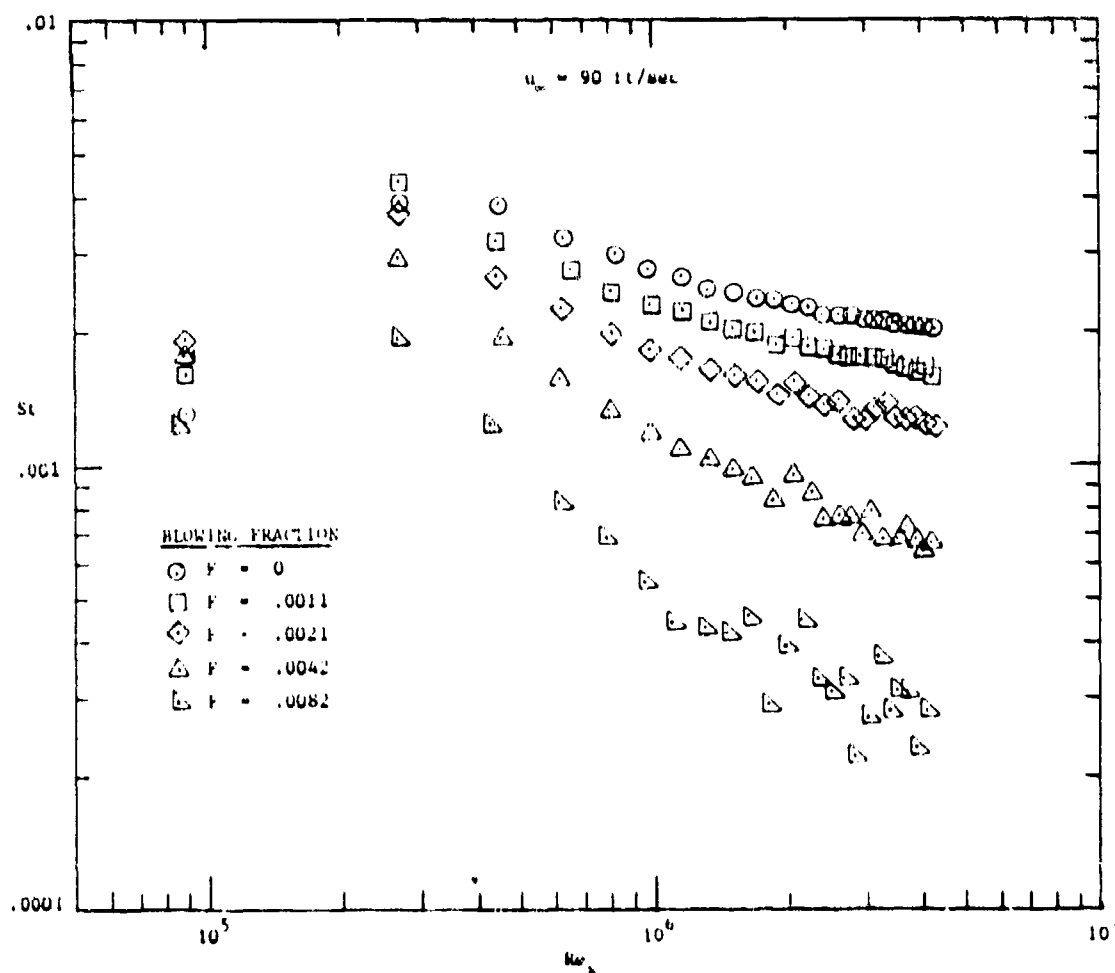


Fig. 3.11 Rough surface Stanton number versus x-Reynolds number at $u_\infty = 90$ fps

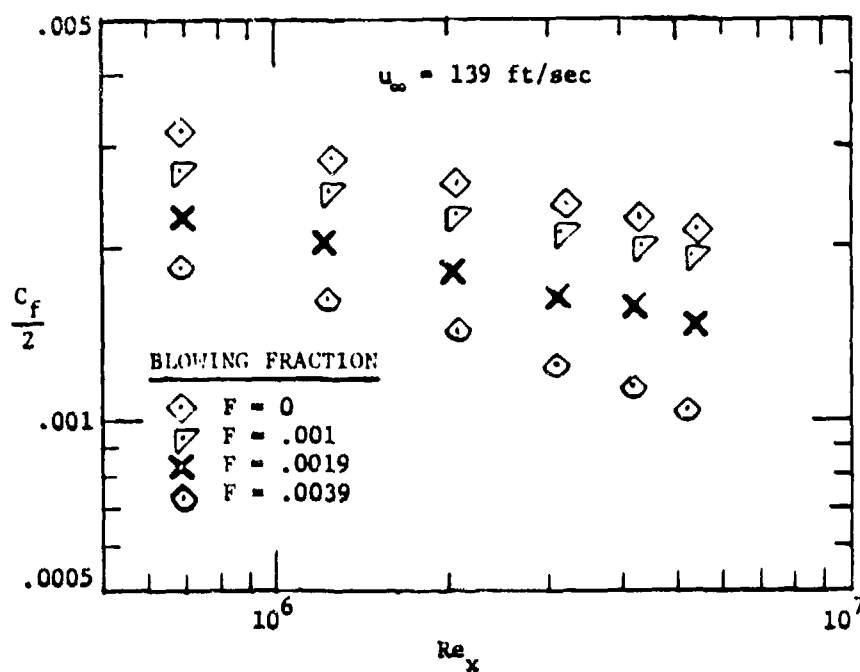


Fig. 3.12 Rough surface skin friction versus x-Reynolds number at $u_\infty = 139$ fps

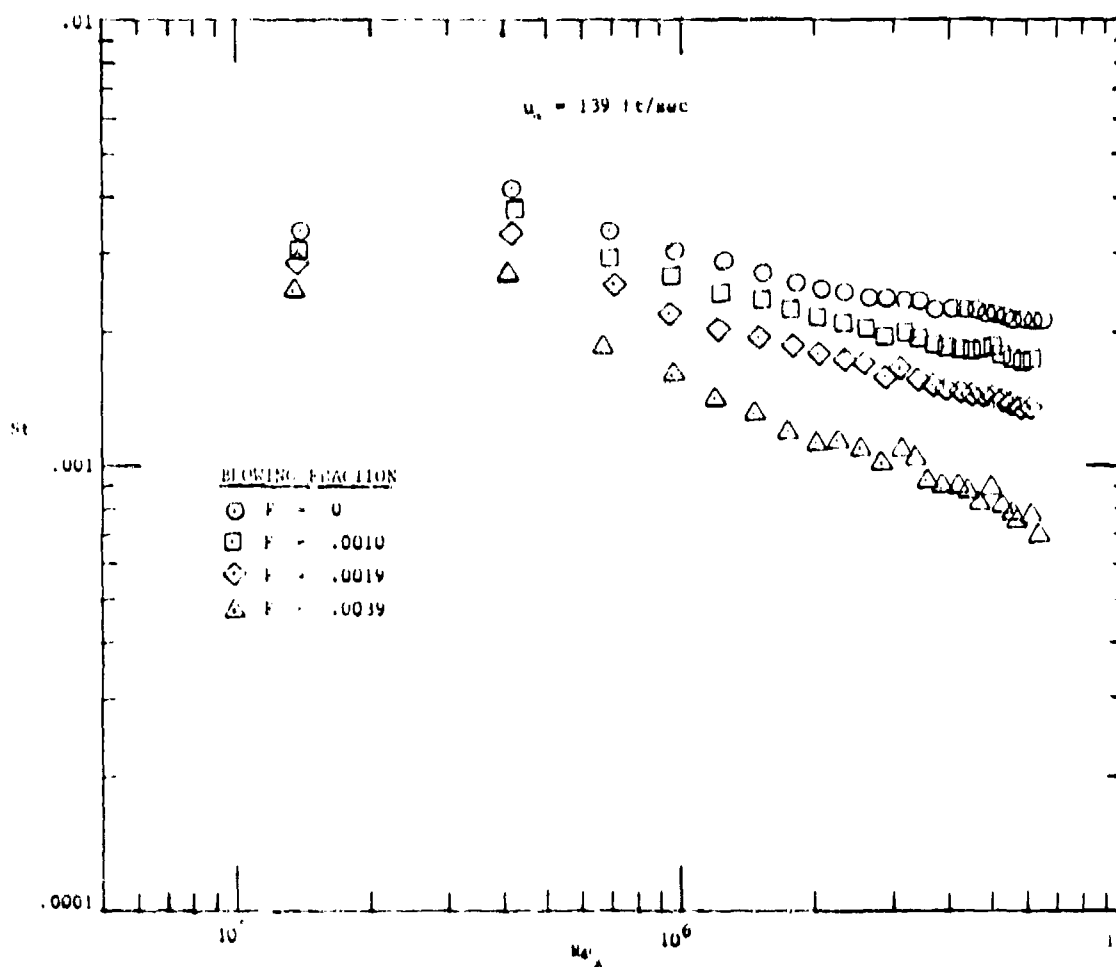


Fig. 3.13 Rough surface Stanton number versus x-Reynolds number at $u_\infty = 139$ fps

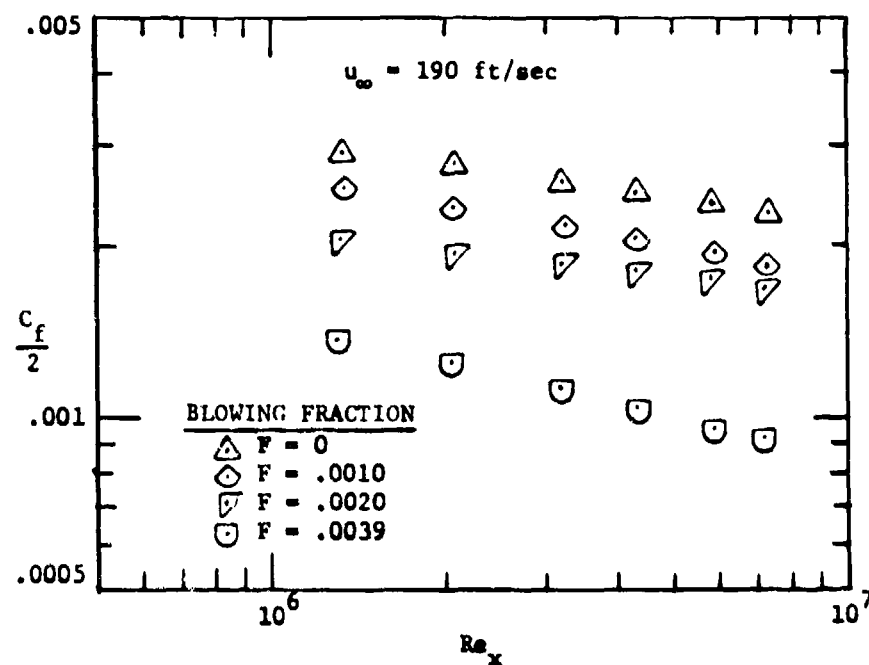


Fig. 3.14 Rough surface skin friction versus x-Reynolds number at $u_\infty = 190$ fps

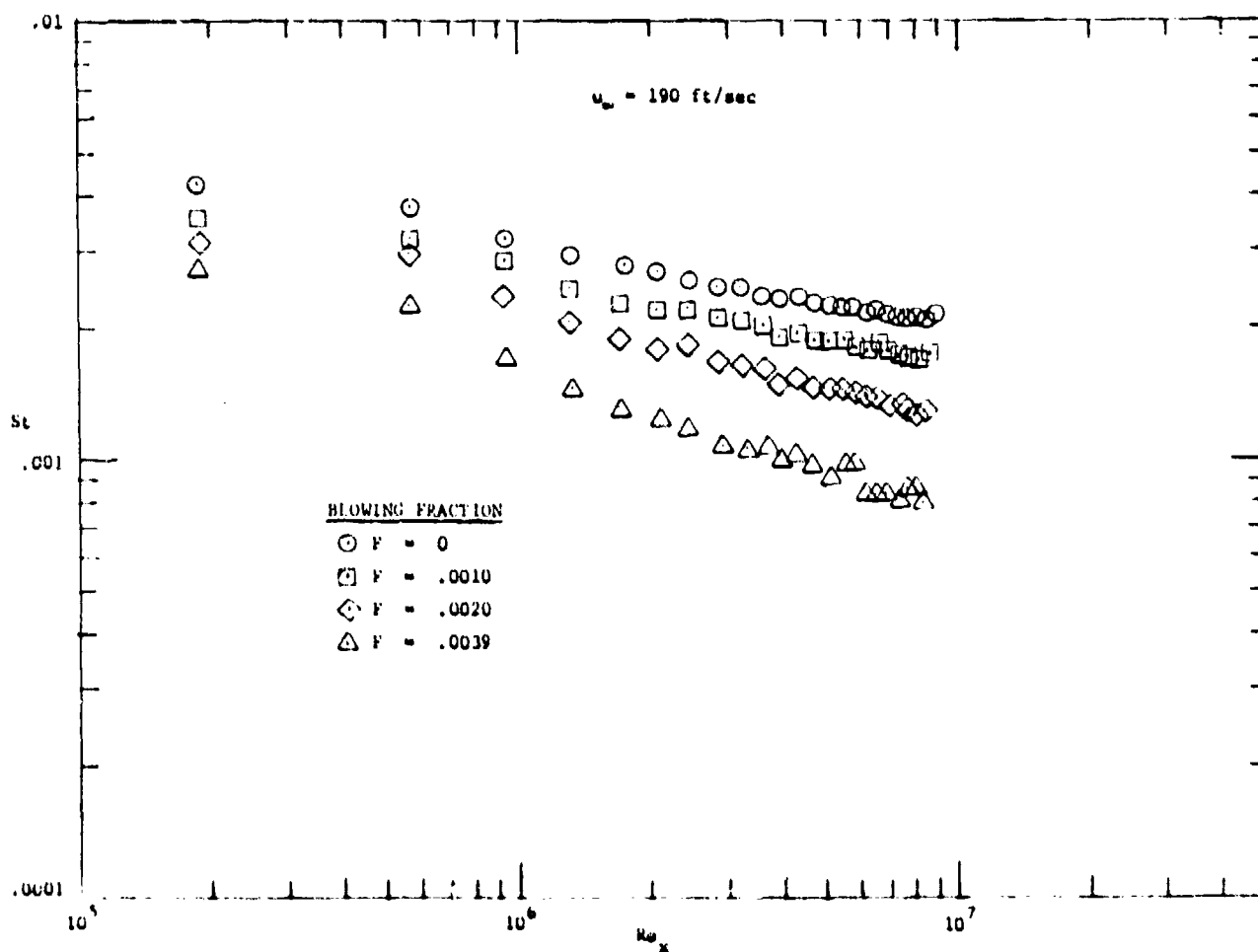


Fig. 3.15 Rough surface Stanton number versus x-Reynolds number at $u_\infty = 190$ fps

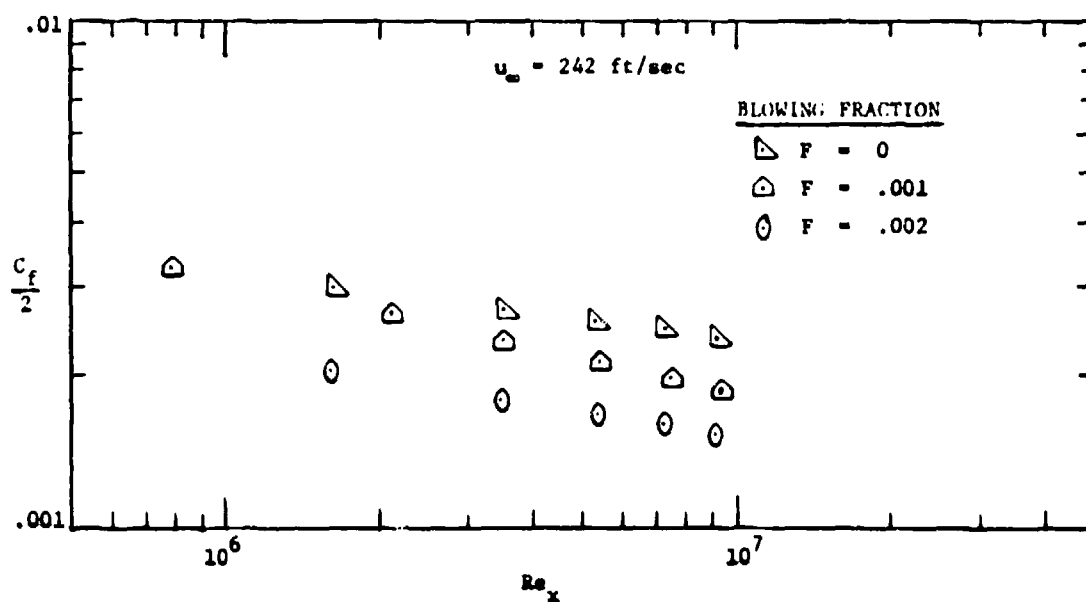


Fig. 3.16 Rough surface skin friction versus x-Reynolds number at $u_\infty = 242$ fps

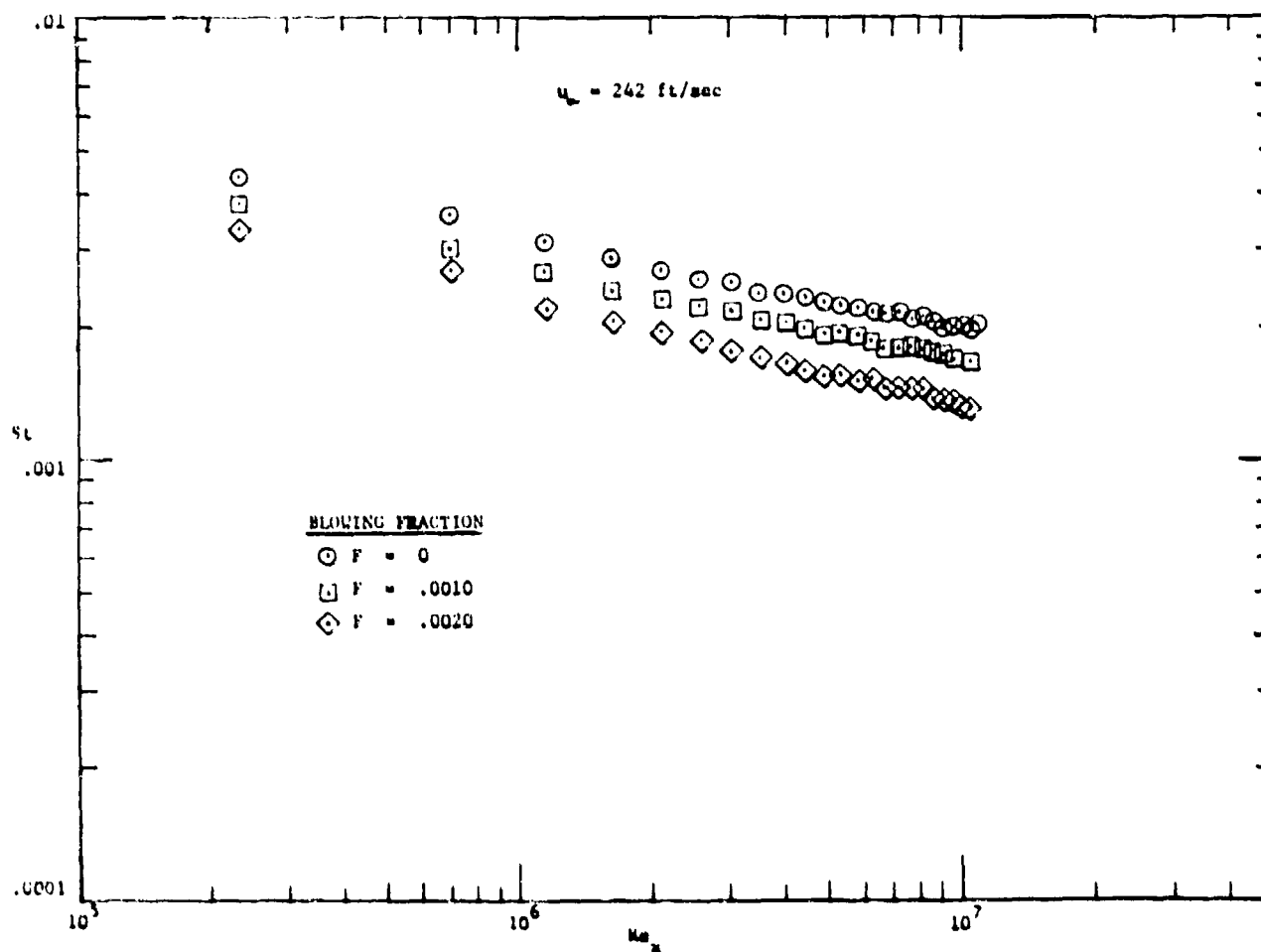


Fig. 3.17 Rough surface Stanton number versus x-Reynolds number at $u_\infty = 242$ fps

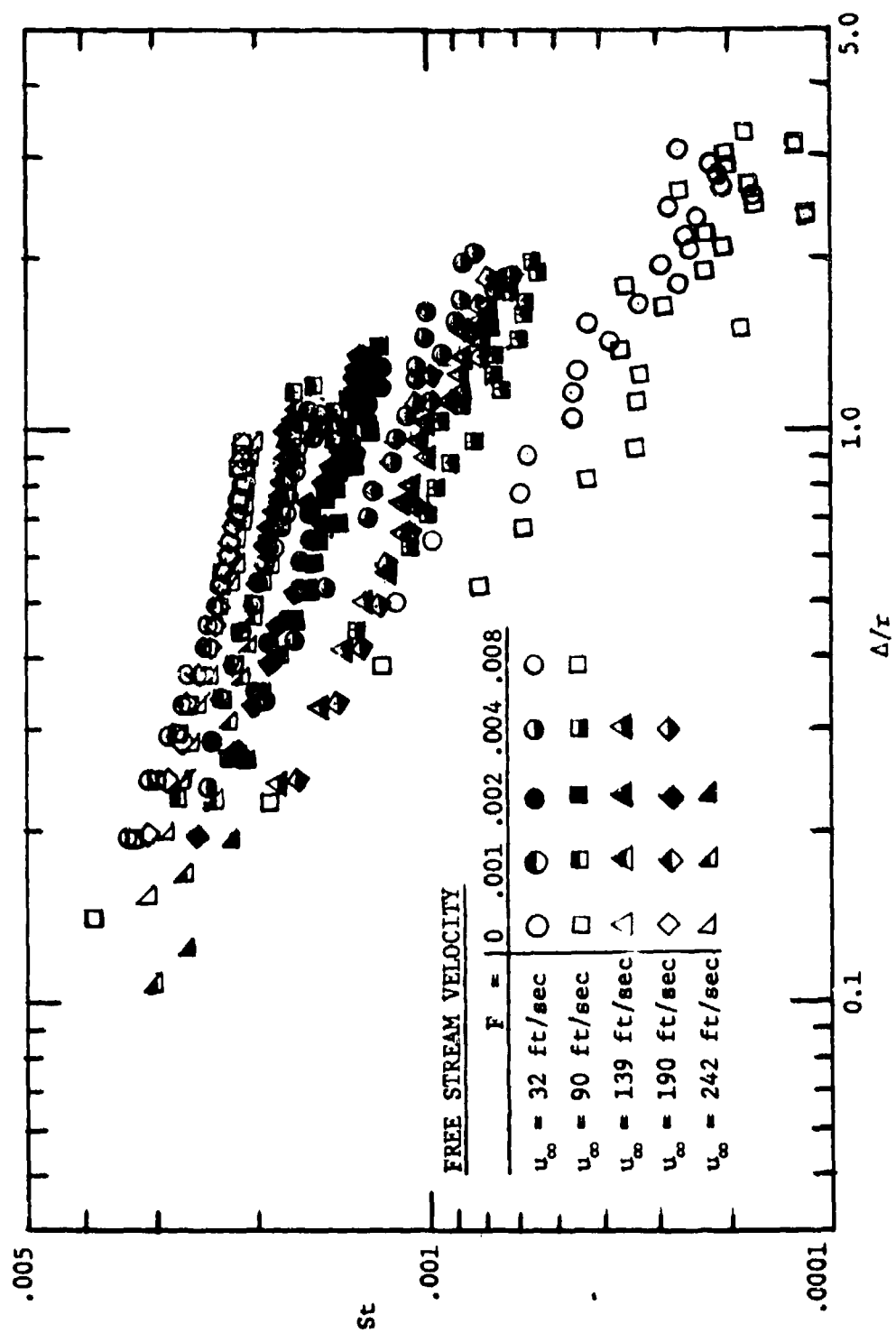


Fig. 3.18 Stanton number versus (enthalpy thickness)/(ball radius) for all boundary layers

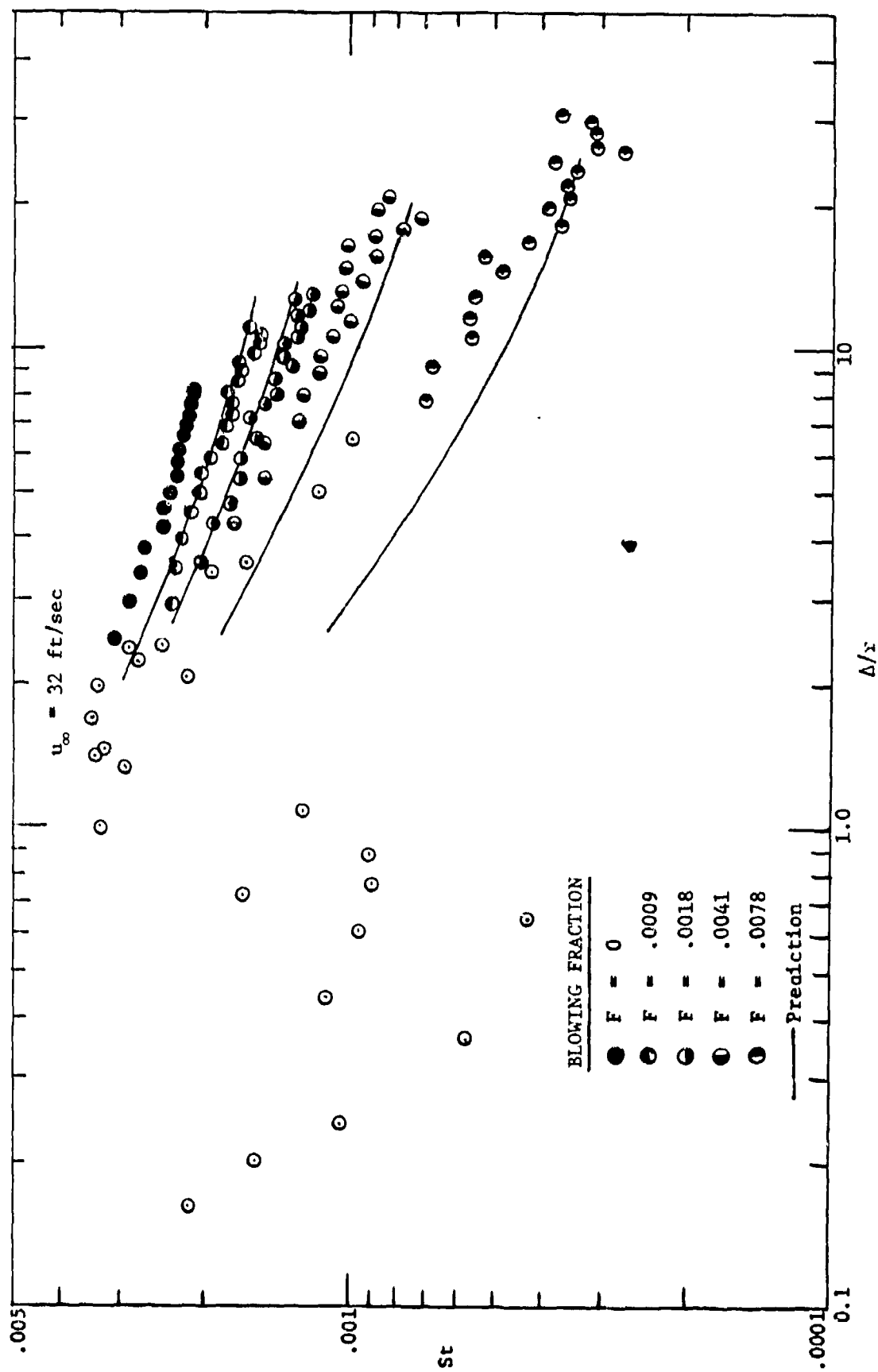


Fig. 3.19 Stanton number versus (enthalpy thickness)/(ball radius) at $u_{\infty} = 32 \text{ fps}$

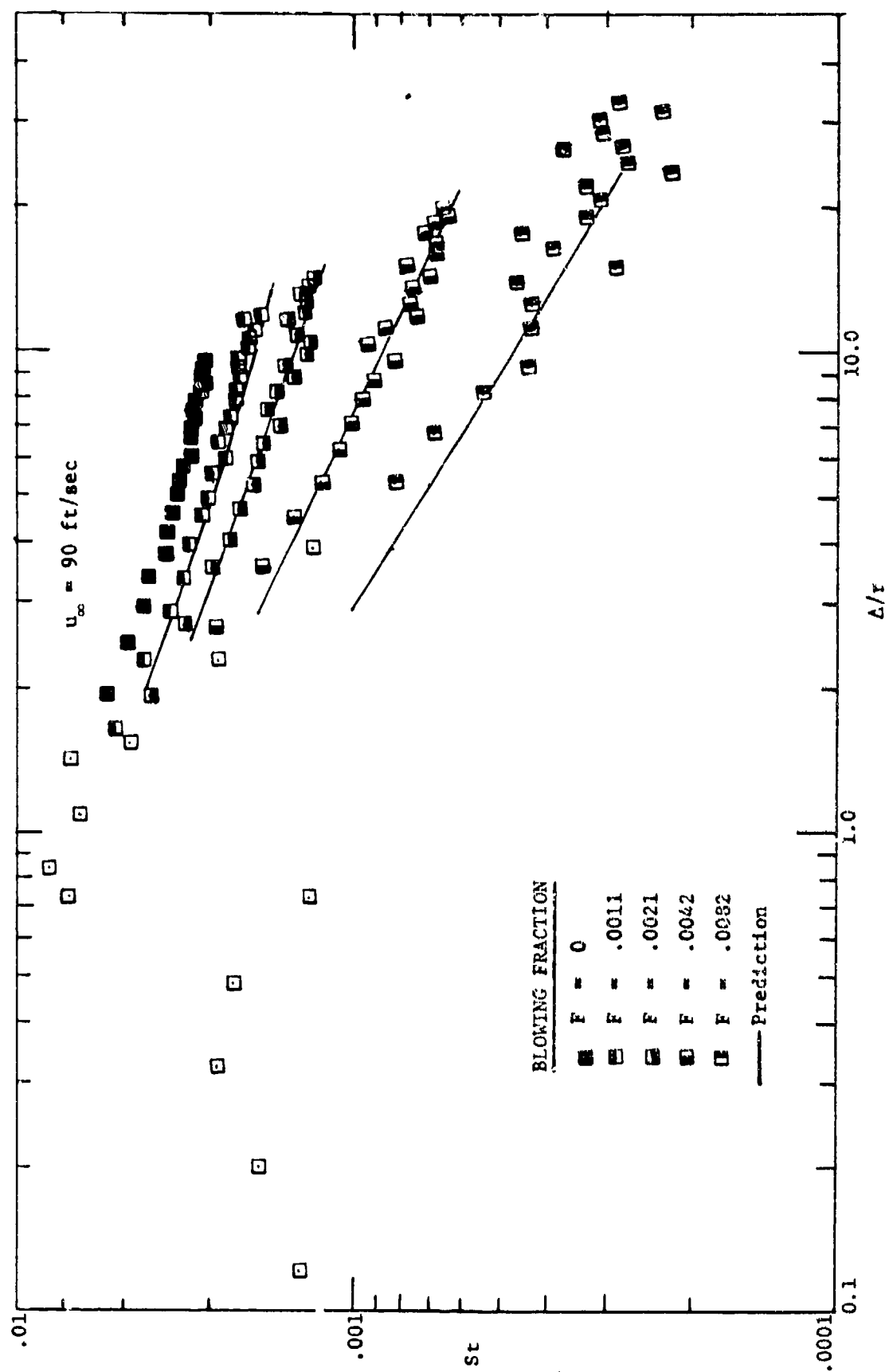


Fig. 3.20 Stanton number versus (enthalpy thickness)/(ball radius) at $u_{\infty} = 90 \text{ fps}$

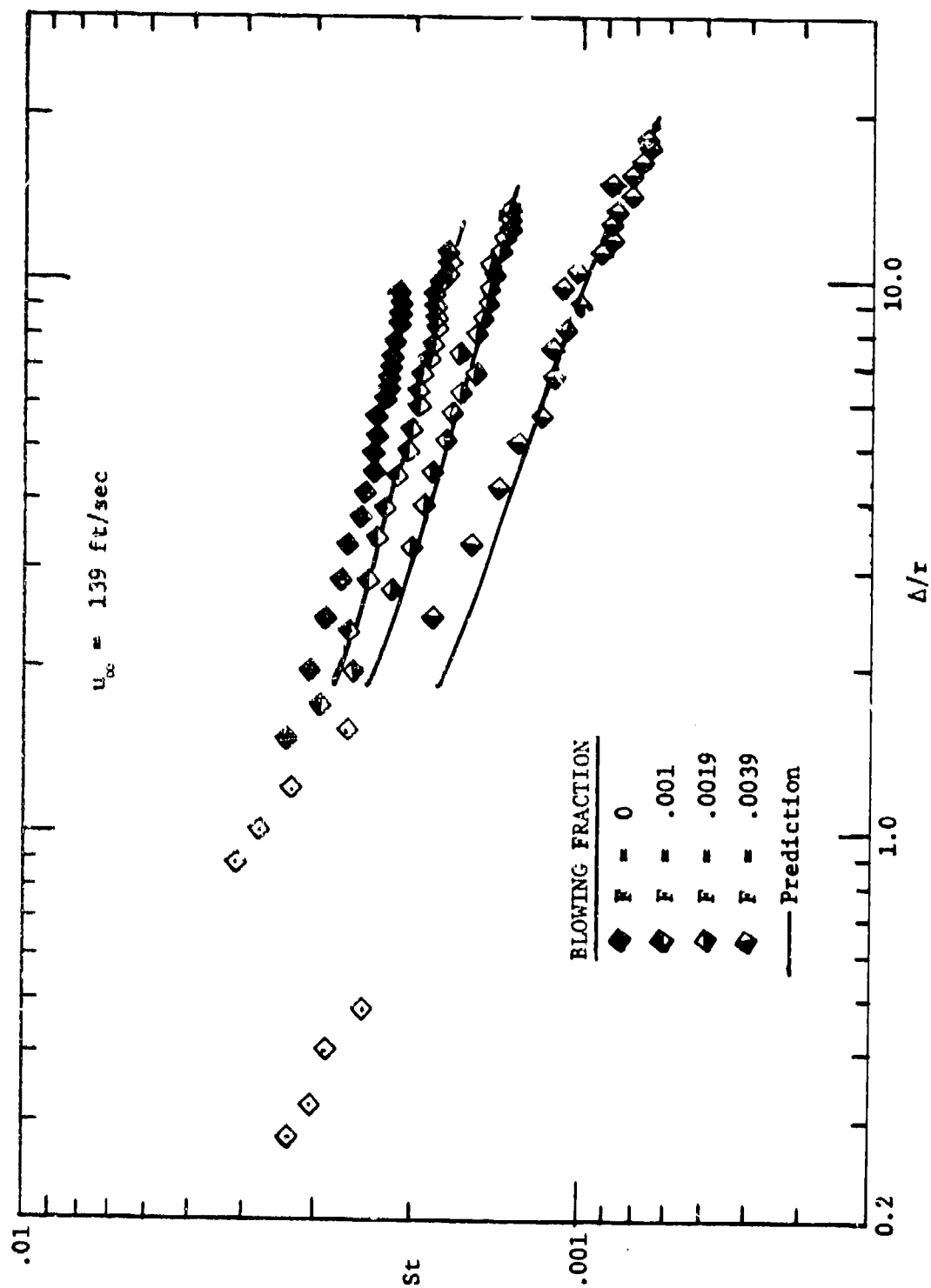


Fig. 3.21 Stanton number versus (enthalpy thickness)/(ball radius) at $u_{\infty} = 139 \text{ fps}$

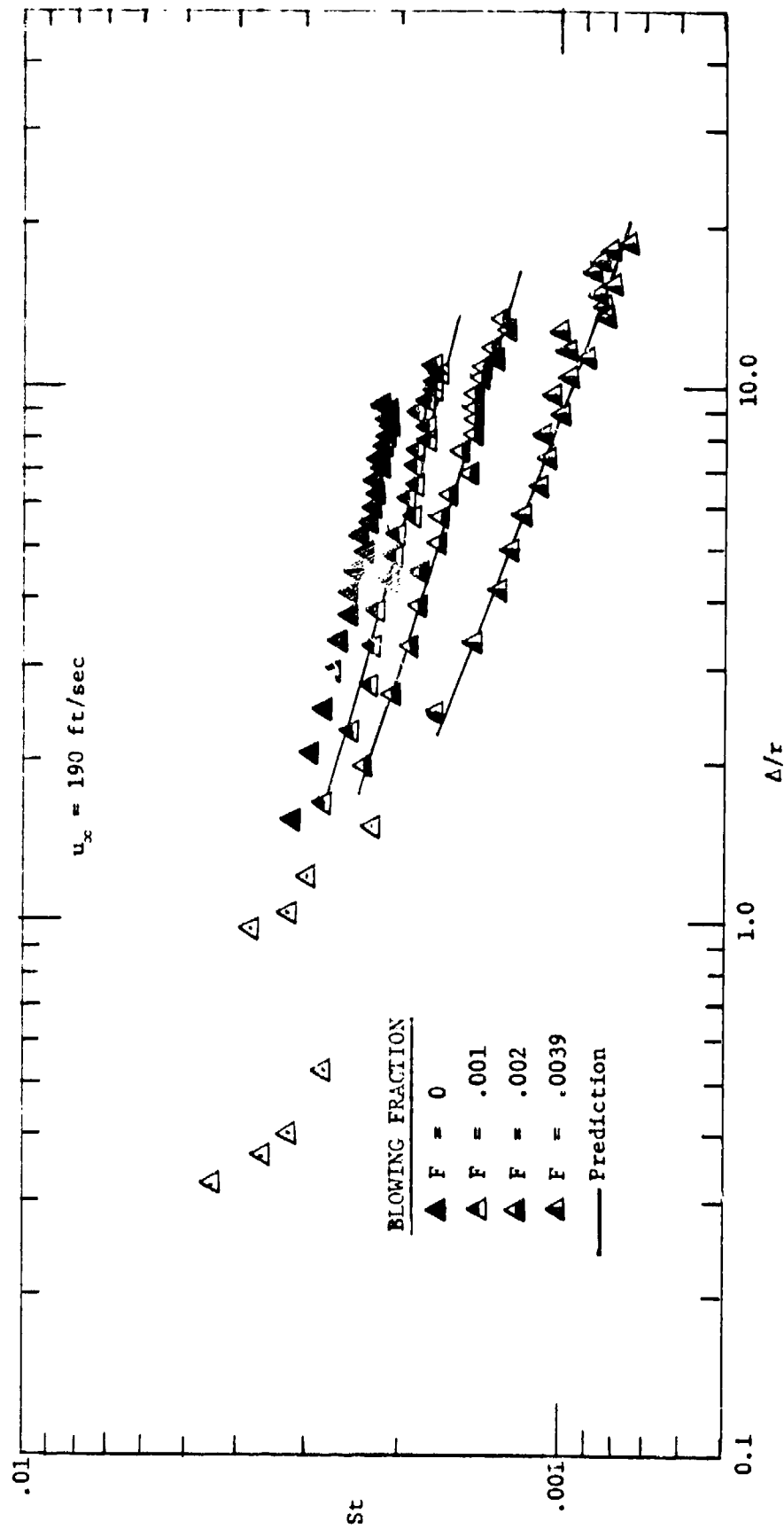


Fig. 3.22 Stanton number versus (enthalpy thickness)/(ball radius) at $u_{\infty} = 190 \text{ fps}$

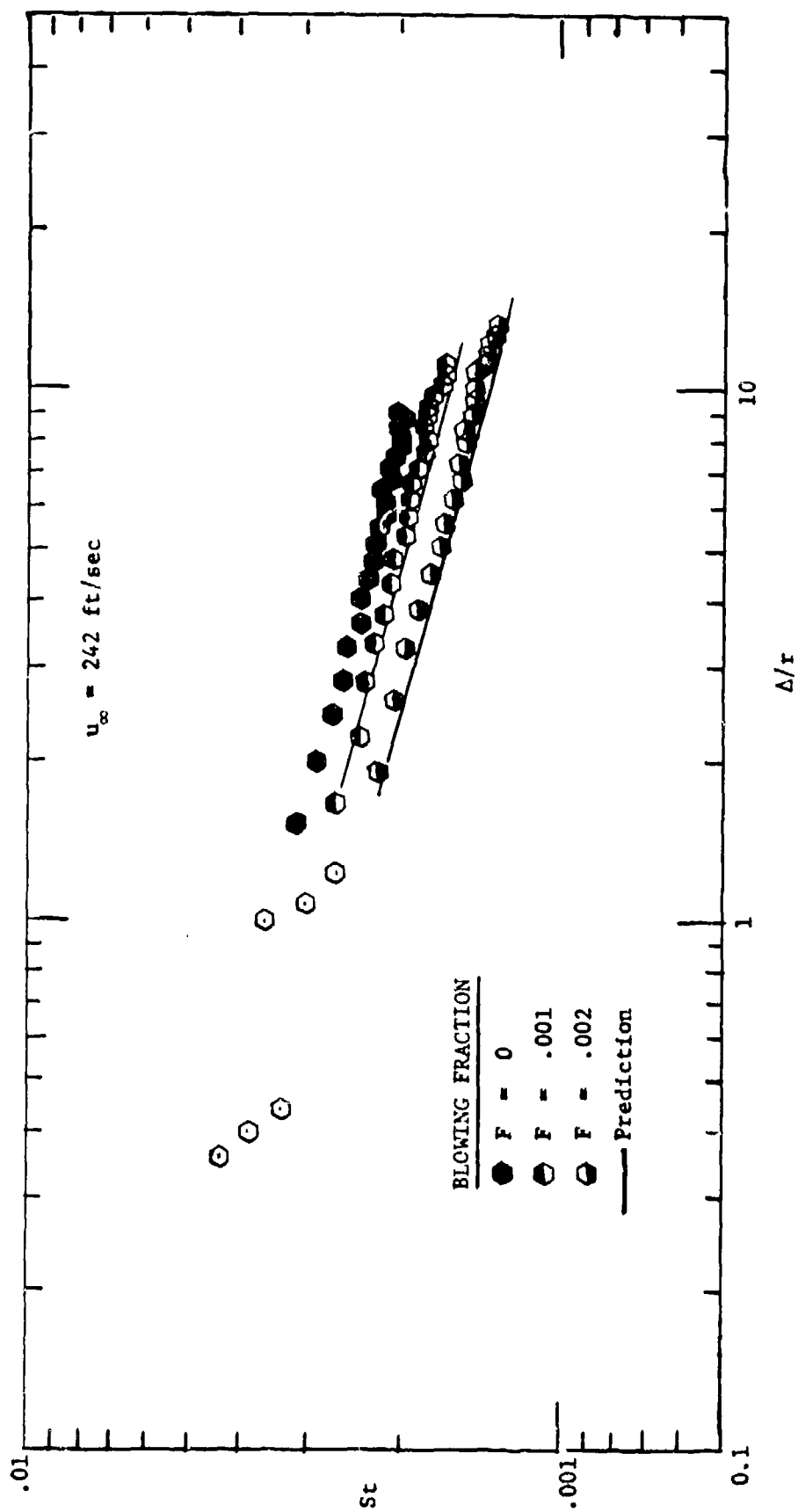


Fig. 3.23 Stanton number versus (enthalpy thickness)/(ball radius) at $u_{\infty} = 242 \text{ fps}$

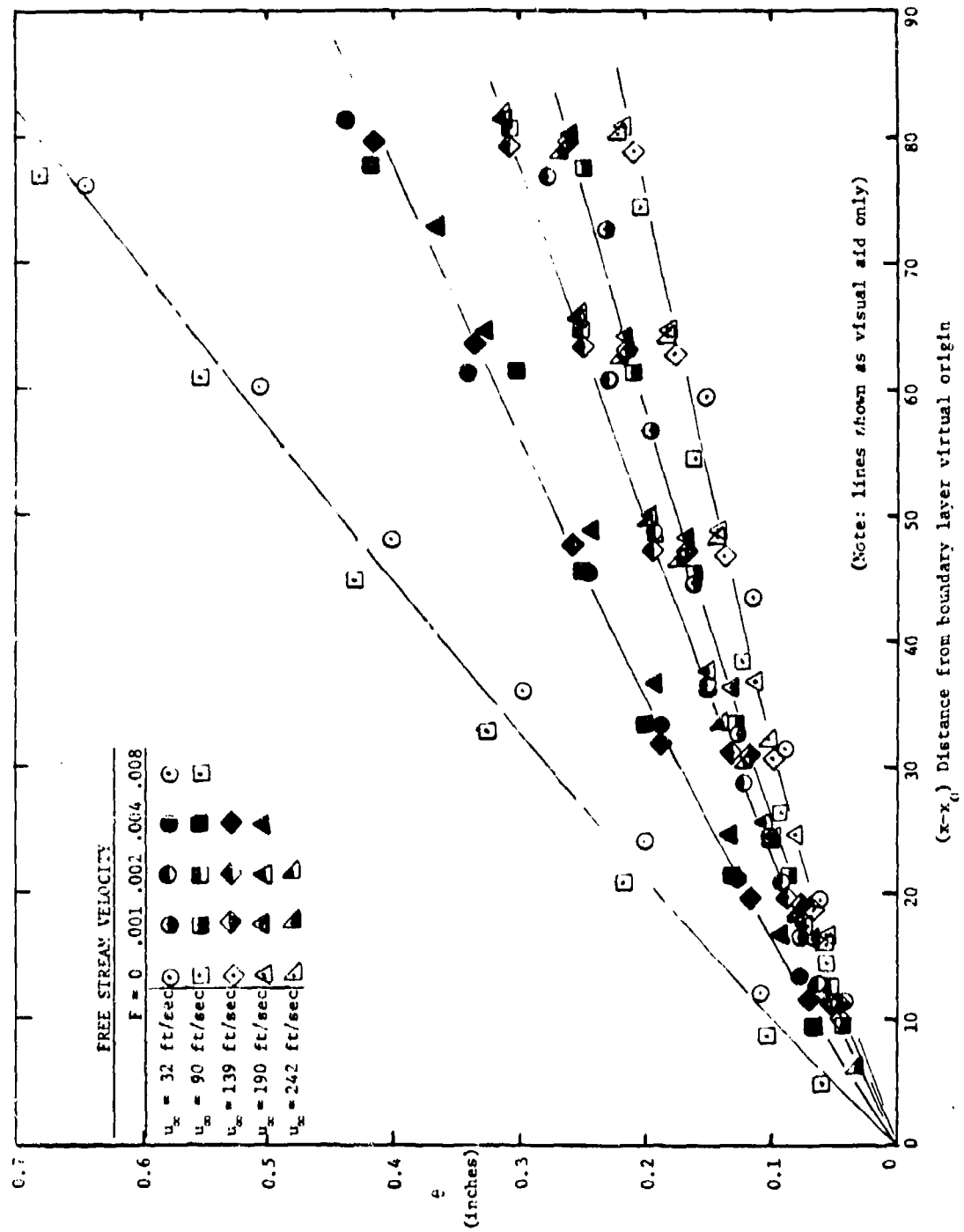


Fig. 3.24 Momentum thickness versus distance from virtual origin for all boundary layers

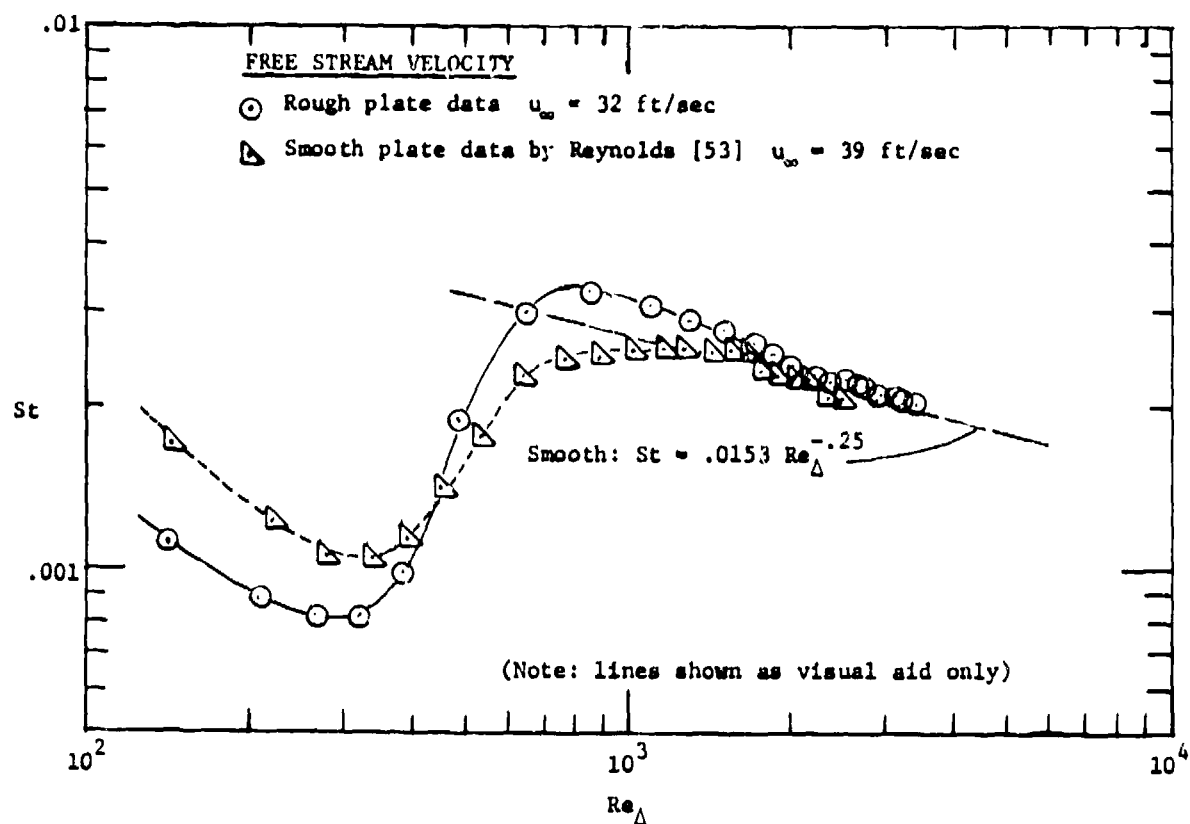


Fig. 3.25 Comparison of rough surface transition Stanton number to smooth plate transition data by Reynolds [53]

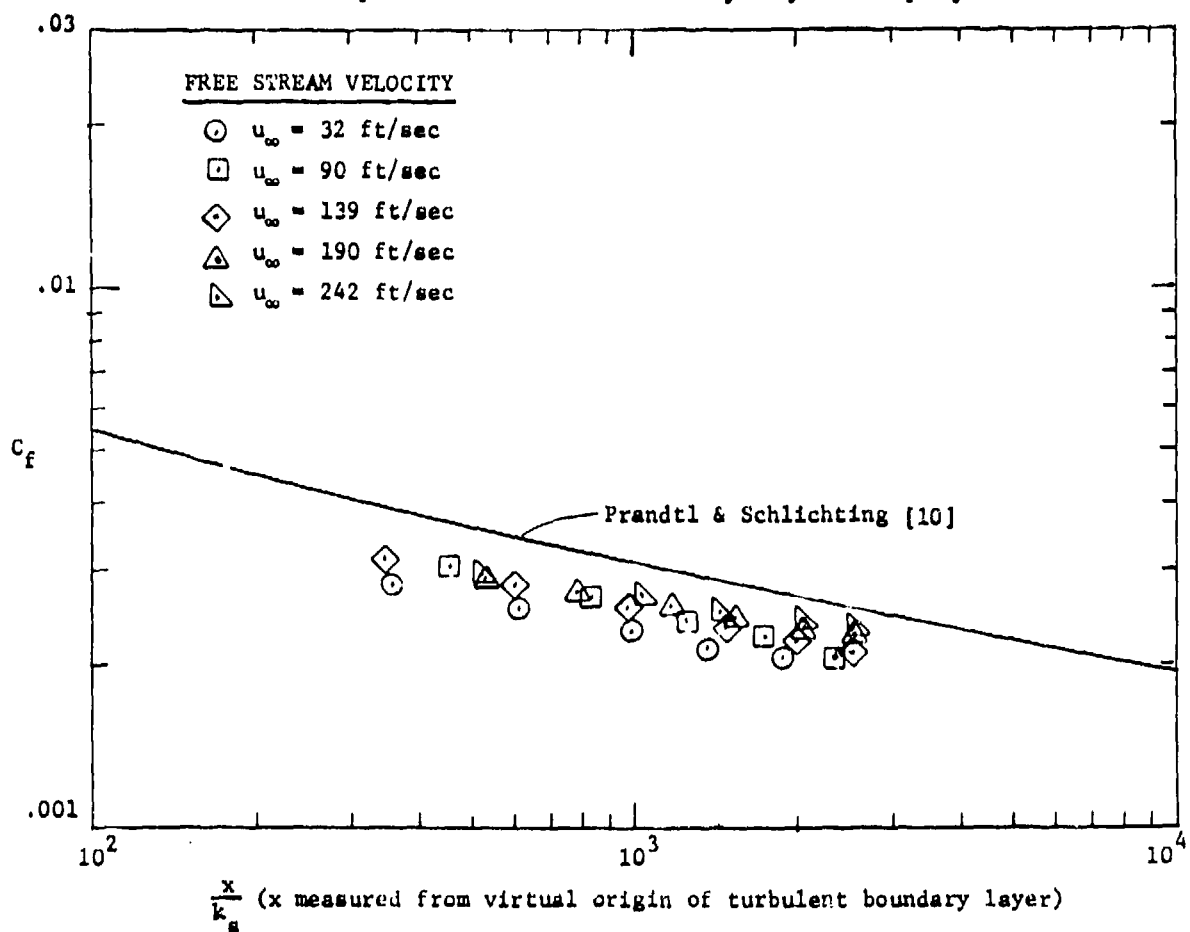


Fig. 3.26 Comparison of skin friction data with Prandtl-Schlichting correlation

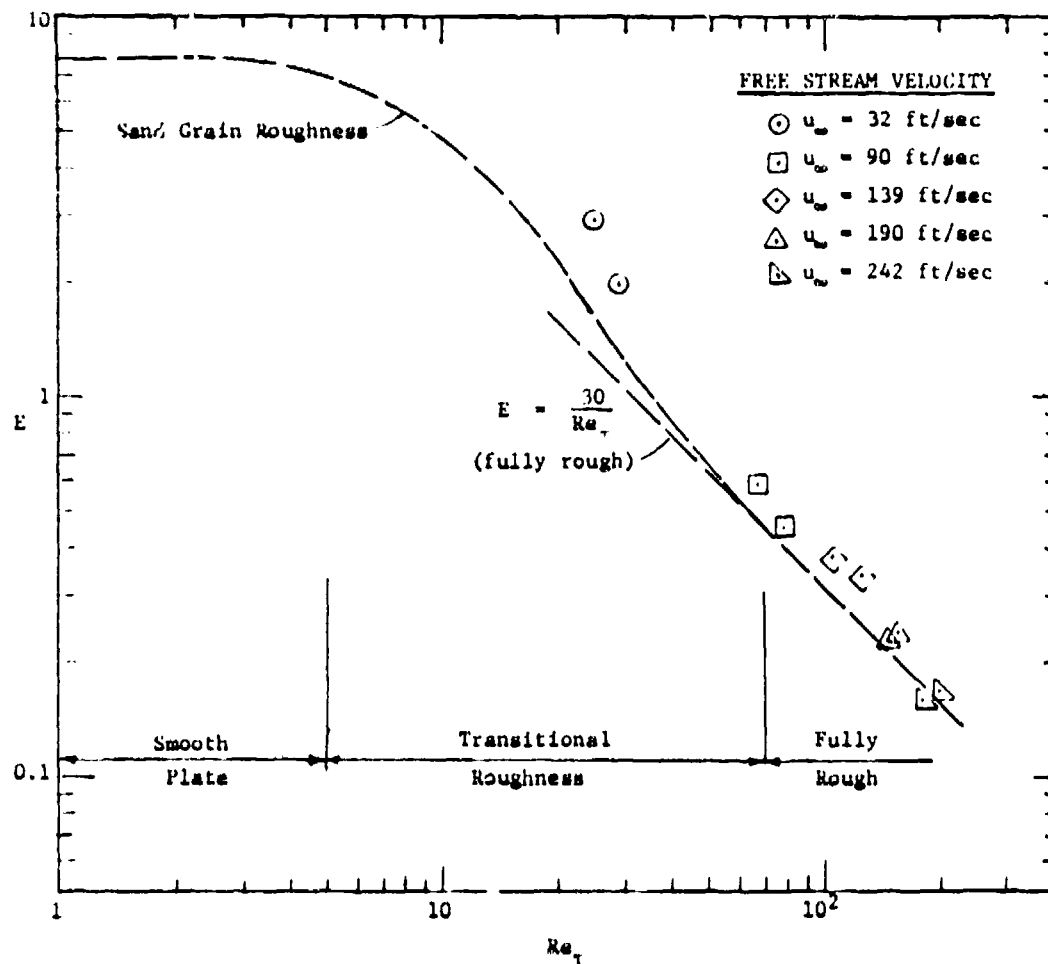


Fig. 3.27 Comparison of skin friction data in E versus Re_T coordinates

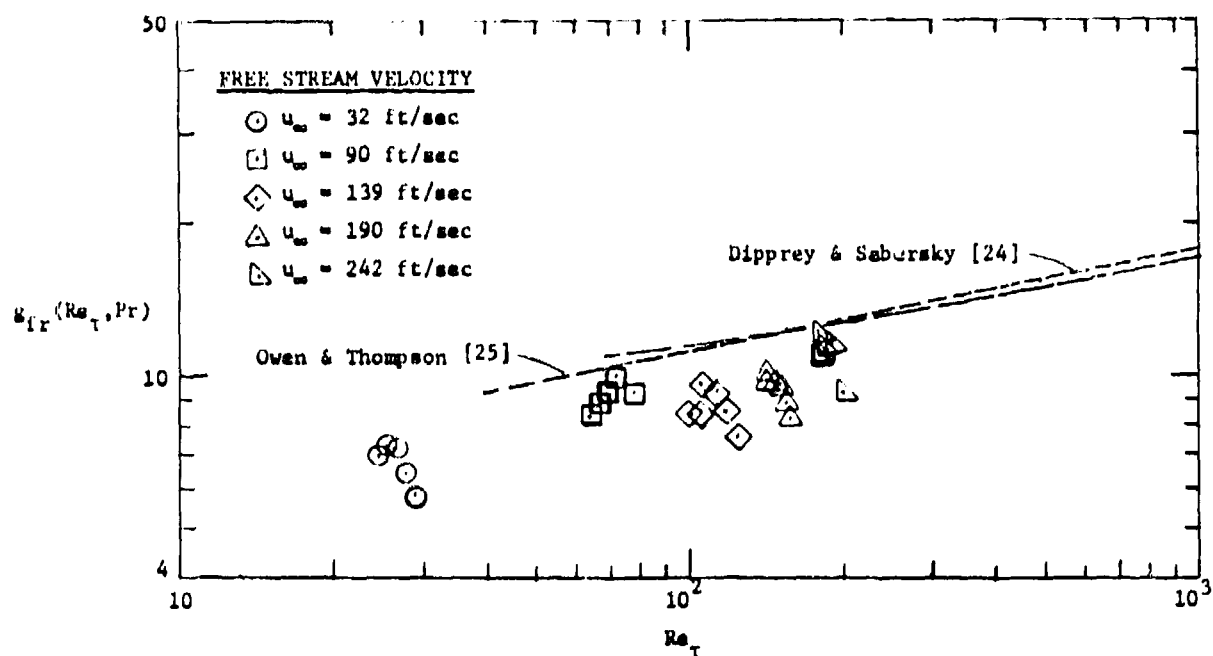


Fig. 3.28 Comparison of heat transfer data to correlations by Dipprey and Sabersky [24] and Owen and Thompson [25]

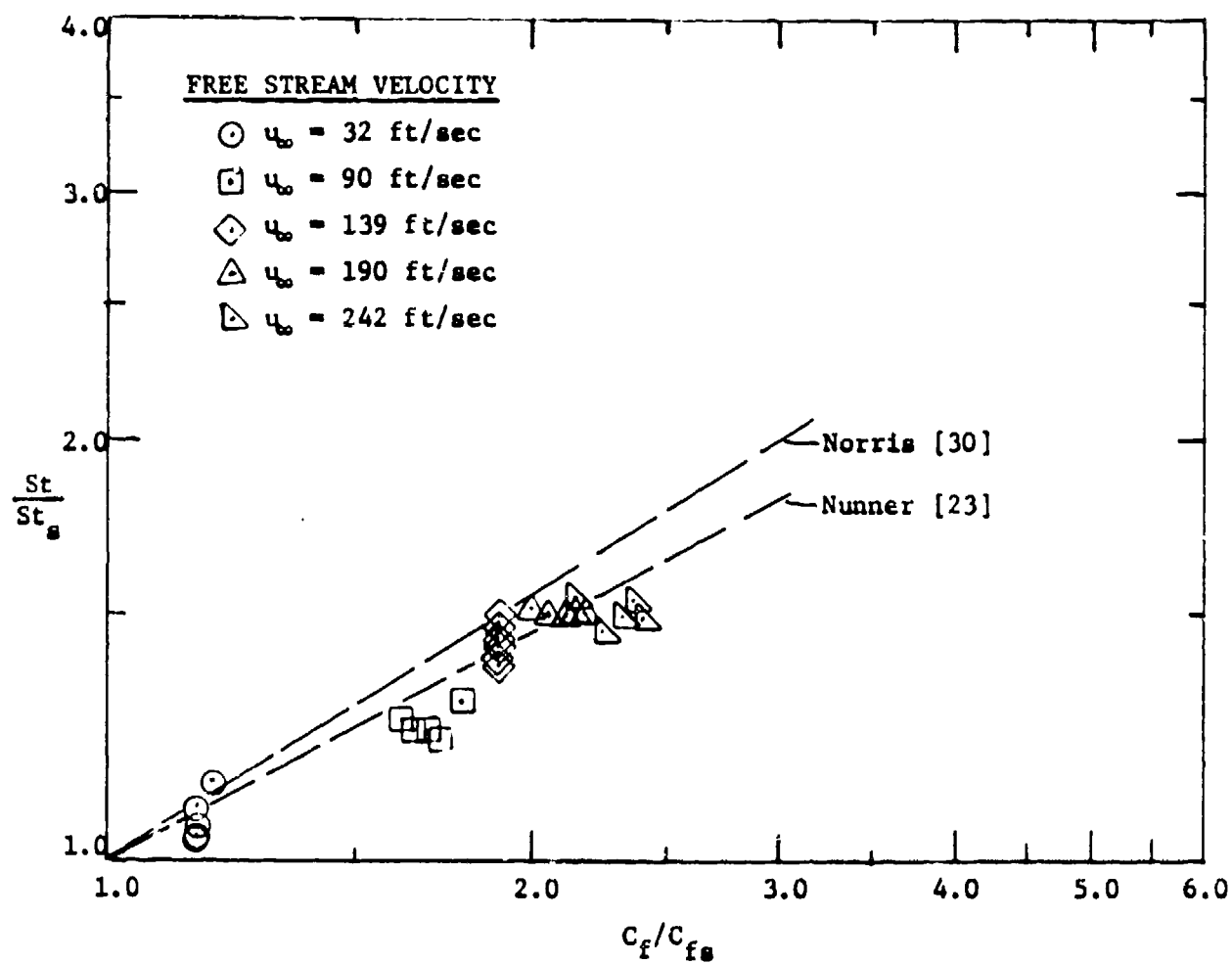


Fig. 3.29 Comparison of heat transfer data to correlations by Nunner [23] and Norris [30]

CHAPTER IV

PREDICTION OF THE ROUGH SURFACE DATA

Predictions of the rough surface boundary layers have been made using a finite-difference prediction scheme based on the computer program originated by Patankar and Spalding [37]. The turbulence model used in this program has undergone substantial development at Stanford in order to equip it to predict smooth surface, transpired turbulent boundary layers with pressure gradients. A brief description of the program is given by Kays [38], who also gives examples of its use.

A. Hydrodynamic Predictions of the Rough Surface Boundary Layer

Closure of the boundary layer equations is provided by a mixing-length scheme using a modified van Driest model in the inner region. This model has been extensively and successfully used by several similar prediction programs. In wall coordinates, it is given by:

$$l_m^+ = \kappa y^+ (1 - e^{-y^+/A^+}) \quad (4-1)$$

Near a smooth wall, the mixing-length is 'damped' to allow viscous effects to become important, since molecular viscosity dominates the flow in that region. Farther away from the wall, the mixing-length becomes a linear function of distance from the wall, following Prandtl's assumption for mixing-length behavior in the logarithmic region.

The van Driest parameter A^+ may be interpreted as a measure of the sublayer thickness. Based on this interpretation, several authors have represented A^+ as a function of pressure gradient and blowing. These parameters are known to affect the thickness of the wall region of the boundary layer. Andersen [8] gives a brief discussion of the role of A^+ and reviews some interpretations which have been given to it.

In the outer region of the boundary layer, the mixing length is held at a constant fraction of the 99% boundary layer thickness.

$$\lambda_m = \lambda \delta_{99}$$

(4-2)

Values of $\lambda = 0.08$ to 0.09 have been demonstrated to be satisfactory for smooth wall boundary layers by several authors [35,38,50]. In these predictions, $\lambda = 0.08$ was used.

It was suggested by van Driest [39] that roughness effects could be simulated by changing the damping expression, since the presence of roughness elements in the flow seemed to reduce the sublayer thickness. This can be simulated in the van Driest mixing-length model by reducing A^+ . In the present program, the relationship between A^+ and roughness was investigated by systematically predicting pipe flows over a series of Reynolds numbers. It was felt that the relative simplicity of the pipe geometry would provide results which could then be generalized to the boundary layer case. Pipe flow predictions using different damping constants produced results which verified that roughness effects could indeed be simulated by making A^+ a function of the roughness Reynolds number. Fig. 4.1 shows the functional forms of A^+ which were determined for sand-grain roughness, commercial roughness, and the rough surface used in the present experiments. The A^+ correlation for sand-grain roughness was obtained using Nikuradse's expression [9] relating friction factor to the roughness Reynolds number. The commercial roughness A^+ correlation was based on relative roughness read directly from a Moody chart at friction factors calculated for various pipe Reynolds numbers. The A^+ correlation for the rough surface used in these experiments was based on the friction factor measurements made at the 32 ft/sec tunnel velocity. This was the only tunnel velocity at which the roughness Reynolds number, based on an equivalent sand-grain roughness, was below 55. It is not surprising that the A^+ behavior of the uniform-ball roughness used in these experiments is different than either commercial or sand-grain roughness. Roughness elements in a commercially rough surface are irregular and may include some very large elements which can become 'active' and begin to produce roughness effects at relatively low values of the nominal roughness Reynolds number. The roughness elements in the sand-grain roughened surface are more uniform, and the onset of

'transitional roughness' is delayed to higher roughness Reynolds numbers. The extremely uniform nature of the roughness used in these experiments still further delayed the onset of transitional roughness. This is the behavior shown in the A^+ correlations for the different surfaces. As would be expected, the different A^+ correlations come together as the roughness Reynolds number approaches the 'fully rough' value and at a roughness Reynolds number of 55, A^+ has reached zero for all surfaces. This is consistent with the idea that at the onset of 'fully rough' behavior, the roughness elements protrude outside the sublayer. The sublayer thickness has effectively gone to zero when A^+ has gone to zero. Without a sublayer, form drag replaces viscous shear and the flow resistance becomes independent of viscosity -- an important characteristic of 'fully rough' flow.

In the prediction program, the turbulent shear transmitted to the wall is calculated from an eddy diffusivity which is based on the mixing-length model. One way to represent the 'fully rough' behavior at the wall is to make the mixing-length and, therefore, the eddy diffusivity non-zero at the wall. There is evidence that the rough wall affects mainly the flow very near the wall. Clauser [48] has shown that velocity profiles taken over both smooth and rough surfaces are similar when plotted in defect coordinates. His conclusion was that the outer flow (which is some 90% of the boundary layer) is not affected by the surface roughness. In these coordinates both smooth and rough wall velocity profiles are similar. The prediction scheme of the present work is based on these observations.

The mixing-length was made non-zero at the wall, becoming asymptotic to the smooth wall behavior away from the wall by expressing the mixing-length in the following manner:

$$\ell_m^+ = \sqrt{(ky^+)^2 + (\Delta\ell_o^+)^2} \quad (4-3)$$

By again predicting pipe flows, a correlation of the value of the mixing length at the wall, $\Delta\ell_o^+$, versus roughness Reynolds number was obtained.

$$\Delta \ell_o^+ = \sqrt{\left(\frac{Re_\tau - 46}{39}\right)^2} - .05325 \quad (4-4)$$

Figure 4.2 shows the variation of $\Delta \ell_o^+$ with roughness Reynolds number along with the data predictions used to obtain Eqn. (4-4). It is interesting to note that for large values of roughness Reynolds number ($Re_\tau > 100$) the functional relationship reduces to a simple linear variation between mixing-length offset, $\Delta \ell_o$, and equivalent sand-grain roughness. The effect of roughness on mixing-length is related only to the size of the roughness elements, an important characteristic of 'fully rough' behavior. With this correlation, it is possible to predict the behavior of all of the surface roughnesses which require different A^+ correlations. This was expected, since in fully developed roughness the behavior of many different surfaces can be expressed in terms of an equivalent sand-grain roughness.

The mixing-length variation as a function of roughness Reynolds number is shown in Fig. 4.3. Fig. 4.4 shows predictions of Nikuradse's [9] rough pipe data. These predictions were made by modeling the Nikuradse experiment with the prediction program using the mixing-length model just described. The sand-grain roughness A^+ correlation was used for roughness Reynolds numbers below 55 and the correlation for mixing-length value at the wall, $\Delta \ell_o^+$, above 55. The rough pipe behavior was well predicted over a wide range of roughnesses and pipe Reynolds numbers.

Predictions were made of the rough surface boundary layer from the present experiments using these same correlations. For roughness Reynolds numbers below 55, it was necessary to use an A^+ correlation selected for this particular type of roughness. For roughness Reynolds numbers greater than 55, the same mixing-length offset correlation already described was used. Figs. 4.5 and 4.6 show a comparison of measured and predicted velocity profiles at velocities of 32 fps and 139 fps. In general, measured and predicted profiles in wall coordinates compare favorably as long as the measured and predicted skin frictions are comparable. This is generally the case over the last two-thirds of the test section. Fig. 4.7 compares the measured and predicted skin friction for

three test section velocities. In nearly every case the predicted values are greater than measured near the front of the test section. This same trend has also been observed in the smooth wall predictions and probably results because initially the boundary layer is still recovering from transition and attempting to reach an equilibrium state.

In making these predictions, it was found that blowing decreased the predicted skin friction. In order to keep this reduced skin friction from reducing the effect of the roughness, a first-order blowing correction has been added to the correlation for the mixing-length at the wall, $\Delta \ell_o^+$. With the blowing correction, it becomes:

$$\Delta \ell_o^+ = \sqrt{\left[\frac{Re_\tau \{ 1 + f(v_o^+) \} - 46}{39} \right]^2} - .05325 \quad (4-5)$$

$$f = \begin{cases} Re_\tau/5 & \text{for } Re_\tau \leq 80 , \\ 16 & \text{for } Re_\tau > 80 . \end{cases}$$

One would expect that blowing should play the same role in the mixing-length formulation no matter if the wall is rough or smooth. The expression for roughness Reynolds number with its blowing correction can be rewritten as the sum of two roughness related Reynolds numbers:

$$Re_\tau \{ 1 + f(v_o^+) \} = \left(\frac{v_\tau k_s}{v} \right) + f \left(\frac{v_o k_s}{v} \right) . \quad (4-6)$$

It is reasonable that if there is blowing at the wall this should affect the mixing-length correlation and that the effect be similar to the correction that other investigators [8,35,49,50] have applied to A^+ to ensure correct prediction of smooth surface skin friction with blowing.

B. Heat Transfer Predictions for the Rough Surface Boundary Layer

Heat transfer predictions were made by solving the boundary layer energy equation using a turbulent Prandtl number model for closure. A constant turbulent Prandtl number is often used for smooth surface boundary layer predictions. There is not complete agreement among experimenters about the behavior of the turbulent Prandtl number with distance from the wall, but most agree that it increases near the wall. One turbulent Prandtl number expression which has been used successfully for air [38] and which reflects this trend is given by:

$$Pr_{t,smooth} = (1.43 - 0.17 y^{+1/4}) \quad (4-7)$$

for $Pr_{t,smooth} \geq 0.86$. If $Pr_{t,smooth} < 0.86$, then

$$Pr_{t,smooth} = 0.86 .$$

A plot of this model is shown in Fig. 4.8, and it can be noted that near the wall the Prandtl number increases to 1.43, which is approximately the reciprocal of the molecular Prandtl number for air. Also shown is the constant turbulent Prandtl number model often used for air as well as other, higher Prandtl number fluids.

Figure 4.9 illustrates the results obtained using the smooth surface turbulent Prandtl number model for rough pipe heat transfer to air. The predictions are plotted in the coordinates used by Nunner [23] to organize his rough pipe heat transfer data; rough-to-smooth Stanton number versus rough-to-smooth skin friction. While the predictions are reasonably well organized in these coordinates, probably due to the correct modeling of the skin friction, the general trend of the data is high. Use of this smooth wall turbulent Prandtl number over-predicts the heat transfer. This was not unexpected. The smooth surface turbulent Prandtl number model forces the momentum and thermal eddy diffusivities, and therefore the transport process, themselves, to be similar. In solving the momentum problem, the mixing-length has been increased near the wall to account for form drag and increased mixing at and near the surface due

to the presence of roughness elements. In the heat-transfer problem, the increased mixing will increase the thermal transport across the boundary layer near the wall, but at the wall there is no heat transfer mechanism analogous to the pressure force transmitted to the wall as form drag. At the wall, heat can be transferred only by conduction. To account for this difference using only the parameters available to the prediction program, the turbulent Prandtl number must be increased both at and near the wall. To accomplish this, a thermal mixing-length has been defined. The rough surface turbulent Prandtl number is then expressed as:

$$Pr_{t,rough} = Pr_{t,smooth} \left(\frac{\ell_m}{\ell_H} \right)^2 \quad (4-8)$$

The thermal mixing-length is defined with the same modified van Driest model used for the momentum mixing-length and uses the same roughness correlations. However, when evaluating the thermal mixing-length, a reduced roughness Reynolds number is used. Since the roughness effects are built into the models only near the wall, the thermal mixing-length is less than the momentum mixing-length near the wall, but both approach smooth surface behavior away from the wall. This produces an increased turbulent Prandtl number near the wall, but approaching the smooth surface correlation away from the wall. It was decided to first apply this model to rough pipe heat transfer data and then generalize these results to the boundary layer case. The Dipprey and Sabersky [24] pipe data were chosen because of the wide range of roughness and fluid Prandtl numbers. It soon became evident when predicting these data that the thermal mixing-length correlation, to be successful, must be a function of Prandtl number as well as roughness Reynolds number. At high roughness Reynolds numbers, the increased mixing-length used for the hydrodynamic predictions almost entirely masked any molecular Prandtl number effects on heat transfer. To correctly predict the heat transfer results, the amount by which the roughness Reynolds number is reduced when evaluating the thermal mixing-length must be a function of molecular Prandtl number. Predictions of the Dipprey and Sabersky data are shown

in Figs. 4.10 and 4.11. It's apparent that the Prandtl number effects persist even in the very rough data. In making these predictions, the roughness Reynolds numbers were reduced by the factor C_H , which was given by:

$$C_H = 0.5 \quad \text{for } Re_\tau \leq 40, \quad (4-9)$$

$$C_H = 0.5 - .0454(1.9+Pr)(\log Re_\tau - 1.602) .$$

In using this correlation, C_H is never allowed to become less than 0.1. A plot of C_H is shown in Fig. 4.12. It should be pointed out that C_H simply provides a convenient means by which to reduce the effects of roughness on the thermal mixing-length at and near the wall and therefore produce a higher turbulent Prandtl number at and near the wall.

To predict the heat transfer data from the present tests, it is sufficient to simply reduce the roughness Reynolds number by half. As can be seen from Fig. 4.12, over the limited roughness Reynolds number range of these experiments, this is essentially the same C_H which would be produced by the correlation used for prediction of the Dipprey and Sabersky data. Fig. 4.13 compares the Stanton number predictions for the present experiments with the data. As can be seen, the agreement of the predictions with the data is very good.

Finally, it should be pointed out that the models used here are based primarily on the observation that the roughness effect is confined to a region very near the wall, with the outer region of the boundary layer being relatively unaffected. In the present heat transfer model, if the reduced roughness correction were not used, the increased turbulent transport at the wall would overshadow any molecular effects. This has been shown experimentally not to be the case -- the Prandtl number of the fluid plays an important role in rough surface heat transfer. As a result, a Prandtl number effect must be included in the correlations used for the Stanton number predictions. A possible reason why molecular effects persist in rough surface heat transfer lies in the fact that conduction is the only mechanism available for the exchange at the wall.

As the height of the roughness elements increases it is likely that the inner regions can be modeled as a nearly stationary fluid film. Heat must be transferred through this film by conduction, hence the molecular Prandtl number becomes important. This fluid film is not part of the present finite-difference prediction program. An improved modeling might include a thermal conduction layer in the energy equation to better represent the molecular effect that is present in the rough surface heat transfer data.

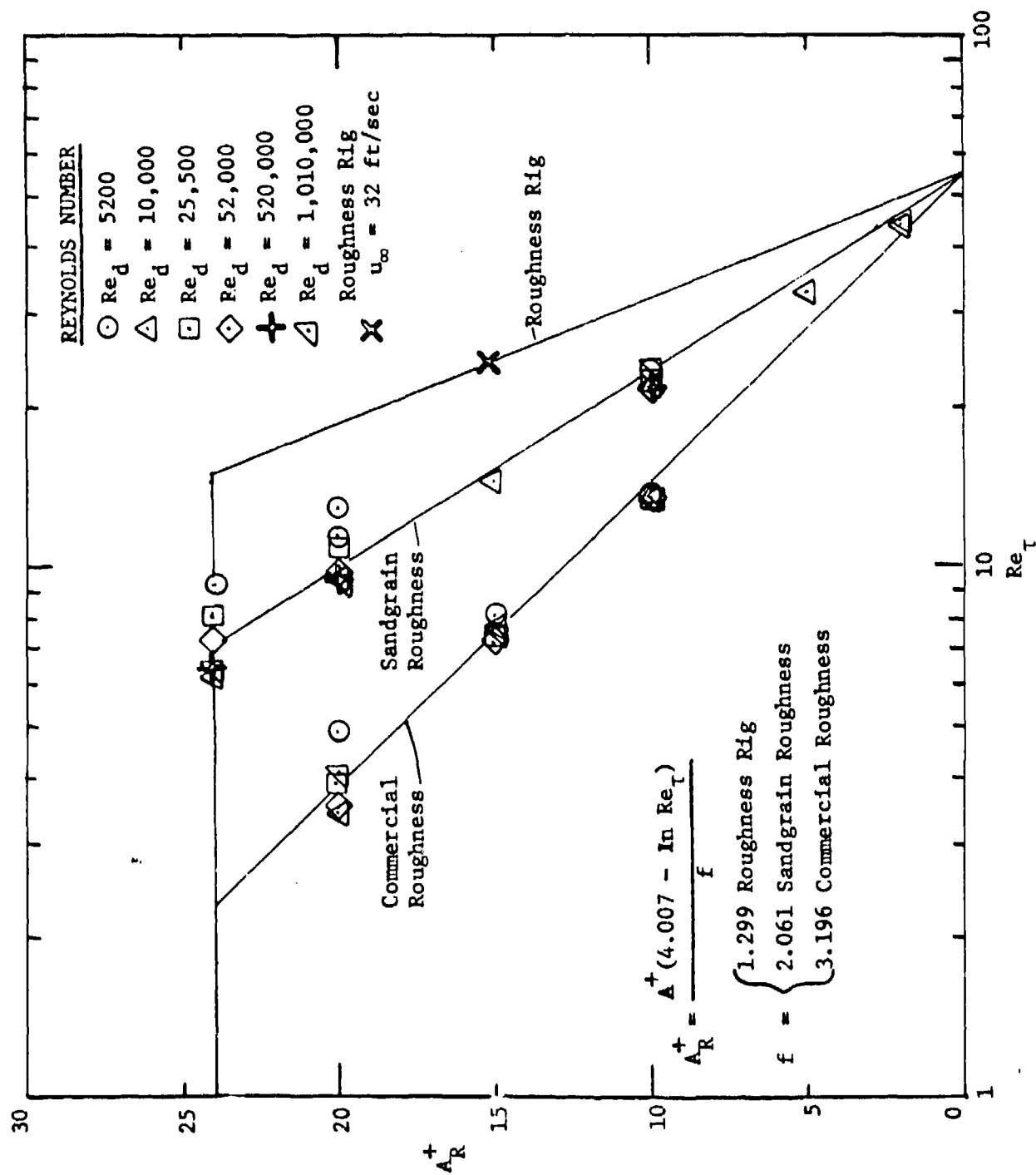


Fig. 4.1 Rough surface damping constant, A^+ , versus roughness Reynolds number

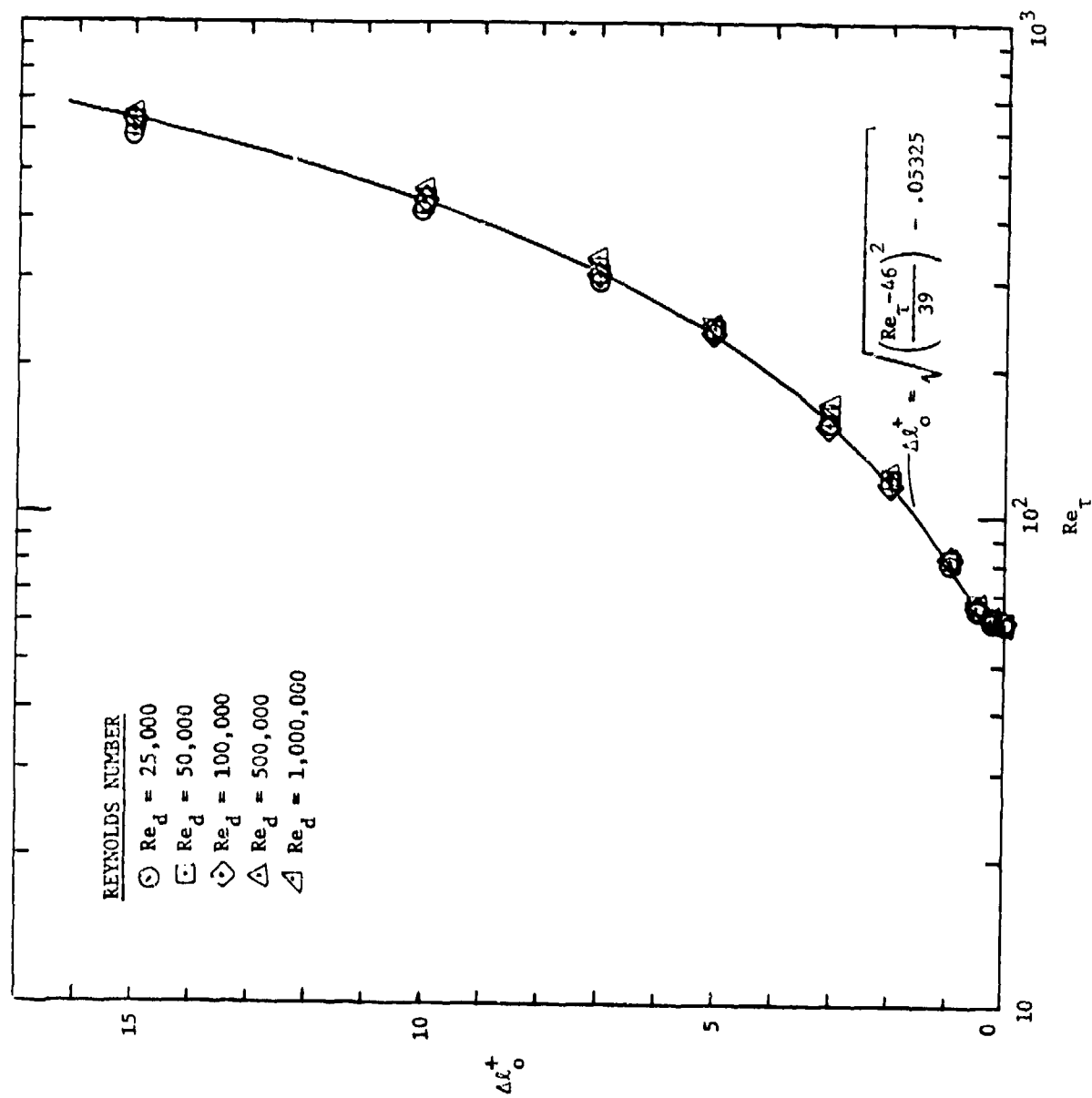


Fig. 4.2 Mixing-length wall value, $\Delta \ell_0^+$, versus roughness Reynolds number

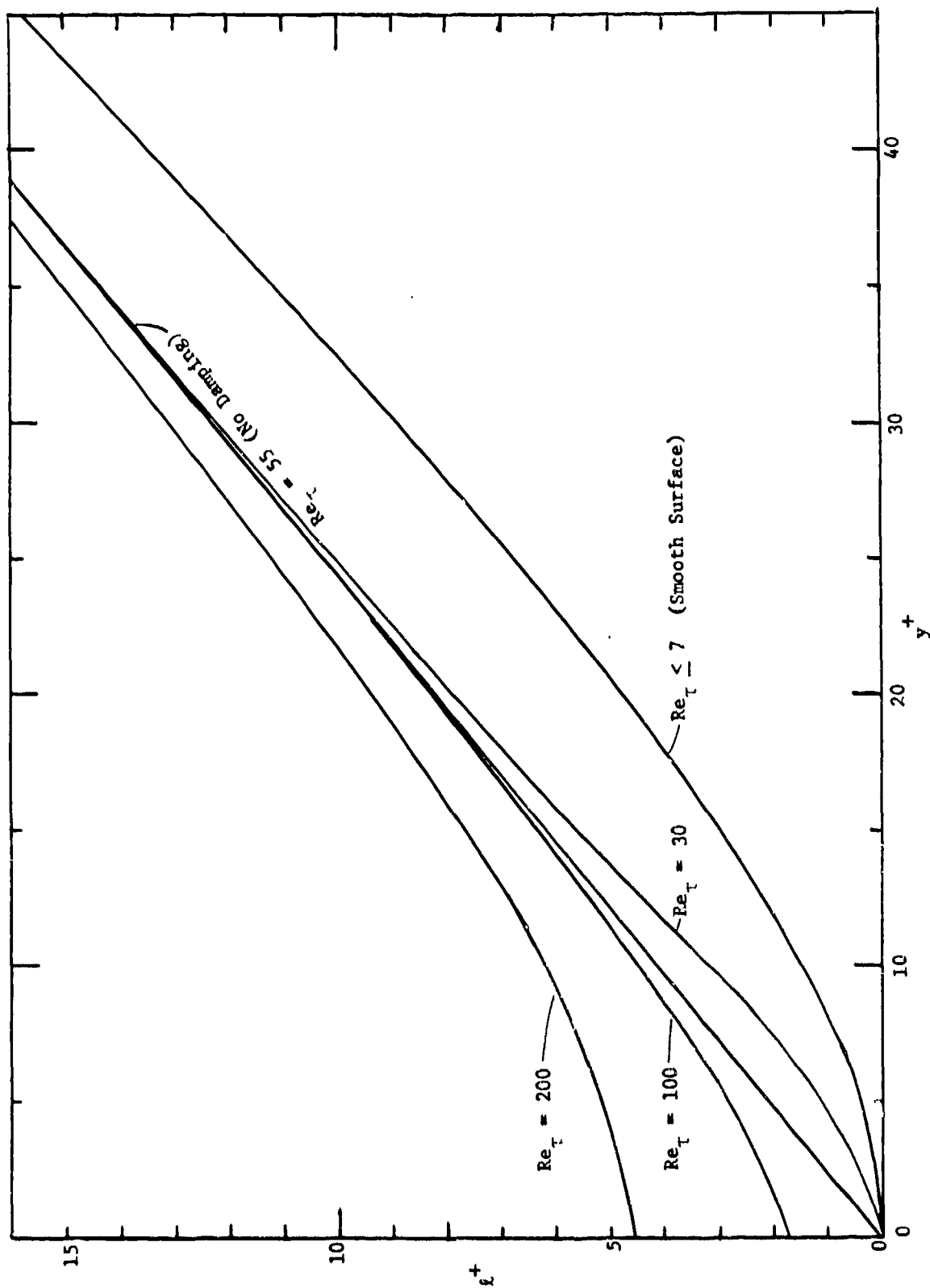


Fig. 4.3 Rough surface mixing-length, l^+ , versus y^+

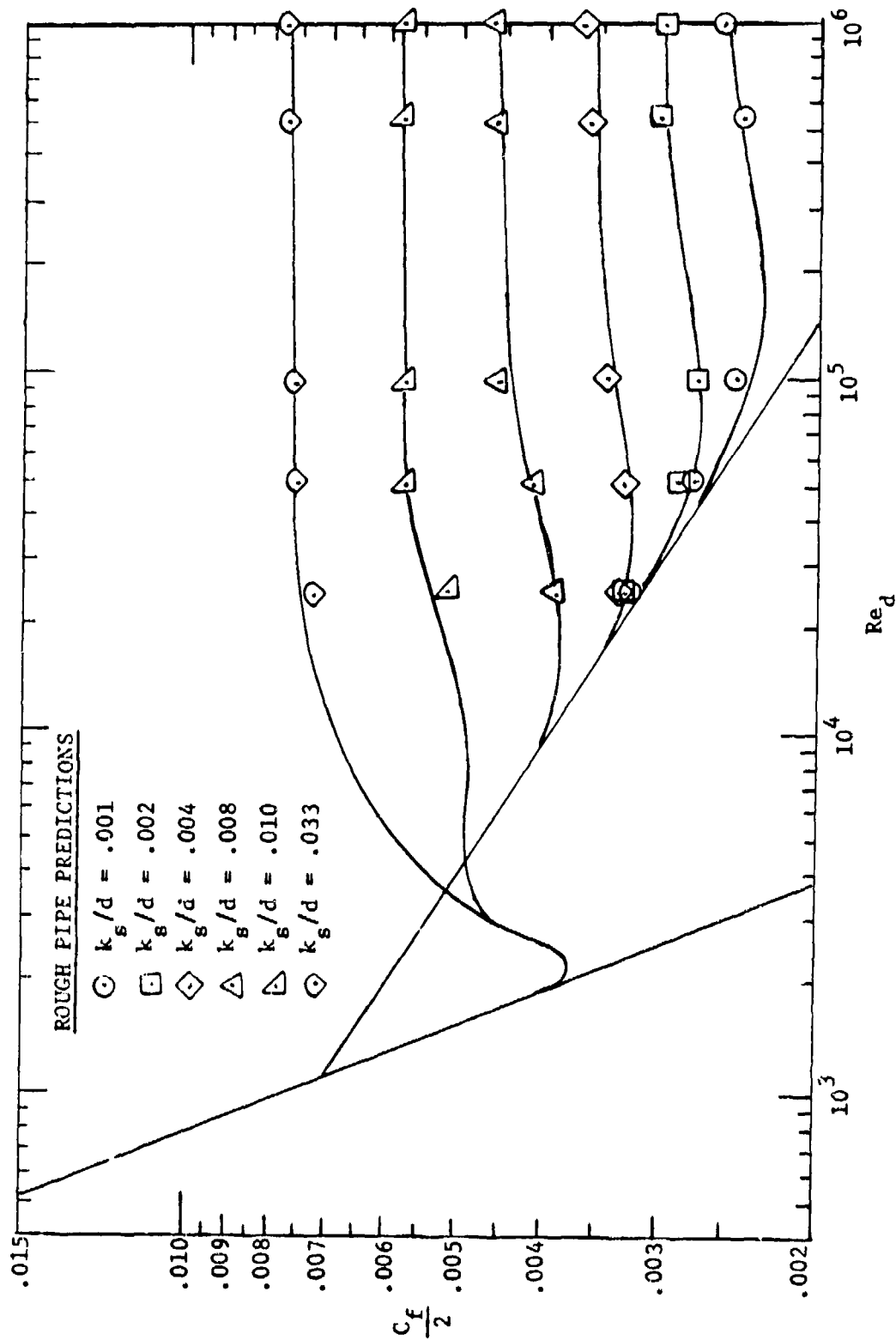


Fig. 4.4 Prediction of rough pipe friction factor data

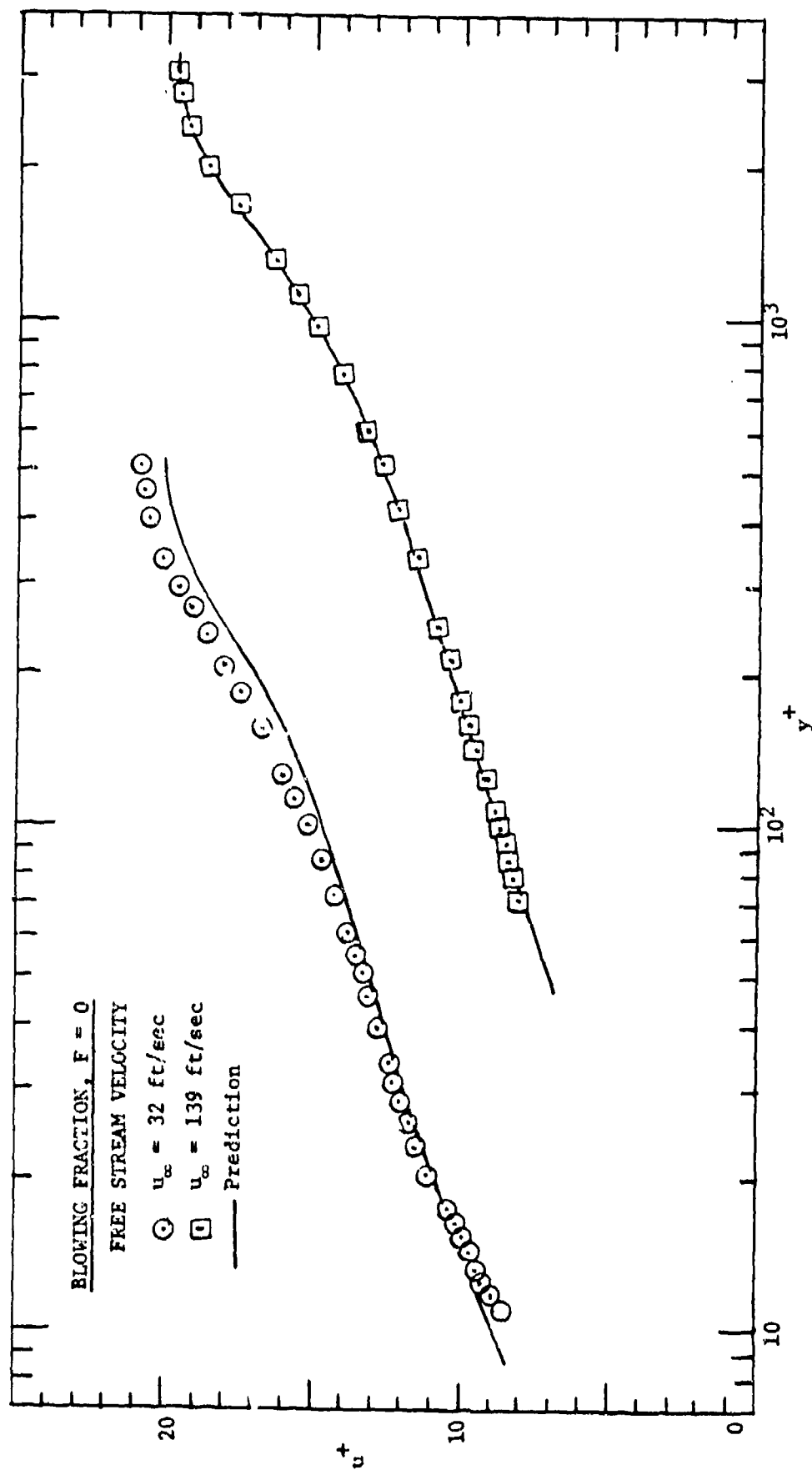


Fig. 4.5 Predicted and measured rough surface velocity profiles at $u_\infty = 32 \text{ fps}$ and $u_\infty = 139 \text{ fps}$ with no blowing

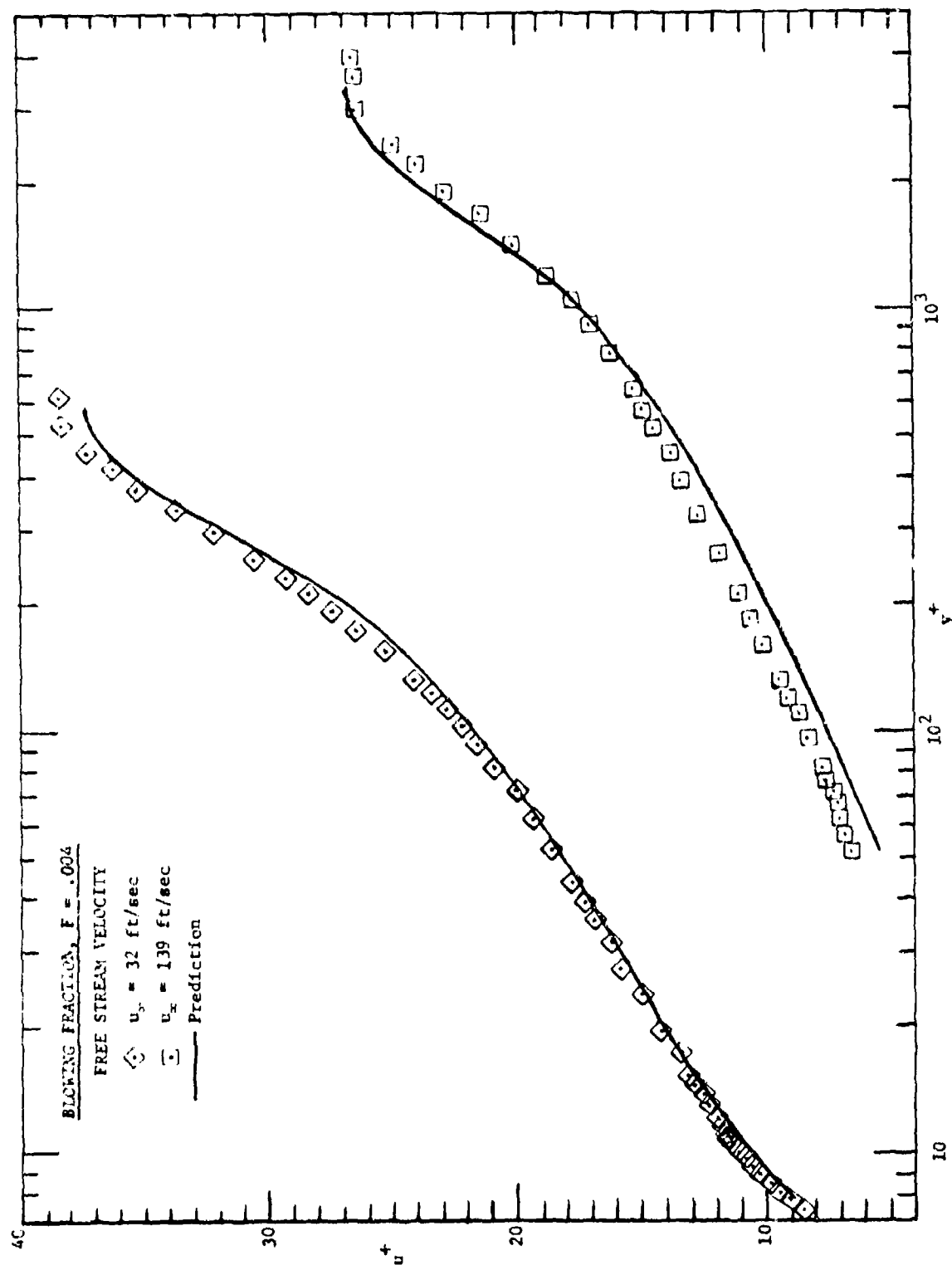


Fig. 4.6 Predicted and measured rough surface velocity profiles at $u_\infty = 32$ fps and $u_\infty = 139$ fps with $F = .004$

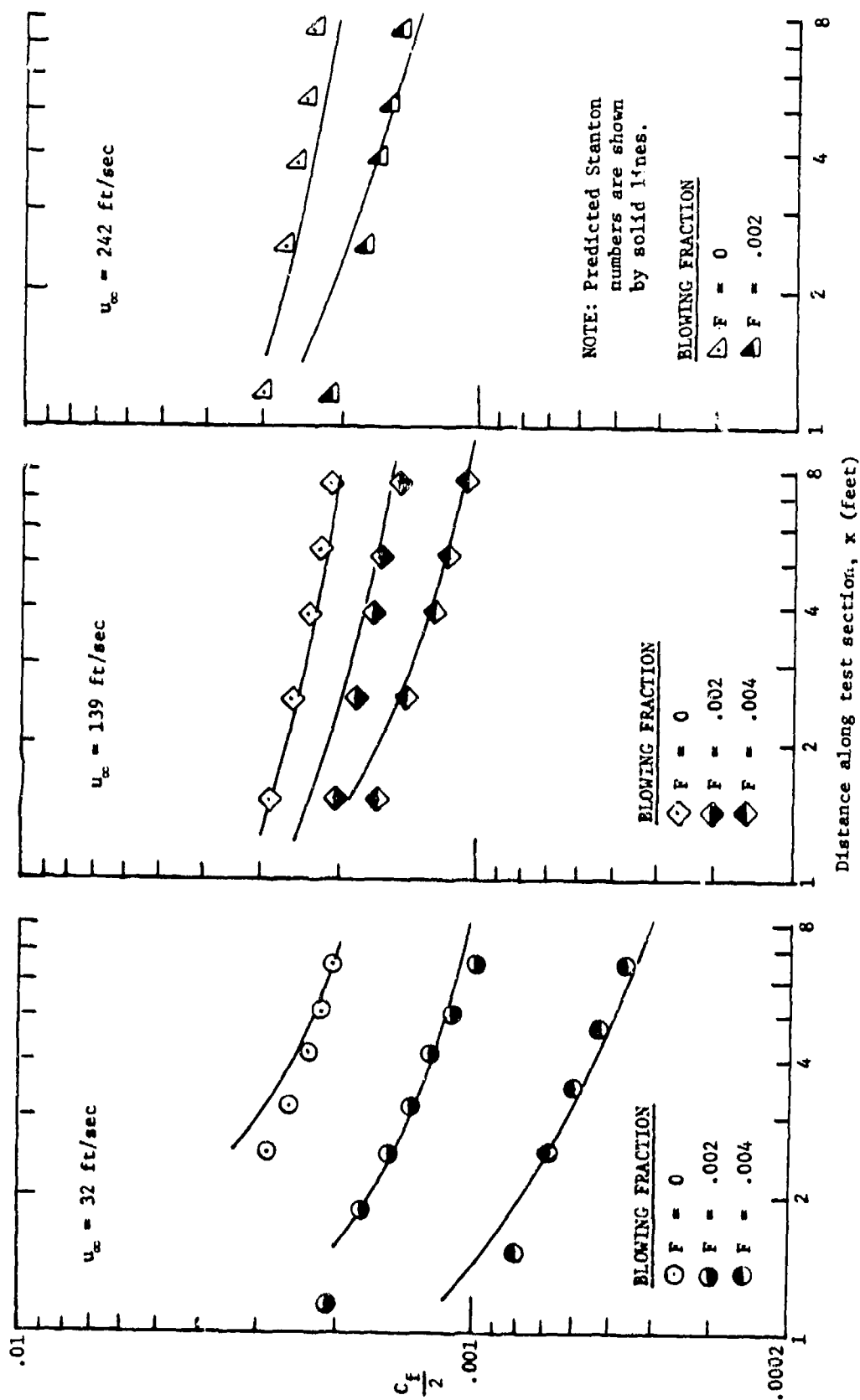


Fig. 4.7 Prediction of rough surface skin friction data

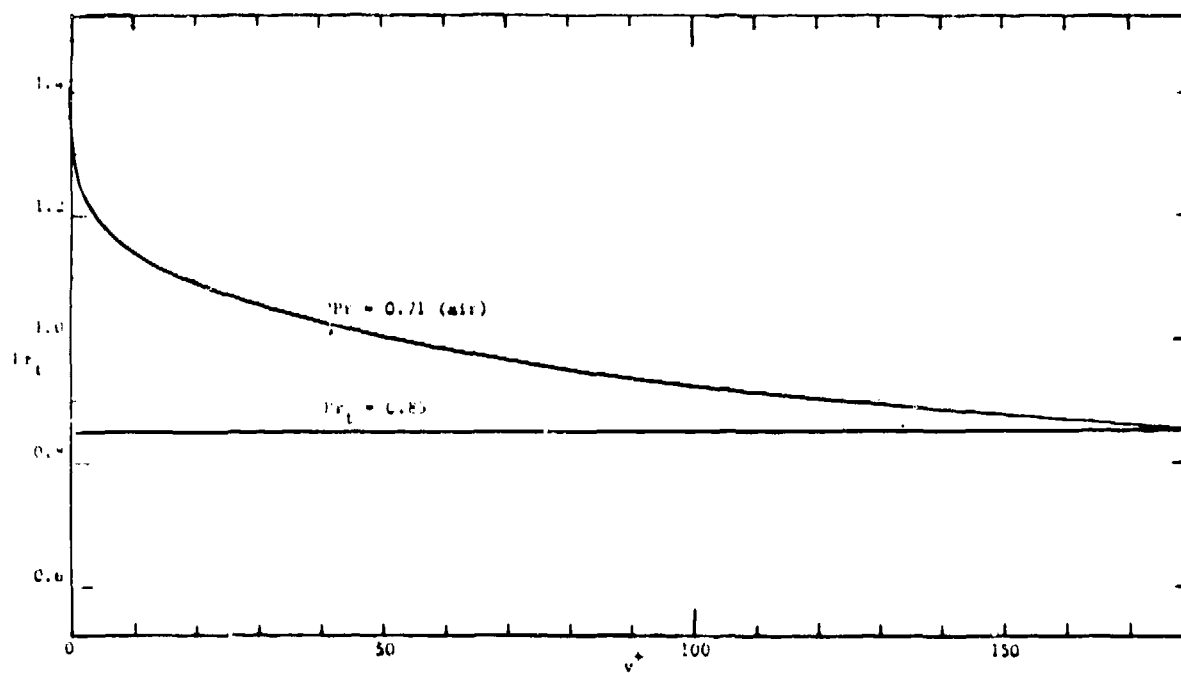


Fig. 4.8 Smooth surface turbulent Prandtl number model

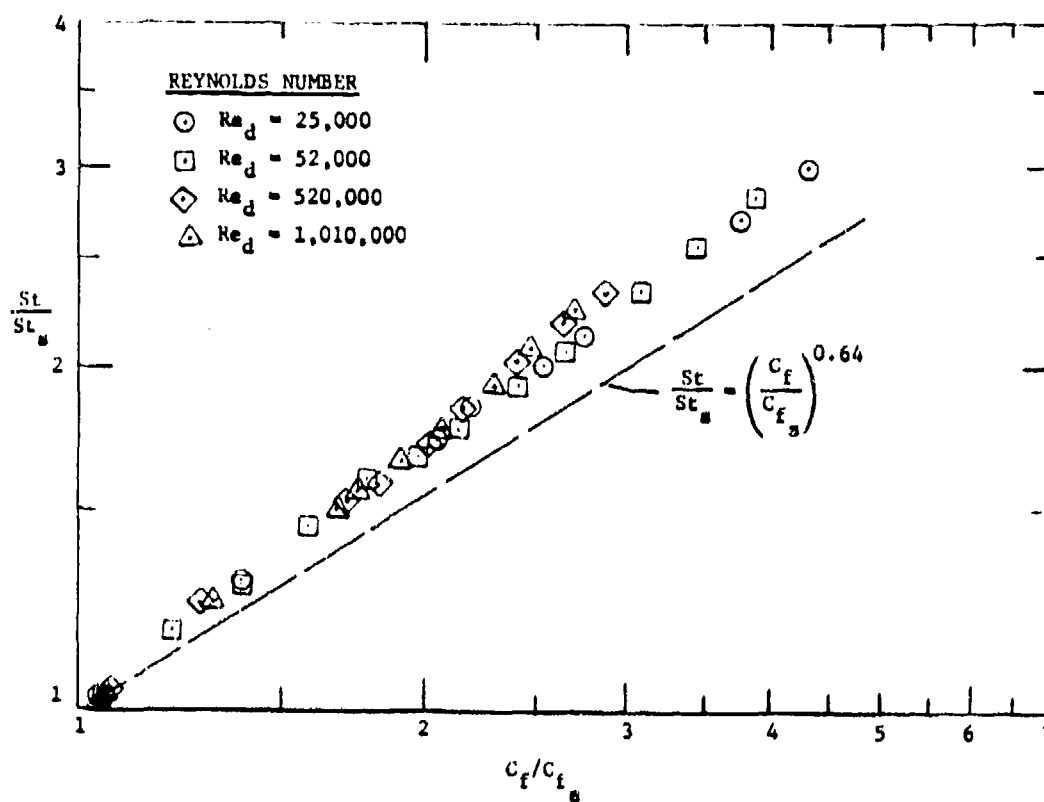


Fig. 4.9 Rough pipe heat transfer predictions with smooth surface turbulent Prandtl number model

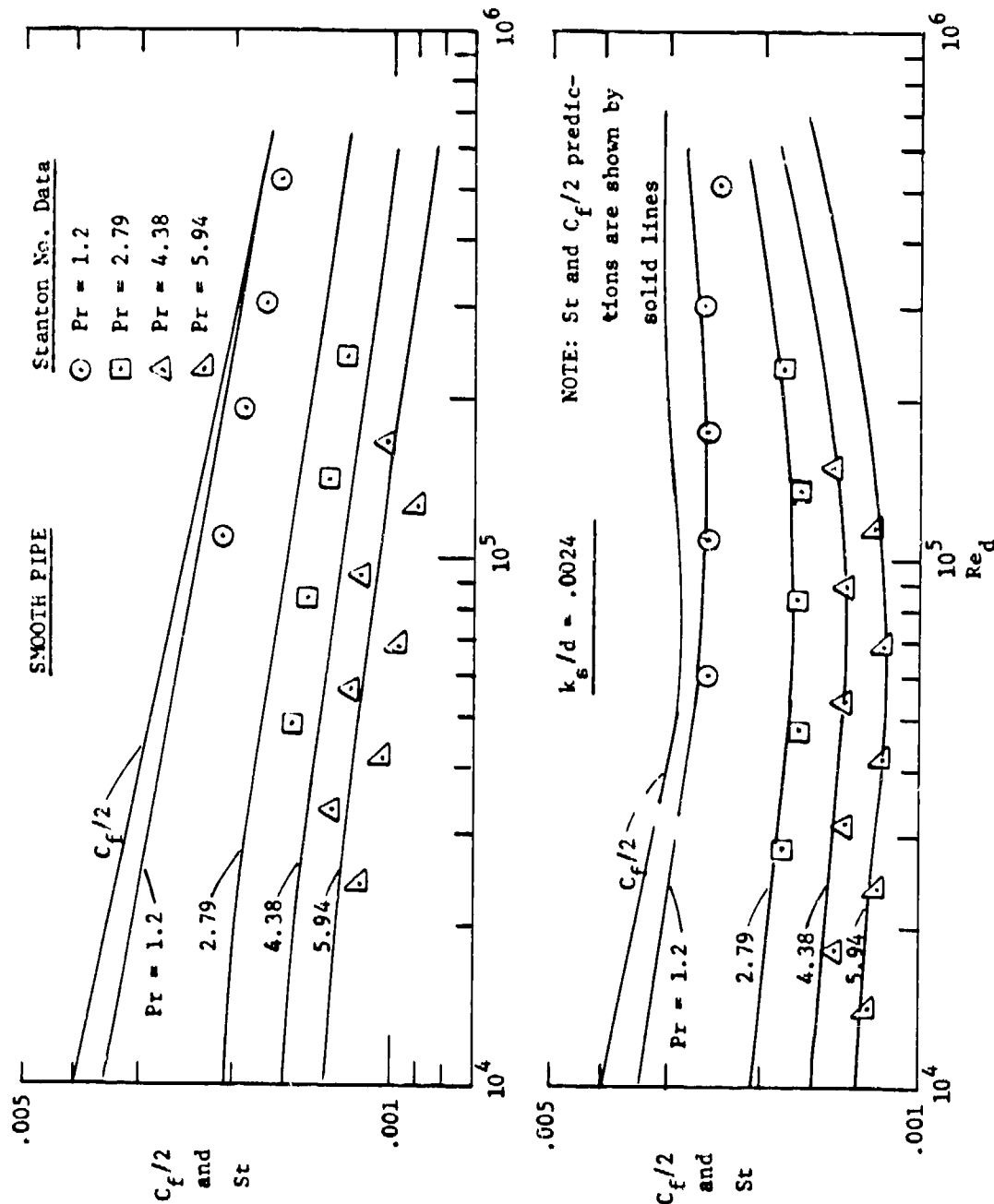


Fig. 4.10 Prediction of Dipprey and Sabersky [24] data for smooth tube and $k_s/d = .0024$

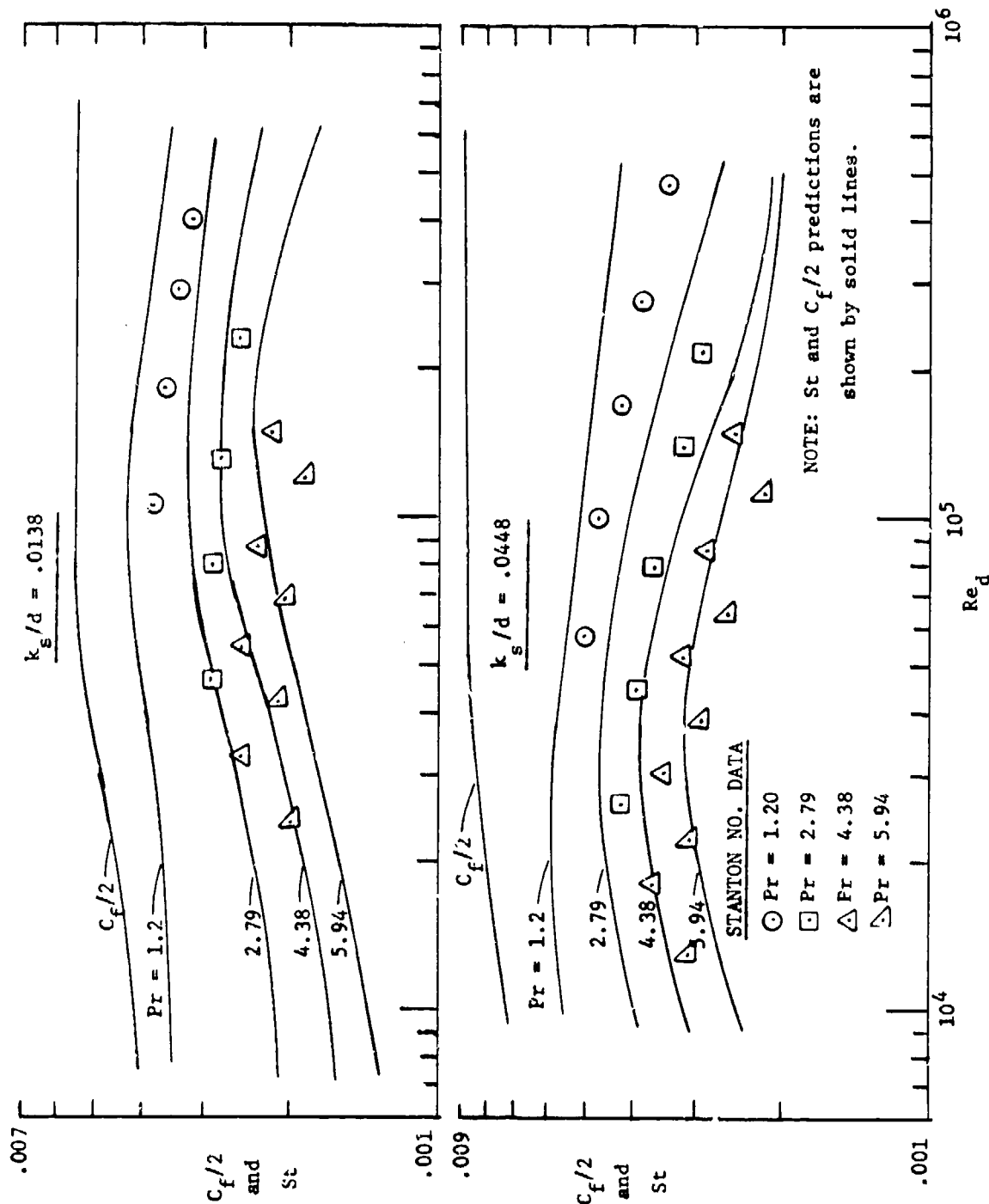


Fig. 4.11 Prediction of Dipprey and Sabersky [24] data for $k_s/d = .0138$ and $k_s/d = .0448$

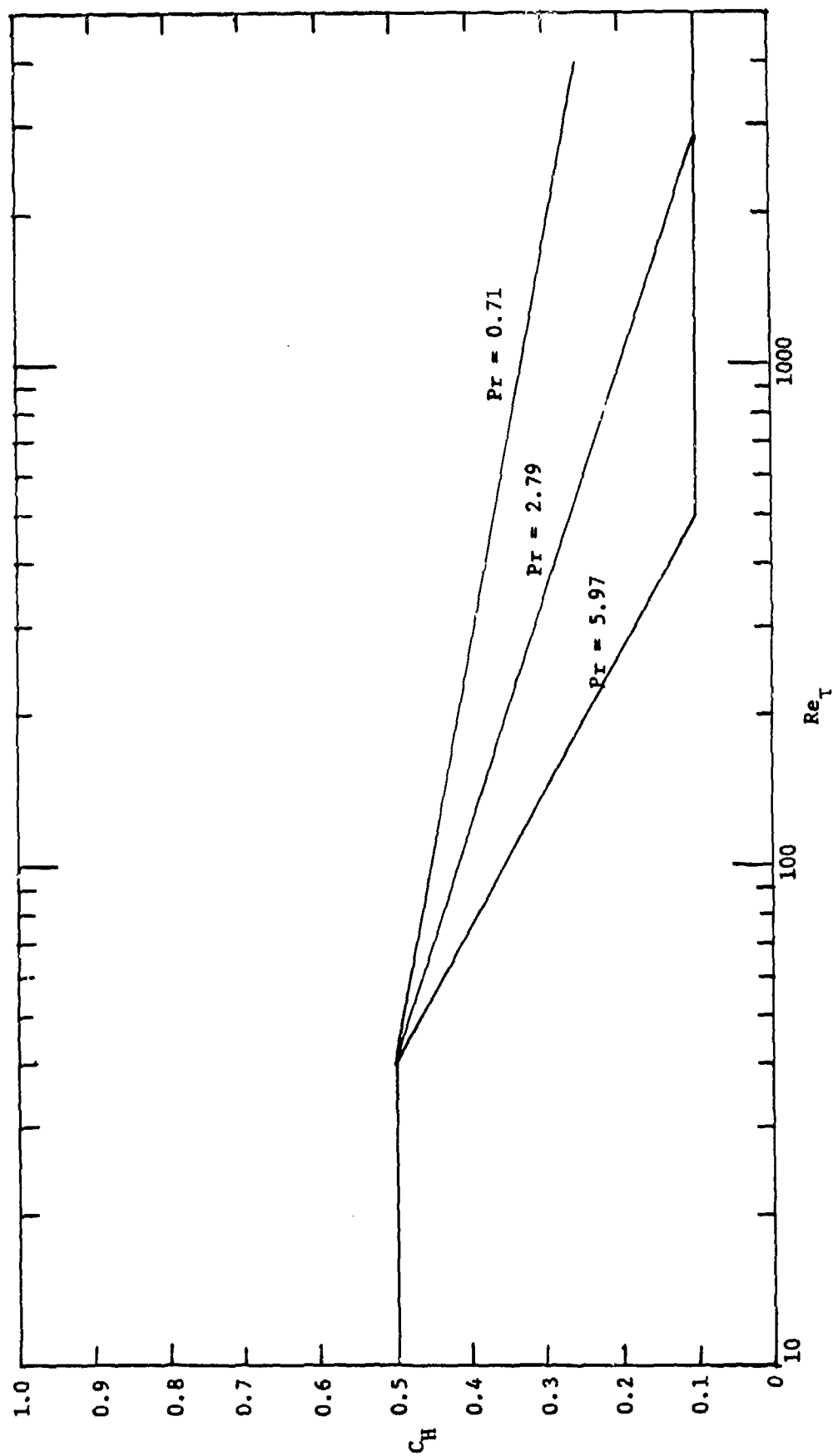


Fig. 4.12 Rough surface thermal mixing-length factor, C_H , versus roughness Reynolds number

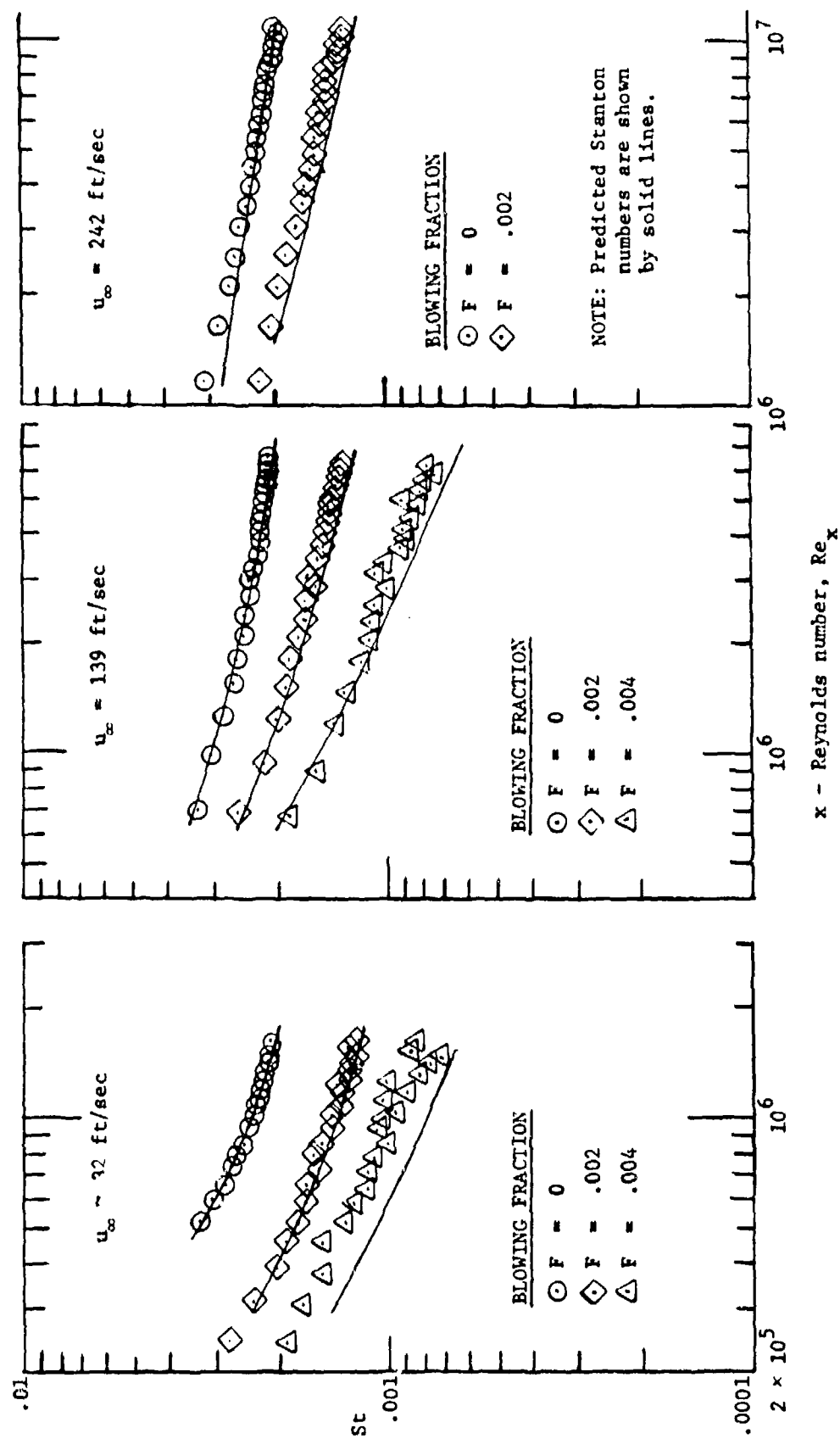


Fig. 4.13 Prediction of rough surface Stanton number data with blowing

CHAPTER V

SUMMARY AND CONCLUSIONS

The principal results and conclusions of the present rough surface experiments can be summarized as follows:

1. The present study has used a deterministic roughness, 0.050 inch diameter spherical elements arranged into a most-dense array. The thermal and hydrodynamic performance of the boundary layer on this surface was quite likely affected by its highly regular roughness. In particular, the marked absence of any 'transitional' behavior may be due, in part, to this effect.

2. The range of roughness Reynolds numbers $u_{\tau} k_s / \nu$, for the no-blowing tests was from 24 to 200, covering the transitional roughness range and extending well into the fully rough range by conventional definitions. The fully rough state seems to have been attained: it certainly was for the heat transfer data and probably was for the friction factor data. The measured Stanton numbers are not dependent on free-stream velocity, but are functions only of the enthalpy thickness of the boundary layer and the blowing fraction, $\rho_o v_o / \rho_{\infty} u_{\infty}$. The unblown Stanton number data for all five velocities tested lie within a few percent of each other when compared at the same enthalpy thickness. With blowing, the uncertainty in the measurements increases but the tendency to be independent of velocity remains, even at very high blowing.

These comments seem also to apply to the friction factor behavior, but with less certainty, since the data are more sensitive to errors and show more scatter.

3. The behavior of the boundary layer at low roughness Reynolds numbers was investigated by an additional test with the boundary layer thickened by blowing through the first two feet of the eight foot test section. This action reduced the roughness Reynolds number to 14 at the downstream end of the plate. Even at this low roughness Reynolds numbers the heat transfer data continued to exhibit 'fully rough' behavior: Stanton number was the same function of enthalpy thickness as observed

at higher roughness Reynolds numbers. It remained independent of stream velocity.

The expected approach to smooth plate behavior was not observed. If smooth plate heat transfer represents the asymptotic behavior of the rough surface as the roughness Reynolds number is reduced, it was not apparent from these experiments.

4. Blowing through a rough surface diminishes the Stanton number. The effect of blowing is predictable using the same relationship found valid in smooth plate studies:

$$\left. \frac{St}{St_0} \right|_{\Delta} = \left[\frac{\ln(1+B)}{B} \right]^{1.25} (1+B)^{.25}, \quad (5-1)$$

where St and St_0 are evaluated at the same enthalpy thickness, Δ (for a smooth plate, the Stanton numbers are to be evaluated at the same enthalpy thickness Reynolds number).

5. Transition on the rough surface began at approximately the same momentum thickness Reynolds number (350-450) for all of the conditions tested. For the surface tested here, transition occurs at about the same momentum thickness Reynolds number that would be expected for transition on a smooth plate. The transition moves upstream with increasing free-stream velocity and with blowing.

6. Blowing in a region which would otherwise have remained laminar may greatly increase the local heat load. The turbulent heat transfer coefficient, even with moderately strong blowing, is much larger than the laminar, unblown value.

7. The effects of roughness on skin friction can be accounted for in a finite-difference boundary layer prediction scheme, using a mixing-length model for mean field closure, by modifying the mixing-length variation very near the wall. Successful prediction of rough surface heat transfer requires modification of the turbulent Prandtl number distribution very near the wall.

In conclusion, it is safe to say that the work reported here is just the beginning of the rough surface investigations at Stanford. Already under way is an extensive program to make detailed hydrodynamic

measurements in the rough surface boundary layer. When complete, these should provide a much better basis for formulating realistic prediction models.

REFERENCES

1. Moffat, R.J., and Kays, W.M., "The Turbulent Boundary Layer on a Porous Plate: Experimental Heat Transfer with Uniform Blowing and Suction," Report No. HMT-1, Thermosciences Division, Dept. of Mech. Engrg., Stanford Univ., 1967.
2. Simpson, R.L., Kays, W.M., and Moffat, R.J., "The Turbulent Boundary Layer on a Porous Plate: An Experimental Study of the Fluid Dynamics with Injection and Suction," Report No. HMT-2, Thermosciences Division, Dept. of Mech. Engrg., Stanford Univ., 1967.
3. Whitten, D.G., Kays, W.M., and Moffat, R.J., "The Turbulent Boundary Layer on a Porous Plate: Experimental Heat Transfer with Variable Suction, Blowing and Surface Temperature," Report No. HMT-3, Thermosciences Division, Dept. of Mech. Engrg., Stanford Univ., 1967.
4. Julien, H.L., Kays, W.M., and Moffat, R.J., "The Turbulent Boundary Layer on a Porous Plate: Experimental Study of the Effects of a Favorable Pressure Gradient," Report No. HMT-4, Thermosciences Division, Dept. of Mech. Engrg., Stanford Univ., 1969.
5. Thielbahr, W.H., Kays, W.M., and Moffat, R.J., "The Turbulent Boundary Layer: Experimental Heat Transfer with Blowing, Suction, and Favorable Pressure Gradient," Report No. HMT-5, Thermosciences Division, Dept. of Mech. Engrg., Stanford Univ., 1969.
6. Kearney, D.W., Moffat, R.J., and Kays, W.M., "The Turbulent Boundary Layer: Experimental Heat Transfer with Strong Favorable Pressure Gradients and Blowing," Report No. HMT-12, Thermosciences Division, Dept. of Mech. Engrg., Stanford Univ., 1970.
7. Loyd, R.J., Moffat, R.J., and Kays, W.M., "The Turbulent Boundary Layer on a Porous Plate: An Experimental Study of the Fluid Dynamics with Strong Favorable Pressure Gradients and Blowing," Report No. HMT-13, Thermosciences Division, Dept. of Mech. Engrg., Stanford Univ., 1970.
8. Andersen, P.S., Kays, W.M., and Moffat, R.J., "The Turbulent Boundary Layer on a Porous Plate: An Experimental Study of the Fluid Mechanics for Adverse Free-Stream Pressure Gradients," Report No. HMT-15, Thermosciences Division, Dept. of Mech. Engrg., Stanford Univ., 1972.
9. Nikuradse, J. "Stromungsgesetze in rauhen Rohren," VDI Forschungsheft, No. 361, 1950, English Translation, NACA TM 1292.
10. Prandtl, L., and Schlichting, H. "Das Widerstandsgesetz rauher Platten," Werft, Reederei, und Hafen, 1934, p. 1.

11. Karman, Th. von, "Turbulence and Skin Friction," Jn. Aero. Sci-ences, Vol. 1, No. 1, January 1934.
12. Moore, W.L., "An Experimental Investigation of Boundary Layer Development Along A Rough Surface," PhD Dissertation, State University of Iowa, August 1951.
13. Hama, F.R., "Boundary Layer Characteristics for Smooth and Rough Surfaces," Trans. SNAME, Vol. 62, pp. 333-354, 1954.
14. Perry, A.E., Schofield, W.H., and Joubert, P.H., "Rough Wall Turbulent Boundary Layers," Jn. Fl. Mech., Vol. 37, pp. 383-413, 1969.
15. Perry, A.E. and Joubert, P.H., "Rough-wall Boundary Layers in Adverse Pressure Gradients," Jn. Fl. Mech., Vol. 17, pp. 193-211, 1963.
16. Liu, C.K., Kline, S.J., and Johnston, J.P., "An Experimental Study of Turbulent Boundary Layer on Rough Walls," Report No. MD-15, Thermosciences Division, Dept. of Mech. Engrg., Stanford Univ., July 1966.
17. Grass, A.J., "Structural Features of Turbulent Flow Over Smooth and Rough Boundaries," Jn. Fl. Mech., Vol. 50, pp. 233-255, 1971.
18. Wu, J., "Flow in Turbulent Wall Layer Over Uniform Roughness," ASME paper 73-APM-U, to be published in Jn. Appl. Mech., Trans. ASME.
19. Tsuji, Yutaka, and Iida, Shusuke, "Velocity Distributions of Rough Wall Turbulent Boundary Layers Without Pressure Gradient," Trans. Japan Soc. Aero. Space Sci., Vol. 16, No. 31, pp. 60-70, 1973.
20. Antonio, R.A. and Luxton, R.T., "The Response of a Turbulent Boundary Layer to a Step Change in Surface Roughness, Part I: Smooth to Rough," Jn. Fl. Mech., Vol. 48, Part 4, pp. 721-761, 1971.
21. Townes, H.W., Gow, J.L., Powe, R.E. and Weber, N., "Turbulent Flow in Smooth and Rough Pipes," Jn. Basic Eng., Trans. ASME, Series D, Vol. 94, No. 2, pp. 353-362, June 1972.
22. Townes, H.W. and Powe, R.E., "Turbulence Structure for Fully Developed Flow in Rough Pipes," Jn. Fl. Engrg., Trans. ASME, Series I, Vol. 95, No. 2, pp. 255-261, July 1973.
23. Nunner, W., "Heat Transfer and Pressure Drop in Rough Tubes," VDI Forschungsheft, No. 455, Series B, Vol. 22, pp. 5-39, 1956, English Translation, A.E.R.E. Library/Transactions 786, 1958.

24. Dipprey, D.F., and Sabersky, R.H., "Heat and Momentum Transfer in Smooth and Rough Tubes at Various Prandtl Numbers," Intl. Jn. of Heat Mass Transfer, Vol. 6, pp. 329-353, 1963.
25. Owen, P.R. and Thomson, W.R., "Heat Transfer Across Rough Surfaces," Jn. Fl. Mech., Vol. 15, pp. 321-334, 1963.
26. Gowen, R.A. and Smith, J.W., "Turbulent Heat Transfer from Smooth and Rough Surfaces," Intl. Jn. of Heat Mass Transfer, Vol. 11, pp. 1657-1673, 1968.
27. Reshotko, M., "Roughness Effects on Heat Transfer in the Supersonic Region of a Conical Nozzle," Jn. Spacecraft and Rockets, Vol. 8, No. 10, pp. 1097-1099, October 1971.
28. Boldman, D.R. and Graham, R.W., "Heat Transfer and Boundary Layer in Conical Nozzles," NASA TN D-6594, February 1972.
29. Sood, N.S. and Jonsson, V.K., "Some Correlations for Resistances to Heat and Momentum Transfer in the Viscous Sublayer at Rough Walls," Jn. Heat Transfer, Trans. ASME, pp. 488-494, November 1969.
30. Norris, R.H., "Some Simple Approximate Heat Transfer Correlations for Turbulent Flow in Ducts with Surface Roughness," Augmentation of Convective Heat and Mass Transfer, published by the ASME, 1971.
31. Chen, Karl, K., "Compressible Turbulent Boundary-Layer Heat Transfer to Rough Surfaces in Pressure Gradient," AIAA Journal, Vol. 10, No. 5, pp. 623-629, May 1972.
32. Dvorak, F. A., "Calculation of Turbulent Boundary Layers on Rough Surfaces in Pressure Gradient," AIAA Journal, Vol. 7, No. 9, pp. 1752-1759, Sept. 1969.
33. Dvorak, R. A., "Calculations of Compressible Turbulent Boundary Layers with Roughness and Heat Transfer," AIAA Journal, Vol. 10, No. 11, pp. 1447-1451, November 1972.
34. Nestler, D. E., "Compressible Turbulent Boundary-Layer Heat Transfer to Rough Surfaces," AIAA Journal, Vol. 9, No. 9, Sept. 1971.
35. Lumsdaine, E., Wen, H. W., and King, F. K., "Influence of Surface Roughness and Mass Transfer on Boundary Layer and Friction Coefficient," Developments in Mechanics, Vol. 6, Proceedings of the 12th Midwestern Mechanics Conference, pp. 305-318.
36. McDonald, H., and Fish, R. W., "Practical Calculations of Transitional Boundary Layers," International Journal of Heat Mass Transfer, Vol. 16, pp. 1729-1744, 1973.

37. Spalding, D. B. and Pantanker, S. V., Heat and Mass Transfer in Boundary Layers, Morgan-Granpian, London, 1967.
38. Kays, W. M., "Heat Transfer to the Transpired Turbulent Boundary Layer," Report No. HMT-14, Thermosciences Div., Dept. of Mech. Engrg, Stanford University, Stanford, California, June 1971.
39. van Driest, E. F., "On Turbulent Flow Near a Wall," Heat Transfer and Fluid Mechanics Institute, 1955.
40. Wolf, S., "Flow Losses for Heat Exchangers with Oblique Flow Headers," Technical Report No. 60, Department of Mechanical Engrg., Stanford Univ., June 1964.
41. Schubauer, G. E., Spangenberg, W. G., and Klebanoff, P. S., "Aerodynamic Characteristics of Damping Screens," NACA TN 2001, January 1950.
42. Rause, H., and Hassan, M. M., "Cavitation Free Inlets and Contractions," Mechanical Engineering, 71, 3, 213, 216 1949.
43. Cochran, D. L. and Kline, S. J., "The Use of Short Flat Vanes for Producing Efficient Wide-Angle Two-Dimensional Subsonic Diffusers," NACA TN 4309, September 1958.
44. Bradshaw, P., "The effect of Wind-Tunnel Screens in Nominally Two-Dimensional Boundary Layers," Journal of Fluid Mechanics, Vol. 22, Part 4, pp. 679-687, 1965.
45. Morgan, P. G., "The Stability of Flow Through Porous Screens," Journal of the Royal Aeronautical Society, Vol. 64, p. 359-363, 1960.
46. Scarborough, James R., Numerical Mathematical Analysis, 6th Edition, Johns Hopkins Press, pp. 541-551, 1964.
47. Kline, S. J. and McClintock, F. A., "Describing Uncertainties in Single Sample Experiments," Mechanical Engineering, Jan. 1953.
48. Clauser, F. H., "The Turbulent Boundary Layer," Advances in Applied Mechanics, Vol. IV, pp. 1-51, Academic Press, New York, 1956.
49. Cebeci, T., "Behavior of Turbulent Flow near a Porous Wall with Pressure Gradient," AIAA Journal, Vol. 8, No. 12, pp. 2152-2156, Dec. 1970.
50. Pletcher, R. H., "Prediction of Transpired Turbulent Boundary Layers," Journal of Heat Transfer, Trans. ASME, Series C, pp. 89-94, Feb. 1974.

51. Schlichting, H., Boundary Layer Theory, 6th Edition, McGraw-Hill Book Co., Inc., New York, 1968.
52. Lakshman, C. and Jayatilleke, V., "The Influence of Prandtl Number and Surface Roughness on the Resistance of the Laminar Sublayer to Momentum and Heat Transfer", Progress in Heat and Mass Transfer, Vol. 1, Pergamon Press, pp. 193-330, 1969.
53. Reynolds, W. C., Kays, W. M., and Kline, S. J., "Heat Transfer in the Turbulent Incompressible Boundary Layer, Part IV", NASA Memo 12-4-58W, 1958.

APPENDIX A

MAIN AIR SUPPLY SYSTEM COMPONENTS

The following is a brief description of the construction details of the major components in the main air supply system.

A.1 Inlet Header and Screen Box

The heat exchanger inlet header and screen box are shown with their overall dimension in Fig. A.1. One side of the box is removable to allow removal of the screens and screen spacers. The screen material is #40 mesh, .0065 stainless steel wire stretched on 1 x 4 inch clear pine frames. Four such frames are used with 2 x 4 inch clear pine spacer frames between each screen. Both sides of each screen and spacer frame are lined with felt gasket material to avoid leakage around the screen pack. Alignment pins are used to insure that the screen and spacer frames are properly aligned in the box. A photograph of the header, heat exchanger and screen box assembly before the nozzle was installed is shown in Fig. A.2.

A.2 Wind Tunnel Nozzle

The Roughness Rig nozzle shape is shown in Fig. A.3. The nozzle was fabricated in two halves from fiberglass and then hand fitted together. The nozzle wall shapes were first layed out on 1/16 inch aluminum templates from which the mold for the fiberglass build-up was made using high density, closed cell polyurethane foam. The approximate nozzle shape was carved from a block of polyurethane foam with a hot chromel wire using the aluminum templates as guides. The final shape was obtained by hand sanding the foam block and then reinforcing its surface with a thin layer of polyester resin which was sanded to conform to the final nozzle surface shape and surface smoothness.

Before the fiberglass layup was made, the mold was waxed and sprayed with a release agent. The first coat of resin was a white gel coat, sprayed on the mold. This was followed by two layers of fiberglass mat,

a layer of fiberglass cloth and two additional layers of fiberglass mat. An additional layer of mat was added to the nozzle flange for reinforcement.

Reinforcing ribs made from one-eighth inch thick masonite were attached to provide added strength and the nozzle halves were bolted together along the horizontal midplane. The final shape of the nozzle surface conformed to the design shape within .020 inches total run out. Figure 4.4 is a photograph of the two nozzle halves. The male nozzle mold is shown in the background.

A.3 Multistage Diffuser

The Roughness Rig diffuser is a multistage vaned diffuser unlike any previously built at Stanford in that several two dimensional diffusers are arranged in series. Figure A.5 shows a sketch of the diffuser with its overall dimensions. A photograph of the diffuser before it was installed in the rig is shown in Fig. A.6. The first stage of the diffuser has a movable top which can be adjusted to align itself with the test section top and form a smooth transition at the test section exit. Following the adjustable inlet section is a two-dimensional expansion which employs five vertical vanes to expand the diffuser width from 20 to 24 inches. Next are two separate two-dimensional expansions employing five and then eight vanes to expand the diffuser height to 24 inches. This empties into a plenum box connected to the blower inlet with a flexible connection. As can be noted from the photograph, the diffuser variable area inlet section and first vaned expansion has been constructed from plexiglass with aluminum vanes. At the bottom of the plenum box is a flange for connection to the small charging blower used to control the tunnel static pressure level. The estimated efficiency of this diffuser, had each of the stages performed in the assembly as it would have individually, would have been in excess of 50%. The actual diffuser efficiency is closer to 40% and even less at lower test section velocities. This performance is however acceptable and the wind tunnel does achieve its test section design velocities. Part of the difficulty with the diffuser performance is that the inlet flow into the diffuser is almost all boundary layer fluid, particularly when there is blowing in the test section. This contributes to its reduced performance.

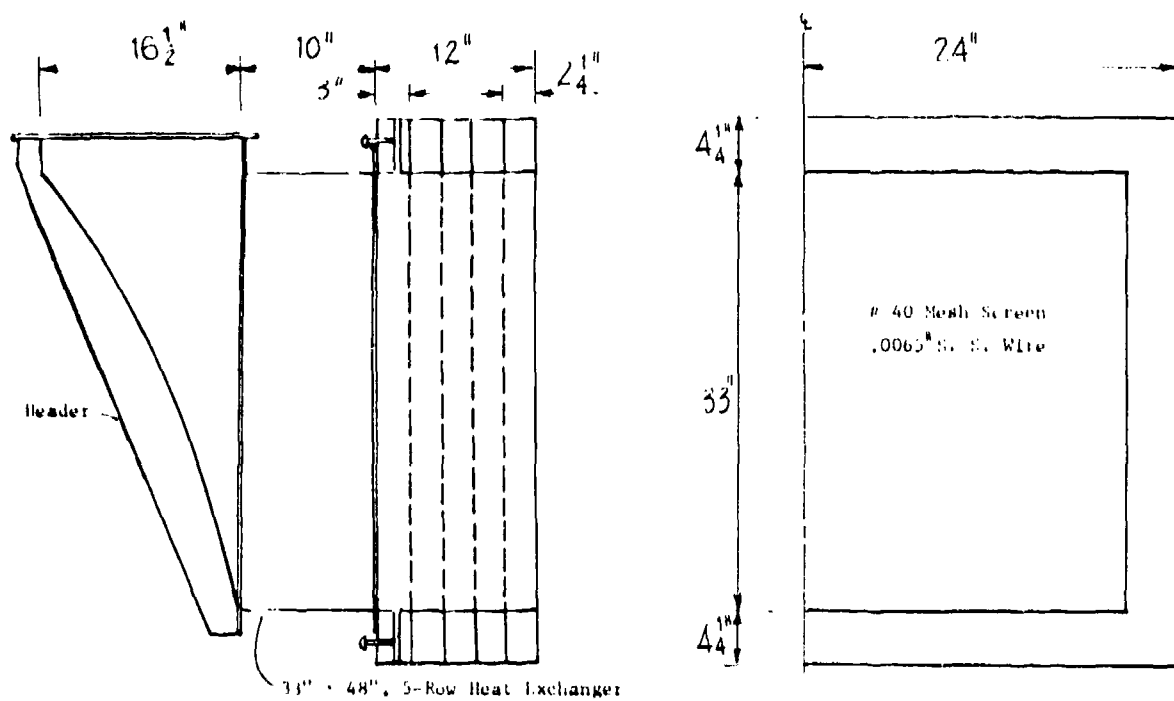


Fig. A.1 Heat exchanger oblique header and screen box

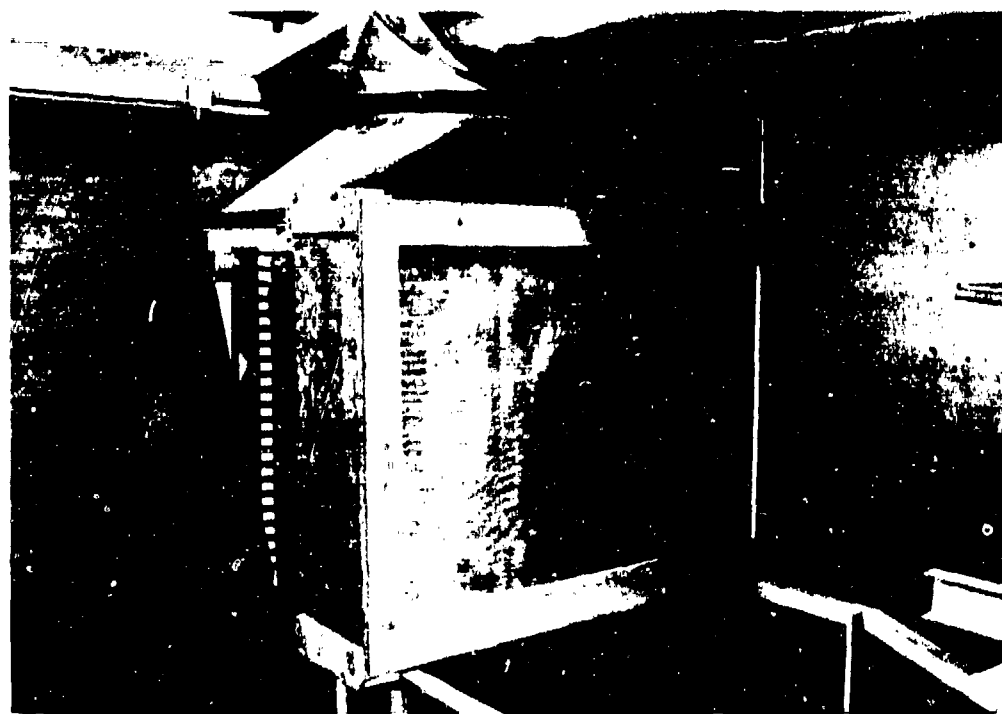


Fig. A.2 Photograph of the screen box, heat exchanger and header assembly

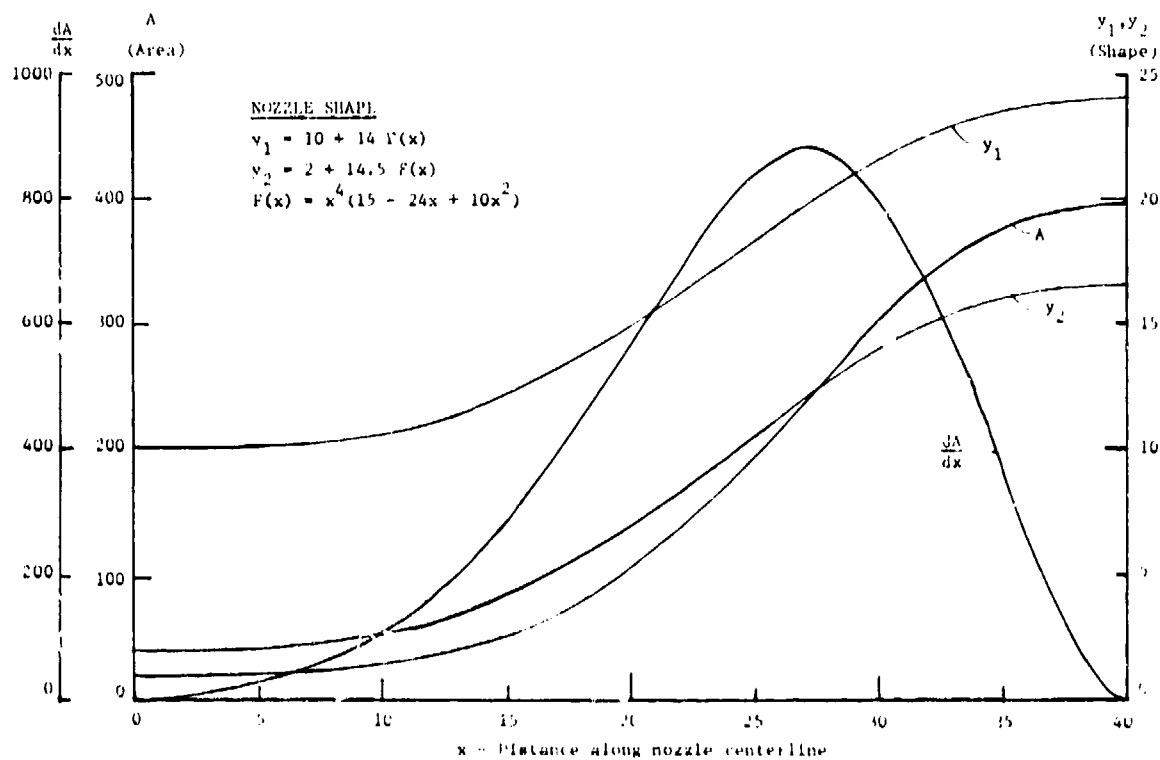


Fig. A.3 Nozzle wall shape



Fig. A.4 Photograph of the nozzle halves and mold before assembly

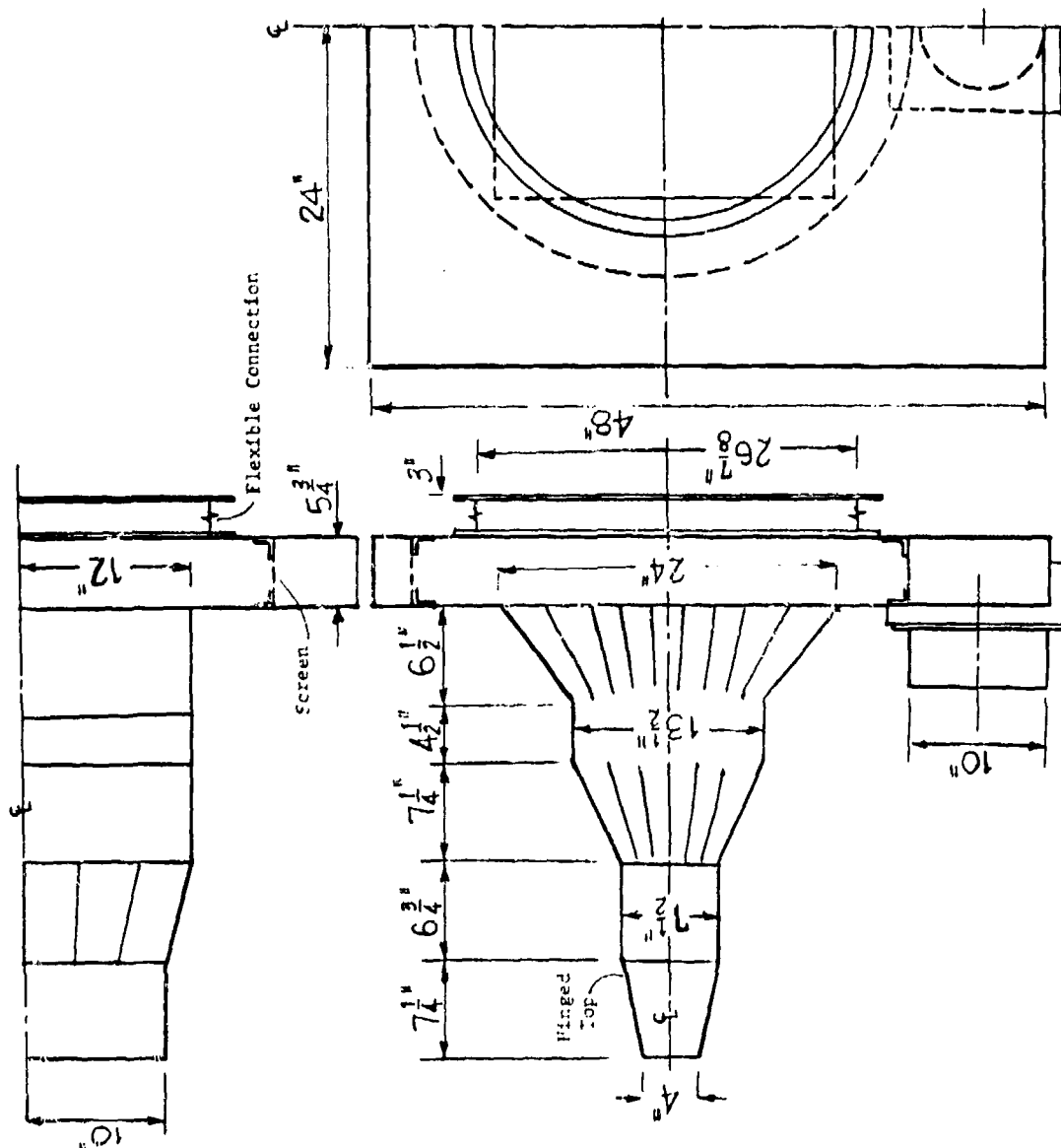


Fig. 4.5 Multistage, vaned diffuser



Fig. A.6 Photograph of the diffuser before installation in the wind tunnel

APPENDIX B

TRANSPIRATION FLOW METERING SYSTEM

Constant current, hot wire type flow meters are used to measure flow rate in each of the individual plate transpiration air supply lines. These flow meters consist of two side-by-side probes installed in the center of a 3 foot long tube used as a riser between the transpiration header box and the control valves. Each unit is individually calibrated. The probes are small tubes which span the delivery pipe and contain the junctions of a differential iron-constantan thermocouple. One junction is in a thin wall, 0.025 inch diameter glass tube which is a passive probe. The other junction is in the center of a heated rod. The current in the heater is held constant during flow meter operation and the differential thermocouple output is the signal used to measure flow rate in the tube. A schematic of the circuit is shown in Fig. B.1. The heated probe consists of a #2-56 nylon screw, center-drilled with a #50 drill. Each end of the screw is threaded into a short piece of #8 brass screw stock, which serves as an end terminal for the heater power connections. Nichrome heater wire is wound onto the nylon screw using the threads to space the heater wire and is soldered at each end to the brass terminals. The heater wire is then potted in place with Permabond cement. A photograph showing the soldering of the heater wire to the brass end terminals on a flow meter probe is shown in Fig. B.2. Typical resistance of a probe heater is 5 ohms, although this value varies a few percent from heater to heater.

Each flow meter unit, consisting of the riser tube with differential thermocouple and heater, was individually calibrated on the flow bench in the Thermosciences Measurement Center. The meters were calibrated in both upward and downward flow, for blowing and suction, using a bank of Meriam Laminar Flow Meters as secondary standards. These laminar flow meters had been previously calibrated against standard ASME flow orifices. In the controlled environment of the Measurement Center, it is felt that the flow measurements were accurate to within $\pm 1\%$, the accuracy normally claimed for the ASME orifice.

At each flow calibration point, the heater current was set and the differential thermocouple signal allowed to stabilize. A Hewlett-Packard 2401 IDVM using an external clock to allow integration of the flow meter signal over a 10-second interval was used to read the differential thermocouples. A typical flow meter calibration curve is shown in Fig. B.3.

The flow meters installed in the rig can operate in two modes. In the first mode, the power and differential thermocouple connections are made through a series of double pole switches such that flow meter operation is restricted to a single channel at a time. Activation of each successive flow meter heater circuit also activates its read-out circuit. The flow meters are operated in this mode while setting up the rig-running conditions. In the second mode of operation, power is supplied to the meters in blocks of 6 at a time. This mode is used during data-taking. A short computer program is used, called FLOMET, which calculates the flow meter signal required for the desired transpiration flow for each individual meter. The flow control valves must be adjusted, one at a time, such that each flow meter produces its desired signal. The same flow meter calibration tables in FLOMET are also contained in the data-reduction program, and the flow meter readings are re-recorded when the actual heat transfer data are taken, so accurate flow measurement is assured.

The flow calibration tables contain flow and flow meter response in terms of SCFM and EMFO -- that is, cubic feet per minute of air at standard conditions and the emf reading the flow meter would have produced if air at standard conditions had been flowing through the transpiration system. To convert from actual to standard conditions, the following arguments must be used. The flow meter differential thermocouple signal is proportional to the temperature difference between the heated and the passive probes of the meter.

$$\text{emf} \propto \Delta T$$

(B-1)

The temperature difference can be related to the heat transfer coefficient between the flow and the heated probe, and finally to the Nusselt number.

$$\text{emf} \propto \Delta T = \frac{q}{Ah} = \left(\frac{qd}{Ak} \right) \frac{k}{hd} = \frac{qd}{Ak} \left(\frac{1}{Nu} \right) \quad (\text{B-2})$$

A similar expression can be written for a flow meter operating at standard conditions, denoted by the subscript 'o'.

$$\text{emf}_o \propto \frac{q_o d_o}{A_o k_o} \left(\frac{1}{Nu_o} \right) \quad (\text{B-3})$$

Taking the ratio of the two and noting that the area, diameter and heat flux will remain the same between the two conditions,

$$\frac{\text{emf}_o}{\text{emf}} = \frac{Nu}{Nu_o} \frac{k}{k_o} \quad (\text{B-4})$$

From the flow meter calibration data, the signal is seen to vary with the 0.45 power of the flow Reynolds number. Using the normal 0.3 dependence on Prandtl number, we can write

$$Nu \propto Re^{0.45} Pr^{0.3} = Re^{0.45} (k/\mu c)^{0.3} \quad (\text{B-5})$$

Also,

$$Re \propto \text{SCFM} (\mu^{-1}) \quad (\text{B-6})$$

With this, holding SCFM constant yields

$$\frac{\text{emf}_o}{\text{emf}} = \left(\frac{\text{SCFM}}{\text{SCFM}_o} \right)^{0.45} \left(\frac{\mu_o}{\mu} \right)^{0.45} \left(\frac{k_o}{k} \frac{\mu}{\mu_o} \frac{c}{c_o} \right)^{0.3} \left(\frac{k}{k_o} \right) = \left(\frac{\mu_o}{\mu} \right)^{0.15} \left(\frac{c}{c_o} \right)^{0.3} \left(\frac{k}{k_o} \right)^{0.7} \quad (\text{B-7})$$

The following temperature and humidity dependence is assumed for the air properties:

$$k/k_o = (T/T_o)^{0.74}$$

$$\mu/\mu_o = (T/T_o)^{0.725}$$

$$c/c_o = \text{not temperature dependent in the range of the test data}$$

$$\omega = \text{absolute humidity of the air}$$

$$(k/k_o) = \text{not humidity dependent in the range of the test data}$$

$$(\mu/\mu_o) = (1 - 0.7 \omega)$$

$$(c/c_o) = (1 + 0.9 \omega)$$

Substituting these into the expression for emf gives

$$\frac{\text{emf}_o}{\text{emf}} = \left(\frac{T}{T_o}\right)^{0.41} \frac{(1 + 0.9 \omega)^{0.3}}{(1 - 0.7 \omega)^{0.15}} \quad (\text{B-8})$$

Using binomial expansions for the humidity terms, this can be simplified to

$$\text{emf}_o = \text{emf}(T/T_o)^{0.41} (1 + 0.38 \omega) \quad (\text{B-9})$$

All flow meter calibration data have been converted into standard conditions with this expression, for use in the data reduction program. Flow meter readings taken at test conditions are then converted to standard conditions before entering the calibration tables.

Experience with this metering system has been highly satisfactory. At relatively high flows, 10 cfm and over, adjustment of the valves to give the desired flow meter signal is relatively easy. At lower flow rates, flow valve adjustment is a bit more tedious because of the slower response of the meter and the coarse adjustment that the ball valves afford in their nearly closed positions. The meters themselves seem stable and do not show any appreciable drift during a data run. On at least two occasions during the rig shakedown, flow meters were removed from the rig and recalibrated to be sure that the heaters and differential thermocouples were not 'aging' and changing with use. In only two cases

were changes in the meter calibrations noted, and each of those occurred because of overheating of the heater probe. The two probes had been inadvertently activated when there was no flow in the transpiration system. In all other cases, there had been virtually no change in the flow meter calibrations.

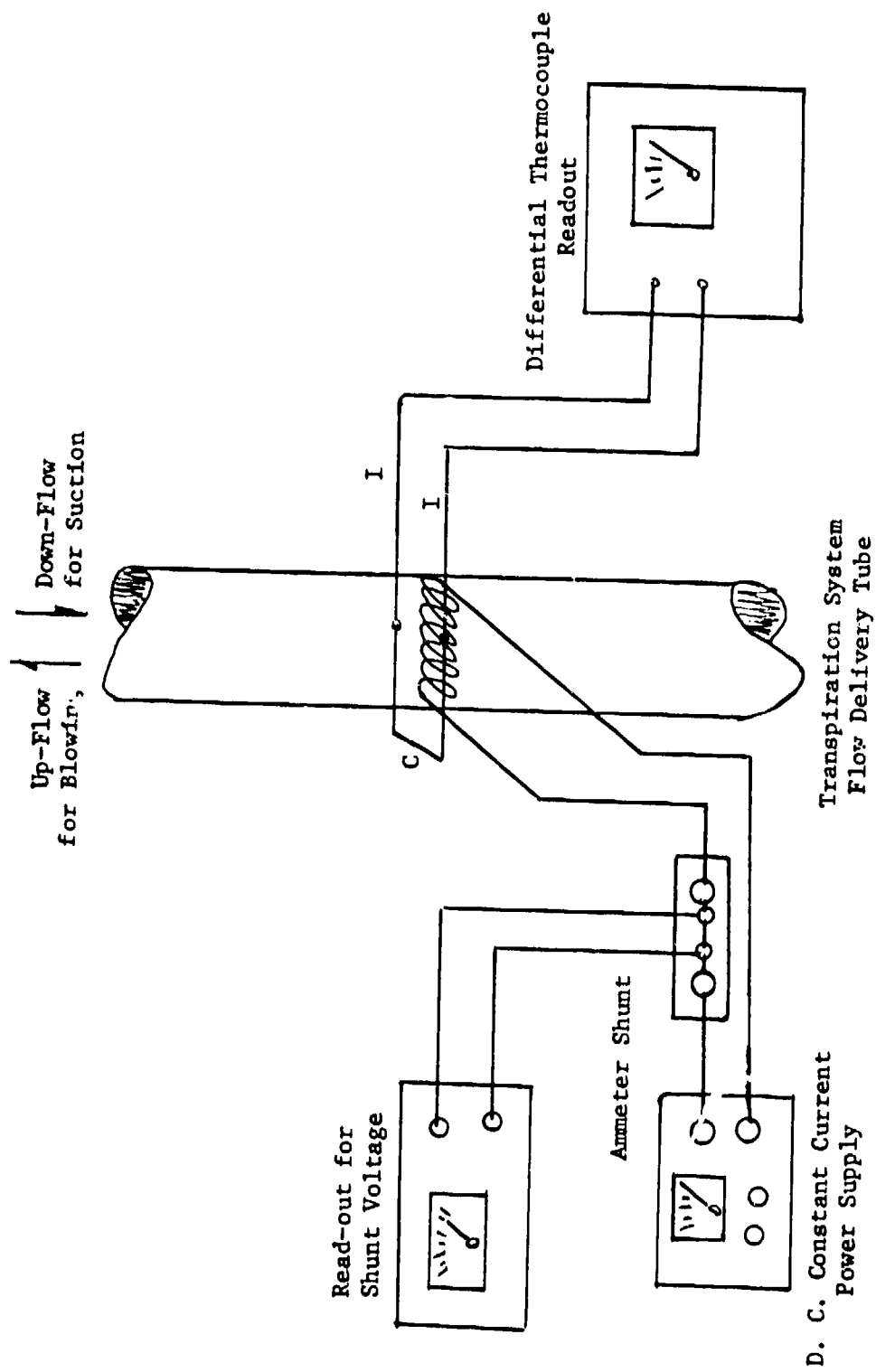


Fig. B.1 Schematic of the constant current, hot wire type flow meter



Fig. B.2 Photograph of the flow meter heater element

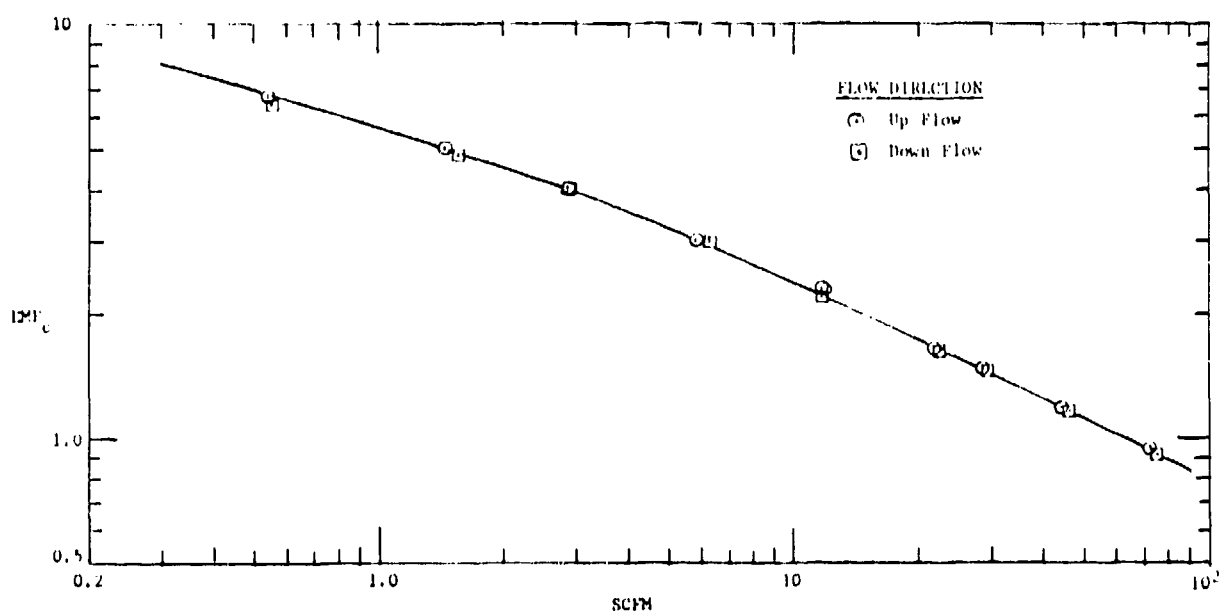


Fig. B.3 Typical flow meter calibration curve

APPENDIX C

PLATE POWER CONTROL CIRCUIT

Plate power control is achieved by controlling heater voltage using a solid-state control circuit for each plate, as shown in Fig. C.1. The circuit was designed by T. R. Mogel, of the Civil Engineering Department at Stanford, who also did the printed circuit board layout and acted as general consultant in shaking down the Roughness Rig power control system. The following description is paraphrased from a discussion of the control circuit written by T. R. Mogel for the seventh quarterly progress report on the research contract which funded the Roughness Rig project.

The power control circuit consists of three main parts: an operational amplifier, a high-power output amplifier, and a feedback network. The heater voltage is set by a 10 turn pot with $\pm 0.2\%$ linearity, which sends a proportional amount of the -10 volt reference to the heater controller. The voltage appearing across the heater is determined by the feedback network. The whole circuit can be thought of as an operational amplifier whose D.C. transfer characteristic will be:

$$V_{out} = -V_{in} R_1/R_3 \quad (R_1 = R_2, R_3 = R_4) \quad (C-1)$$

The output voltage will be

$$V_{heater} = -V_{ref} \alpha R_1/R_3 \quad (C-2)$$

For the resistances used in the circuit,

$$V_{heater} = 22.1 \alpha \quad (C-3)$$

where α is 0 when the pot resistance is at the counterclockwise stop and when 1 is at the clockwise stop.

The capacitor is used to stabilize the amplifier by rolling off the high frequencies. A diode is used to prevent the output of the operational

amplifier from going negative. A second diode is used to allow the highest of the heater voltages from all the channels to be known.

A feature of this system is that the heater voltage stability is a function of the stability of the -10 volt reference and not the heater supply. The voltage drop of the lead wires of the heaters is compensated for, since the amplifier 'looks at' the voltage directly across the heater.

A shunt is placed in series with each heater element to measure the current. The heater voltage is also measured so that heater power can be determined independently from the control circuit. The accuracy of the data is not, therefore, in any way related to the operation of the control circuit.

The circuitry in the dotted box is on a printed circuit card (6 channels per board).

A protection system has also been designed which provides for shut-down of the heater power supply in any of the following cases: over-voltage on the bus bar, over-voltage on any individual plate or over-current on the bus. The system guards against exceeding a total bus current of 750 amps or bus voltage of 22 volts using fixed-level detectors. A variable-level detector circuit is used as a check against individual plate over-voltage. One potentiometer setting guards all of the plate circuits against the same maximum plate voltage. If any of the individual plate voltages exceeds the set value, the D.C. power supply is shut down. Circuit diagrams for these protection circuits are shown in Fig. C.2. They have been wired on a single printed circuit board and are included with the control circuits in a common card box behind the circuit control panel. A photograph of the back of the plate power control panel is shown in Fig. C.3. One of the four printed circuit boards is shown on an extender card above the card box. The bundle of wires at the bottom of the box include both the control leads to the power transistors mounted on the water-cooled bus bar and the heater voltage sense leads. A photograph of the bus bar box is shown in Fig. C.4. The heavy cables at the rear of the box are the power leads from the overhead bus bars.

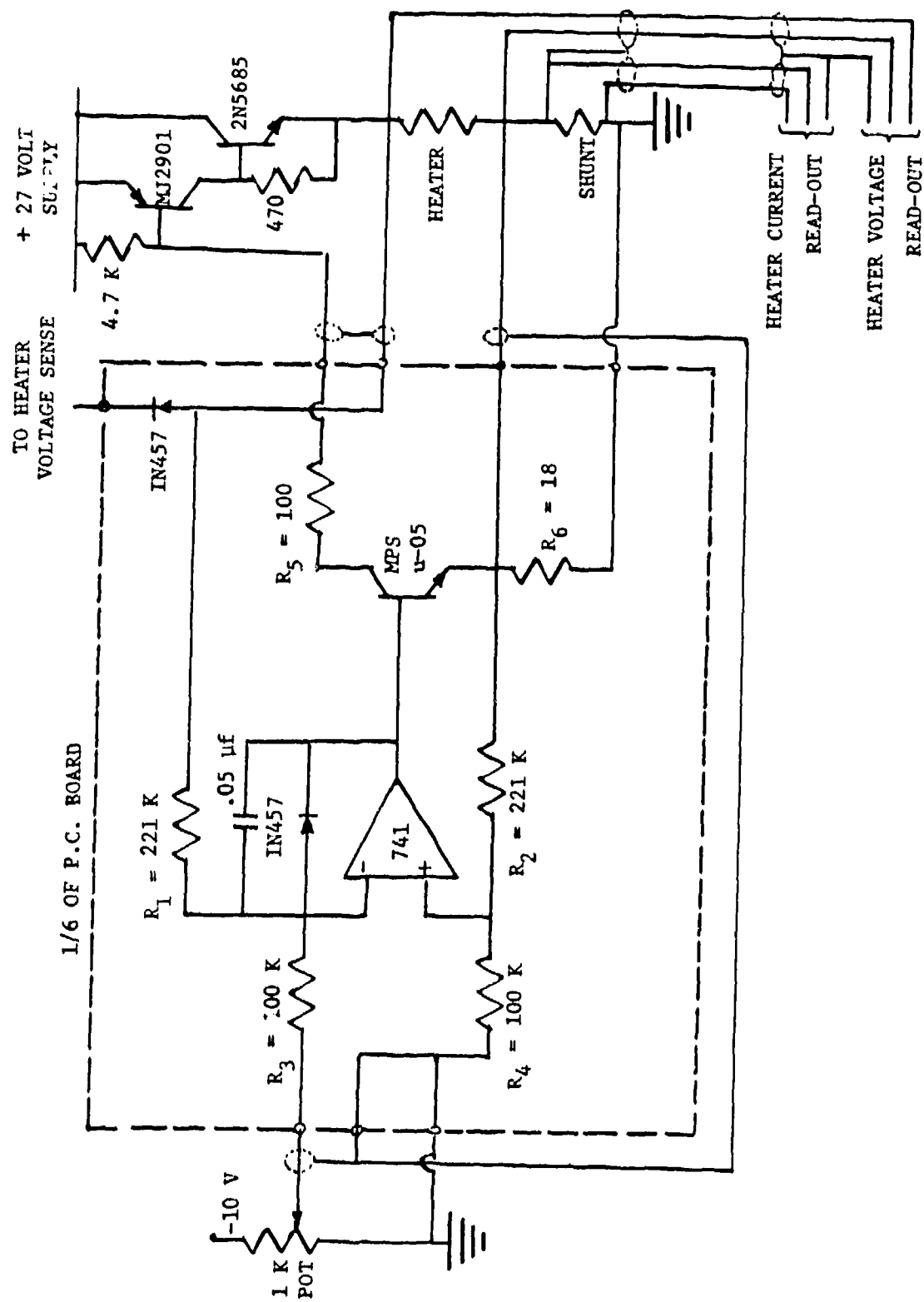


Fig. C.1 Plate power control circuit schematic

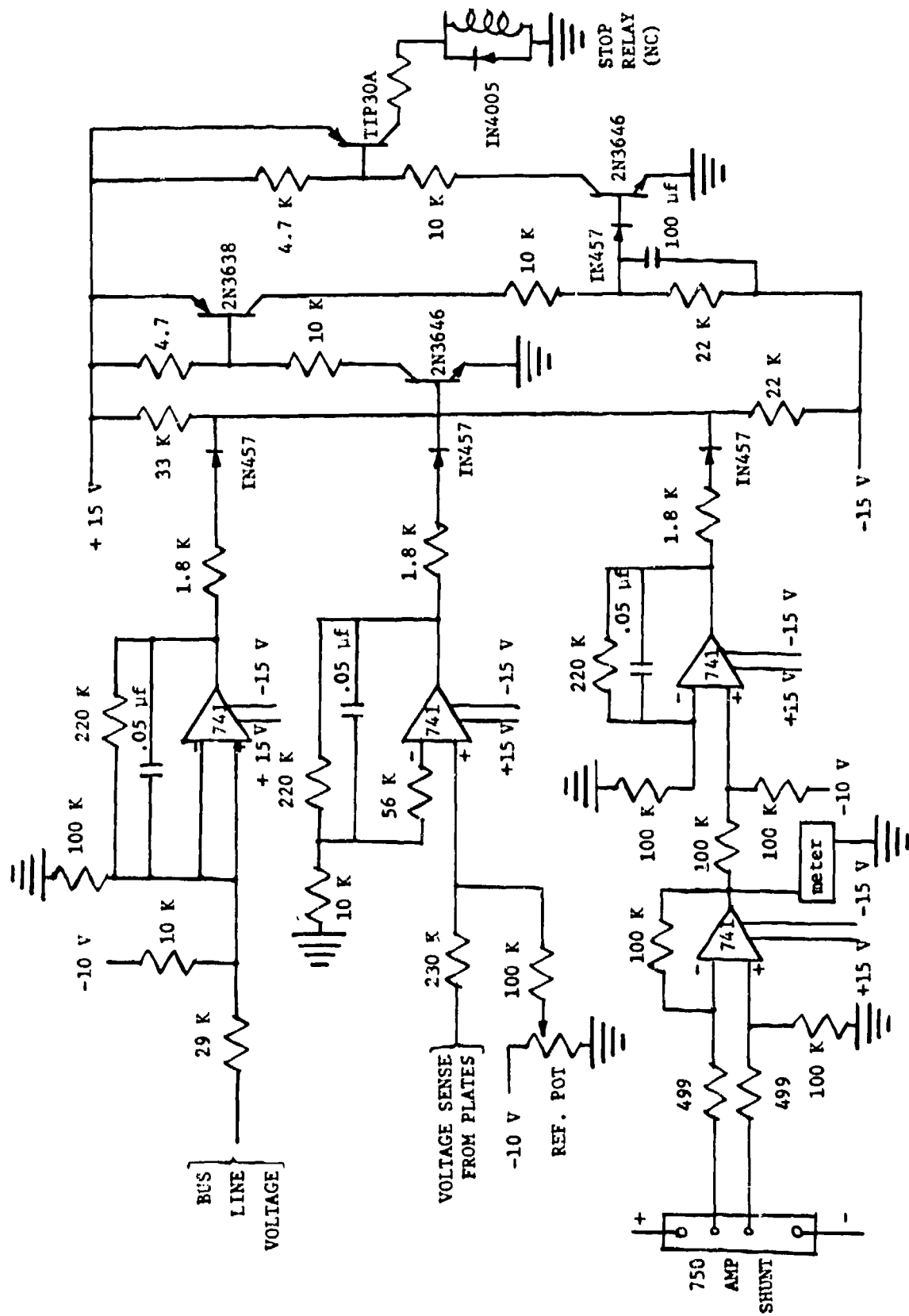


Fig. C.2 Plate power control protection circuit schematic



Fig. C.4 Photograph of the bus bar box

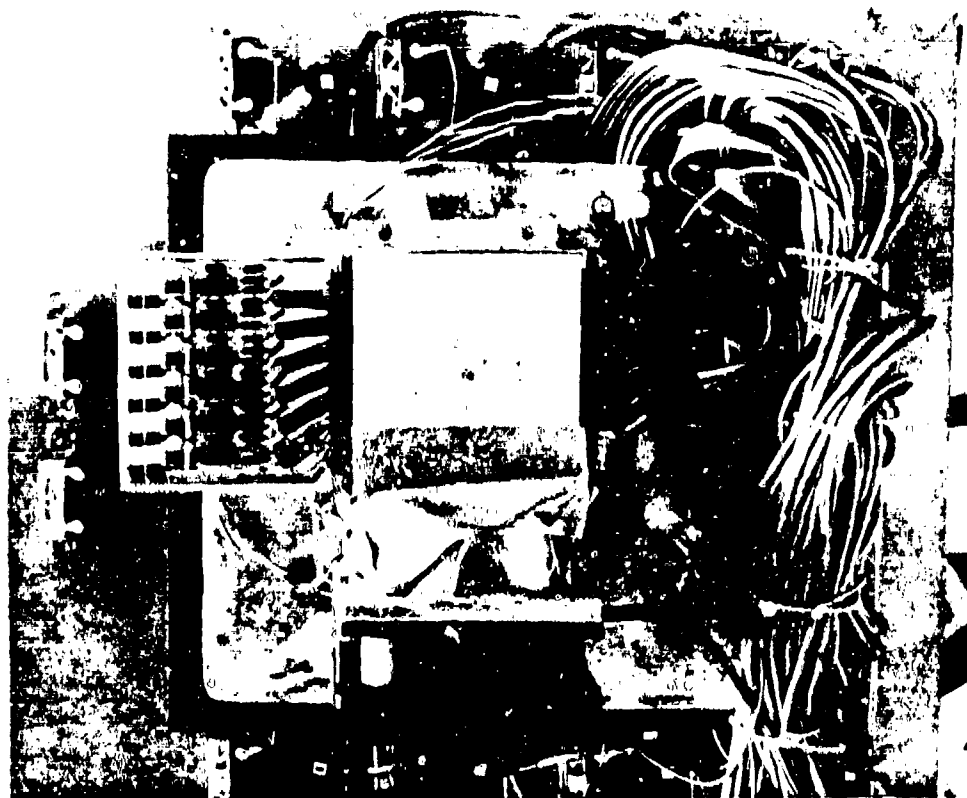


Fig. C 3 Photograph of the rear of the plate
power control panel

APPENDIX D

POROUS PLATE FABRICATION

In order to evaluate the practicality of brazing the porous plates, the brazing of 'logpiles' made of segments of copper wire was attempted first. This was done by plating (with electroless nickel) several 1/2 inch long pieces of 0.050 inch diameter copper wire which were then placed into a stainless steel mold and heated for seven minutes at 1700°F in a hydrogen atmosphere furnace. The result was a success: a brazed 'logpile' of copper wires. With this established, a search was begun for a supplier of copper balls for the porous plates. A 5 lb. sample of copper balls was obtained from the Pioneer Steel Ball Company of Unionville, Connecticut. Finding a plating contractor to plate the balls proved more difficult than had been anticipated. A part of the first sample of copper balls was sent to the Naval Weapons Lab Plating Shop at China Lake. The remainder were distributed among several local plating shops who were asked to bid on the job of plating 100 lbs. of the balls. As each sample was returned, a small plug was brazed in the Hansen Labs furnace using a quartz tube as a mold to test the quality of the braze. The ball sample sent to China Lake was used to assemble a 4 inch square plate for the first large-scale demonstration of the brazing technique. The mold for this sample was constructed with OFHC side rails and a sheet of 1/8 inch quartz for the bottom. The advantage of the transparent bottom was that the ball arrangement could be examined to ensure the ball array on the bottom of the mold had not been disturbed as successive layers were added. There was some hope initially that if the balls were carefully shaken or jarred they would arrange themselves in their most dense array; but after considerable experimentation this hope was finally abandoned and the balls were arranged by hand, one layer at a time, until the desired thickness was achieved. The 4-inch mold was successfully fired in the Hansen Lab furnace.

Work on four full-size mold cavities was then begun. High cost and slow delivery for the quartz bottoms mitigated against their use for

these molds and OFHC copper was used instead. An order for the full 100 lbs. of balls was placed, and Electro-Coatings, Inc. of Emeryville, California, was selected as the plating contractor. They had developed a small stainless steel basket to tumble the balls to improve the plating uniformity. Samples were then obtained with various plating thicknesses and used to determine the plating thickness which would provide the strongest bond without excessive buildup of the braze material at the ball connections. A small mold which produced 1 inch square samples was used for these test braze samples. A plating thickness of 0.0005 inches was finally selected. The plating contractor agreed to plate the balls in 9 lb. batches, which was just sufficient for a single 4 x 18 inch plate 1/2 inch thick. It was found that difficulty was encountered if a plate was assembled with balls from different plating batches. Small differences in plating thicknesses resulted in small differences in the ball sizes which didn't show up until several hundred of them had been arranged in rows in the mold.

The firing of these large molds was not possible in the Hansen Lab tube shop, but space and furnace time were provided to us at the Stanford Linear Accelerator (SLAC) tube shop. The SLAC tube shop has a 24" hydrogen atmosphere brazing furnace, one of the few of this size on the West Coast. The tube shop supervisor, Mr. Bob Bosenburg, and his people spent considerable time educating us in 'brazing technique'. Keeping the molds and balls clean and use of the proper release agent to keep the plates from sticking in the molds were only part of this help. The balls were assembled in the molds by hand, filling four molds each time before firing. To assist in this phase of the project, two temporary employees were hired. The ball pack used consisted of 11 layers of balls, each layer 91 rows wide at the test surface with 357 balls in each row. The ball layer behind the surface layer contained 90 rows and all other layers used 89 rows. This construction provided a lip at the top surface of the plate so that when two plates were laid side by side they would form a continuous surface but there would be space between them beneath the top layer for the phenolic support strips. As already noted, the final layer of balls was arranged so that a ball row was omitted between every ten

rows to form grooves for the heater wires. A photograph of a ball assembly nearly completed in a copper mold before firing is shown in Fig. D.1. Fig. D.2 shows a photograph of the molds being filled. As shown in this photograph, most of the ball arrangement was done with small brushes. With some practice it became possible to literally paint the ball rows into place. Each plate contained on the order of 350,000 balls. Assembly of the ball pack took between three and four days for an experienced worker.

Another problem that the SLAC tube shop personnel worked out for us was the correct 'heating pattern' for the brazing of the full-size plates. The heating pattern finally adopted was to heat the plates to 840°C and allow the molds and plates to equalize at this temperature. This appears to be just under the melting temperature of the phosphor nickel plating on the copper balls. After equalizing all the furnace thermocouples to within a few degrees, the plate and mold temperature was increased to 910°C and held for ten minutes. During this final heating, all mold thermocouples were held within a ten degree band to avoid uneven heating. At the end of the ten minute cycle the furnace heating element was removed and the steel retort was air-quenched. Typical cooling times for this process was usually in excess of twelve hours before the plates could be removed from their molds. This particular heating pattern seemed to optimize the brazing process. At lower temperature, the braze fillets formed between balls were smaller and often would not hold. At higher temperatures, the plating seemed to evaporate or be absorbed into the balls and there was less available for the braze.

Figure D.3 is a photograph of the arrangement used for the molds on the pedestal of the 24 inch SLAC furnace. A photograph of a tube shop technician removing the heating element from the steel retort after firing is shown in Fig. D.4. A photograph of the finished plate, after the copper molds were removed is shown in Fig. D.5. The black material on the mold is the release agent used to avoid having the balls braze themselves to the mold. It was found after several firings the copper molds became extremely soft and lost all temper. Inspection was needed after each firing, before reassembly, to ensure that the side walls were

straight and square. Fig. D.6 is a close-up of the plate edge after firing. The ball layer lip is clearly shown. As described earlier, this lip made it possible to construct the rough surface test section without interruptions in the roughness pattern at plate joints.

The successful fabrication of the Roughness Rig plates was possible thanks to the help of several people. Particularly, the author is thankful to Nick Andrews, foreman at the Hansen Lab Tube Shop who first helped me successfully braze the trial samples. To Manny Gill of Electro-Coatings, Inc., who worked out the batch process which allowed the successful plating of the 8 million balls that were used. To Bob Rosenberg, Supervisor of the SLAC Tube Shop, and his people, who gave us space, furnace time and the benefit of their many years of experience in brazing the full size plates. Finally, we're thankful to the two temporary employees who helped assemble the plates, Jim Burlison and George Zanetti, whose ball-stacking ability was surpassed only by their patience and good humor.

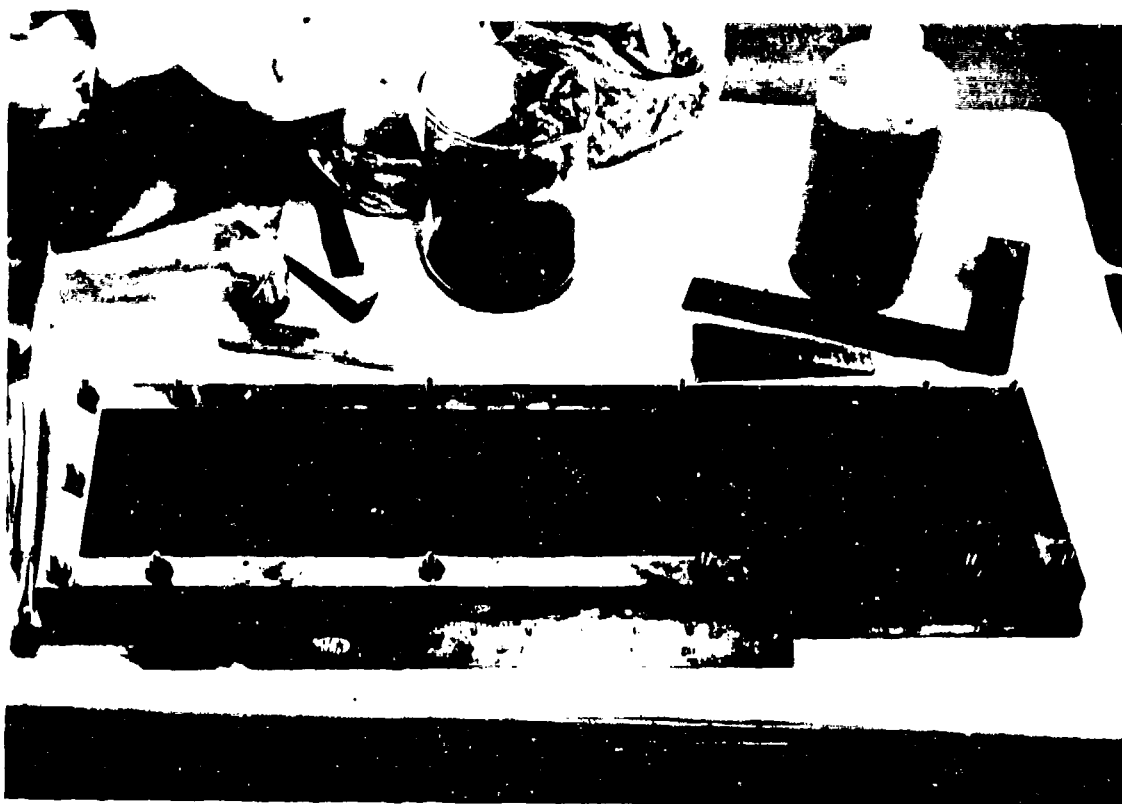


Fig. D.1 Photograph of ball assembly in mold, almost complete



Fig. D.2 Photograph of balls being arranged in the molds

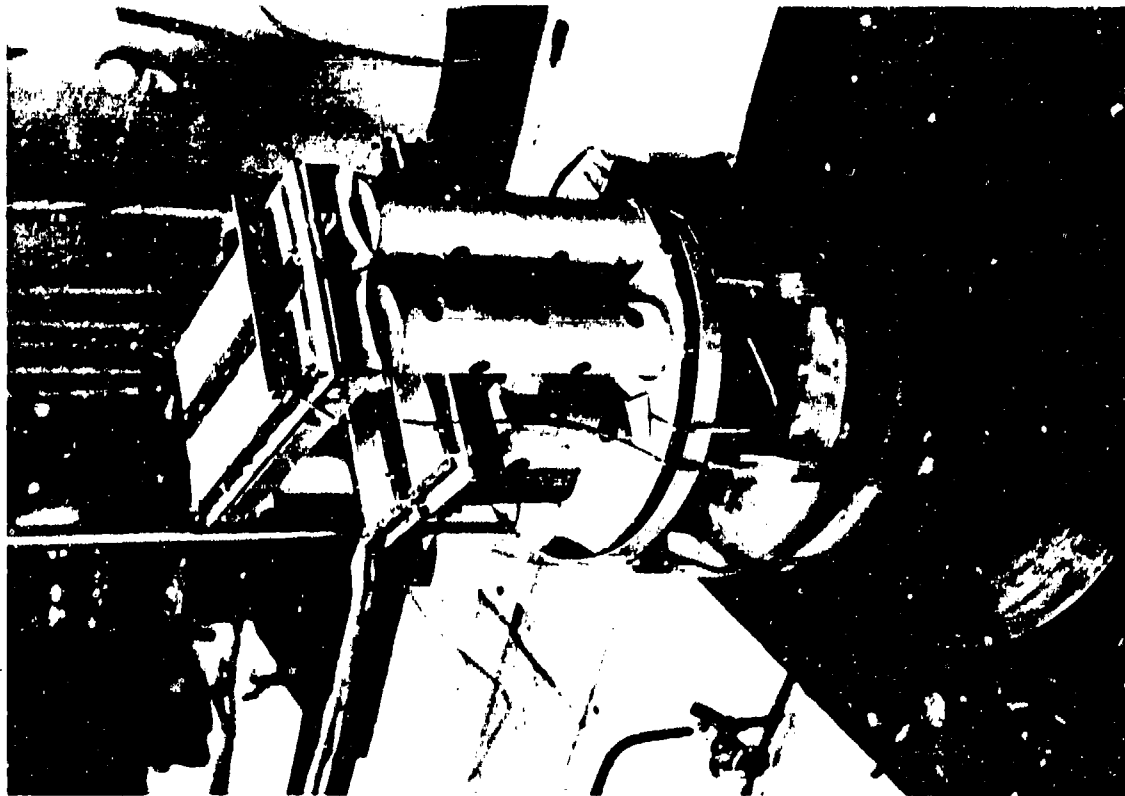


Fig. D.3 Photograph of the molds on the furnace pedestal before firing

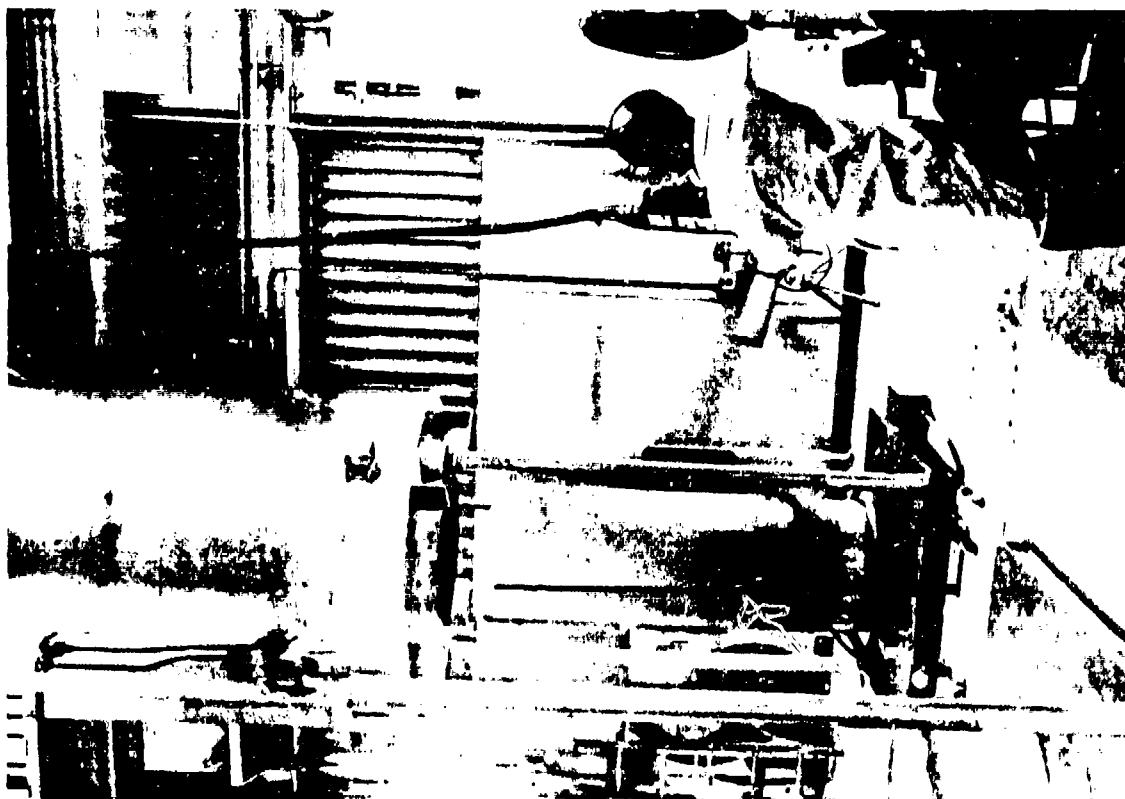


Fig. D.4 Photograph of furnace being raised after brazing the ball assembly

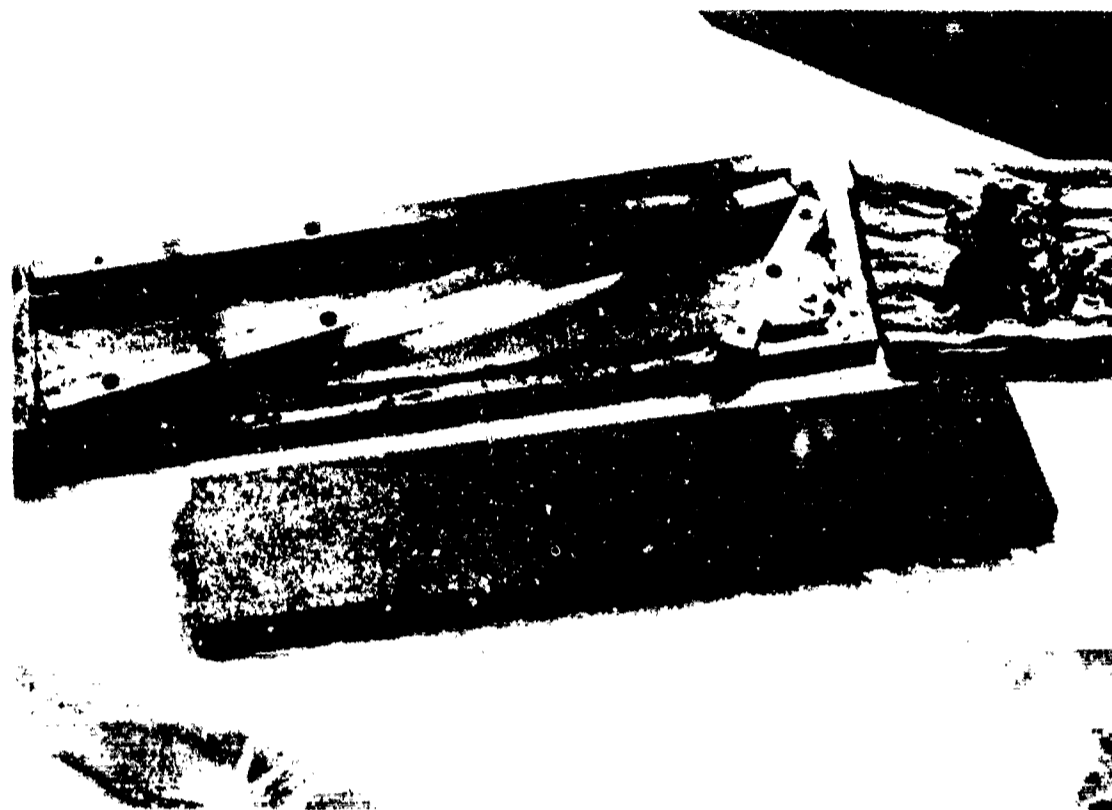


Fig. D.5 Photograph of the brazed ball plate with mold after firing



Fig. D.6 Photograph of an end view of the plate after firing

APPENDIX E

TABULATION OF EXPERIMENTAL RESULTS

This appendix contains a summary of the Stanton number data taken in these tests, along with a limited number of velocity profiles. Included are Stanton data for each blowing fraction and for each free-stream velocity tested. For each of the test conditions, an initial velocity profile has been included. This is typically the first profile measured once the boundary layer was fully turbulent. The purpose of including this profile is to provide a 'starting point' for prediction schemes, for those wishing to use these data to check a predictive method. The following is a summary of the abbreviations used in the data listings.

E.1 Stanton Number Data Listings

VEL	Free-stream velocity for the test.
T, TO	Free-stream static and total temperature.
RHO	Free-stream density.
P	Free-stream static pressure.
TDB, TWB	Dry and wet bulb temperatures.
PAMB	Ambient pressure.
VIR ORIG	Turbulent boundary layer virtual origin, determined from the curve fit to momentum thicknesses. Measured from the test section inlet, positive values are downstream.
PL NO	Plate number.
X	Distance along test section, from inlet.
STN NO	Stanton number.
MOM REY NO	Momentum thickness Reynolds number.
ENTH REY NO	Enthalpy thickness Reynolds number.
X REY NO	x-Reynolds number, measured from test section inlet.
(X-XO) REY NO	x-Reynolds number measured from the virtual origin.
F	Blowing fraction.
B	F/St .

TPL, TAIR	Plate surface and transpiration air thermocouple readings.
MOMTH, ENTH	Momentum and enthalpy thickness for each plate. Momentum thicknesses were obtained by plotting the 6 or 7 measured values of momentum thicknesses and interpolating to find values for each plate. Enthalpy thickness for each plate was obtained from the integral energy equation using the measured Stanton numbers.
DIS TH	Displacement thickness from measured velocity profiles.
MOM TH	Momentum thickness from measured velocity profiles.
SHAPE FACTOR	Displacement thickness/momentum thickness.
X-XO	Distance from virtual origin.
MOM TH (FIT)	Momentum thickness from least-squares fit to momentum thickness data.
DIFF	Difference between the measured momentum thickness and that from the curve fit.
CF2 (FIT)	Skin friction based on momentum thickness fit.
CF2 SMOOTH	Smooth surface skin friction, taken from

$$\frac{c_f}{2} = .0125 \operatorname{Re}_\theta^{-0.25} \left[\frac{\ln(1+B)}{B} \right]^{0.7} \quad (E-1)$$

RATIO	Rough surface skin friction/smooth surface skin friction.
ROUGH RE NO	Roughness Reynolds number.

E.2 Velocity Profile Listings

F S VEL	Free-stream velocity.
BLO FR	Nominal blowing fraction for the run
STAT TEMP	Free-stream static temperature.
STAT PRES	Free-stream static pressure.
PORT	Plate over which the velocity profile was taken.
DIST	Distance from test section inlet.
Y - YTOP	Distance from crest of rough surface balls to center of probe, with no corrections applied.
V/VINF	Local-to-free-stream velocity ratio.

STANTON RUN 7/6/73 NO BLOW V=32 FT/SEC
 VEL= 34.9 FT/SEC T= 76.4 DEGF TO= 76.5 DEGF RH=0.073 LBS/FT3 P= 14.63 PSI
 TOW= 86.0 DEGF THW= 70.0 DEGF PAMU= 29.72 IN HG VIR ORIG X= 11.72 IN

PL	X	STN	MOM	ENTH	X	(X-X0)	F	B	TPL	TAIR	MOMTH	ENTH
NO	INCH	NO	REYNO	REYNO	REYNO	REYNO			DEGF	DEGF	INCH	INCH
1	2	0.00215	243	75	34693	0.0	0.	102.3	97.6	0.014	0.004	
2	6	0.00111	245	188	104079	0.0	0.	102.4	97.3	0.017	0.011	
3	10	0.00095	347	259	173466	0.0	0.	102.6	97.4	0.020	0.015	
4	14	0.00089	399	323	242852	0.0	0.	102.7	96.9	0.023	0.019	
5	18	0.00090	434	386	312238	0.0	0.	102.7	97.2	0.025	0.022	
6	22	0.00126	451	461	381624	50723	0.	102.9	96.9	0.026	0.027	
7	26	0.00321	555	616	451010	126109	0.	102.8	98.3	0.032	0.036	
8	30	0.00332	711	842	520397	195496	0.	102.4	99.1	0.041	0.049	
9	34	0.00305	867	1063	589783	264082	0.	102.4	96.3	0.050	0.061	
10	38	0.00285	1041	1268	659169	334268	0.	102.4	96.2	0.060	0.073	
11	42	0.00270	1214	1461	728555	403654	0.	102.4	97.2	0.070	0.084	
12	46	0.00264	1388	1646	797942	473041	0.	102.4	98.8	0.080	0.095	
13	50	0.00246	1561	1823	867328	542427	0.	102.4	98.2	0.090	0.105	
14	54	0.00242	1717	1993	936714	611813	0.	102.4	94.2	0.099	0.115	
15	58	0.00236	1891	2158	1006100	681199	0.	102.4	98.3	0.109	0.124	
16	62	0.00229	2047	2319	1075487	750586	0.	102.4	97.3	0.118	0.134	
17	66	0.00229	2186	2478	1144873	819972	0.	102.5	96.9	0.126	0.143	
18	70	0.00225	2324	2635	1214259	884358	0.	102.4	97.3	0.134	0.152	
19	74	0.00220	2463	2790	1283645	953744	0.	102.3	95.9	0.142	0.161	
20	78	0.00218	2602	2942	1353031	1028130	0.	102.3	98.1	0.150	0.170	
21	82	0.00215	2723	3092	1422418	1097517	0.	102.4	98.1	0.157	0.178	
22	86	0.00212	2845	3240	1491804	1166903	0.	102.4	98.1	0.164	0.187	
23	90	0.00211	2984	3387	1561190	1236289	0.	102.4	98.0	0.172	0.195	
24	94	0.00211	3105	3534	1630576	1305675	0.	102.4	98.5	0.179	0.204	

SKIN FRI COEFF AND VIRTUAL ORIGIN FROM CURVE FIT TO MOM TH MEASUREMENTS
 CURVE FIT THETA= 0.0059*(X-X0)** 0.7937 VIR ORIG(X0)= 18.723 INCHES

PL	X	DIS TH	MOM TH	SHAPE	X-X0	MOM TH	DIFF	CF2	CF2	RATIO	ROUGH
NO	IN	INCH	INCH	FACTOR	INCH (FIT)	INCH (FIT)	SMOOTH				RE NO
2	6	0.0417	0.0173	2.4113							
4	14	0.0520	0.0227	2.2891							
6	22	0.0590	0.0263	2.2469							
8	30	0.0699	0.0314	1.6889	11.28	0.0406	-0.0008	0.00286	0.00242	1.18	29.09
10	38	0.0903	0.0606	1.4894	19.28	0.0621	0.0015	0.00256	0.00220	1.16	27.53
13	50	0.1539	0.0909	1.4730	31.28	0.0912	0.0003	0.00231	0.00198	1.17	26.18
16	62	0.1707	0.1198	1.4749	43.28	0.1160	-0.0018	0.00216	0.00145	1.17	25.32
20	78	0.2103	0.1506	1.4492	59.28	0.1515	0.0008	0.00203	0.00175	1.16	24.51

STANTON RUN 8/22/73 V=32 FT/SEC F=0.01
 VEL= 35.3 FT/SEC T= 74.8 DEGF TO= 74.9 DEGF RH=0.0746 LBS/FT3 P= 14.80 PSI
 TOW= 72.0 DEGF THW= 62.0 DEGF PAMU= 30.06 IN HG VIR ORIG X= 5.38 IN

PL	X	STN	MOM	ENTH	X	(X-X0)	F	B	TPL	TAIR	MOMTH	ENTH
NO	INCH	NO	REYNO	REYNO	REYNO	REYNO			DEGF	DEGF	INCH	INCH
1	2	0.00156	321	89	35609	0.00004	0.000	103.5	79.9	0.018	0.005	
2	6	0.00081	393	238	107067	11064	0.0009	1.085	103.7	79.7	0.022	0.013
3	10	0.00325	714	448	178445	82441	0.0010	0.293	103.4	79.1	0.040	0.025
4	14	0.00340	981	753	249822	153819	0.0009	0.276	103.5	80.2	0.055	0.042
5	18	0.00286	1196	1047	321200	225197	0.0011	0.369	103.6	80.5	0.067	0.059
6	22	0.00236	1410	1307	392578	296575	0.0010	0.421	103.6	79.1	0.079	0.073
7	26	0.00229	1642	1542	463956	367953	0.0009	0.408	103.6	79.7	0.092	0.086
8	30	0.00223	1856	1770	535334	439330	0.0010	0.429	103.7	81.4	0.104	0.099
9	34	0.00213	2070	1992	606711	510708	0.0009	0.410	103.8	78.6	0.116	0.112
10	38	0.00205	2284	2206	678089	582086	0.0009	0.454	103.8	79.1	0.128	0.124
11	42	0.00202	2498	2418	749467	653464	0.0009	0.467	103.6	79.9	0.140	0.136
12	46	0.00195	2712	2623	820845	724842	0.0008	0.426	103.8	80.8	0.152	0.147
13	50	0.00185	2926	2826	892223	796214	0.0010	0.558	103.5	80.8	0.164	0.158
14	54	0.00180	3105	3026	963600	867597	0.0009	0.516	103.9	80.8	0.174	0.170
15	58	0.00176	3301	3219	1034978	938975	0.0009	0.525	103.7	78.5	0.185	0.180
16	62	0.00175	3498	3410	1106356	1010353	0.0009	0.523	103.7	78.5	0.196	0.191
17	66	0.00179	3658	3599	1177734	1081731	0.0009	0.475	103.6	78.6	0.205	0.202
18	70	0.00170	3837	3786	1249112	1153108	0.0009	0.534	103.7	78.9	0.215	0.212
19	74	0.00168	3997	3970	1320489	1224486	0.0009	0.521	103.5	79.0	0.224	0.223
20	78	0.00170	4158	4154	1391867	1295864	0.0009	0.516	103.7	80.7	0.233	0.233
21	82	0.00159	4336	4338	1463245	1367242	0.0010	0.637	103.4	78.3	0.243	0.243
22	86	0.00156	4497	4523	1534623	1438620	0.0010	0.66	103.8	80.6	0.252	0.253
23	90	0.00153	4657	4704	1606001	1509997	0.0010	0.637	103.7	80.3	0.261	0.264
24	94	0.00163	4872	4885	1677378	1581375	0.0009	0.582	103.6	80.7	0.273	0.274

SKIN FRI COEFF AND VIRTUAL ORIGIN FROM CURVE FIT TO MOM TH MEASUREMENTS
 CURVE FIT THETA= 0.0099*(X-X0)** 0.7581 VIR ORIG(X0)= 5.379 INCHES

PL	X	DIS TH	MOM TH	SHAPE	X-X0	MOM TH	DIFF	CF2	CF2	RATIO	ROUGH
NO	IN	INCH	INCH	FACTOR	INCH (FIT)	INCH (FIT)	SMOOTH				RE NO
1	2	0.0460	0.0177	2.6010							
2	6	0.0697	0.0223	2.4083							
4	14	0.0839	0.0346	1.5364							
6	22	0.1220	0.0795	1.5356	14.62	0.0785	-0.0010	0.00254	0.00172	1.48	27.55
8	30	0.1583	0.1037	1.5265	24.62	0.1049	0.0012	0.00220	0.00159	1.38	25.64
10	38	0.1944	0.1280	1.5185	32.62	0.1291	0.0011	0.00190	0.00150	1.32	24.30
13	50	0.2409	0.1626	1.5181	44.62	0.1627	0.0000	0.00175	0.00139	1.26	22.95
16	62	0.2963	0.1966	1.5075	56.62	0.1939	-0.0027	0.00159	0.00132	1.21	21.76
20	78	0.3440	0.2316	1.4852	72.62	0.2330	0.0014	0.00143	0.00125	1.14	20.64

STANTON RUN 8/21/73 V=32 FT/SEC F=0.004
 VLL= 34.4 FT/SEC L= 75.1 DLG TO= 75.2 DLG RHO=0.0744 LHS/FTS P= 14.76 PSI
 TUB= 81.0 DLG TWH= 64.0 DLG PAMU= 29.97 IN HG VIR ORIG X0= 1.16 IN

PL	X	STA	MOM	ENTH	X	(X-X0)	F	B	TPL	DEGF	DEGF	INCH	INCH
NO	INCH	NO	REYNO	REYNO	REYNO	REYNO							
1	2	0.00105	328	98	34571	14520	0.0018	1.693	99.5	77.5	0.019	0.006	
2	6	0.00166	536	313	103713	83662	0.0017	1.084	99.5	76.7	0.031	0.018	
3	10	0.00335	847	611	172055	152804	0.0018	0.551	99.0	76.5	0.049	0.055	
4	14	0.00271	1106	948	241998	221946	0.0018	0.679	99.2	76.6	0.064	0.055	
5	18	0.00231	1383	1252	311140	291089	0.0019	0.829	99.3	77.1	0.080	0.072	
6	22	0.00202	1625	1530	380282	360231	0.0018	0.893	99.2	76.9	0.094	0.090	
7	26	0.00191	1884	1792	449424	429373	0.0018	0.965	99.4	77.2	0.109	0.104	
8	30	0.00174	2109	2046	518566	498515	0.0018	1.036	99.4	78.4	0.122	0.118	
9	34	0.00170	2368	2292	587708	567657	0.0018	1.085	99.3	76.6	0.137	0.133	
10	38	0.00170	2593	2534	656851	636799	0.0018	1.066	99.4	76.9	0.150	0.147	
11	42	0.00155	2835	2773	725993	705942	0.0018	1.190	99.4	77.5	0.164	0.160	
12	46	0.00161	3077	3003	795135	775084	0.0016	1.016	99.4	78.2	0.178	0.174	
13	50	0.00151	3302	3230	864277	844226	0.0018	1.195	99.4	77.5	0.191	0.187	
14	54	0.00142	3526	3457	933419	913368	0.0018	1.295	99.4	78.0	0.204	0.200	
15	58	0.00143	3734	3682	1002561	982510	0.0018	1.271	99.4	77.0	0.216	0.213	
16	62	0.00132	3958	3904	1071704	1051652	0.0019	1.406	99.4	77.5	0.229	0.226	
17	66	0.00136	4166	4121	1140846	1120795	0.0018	1.283	99.5	77.6	0.241	0.238	
18	70	0.00139	4373	4331	1209988	1189937	0.0016	1.130	99.4	77.8	0.253	0.251	
19	74	0.00129	4581	4538	1279130	1259079	0.0017	1.341	99.4	77.1	0.265	0.263	
20	78	0.00127	4771	4746	1348272	1328221	0.0017	1.362	99.4	76.8	0.276	0.275	
21	82	0.00129	4969	4960	1417414	1397363	0.0019	1.493	99.4	76.4	0.289	0.287	
22	86	0.00121	5203	5176	1486557	1466505	0.0019	1.565	99.4	77.3	0.301	0.299	
23	90	0.00130	5410	5343	1555699	1535648	0.0019	1.466	99.2	78.0	0.313	0.312	
24	94	0.00120	5618	5609	1624841	1604790	0.0018	1.537	99.4	78.3	0.325	0.324	

SKIN FRI COEFF AND VIRTUAL ORIGIN FROM CURVE FIT TO MOM TH MEASUREMENTS
 CURVE FIT THETA= 0.0077*(X-X0)** 0.0264 *VIR ORIG(X0)= 1.157 INCHES

PL	X	WIS	TH	MOM	TH	SHAPE	X-X0	MOM	TH	DIFF	CF2	CF2	RATIO	ROUGH
NO	IN	INCH	INCH	FACTOR	INCH	(FIT)	INCH	(FIT)	INCH	(FIT)	SMOOTH			RE NO
1	2	0.0580	0.0193	5.0075										
2	6	0.0671	0.0313	2.1443										
4	14	0.0985	0.0639	1.5428	12.84	0.0632	-0.0006	0.0020	0.0015	1.33	24.11			
6	22	0.1469	0.0941	1.5607	20.84	0.0943	0.0002	0.00174	0.00136	1.28	22.12			
8	30	0.1905	0.1222	1.5588	28.84	0.1234	0.0012	0.00153	0.00125	1.23	20.77			
10	38	0.2329	0.1500	1.5529	36.84	0.1510	0.0011	0.00139	0.00116	1.20	19.75			
13	50	0.2964	0.1927	1.5385	48.84	0.1907	-0.0020	0.00123	0.00106	1.15	18.06			
16	62	0.3483	0.2293	1.5188	60.84	0.2286	-0.0007	0.00111	0.00100	1.11	17.05			
20	78	0.4085	0.2763	1.4781	76.84	0.2773	0.0009	0.00094	0.00093	1.05	16.01			

STANTON NUMBER RUN 8/30/73 V=32 FT/SEC F=0.004
 VLL= 33.3 FT/SEC L= 68.1 DLG TO= 68.2 DLG RHO=0.0744 LHS/FTS P= 14.60 PSI
 TUB= 77.0 DLG TWH= 68.0 DLG PAMU= 29.78 IN HG VIR ORIG X0= -3.32 IN

PL	X	STA	MOM	ENTH	X	(X-X0)	F	B	TPL	DEGF	DEGF	INCH	INCH
NO	INCH	NO	REYNO	REYNO	REYNO	REYNO							
1	2	0.00057	592	160	34067	40618	0.0041	7.276	99.4	72.3	0.023	0.009	
2	6	0.00290	954	560	102201	158752	0.0041	1.421	99.4	71.5	0.056	0.033	
3	10	0.00245	1346	1024	170335	226886	0.0041	1.687	99.9	71.2	0.074	0.060	
4	14	0.00192	1737	1454	238469	295020	0.0041	2.157	99.8	71.4	0.102	0.085	
5	18	0.00171	2146	1859	306603	363155	0.0041	2.414	99.7	71.8	0.126	0.109	
6	22	0.00150	2487	2242	374737	431289	0.0039	2.618	99.6	71.8	0.146	0.132	
7	26	0.00151	2845	2617	442871	499423	0.0041	2.711	99.6	72.4	0.167	0.154	
8	30	0.00129	3202	2994	511005	567557	0.0041	3.147	99.7	73.1	0.188	0.176	
9	34	0.00125	3560	3361	579140	635691	0.0041	3.304	99.7	71.9	0.209	0.197	
10	38	0.00116	3918	3724	647274	703825	0.0041	3.548	99.8	72.0	0.230	0.219	
11	42	0.00116	4275	4083	715408	771959	0.0041	3.544	99.6	72.3	0.251	0.240	
12	46	0.00110	4633	4442	783542	840093	0.0042	3.707	99.7	73.1	0.272	0.261	
13	50	0.00099	5003	4740	851676	908227	0.0040	3.987	99.8	72.0	0.294	0.281	
14	54	0.00108	5366	5137	919810	976361	0.0042	3.805	99.8	72.4	0.315	0.302	
15	58	0.00106	5723	5491	987944	1044495	0.0041	3.805	99.9	71.3	0.336	0.322	
16	62	0.00095	6098	5859	1056078	1112629	0.0041	4.354	99.8	72.6	0.358	0.343	
17	66	0.00103	6456	6187	1124212	1180763	0.0041	4.013	99.8	72.0	0.379	0.363	
18	70	0.00089	6813	6534	1192346	1246897	0.0041	4.609	99.7	72.2	0.400	0.384	
19	74	0.00101	7171	6882	1260480	1317031	0.0042	4.107	99.8	72.3	0.421	0.404	
20	78	0.00082	7529	7227	1328614	1385165	0.0041	5.012	99.8	72.0	0.442	0.424	
21	82	0.00077	7887	7562	1396748	1453300	0.0041	5.373	99.9	71.9	0.463	0.444	
22	86	0.00071	8244	7893	1464882	1521434	0.0041	5.807	99.8	72.5	0.484	0.463	
23	90	0.00087	8619	8227	1533016	1589568	0.0041	4.721	99.7	73.3	0.506	0.483	
24	94	0.00084	8977	8565	1601150	1657702	0.0041	4.919	99.6	73.2	0.527	0.503	

SKIN FRI COEFF AND VIRTUAL ORIGIN FROM CURVE FIT TO MOM TH MEASUREMENTS
 CURVE FIT THETA= 0.0066*(X-X0)** 0.9536 *VIR ORIG(X0)= -3.319 INCHES

PL	X	WIS	TH	MOM	TH	SHAPE	X-X0	MOM	TH	DIFF	CF2	CF2	RATIO	ROUGH
NO	IN	INCH	INCH	FACTOR	INCH	(FIT)	INCH	(FIT)	INCH	(FIT)	SMOOTH			RE NO
0	0	0.0233	0.0132	1.7616										
1	2	0.0734	0.0233	3.1527										
2	6	0.0927	0.0557	1.6645										
3	10	0.1218	0.0773	1.5752	13.32	0.0784	0.0010	0.00091	0.00098	0.93	14.69			
5	18	0.2076	0.1256	1.6530	21.32	0.1227	-0.0028	0.00079	0.00080	0.99	13.08			
8	30	0.3139	0.1880	1.6700	33.32	0.1679	-0.0001	0.00068	0.00067	1.02	12.67			
11	42	0.4152	0.2452	1.6456	45.32	0.2519	0.0008	0.00060	0.00059	1.02	11.94			
15	58	0.5726	0.3431	1.6688	61.32	0.3361	-0.0070	0.00053	0.00050	1.05	11.18			
20	78	0.7514	0.4378	1.6705	81.32	0.4400	0.0021	0.00046	0.00045	1.02	10.43			

STATION RUN 8/22/73 VE=32.9 FT/SEC F=0.008
 VEL= 32.9 FT/SEC T= 75.8 DEGR TOE 75.8 DEGR RHO=0.0745 LBS/FT3 PT 14.78 PSI
 TDB= 77.0 DEGR TWD= 63.0 DEGR PAMB= 30.01 IN HG VIR ORIG(X)= -2.00 IN

PL	X	STN	MOM	ENTH	X	(X-X0)	F	B	TPL	TAIR	MOMTH	ENTH
NO	INCH	NO	REYNO	REYNO	REYNO	REYNO			DEGR	DEGR	INCH	INCH
1	2	0.00042	612	260	33054	66109	0.007517	8.25	103.3	76.7	0.037	0.016
2	6	0.00216	1240	842	99163	132218	0.0076	3.501	103.1	76.3	0.075	0.051
3	10	0.00163	1801	1468	165272	198326	0.0076	4.631	103.2	76.1	0.109	0.089
4	14	0.00114	2312	2058	231381	264435	0.0075	6.584	103.2	76.2	0.140	0.125
5	18	0.00098	2826	2637	297490	330544	0.0074	8.076	103.3	76.6	0.171	0.160
6	22	0.00069	3327	3206	363599	396653	0.007711	1.185	103.3	76.6	0.201	0.194
7	26	0.00067	3851	3754	429707	462762	0.007611	1.339	103.2	76.6	0.233	0.227
8	30	0.00056	4396	4295	495816	528871	0.007613	1.550	103.2	76.9	0.266	0.260
9	34	0.00056	4925	4824	561925	594979	0.007513	1.306	103.2	76.0	0.298	0.292
10	38	0.00055	5504	5359	628034	661088	0.007513	1.501	103.3	76.1	0.333	0.324
11	42	0.00049	6065	5901	694143	727197	0.007915	1.004	103.2	76.5	0.367	0.357
12	46	0.00053	6611	6423	760251	793306	0.006913	1.084	103.3	77.5	0.400	0.389
13	50	0.00043	7206	6926	826360	859415	0.007417	1.001	103.3	76.2	0.436	0.429
14	54	0.00037	7784	7492	892464	925524	0.007720	1.757	103.3	76.5	0.471	0.461
15	58	0.00039	8363	7976	958578	991632	0.007318	1.989	103.3	75.7	0.506	0.493
16	62	0.00035	8925	8500	1024687	1057241	0.007822	1.000	103.2	76.7	0.540	0.514
17	66	0.00036	9503	9040	1090746	1123850	0.007821	1.734	103.2	76.2	0.575	0.547
18	70	0.00034	10065	9573	1156804	1189959	0.007622	1.282	103.2	76.2	0.609	0.579
19	74	0.00038	10644	10094	1223813	1256068	0.00719	1.534	103.4	76.5	0.644	0.611
20	78	0.00027	11222	10609	1289122	1322176	0.007527	1.870	103.4	76.0	0.679	0.642
21	82	0.00031	11800	11120	135531	1388285	0.007423	1.934	103.3	76.0	0.714	0.673
22	86	0.00031	12379	11631	1421340	1454394	0.007424	1.054	103.4	76.5	0.749	0.704
23	90	0.00032	12941	12152	1487499	1520553	0.007724	1.184	103.3	77.0	0.783	0.735
24	94	0.00037	13519	12675	1553557	1586612	0.007420	1.326	103.4	77.1	0.818	0.767

SKIN FRI COEFF AND VIRTUAL ORIGIN FROM CURVE FIT TO MOM TH MEASUREMENTS
 CURVE FIT THETA= 0.0083*(X-X0)** 1.0044 VIR ORIG(X)= -2.00 INCHES

PL	X	STN	MOM	TH	SHAPE	X-X0	MOM	TH	DIFF	CF2	CF2	RATIO	ROUGH
NO	IN	INCH	INCH	FACTOR	INCH	(FIT)	INCH	(FIT)	INCH	(FIT)	SMOOTH	RE	NO
1	2	0.1802	0.1093	1.6984	17.00	0.1005	-0.0089	0.00061	0.00000	-0.07.93	12.54		
6	22	0.3808	0.2012	1.8929	24.00	0.2015	0.0004	0.00063	0.00000	633.65	12.55		
9	34	0.5617	0.2980	1.8849	36.00	0.3028	0.0048	0.00065	0.00000	648.73	13.00		
12	46	0.7911	0.4002	1.4772	48.00	0.4043	0.0041	0.00066	0.00000	659.45	13.11		
15	58	1.0260	0.5061	2.0274	60.00	0.5058	-0.0002	0.00067	0.00000	667.77	13.19		
19	74	1.2877	0.6445	1.9981	76.00	0.6414	-0.0031	0.00068	0.00000	676.59	13.28		

STATION RUN 5/30/73 NO FLOW VE=90 FT/SEC
 VEL= 90.8 FT/SEC T= 76.5 DEGR TOE 77.2 DEGR RHO=0.0735 LBS/FT3 PT 14.63 PSI
 TDB= 84.0 DEGR TWD= 67.5 DEGR PAMB= 29.71 IN HG VIR ORIG(X)= 5.53 IN

PL	X	STN	MOM	ENTH	X	(X-X0)	F	B	TPL	TAIR	MOMTH	ENTH
NO	INCH	NO	REYNO	REYNO	REYNO	REYNO			DEGR	DEGR	INCH	INCH
1	2	0.00130	406	117	70158	0	0.	0.	99.9	97.4	0.009	0.003
2	6	0.00389	811	584	270473	111345	0.	0.	99.7	100.6	0.018	0.013
3	10	0.00383	1378	1280	450748	201660	0.	0.	99.7	97.7	0.035	0.028
4	14	0.00325	2164	1918	631103	471975	0.	0.	99.6	96.8	0.048	0.043
5	18	0.00295	2750	2477	811418	652290	0.	0.	99.6	96.9	0.061	0.055
6	22	0.00273	3291	2989	991733	832605	0.	0.	99.6	95.7	0.073	0.066
7	26	0.00265	3787	3473	1172048	1012920	0.	0.	99.7	96.7	0.084	0.077
8	30	0.00247	4192	3955	1352363	1193235	0.	0.	99.7	97.6	0.093	0.087
9	34	0.00245	4688	4374	1532679	1373551	0.	0.	99.7	95.3	0.104	0.097
10	38	0.00237	5139	4812	1712994	1553866	0.	0.	99.7	94.9	0.114	0.107
11	42	0.00234	5590	5236	1893309	1734181	0.	0.	99.7	98.2	0.119	0.116
12	46	0.00230	6041	5654	2073624	1914496	0.	0.	99.7	97.7	0.134	0.125
13	50	0.00227	6446	6066	2253939	2094811	0.	0.	99.8	96.8	0.143	0.135
14	54	0.00218	6852	6467	2434254	2275126	0.	0.	99.7	97.9	0.152	0.143
15	58	0.00218	7303	6860	2614569	2455441	0.	0.	99.7	97.1	0.162	0.152
16	62	0.00218	7663	7253	2794884	2635756	0.	0.	99.7	96.3	0.170	0.161
17	66	0.00213	8069	7642	2975200	2816071	0.	0.	99.6	95.8	0.179	0.170
18	70	0.00213	8430	8026	3155515	2996387	0.	0.	99.6	95.9	0.187	0.178
19	74	0.00211	8790	8408	3335830	3176702	0.	0.	99.7	94.7	0.195	0.187
20	78	0.00209	9196	8786	3516145	3357017	0.	0.	99.7	96.4	0.204	0.195
21	82	0.00205	9557	9159	3696460	3537332	0.	0.	99.7	96.5	0.212	0.203
22	86	0.00208	9917	9532	3876775	3717647	0.	0.	99.6	97.2	0.220	0.211
23	90	0.00204	10278	9903	4057090	3897962	0.	0.	99.6	97.0	0.228	0.220
24	94	0.00204	10639	10271	4237405	4078277	0.	0.	99.6	99.2	0.236	0.228

SKIN FRI COEFF AND VIRTUAL ORIGIN FROM CURVE FIT TO MOM TH MEASUREMENTS
 CURVE FIT THETA= 0.0079*(X-X0)** 0.7547 VIR ORIG(X)= 3.53 INCHES

PL	X	STN	MOM	TH	SHAPE	X-X0	MOM	TH	DIFF	CF2	CF2	RATIO	ROUGH
NO	IN	INCH	INCH	FACTOR	INCH	(FIT)	INCH	(FIT)	INCH	(FIT)	SMOOTH	RE	NO
0	0	0.0190	0.0090	2.1178									
1	2	0.0237	0.0095	2.5047									
2	6	0.0307	0.0182	1.6921									
3	10	0.0611	0.0360	1.6946									
5	18	0.0943	0.0596	1.5842	14.47	0.0543	-0.0003	0.00309	0.00174	1.78	78.71		
8	30	0.1454	0.0929	1.5660	26.47	0.0935	0.0007	0.00267	0.00155	1.72	73.09		
11	42	0.1908	0.1241	1.5372	38.47	0.1240	-0.0001	0.00243	0.00145	1.68	69.81		
15	58	0.2426	0.1618	1.4996	54.47	0.1612	-0.0006	0.00223	0.00135	1.65	66.90		
20	78	0.3030	0.2039	1.4863	74.47	0.2041	0.0003	0.00207	0.00128	1.62	64.38		

STANTON, RUN 8/24/73 V=90 FT/SEC FZ=0.01
 VEE= 90.5 FT/SEC T= 77.0 DEG TOE= 77.7 DEG RHO=0.0756 LBS/FT3 P= 14.65 PSI
 TDB= 80.0 DEG THW= 64.0 DEG PAMU= 29.79 IN HG VIR ORIG=XOZ 0.58 IN

PL	X	STN	MOM	ENTH	X	(X-XO)	F	U	TPL	TAIR	MOMTH	ENTH
NO	INCH	NO	REYN	REYN	REYN	REYN			DEG	DEG	INCH	INCH
1	2	0.00159	494	241	89035	63783	0.0011	0.682	100.9	78.0	0.011	0.005
2	6	0.00432	1258	964	269506	243454	0.0010	0.243	100.7	77.4	0.028	0.001
3	10	0.00315	2066	1828	449177	423125	0.0011	0.349	100.6	77.1	0.046	0.041
4	14	0.00271	2695	2552	628848	602796	0.0011	0.404	100.7	77.3	0.060	0.057
5	18	0.00243	3324	3217	868519	782466	0.0012	0.477	100.8	77.8	0.074	0.072
6	22	0.00229	3908	3840	948184	962137	0.0011	0.462	100.8	77.8	0.087	0.085
7	26	0.00221	4492	4438	1167860	1141808	0.0011	0.495	100.8	77.8	0.100	0.099
8	30	0.00207	5121	5020	1347531	1321474	0.0011	0.533	100.8	78.4	0.114	0.112
9	34	0.00201	5705	5582	1527202	1501150	0.0011	0.531	100.7	77.2	0.127	0.124
10	38	0.00198	6244	6132	1706875	1680820	0.0011	0.544	100.8	77.5	0.139	0.137
11	42	0.00186	6827	6675	1886543	1860491	0.0011	0.606	100.7	77.9	0.152	0.149
12	46	0.00192	7367	7205	2066214	2040162	0.0010	0.512	100.8	78.7	0.164	0.160
13	50	0.00185	7861	7723	2245885	2219833	0.0010	0.547	100.8	78.1	0.175	0.172
14	54	0.00181	8400	8243	2425556	2399504	0.0011	0.616	100.8	78.2	0.187	0.184
15	58	0.00177	8948	8765	2605227	2579174	0.0011	0.615	100.8	77.3	0.198	0.195
16	62	0.00175	9435	9279	2784897	2758845	0.0011	0.644	100.7	78.1	0.210	0.207
17	66	0.00174	9927	9792	2964568	2938516	0.0011	0.624	100.9	77.8	0.221	0.218
18	70	0.00175	10421	10294	3144239	3118187	0.0010	0.573	100.8	78.1	0.232	0.229
19	74	0.00173	10915	10791	3323910	3297857	0.0010	0.604	100.9	77.9	0.243	0.240
20	78	0.00166	11409	11285	3503581	3477528	0.0011	0.636	100.7	77.2	0.254	0.251
21	82	0.00164	11903	11776	3683251	3657199	0.0011	0.675	100.7	77.0	0.265	0.262
22	86	0.00161	12397	12266	3862922	3836870	0.0011	0.685	100.7	77.8	0.276	0.273
23	90	0.00170	12891	12762	4042593	4016541	0.0012	0.659	100.6	78.8	0.287	0.284
24	94	0.00158	13385	13255	4222264	4196211	0.0011	0.697	100.6	78.9	0.298	0.295

SKIN FRI COEFF AND VIRTUAL ORIGIN FROM CURVE FIT TO MOM TH MEASUREMENTS
 CURVE FIT THETA= 0.0072*(X-XO)** 0.8187 *VIR ORIG(XO)= 0.579 INCHES

PL	X	DIS TH	MOM TH	SHAPE	X-XO	MOM TH	DIFF	CF2	CF2	RATIO	HOUGH
NO	IN	INCH	INCH	FACTOR	INCH (FIT)	INCH (FIT)	INCH (FIT)	SMOOTH			RE NO
0	0	0.0177	0.0088	2.0182							
1	2	0.0283	0.0109	2.0093							
3	10	0.0740	0.0465	1.5493	9.42	0.0450	-0.0015	0.00291	0.00158	1.94	77.30
6	22	0.1326	0.0849	1.5624	1.42	0.0862	0.0033	0.00237	0.00125	1.90	70.20
9	34	0.1976	0.1270	1.5562	33.42	0.1264	-0.0008	0.00211	0.00110	1.92	86.22
12	46	0.2512	0.1639	1.5329	45.42	0.1632	-0.0007	0.00194	0.00102	1.91	63.92
16	62	0.3259	0.2125	1.5360	61.42	0.2104	-0.0035	0.00174	0.00093	1.91	60.11
20	78	0.3766	0.2500	1.5060	77.42	0.2525	0.0025	0.00167	0.00084	1.88	58.92

STANTON, RUN 8/23/73 V=90 FT/SEC FZ=0.02
 VEE= 89.7 FT/SEC T= 75.0 DEG TOE= 75.7 DEG RHO=0.0743 LBS/FT3 P= 14.75 PSI
 TDB= 77.0 DEG THW= 64.0 DEG PAMU= 29.96 IN HG VIR ORIG=XOZ 0.40 IN

PL	X	STN	MOM	ENTH	X	(X-XO)	F	U	TPL	TAIR	MOMTH	ENTH
NO	INCH	NO	REYN	REYN	REYN	REYN			DEG	DEG	INCH	INCH
1	2	0.00190	541	357	90244	72195	0.0021	1.084	101.8	76.8	0.012	0.008
2	6	0.00370	1534	1236	270732	252683	0.0021	0.561	101.8	76.3	0.034	0.0.7
3	10	0.00265	2437	2186	451220	433171	0.0021	0.793	101.4	76.0	0.054	0.044
4	14	0.00224	3204	3008	631708	613654	0.0021	0.451	101.4	76.1	0.071	0.067
5	18	0.00197	3971	3778	812196	794147	0.0022	1.123	101.4	76.4	0.088	0.080
6	22	0.00181	4602	4504	992684	974635	0.0021	1.170	101.4	76.5	0.102	0.100
7	26	0.00175	5324	5214	1175172	1155123	0.0021	1.229	101.4	76.4	0.118	0.116
8	30	0.00163	6001	5903	1353600	1333611	0.0021	1.302	101.4	76.7	0.133	0.131
9	34	0.00159	6678	6573	1534144	1514099	0.0021	1.311	101.9	76.7	0.148	0.146
10	38	0.00153	7310	7231	1714636	1694587	0.0021	1.368	102.0	76.9	0.162	0.160
11	42	0.00143	7987	7887	1895174	1875075	0.0022	1.542	101.8	76.3	0.177	0.175
12	46	0.00143	8618	8528	2075612	2057563	0.0019	1.263	102.0	77.5	0.191	0.189
13	50	0.00144	9295	9156	2256100	2238051	0.0021	1.432	101.8	76.4	0.206	0.203
14	54	0.00135	9972	9793	2436588	2418534	0.0022	1.634	101.6	76.6	0.221	0.217
15	58	0.00134	10604	10423	2617076	2599027	0.0020	1.460	101.4	75.7	0.235	0.231
16	62	0.00127	11326	11051	2777664	2759515	0.0023	1.779	101.8	76.7	0.251	0.245
17	66	0.00124	11957	11684	2978052	2960003	0.0022	1.744	101.6	76.2	0.265	0.259
18	70	0.00133	12634	12304	3158540	3140441	0.0021	1.560	101.8	76.4	0.280	0.273
19	74	0.00137	13266	12914	3339028	3320979	0.0020	1.483	101.8	76.5	0.294	0.286
20	78	0.00128	13943	13526	3519516	3501467	0.0020	1.543	101.7	76.0	0.309	0.300
21	82	0.00127	14574	14127	3700004	3681955	0.0021	1.629	101.9	75.9	0.323	0.313
22	86	0.00124	15251	14778	3880492	3862443	0.0020	1.582	101.9	76.4	0.338	0.328
23	90	0.00124	15928	15333	4060980	4042931	0.0021	1.719	101.9	77.1	0.353	0.340
24	94	0.00121	16605	15936	4241468	4223419	0.0021	1.713	101.9	77.3	0.368	0.353

SKIN FRI COEFF AND VIRTUAL ORIGIN FROM CURVE FIT TO MOM TH MEASUREMENTS
 CURVE FIT THETA= 0.0071*(X-XO)** 0.8677 *VIR ORIG(XO)= 0.400 INCHES

PL	X	DIS TH	MOM TH	SHAPE	X-XO	MOM TH	DIFF	CF2	CF2	RATIO	HOUGH
NO	IN	INCH	INCH	FACTOR	INCH (FIT)	INCH (FIT)	INCH (FIT)	SMOOTH			RE NO
0	0	0.0186	0.0094	1.9800							
1	2	0.0328	0.0115	2.8521							
3	10	0.0875	0.0537	1.6273	9.60	0.0503	-0.0034	0.00245	0.00115	1.12	70.40
6	22	0.1656	0.1022	1.6211	21.60	0.1017	-0.0005	0.00194	0.00092	2.17	63.40
9	34	0.2363	0.1487	1.5896	33.60	0.1442	0.0006	0.00175	0.00080	2.20	54.98
12	46	0.2995	0.1911	1.5674	45.60	0.1945	0.0034	0.00160	0.00072	2.21	56.93
16	62	0.3965	0.2517	1.5749	61.60	0.2525	0.0008	0.00148	0.00065	2.24	54.30
20	78	0.4844	0.3107	1.5592	77.60	0.3085	-0.0022	0.00135	0.00060	2.26	52.27

STANTON RUN 8/23/73 V=90 FT/SEC F=0.004
 VLL= 88.8 FT/SEC T= 76.4 DEGE TOE 77.0 DEGE RHO=0.0742 LIP/FIS PT 14.76 PSI
 TOB= 80.0 DEGE TWH= 66.0 DEGE PAMU= 29.99 IN HG VIR OR1(X)= 0.42 IN

PL	X	SIN	MOM	ENTH	X	(X-X0)	F	U	TPL	TAIR	MOMTH	ENTH
NO	INCH	NO	REYNO	REYNO	REYNO	REYNO			DEGE	DEGE	INCH	INCH
1	2	0.00178	579	526	89095	70366	0.0041	2.527	103.8	77.6	0.013	0.012
2	6	0.00291	1916	1686	267135	248436	0.0042	1.948	103.8	77.1	0.043	0.038
3	10	0.00195	3072	2868	445225	426526	0.0042	2.150	103.9	76.8	0.069	0.064
4	14	0.00155	4046	3925	623315	604616	0.0042	2.692	103.9	76.9	0.092	0.088
5	18	0.00132	5120	4939	801405	782706	0.0043	3.294	103.8	77.2	0.115	0.111
6	22	0.00118	6011	5928	979495	960796	0.0043	3.619	103.9	77.2	0.135	0.133
7	26	0.00108	7035	6886	1157585	1138886	0.0042	3.934	103.8	77.1	0.158	0.155
8	30	0.00101	8014	7824	1335675	1316976	0.0042	4.173	103.7	77.2	0.180	0.176
9	34	0.00097	8999	8793	1513765	1495066	0.0041	4.226	103.8	76.4	0.201	0.196
10	38	0.00092	9886	9647	1691855	1673156	0.0041	4.481	103.8	76.5	0.222	0.217
11	42	0.00083	10819	10555	1869945	1851246	0.0043	5.200	103.8	77.0	0.243	0.237
12	46	0.00095	11754	11425	2048035	2029336	0.0037	5.879	103.8	77.9	0.264	0.257
13	50	0.00087	12689	12281	2226125	2207426	0.0041	6.734	103.7	76.8	0.285	0.276
14	54	0.00075	13579	13186	2404215	2385516	0.0044	5.873	103.3	76.9	0.305	0.296
15	58	0.00077	14559	14077	2582305	2563606	0.0041	5.324	103.8	76.4	0.327	0.316
16	62	0.00076	15496	14953	2760395	2741696	0.0042	5.515	103.8	77.2	0.348	0.336
17	66	0.00070	16429	15844	2938485	2919786	0.0043	6.136	103.7	76.9	0.369	0.356
18	70	0.00073	17366	16741	3116575	3097876	0.0043	5.468	103.8	76.9	0.390	0.376
19	74	0.00068	18299	17624	3294665	3275966	0.0042	6.140	104.0	77.0	0.411	0.396
20	78	0.00068	19236	18490	3472755	3454056	0.0042	6.134	103.8	76.5	0.432	0.415
21	82	0.00072	20169	19353	3650845	3632146	0.0041	5.742	103.9	76.5	0.453	0.435
22	86	0.00068	21104	20212	3828935	3810236	0.0041	6.021	104.0	76.9	0.474	0.454
23	90	0.00064	22039	21082	4007025	3988326	0.0043	6.766	103.7	77.4	0.495	0.474
24	94	0.00060	22974	21994	4185115	4166416	0.0041	6.231	103.7	77.6	0.516	0.493

SKIN FRI COEFF AND VIRTUAL ORIGIN FROM CURVE FIT TO MOM THE MEASUREMENTS
 CURVE FIT THEIA= 0.0043*(X-X0)** 0.8769 +VIR OR1(X)= 0.418 INCHES

PL	X	U	TH MOM TH	SHAPE	X-X0	MOM TH	DIFF	CF2	CF2	RATIO	ROUGH
NO	IN	INCH	INCH	FACTOR	INCH	(FIT)	INCH	(FIT)	SMOOTH		PL NO
0	0	0.0191	0.0046	2.0022							
1	2	0.0573	0.0129	4.4256							
3	10	0.1132	0.0693	1.6338	9.58	0.0675	-0.0017	0.00278	0.00074	3.06	67.49
4	22	0.2246	0.1351	1.6618	21.58	0.1376	0.0025	0.00169	0.00055	3.05	58.14
9	34	0.3375	0.2011	1.6883	33.58	0.2028	0.0017	0.00140	0.00046	3.02	52.91
12	46	0.4454	0.2637	1.6989	45.58	0.2651	0.0014	0.00120	0.00041	2.95	48.97
16	62	0.5826	0.3535	1.6478	61.58	0.3551	-0.0024	0.00101	0.00035	2.87	45.03
20	78	0.6824	0.4179	1.6329	77.58	0.4226	0.0047	0.00088	-0.00033	-2.69	41.96

STANTON RUN 8/23/73 V=90 FT/SEC F=0.004
 VLL= 80.2 FT/SEC T= 76.3 DEGE TOE 76.9 DEGE RHO=0.0742 LIP/FIS PT 14.77 PSI
 TOB= 77.0 DEGE TWH= 65.0 DEGE PAMU= 29.99 IN HG VIR OR1(X)= 1.25 IN

PL	X	SIN	MOM	ENTH	X	(X-X0)	F	U	TPL	TAIR	MOMTH	ENTH
NO	INCH	NO	REYNO	REYNO	REYNO	REYNO			DEGE	DEGE	INCH	INCH
1	2	0.00124	605	794	60433	52412	0.0076	6.287	96.9	76.9	0.014	0.018
2	6	0.00191	2725	2465	259299	205270	0.0084	4.426	96.9	76.5	0.063	0.057
3	10	0.00122	4538	4192	432164	378144	0.0080	6.519	96.9	76.4	0.105	0.096
4	14	0.00082	6310	5729	605030	551009	0.0082	10.075	96.9	76.4	0.146	0.133
5	18	0.00068	7952	7200	777086	723875	0.0082	12.091	96.9	76.7	0.184	0.168
6	22	0.00054	9464	8629	950761	896741	0.0085	15.010	96.9	76.6	0.219	0.204
7	26	0.00044	11020	10380	1123627	1069606	0.0085	19.371	96.8	76.7	0.255	0.240
8	30	0.00043	12533	11904	1296443	1242472	0.0085	19.303	96.8	76.6	0.290	0.275
9	34	0.00042	14132	13583	1469358	1415338	0.0080	18.895	96.9	76.2	0.327	0.310
10	38	0.00046	15515	14834	1642224	1588203	0.0079	17.102	96.8	76.2	0.359	0.343
11	42	0.00029	17027	16314	1815090	1761069	0.0084	18.677	96.8	76.4	0.394	0.377
12	46	0.00039	18497	17695	1987955	1933935	0.0081	17.371	96.9	76.6	0.428	0.409
13	50	0.00045	19880	19048	2160821	2106800	0.0080	17.759	97.0	76.4	0.460	0.441
14	54	0.00035	21262	20575	2333687	2279666	0.0089	17.306	96.9	76.4	0.492	0.476
15	58	0.00031	22649	22116	2506552	2452532	0.0083	26.359	96.9	76.1	0.525	0.512
16	62	0.00033	24020	23627	2679418	2625397	0.0086	25.987	96.9	76.5	0.556	0.547
17	66	0.00022	25454	25153	2852284	2798264	0.0085	33.921	97.0	76.4	0.589	0.573
18	70	0.00027	26794	26660	3025144	2971124	0.0084	31.663	97.0	76.3	0.620	0.617
19	74	0.00037	28177	28177	3198015	3143994	0.0083	32.342	97.0	76.5	0.652	0.652
20	78	0.00028	29517	29657	3370881	3316860	0.0084	29.922	97.0	76.2	0.683	0.686
21	82	0.00031	30857	31126	3543746	3489726	0.0080	25.355	97.1	76.1	0.714	0.720
22	86	0.00031	32196	32587	3716612	3662591	0.0083	26.895	97.0	76.4	0.745	0.754
23	90	0.00025	33579	34084	3889478	3835457	0.0085	36.895	97.0	76.6	0.777	0.784
24	94	0.00028	34962	35574	4062343	4008323	0.0082	29.162	97.1	76.7	0.809	0.823

SKIN FRI COEFF AND VIRTUAL ORIGIN FROM CURVE FIT TO MOM THE MEASUREMENTS
 CURVE FIT THEIA= 0.0161*(X-X0)** 0.8626 +VIR OR1(X)= 1.248 INCHES

PL	X	U	TH MOM TH	SHAPE	X-X0	MOM TH	DIFF	CF2	CF2	RATIO	ROUGH
NO	IN	INCH	INCH	FACTOR	INCH	(FIT)	INCH	(FIT)	SMOOTH		PL NO
0	0	0.0227	0.0089	2.5341							
1	2	0.0921	0.0144	6.4153							
2	6	0.1049	0.0627	1.6729	4.75	0.0619	-0.0008	0.00324	0.000043	4.04	77.76
3	10	0.1853	0.1045	1.7735	8.75	0.1049	0.0004	0.00234	0.000058	5.76	66.05
4	22	0.4338	0.2145	1.9785	20.75	0.2209	0.0016	0.00118	0.000088	2.70	46.97
9	34	0.6567	0.3268	2.0096	32.75	0.3275	0.0007	0.00062	0.000024	8.01	34.14
12	46	0.8601	0.4327	1.9877	44.75	0.4287	-0.0040	0.00026	0.000062	2.810	23.14
16	62	1.1075	0.5556	1.9433	60.75	0.5560	0.0024	0.00008	0.000076	4.08	0.
20	78	1.3833	0.6829	2.0256	76.75	0.6827	-0.0003	-0.00033	0.000002	2.77	0.

STATION RUN 5/23/73 NO BLOW V=130 FT/SEC
 VEL=139.7 FT/SEC T= 76.0 DLGF TO= 77.6 DLGF RHO=0.0738 LBS/FT3 P= 14.67 PSI
 IDU= 77.0 DLGF TWID= 64.0 DLGF PAMPE= 29.84 IN HG VIR ORIG(X)= -0.76 IN

PL	X	STN	MOM	ENTH	X	(X-X0)	F	U	TPL	TAIR	MOMTH	ENTH
NO	INCH	NO	REYNO	REYNO	REYNO	REYNO			DEGF	DEGF	INCH	INCH
1	2	0.00333	836	464	139333	192279	0.	0.	105.3	106.0	0.012	0.007
2	6	0.00415	1951	1507	417998	470944	0.	0.	105.2	105.7	0.028	0.022
3	10	0.00334	3065	2552	690663	749610	0.	0.	105.2	103.6	0.044	0.037
4	14	0.00302	3901	3438	975329	1026275	0.	0.	105.1	101.5	0.056	0.049
5	18	0.00286	4668	4257	1253994	1306940	0.	0.	105.2	101.3	0.067	0.061
6	22	0.00269	5504	5030	1532659	1585606	0.	0.	105.2	99.6	0.079	0.072
7	26	0.00263	6270	5771	1811324	1864271	0.	0.	105.2	100.7	0.098	0.083
8	30	0.00248	6967	6483	2089990	2142936	0.	0.	105.2	101.9	0.100	0.093
9	34	0.00245	7733	7169	2368655	2421601	0.	0.	105.2	98.3	0.111	0.103
10	38	0.00236	8360	7834	2647320	2700267	0.	0.	105.2	97.6	0.120	0.113
11	42	0.00238	9057	8500	2925986	2978932	0.	0.	105.2	100.5	0.130	0.122
12	46	0.00233	9684	9155	3204651	3257597	0.	0.	105.2	102.7	0.139	0.131
13	50	0.00232	10380	9803	3483316	3536263	0.	0.	105.2	100.8	0.149	0.141
14	54	0.00224	11007	10438	3761981	3814928	0.	0.	105.2	103.0	0.158	0.150
15	58	0.00222	11704	11059	4040647	4093593	0.	0.	105.2	101.6	0.168	0.159
16	62	0.00222	12331	11677	4319312	4372258	0.	0.	105.2	100.1	0.177	0.168
17	66	0.00220	12958	12242	4597977	4650924	0.	0.	105.2	99.3	0.186	0.176
18	70	0.00219	13515	12904	4876643	4929589	0.	0.	105.2	99.9	0.194	0.185
19	74	0.00218	14142	13514	5155308	5208254	0.	0.	105.2	97.9	0.203	0.194
20	78	0.00214	14700	14116	5433973	5486920	0.	0.	105.2	100.1	0.211	0.203
21	82	0.00211	15257	14708	5712638	5765585	0.	0.	105.2	100.5	0.220	0.211
22	86	0.00211	15884	15295	5991304	6044250	0.	0.	105.2	101.9	0.228	0.220
23	90	0.00211	16441	15883	6269969	6322915	0.	0.	105.2	102.7	0.236	0.228
24	94	0.00213	16999	16474	6548634	6601581	0.	0.	105.2	106.8	0.244	0.236

SKIN FRIC COEFF AND VIRTUAL ORIGIN FROM CURVE FIT TO MOM TH MEASUREMENTS
 CURVE FIT THETA= 0.0065*(X-X0)+ 0.7955 VIR ORIG(X)= -0.761 INCH

PL	X	DIS TH	MOM TH	SHAPE	X-X0	MOM TH	DIFF	CF2	CF2	RATIO	ROUGH
NO	IN	INCH	INCH	FACTOR	INCH	(FIT)	INCH	(FIT)	SMOOTH		RE NO
1	2	0.0207	0.0117	1.7707							
2	6	0.0459	0.0282	1.6269							
3	10	0.0719	0.0436	1.6488	10.76	0.0434	-0.0002	0.0032	0.0016	1.90	123.17
5	18	0.1040	0.0671	1.5511	18.76	0.0675	0.0004	0.0028	0.0015	1.89	117.62
8	30	0.1531	0.1001	1.5288	30.76	0.1000	-0.0002	0.0025	0.0013	1.89	111.5
12	46	0.2075	0.1391	1.4421	46.76	0.1395	0.0004	0.0037	0.0012	1.88	106.59
16	62	0.2615	0.1771	1.4767	62.76	0.1763	-0.0008	0.0025	0.0011	1.88	103.43
20	78	0.3082	0.2108	1.4625	78.76	0.2112	0.0004	0.0021	0.0010	1.88	101.05

STATION RUN 8/27/73 V=139 FT/SEC F=0.01
 VEL=137.0 FT/SEC T= 75.9 DLGF TO= 77.5 DLGF RHO=0.0739 LBS/FT3 P= 14.70 PSI
 IDU= 76.0 DLGF TWID= 65.5 DLGF PAMPE= 29.85 IN HG VIR ORIG(X)= -1.15 IN

PL	X	STN	MOM	ENTH	X	(X-X0)	F	U	TPL	TAIR	MOMTH	ENTH
NO	INCH	NO	REYNO	REYNO	REYNO	REYNO			DEGF	DEGF	INCH	INCH
1	2	0.00302	825	589	137496	216557	0.0010	0.323	102.0	78.2	0.012	0.004
2	6	0.00377	2200	1747	412444	491550	0.0009	0.252	101.9	77.4	0.032	0.025
3	10	0.00293	3300	2433	667482	766542	0.0010	0.336	101.9	77.8	0.048	0.043
4	14	0.00259	4262	3961	962475	1041535	0.0010	0.375	101.9	77.2	0.062	0.054
5	18	0.00241	5362	4923	1237464	1316528	0.0010	0.420	101.6	77.7	0.078	0.072
6	22	0.00232	6256	5846	1512460	1591521	0.0010	0.413	101.8	77.7	0.091	0.085
7	26	0.00225	7081	6739	1767453	1866514	0.0010	0.432	101.8	77.7	0.103	0.094
8	30	0.00213	8112	7609	2067446	2146506	0.0010	0.455	101.9	78.2	0.118	0.111
9	34	0.00207	9075	8452	2337439	2416499	0.0009	0.458	101.8	77.1	0.132	0.123
10	38	0.00203	9900	9276	2617431	2696492	0.0009	0.465	101.8	77.4	0.144	0.135
11	42	0.00196	10793	10091	2887424	2966485	0.0010	0.512	101.9	77.9	0.157	0.147
12	46	0.00199	11550	10892	3167417	3246477	0.0009	0.440	101.8	78.8	0.168	0.158
13	50	0.00192	12443	11678	3437410	3516470	0.0009	0.486	101.8	77.8	0.181	0.170
14	54	0.00189	13337	12473	3712403	3791463	0.0010	0.544	101.8	78.0	0.194	0.181
15	58	0.00185	14093	13260	3987395	4066456	0.0010	0.517	101.8	76.8	0.205	0.193
16	62	0.00182	14916	14037	4262388	4341449	0.0010	0.560	101.9	78.0	0.217	0.208
17	66	0.00142	15675	14814	4537381	4616441	0.0010	0.547	101.9	77.6	0.228	0.215
18	70	0.00193	16500	15574	4812374	4891434	0.0009	0.505	101.9	77.4	0.240	0.227
19	74	0.00183	17325	16339	5087366	5166427	0.0009	0.512	101.8	77.7	0.252	0.234
20	78	0.00178	18150	17092	5362359	5441420	0.0009	0.525	101.8	77.2	0.264	0.249
21	82	0.00172	18906	17833	5637352	5716412	0.0010	0.561	101.7	77.0	0.275	0.259
22	86	0.00171	19662	18569	5912345	5991405	0.0010	0.560	101.7	77.6	0.286	0.270
23	90	0.00174	20418	19311	6187337	6266398	0.0010	0.564	101.7	78.6	0.297	0.281
24	94	0.00157	21174	20032	6462330	6541391	0.0010	0.610	101.6	78.6	0.308	0.291

SKIN FRIC COEFF AND VIRTUAL ORIGIN FROM CURVE FIT TO MOM TH MEASUREMENTS
 CURVE FIT THETA= 0.0059*(X-X0)+ 0.8683 VIR ORIG(X)= -1.154 INCH

PL	X	DIS TH	MOM TH	SHAPE	X-X0	MOM TH	DIFF	CF2	CF2	RATIO	ROUGH
NO	IN	INCH	INCH	FACTOR	INCH	(FIT)	INCH	(FIT)	SMOOTH		RE NO
1	2	0.0278	0.0115	2.4264							
2	6	0.0527	0.0317	1.6633							
3	10	0.0784	0.0480	1.6321	11.15	0.0461	0.0001	0.0027	0.0013	2.10	112.91
5	18	0.1213	0.0770	1.5753	19.15	0.0770	-0.0006	0.0025	0.0014	2.20	107.53
8	30	0.1870	0.1179	1.5870	31.15	0.1174	-0.0004	0.0022	0.0010	2.30	102.79
12	46	0.2602	0.1660	1.5487	47.15	0.1663	0.0003	0.0021	0.0008	2.38	98.42
16	62	0.3296	0.2167	1.5210	63.15	0.2169	0.0002	0.0020	0.0008	2.44	96.05
20	78	0.3767	0.2641	1.5024	79.15	0.2639	-0.0002	0.0015	0.0007	2.49	93.93

STANTON RUN 8/27/73 V=139 FT/SEC F=0.002
 VEL=136.7 FT/SEC T= 76.5 DEGF TO= 78.0 DEGF RHO=0.0739 LBS/FT³ P= 14.70 PSI
 TDB= 78.0 DEGF TWH= 65.0 DEGF PAMB= 29.87 IN HG VIR ORIG.XO= -1.38 IN

PL	X	STN	MOM	ENTH	X	(X-XO)	F	B	TPL	DEGF	DEGF	INCH	ENTH
NO	INCH	NO	REYNO	REYNO	REYNO	REYNO							
1	2	0.00288	955	654	136365	230457	0.0019	0.664	99.4	77.9	0.014	0.010	
2	6	0.00329	2591	2018	409096	503188	0.0019	0.583	99.3	77.4	0.038	0.030	
3	10	0.00254	3545	3337	681026	775418	0.0019	0.752	99.3	77.0	0.052	0.049	
4	14	0.00219	4841	457	954557	1048649	0.0019	0.885	99.2	77.2	0.071	0.066	
5	18	0.00201	6000	5615	1227287	1321379	0.0020	0.992	99.3	77.6	0.088	0.082	
6	22	0.00190	7091	6688	1500018	1594110	0.0020	1.033	99.2	77.6	0.104	0.098	
7	26	0.00185	8182	7730	1772748	1866640	0.0019	1.043	99.2	77.7	0.120	0.113	
8	30	0.00176	9273	8745	2045478	2139571	0.0019	1.085	99.3	77.8	0.136	0.128	
9	34	0.00171	10364	9737	2318209	2412301	0.0019	1.111	99.4	77.0	0.152	0.143	
10	38	0.00168	11386	10718	2590939	2685031	0.0019	1.139	99.5	77.2	0.167	0.157	
11	42	0.00156	12341	11691	2863670	2957762	0.0020	1.274	99.3	77.7	0.181	0.171	
12	46	0.00167	13364	12639	3136400	3230492	0.0017	1.047	99.5	78.7	0.196	0.185	
13	50	0.00155	14318	13573	3409131	3503223	0.0019	1.217	99.3	77.7	0.210	0.199	
14	54	0.00150	15273	14516	3681861	3775953	0.0020	1.319	99.2	77.7	0.224	0.213	
15	58	0.00147	16227	15443	3954592	4048684	0.0019	1.260	99.3	76.8	0.238	0.226	
16	62	0.00147	17182	16365	4227322	4321414	0.0020	1.333	99.4	77.8	0.252	0.240	
17	66	0.00143	18137	17301	4500053	4594145	0.0020	1.394	99.3	77.6	0.266	0.254	
18	70	0.00145	19023	18228	4772783	4866875	0.0019	1.331	99.4	77.6	0.279	0.267	
19	74	0.00140	20046	19139	5045514	5139606	0.0019	1.350	99.3	77.5	0.294	0.281	
20	78	0.00139	20932	20035	5318244	5412336	0.0019	1.360	99.4	77.0	0.307	0.294	
21	82	0.00136	21818	20923	5590974	5685066	0.0019	1.382	99.4	76.8	0.320	0.307	
22	86	0.00133	22773	21803	5863705	5957797	0.0019	1.405	99.3	77.3	0.334	0.320	
23	90	0.00134	23659	22689	6136435	6230527	0.0019	1.449	99.4	77.9	0.347	0.333	
24	94	0.00121	24546	23560	6409166	6503258	0.0019	1.568	99.4	78.0	0.360	0.346	

SKIN FRI COEFF AND VIRTUAL ORIGIN FROM CURVE FIT TO MOM TH MEASUREMENTS
 CURVE FIT THETA= 0.0060*(X-XO)** 0.8495 + VIR ORIGIN(XO)= -1.383 INCHES

PL	X	DIS TH	MOM TH	SHAPE	X-XO	MOM TH	DIFF	CF2	CF2	RATIO	ROUGH
NO	IN	INCH	INCH	FACTOR	INCH (FIT)	INCH	(FIT)	SMOOTH			RE NO
1	2	0.0295	0.0135	2.1785							
2	6	0.0651	0.0384	1.6944							
3	10	0.0870	0.0524	1.6611	11.38	0.0537	0.0013	0.00225	0.00103	2.18	101.00
5	18	0.1462	0.0898	1.6281	19.38	0.0867	-0.0031	0.00202	0.00085	2.39	95.90
8	30	0.2114	0.1311	1.6127	31.38	0.1338	0.0027	0.00183	0.00074	2.50	91.28
12	46	0.3072	0.1959	1.5686	47.38	0.1938	-0.0021	0.00168	0.00062	2.67	87.53
16	62	0.3872	0.2496	1.5511	63.38	0.2517	0.0021	0.00157	0.00057	2.75	83.38
20	78	0.4741	0.3091	1.5335	79.38	0.3082	-0.0009	0.00149	0.00052	2.84	79.38

STANTON RUN 8/27/73 V=139 FT/SEC F=0.004
 VEL=135.3 FT/SEC T= 77.3 DEGF TO= 78.8 DEGF RHO=0.0738 LBS/FT³ P= 14.71 PSI
 TDB= 77.0 DEGF TWH= 65.0 DEGF PAMB= 29.87 IN HG VIR ORIG.XO= -1.68 IN

PL	X	STN	MOM	ENTH	X	(X-XO)	F	B	TPL	DEGF	DEGF	INCH	ENTH
NO	INCH	NO	REYNO	REYNO	REYNO	REYNO							
1	2	0.00246	1212	835	134622	247705	0.0037	1.527	101.6	78.4	0.018	0.012	
2	5	0.00266	3029	2547	403867	516950	0.0039	1.452	101.4	78.0	0.045	0.038	
3	10	0.00185	4712	4185	673112	786195	0.0038	2.052	101.4	77.8	0.070	0.062	
4	14	0.00157	6260	5662	942356	1055439	0.0038	2.384	101.5	77.4	0.093	0.084	
5	18	0.00140	7808	7095	1211601	1324684	0.0039	2.796	101.4	78.2	0.116	0.105	
6	22	0.00130	9222	8514	1480846	1593929	0.0039	3.017	101.4	78.1	0.137	0.126	
7	26	0.00118	10635	9897	1750091	1863173	0.0039	3.283	101.3	77.9	0.158	0.147	
8	30	0.00111	12049	11248	2019335	2132418	0.0039	3.481	101.2	78.0	0.179	0.167	
9	34	0.00112	13395	12572	2288580	2401663	0.0037	3.326	101.2	77.3	0.199	0.187	
10	38	0.00108	14674	13868	2557825	2670908	0.0037	3.406	101.2	77.5	0.218	0.206	
11	42	0.00100	16020	15173	2827069	2940152	0.0039	3.921	101.2	77.9	0.238	0.225	
12	46	0.00108	17249	16424	3096314	3209397	0.0033	3.037	101.2	78.4	0.257	0.244	
13	50	0.00102	18645	17652	3365559	3478642	0.0038	3.682	101.4	77.4	0.277	0.262	
14	54	0.00092	19991	18960	3634804	3747886	0.0040	4.359	101.1	77.8	0.297	0.282	
15	58	0.00088	21338	20255	3904048	4017131	0.0038	4.289	101.3	77.4	0.317	0.301	
16	62	0.00089	22684	21519	4173293	4286376	0.0038	4.329	101.4	78.0	0.337	0.320	
17	66	0.00086	24030	22801	4442538	4555620	0.0039	4.588	101.4	77.9	0.357	0.339	
18	70	0.00081	25376	24089	4711782	4824865	0.0039	4.849	101.4	77.9	0.377	0.358	
19	74	0.00084	26723	25365	4981027	5094110	0.0038	4.294	101.4	78.1	0.397	0.377	
20	78	0.00081	28001	26629	5250272	5363354	0.0039	4.784	101.4	77.6	0.416	0.396	
21	2	0.00078	29348	27878	5519516	5632599	0.0038	4.886	101.3	77.5	0.436	0.414	
22	6	0.00075	30694	29118	5788761	5901844	0.0039	5.144	101.3	77.8	0.456	0.433	
23	10	0.00077	32040	30379	6058006	6171089	0.0040	5.167	101.4	78.2	0.476	0.451	
24	94	0.00069	33319	31628	6327250	6440333	0.0038	5.594	101.4	78.3	0.495	0.470	

SKIN FRI COEFF AND VIRTUAL ORIGIN FROM CURVE FIT TO MOM TH MEASUREMENTS
 CURVE FIT THETA= 0.0074*(X-XO)** 0.9208 + VIR ORIGIN(XO)= -1.677 INCHES

PL	X	DIS TH	MOM TH	SHAPE	X-XO	MOM TH	DIFF	CF2	CF2	RATIO	ROUGH
NO	IN	INCH	INCH	FACTOR	INCH (FIT)	INCH	(FIT)	SMOOTH			RE NO
1	2	0.0405	0.0176	2.2968							
2	6	0.0744	0.0447	1.6631							
3	10	0.1176	0.0699	1.6814	11.68	0.0709	0.0010	0.00184	0.00064	2.89	92.01
5	18	0.1995	0.1159	1.7207	19.68	0.1147	-0.0013	0.00162	0.00051	3.18	86.18
8	30	0.3044	0.1788	1.7028	31.68	0.1778	-0.0010	0.00142	0.00042	3.41	80.71
12	46	0.4298	0.2574	1.6698	47.68	0.2591	0.0017	0.00125	0.00035	3.59	75.88
16	62	0.5584	0.3381	1.6517	63.68	0.3382	0.0001	0.00114	0.00031	3.73	72.37
20	78	0.6819	0.4162	1.6384	79.68	0.4157	-0.0005	0.00105	0.00020	3.84	69.59

STANTON RUN 6/1/73 NO BLOW V=190 FT/SEC
 VEL=191.0 FT/SEC T= 78.1 DEGF TO= 81.1 DEGF RHO=0.0732 LBS/FT3 P= 14.62 PSI
 TDB= 80.5 DEGF TWU= 65.0 DEGF PAMU= 29.69 IN HG VIR ORIG.XO= -2.69 IN

PL	X	STN	MOM	ENTH	X	(X-XO)	F	B	IFL	TAIR	MOMTH	ENTTH
NO	INCH	NO	REYNO	REYNO	REYNO	REYNO			DEGF	DEGF	INCH	INCH
1	2	0.00421	1414	793	188548	442145	0.	0.	96.1	97.8	0.015	0.008
2	6	0.00378	2422	2295	565644	819241	0.	0.	96.3	100.1	0.031	0.024
3	10	0.00319	3960	3613	942740	1196337	0.	0.	96.3	97.2	0.042	0.038
4	14	0.00293	5374	4766	1319836	1573433	0.	0.	96.3	97.4	0.057	0.051
5	18	0.00276	6505	5857	1696932	1950529	0.	0.	96.4	96.2	0.069	0.062
6	22	0.00268	7542	6861	2074028	2327626	0.	0.	96.3	94.6	0.080	0.073
7	26	0.00256	8673	7848	2451124	2704732	0.	0.	96.4	95.5	0.092	0.085
8	30	0.00247	9616	8797	2828231	3081818	0.	0.	96.4	96.2	0.102	0.095
9	34	0.00244	10559	9723	3205317	3458914	0.	0.	96.4	95.3	0.112	0.103
10	38	0.00236	11501	10629	3587413	3836010	0.	0.	96.5	94.3	0.122	0.113
11	42	0.00230	12444	11509	3959539	4213106	0.	0.	96.5	95.7	0.132	0.122
12	46	0.00232	13387	12380	4336605	4590202	0.	0.	96.5	96.9	0.142	0.131
13	50	0.00226	14330	13243	4713701	4967298	0.	0.	96.5	95.3	0.152	0.140
14	54	0.00222	15178	14089	5090797	5344394	0.	0.	96.5	96.8	0.161	0.149
15	58	0.00219	16121	14923	5467893	5721490	0.	0.	96.5	96.4	0.171	0.158
16	62	0.00221	17064	15752	5844989	6098586	0.	0.	96.5	95.6	0.181	0.167
17	66	0.00212	17912	16568	6222085	6475682	0.	0.	96.5	94.3	0.190	0.176
18	70	0.00217	18761	17378	6599181	6852778	0.	0.	96.5	95.1	0.199	0.184
19	74	0.00211	19609	18184	6976277	7229874	0.	0.	96.5	94.3	0.208	0.193
20	78	0.00209	20457	18977	7353373	7606970	0.	0.	96.4	94.7	0.217	0.201
21	82	0.00206	21306	19761	7730469	7984067	0.	0.	96.5	95.1	0.226	0.210
22	86	0.00208	22154	20542	8107565	8361163	0.	0.	96.4	96.2	0.235	0.218
23	90	0.00204	23003	21318	8484661	8738259	0.	0.	96.6	96.6	0.244	0.226
24	94	0.00213	23851	22105	8861757	9115355	0.	0.	96.6	98.1	0.253	0.234

SKIN FRI COEFF AND VIRTUAL ORIGIN FROM CURVE FIT TO MOM TH MEASUREMENTS
 CURVE FIT THETA= 0.0053*(X-XO)** 0.8456 +VIR ORIG(XO)= -2.694 INCHES

PL	X	DIS TH	MOM TH	SHAPE	X-XO	MOM TH	DIFF	CF2	CF2	RATIO	ROUGH
NO	IN	INCH	INCH	FACTOR	INCH (FIT)	INCH (FIT)	INCH (FIT)	SMOOTH	SMOOTH	RE NO	
0	0	0.0107	0.0059	1.8188							
1	2	0.0270	0.0149	1.8138							
2	6	0.0521	0.0306	1.7029							
4	14	0.0930	0.0574	1.6207	16.69	0.0575	0.0001	0.00291	0.00146	2.00	159.89
6	22	0.1246	0.0802	1.5536	24.69	0.0800	-0.0002	0.00274	0.00134	2.05	155.13
9	34	0.1699	0.1120	1.5173	36.69	0.1119	-0.0001	0.00258	0.00123	2.09	150.46
12	46	0.2143	0.1417	1.5117	48.69	0.1421	0.0004	0.00247	0.00116	2.12	147.21
16	62	0.2691	0.1811	1.4862	64.69	0.1807	-0.0003	0.00236	0.00104	2.16	144.02
20	78	0.3198	0.2178	1.4688	80.69	0.2179	0.0001	0.00228	0.00104	2.19	141.56

STANTON RUN 8/28/73 V=190 FT/SEC F=0.001
 VEL=190.8 FT/SEC T= 70.6 DEGF TO= 79.6 DEGF RHO=0.0737 LBS/FT3 P= 14.67 PSI
 TDB= 87.0 DEGF TWU= 68.0 DEGF PAMU= 29.79 IN HG VIR ORIG.XO= -2.20 IN

PL	X	STN	MOM	ENTH	X	(X-XO)	F	B	IFL	TAIR	MOMTH	ENTTH
NO	INCH	NO	REYNO	REYNO	REYNO	REYNO			DEGF	DEGF	INCH	INCH
1	2	0.00356	1519	853	189668	398722	0.0009	0.262	98.2	80.1	0.016	0.009
2	6	0.00320	3418	2490	569603	778458	0.0009	0.292	97.9	78.7	0.036	0.026
3	10	0.00271	4842	3970	949359	1158193	0.0009	0.350	97.4	78.3	0.051	0.042
4	14	0.00245	6266	5315	1329074	1537929	0.0010	0.390	98.0	78.4	0.066	0.056
5	18	0.00226	7595	6500	1708810	1917664	0.0010	0.440	98.1	78.9	0.080	0.069
6	22	0.00221	8829	7745	2088545	2297400	0.0009	0.421	98.1	79.2	0.093	0.082
7	26	0.00220	10063	8986	2468281	2677135	0.0009	0.427	98.1	79.3	0.106	0.095
8	30	0.00208	11297	10155	2848016	3056871	0.0009	0.455	98.0	79.4	0.119	0.107
9	34	0.00206	12531	11297	3227752	3436606	0.0009	0.450	98.0	78.5	0.132	0.119
10	38	0.00200	13765	12420	3607487	3816342	0.0009	0.463	98.0	78.7	0.145	0.131
11	42	0.00189	14905	13523	3987223	4196077	0.0010	0.522	98.1	79.2	0.157	0.142
12	46	0.00193	15949	14624	4366958	4575013	0.0010	0.512	98.0	80.2	0.168	0.154
13	50	0.00185	17088	15707	4746694	4955548	0.0009	0.499	98.0	78.7	0.180	0.165
14	54	0.00185	18227	16776	5126429	5335284	0.0010	0.539	97.9	78.6	0.192	0.177
15	58	0.00186	19367	17845	5506165	5715019	0.0009	0.492	97.9	77.9	0.204	0.188
16	62	0.00178	20506	18902	5885900	6094755	0.0010	0.562	98.0	79.0	0.216	0.194
17	66	0.00176	21645	19953	6265635	6474490	0.0010	0.559	98.0	78.6	0.228	0.210
18	70	0.00163	22689	20994	6645371	6854225	0.0009	0.499	98.0	78.9	0.234	0.221
19	74	0.00177	23733	22022	7025106	7233961	0.0009	0.511	98.0	79.1	0.250	0.232
20	78	0.00171	24778	23029	7404842	7613696	0.0009	0.536	98.0	78.4	0.261	0.243
21	82	0.00170	25822	24025	7784577	7993432	0.0009	0.541	98.0	78.4	0.272	0.253
22	86	0.00166	26866	25014	8164313	8373167	0.0009	0.555	98.1	79.1	0.283	0.263
23	90	0.00172	27911	26012	8544048	8752403	0.0009	0.553	98.1	79.8	0.294	0.274
24	94	0.00150	28860	26978	8923784	9132638	0.0009	0.619	98.1	80.3	0.304	0.284

SKIN FRI COEFF AND VIRTUAL ORIGIN FROM CURVE FIT TO MOM TH MEASUREMENTS
 CURVE FIT THETA= 0.0060*(X-XO)** 0.8601 +VIR ORIG(XO)= -2.203 INCHES

PL	X	DIS TH	MOM TH	SHAPE	X-XO	MOM TH	DIFF	CF2	CF2	RATIO	ROUGH
NO	IN	INCH	INCH	FACTOR	INCH (FIT)	INCH (FIT)	INCH (FIT)	SMOOTH	SMOOTH	RE NO	
0	0	0.0101	0.0056	1.8165							
1	2	0.0297	0.0167	1.7841							
2	6	0.0614	0.0355	1.7275							
4	14	0.1082	0.0662	1.6746	16.20	0.0660	-0.0002	0.00254	0.00108	2.36	153.55
6	22	0.1486	0.0929	1.5995	24.20	0.0932	0.0003	0.00235	0.00097	2.42	147.67
9	34	0.2056	0.1317	1.5606	36.20	0.1317	-0.0000	0.00217	0.00087	2.50	141.86
12	46	0.2568	0.1682	1.5264	48.20	0.1685	0.0003	0.00205	0.00080	2.56	137.78
16	62	0.3263	0.2163	1.5180	64.20	0.2156	-0.0007	0.00193	0.00074	2.62	133.75
20	78	0.3828	0.2608	1.4833	80.20	0.2611	0.0003	0.00184	0.00069	2.66	130.64

STANTON RUN 8/28/73 V=190 FT/SLC F=0.002
 VEL=189.7 FT/SLC I= 77.3 DEGF TO= 80.3 DEGF RHO=0.0736 LBS/FT3 P= 14.67 PSI
 TDB= 86.0 DLGF TWB= 67.0 DLGF PAMB= 29.79 IN HG VIR ORIG X0= -3.55 IN

PL	X	STN	MOM	ENTH	X	(X-X0)	F	B	TPL	TATR	MOMTH	ENTH
NO	INCH	NO	REYNO	REYNO	REYNO	REYNO			DLGF	DLGF	INCH	INCH
1	2	0.00314	1601	966	188361	522701	0.0020	0.634	98.6	79.6	0.017	0.010
2	6	0.00291	3579	2865	565082	899422	0.0020	0.704	98.7	78.9	0.038	0.030
3	10	0.00252	5274	4618	941803	1276143	0.0020	0.873	98.8	78.4	0.056	0.049
4	14	0.00206	6875	6205	1316524	1652064	0.0020	0.979	98.8	78.6	0.073	0.066
5	18	0.00189	8476	7727	1695245	2029585	0.0021	1.114	98.8	79.1	0.090	0.082
6	22	0.00180	9983	9214	2071967	2406307	0.0021	1.159	98.8	79.2	0.106	0.098
7	26	0.00181	11396	10671	2448688	2783028	0.0020	1.130	98.8	79.3	0.121	0.113
8	30	0.00168	12903	12098	2829409	3159749	0.0021	1.222	98.8	79.3	0.137	0.128
9	34	0.00164	14221	13491	3202130	3536470	0.0020	1.232	98.9	78.5	0.151	0.143
10	38	0.00160	15728	14859	3578851	3913191	0.0020	1.250	98.9	78.7	0.167	0.158
11	42	0.00148	17047	16215	3955573	4289913	0.0021	1.437	98.5	79.2	0.181	0.172
12	46	0.00152	18459	17578	4332294	4666634	0.0021	1.394	98.7	79.7	0.196	0.187
13	50	0.00146	19778	18914	4709015	5043355	0.0020	1.361	98.6	78.8	0.210	0.201
14	54	0.00144	21191	20232	5085736	5420076	0.0021	1.462	98.6	78.8	0.225	0.215
15	58	0.00142	22509	21540	5462457	5796797	0.0020	1.393	98.7	78.4	0.239	0.229
16	62	0.00142	23922	22836	5839179	6173519	0.0021	1.456	98.7	79.3	0.254	0.242
17	66	0.00139	25240	24147	6215900	6550240	0.0021	1.513	98.6	79.3	0.268	0.256
18	70	0.00139	26653	25455	6592621	6926961	0.0021	1.498	98.6	79.2	0.283	0.270
19	74	0.00131	28066	26738	6969342	7303682	0.0020	1.553	98.8	79.4	0.298	0.284
20	78	0.00132	29384	27995	7346063	7680403	0.0020	1.530	98.8	78.9	0.312	0.297
21	82	0.00129	30797	29242	7722784	8057125	0.0020	1.541	98.8	78.7	0.327	0.310
22	86	0.00126	32115	30400	8094506	8433846	0.0020	1.618	98.8	79.2	0.341	0.324
23	90	0.00128	33528	31732	8476227	8810567	0.0021	1.626	98.8	79.8	0.356	0.337
24	94	0.00109	34941	32950	8852948	9187288	0.0020	1.847	98.9	80.2	0.371	0.350

SKIN FRI COEFF AND VIRTUAL ORIGIN FROM CURVE FIT TO MOM TH MEASUREMENTS
 CURVE FIT THETA= 0.0050*(X-X0)** 0.9390 VIR ORIG(X0)= -3.548 INCHES

PL	X	IS	TH	MOM	TH	SHAPE	X-X0	MOM	TH	DIFF	CF2	RATIO	ROUGH
NO	IN	INCH	INCH	FACTOR	INCH	(FIT)	INCH	(FIT)	SMOOTH	RE	NO		
0	0	0.0102	0.0055	1.8623									
1	2	0.0286	0.0165	1.7361									
2	6	0.0666	0.0383	1.7303									
4	14	0.1194	0.0725	1.6466	17.55	0.0736	0.0011	0.00204	0.00082	2.47	137.09		
6	22	0.1723	0.1060	1.6250	25.55	0.1047	-0.0013	0.00195	0.00071	2.73	134.05		
9	34	0.2407	0.1509	1.5945	37.55	0.1503	-0.0006	0.00186	0.00062	2.98	130.95		
12	46	0.3043	0.1955	1.5564	49.55	0.1951	-0.0004	0.00180	0.00056	3.18	128.71		
16	62	0.3885	0.2511	1.5471	65.55	0.2537	0.0026	0.00173	0.00051	3.40	126.45		
20	78	0.4774	0.3128	1.5259	81.55	0.3114	-0.0014	0.00169	0.00047	3.61	124.68		

STANTON RUN 8/29/73 V=190 FT/SLC F=0.004
 VEL=190.4 FT/SLC I= 78.0 DEGF TO= 81.0 DEGF RHO=0.0734 LBS/FT3 P= 14.60 PSI
 TDB= 84.0 DLGF TWB= 68.0 DLGF PAMB= 29.76 IN HG VIR ORIG X0= -7.70 IN

PL	X	STN	MOM	ENTH	X	(X-X0)	F	B	TPL	TATR	MOMTH	ENTH
NO	INCH	NO	REYNO	REYNO	REYNO	REYNO			DLGF	DLGF	INCH	INCH
1	2	0.00274	1696	1224	108448	442853	0.0038	1.370	97.7	79.7	0.018	0.013
2	6	0.00225	4334	3547	565344	819749	0.0039	1.713	97.8	79.2	0.046	0.038
3	10	0.00170	6596	5773	942240	1196645	0.0037	2.205	97.8	78.8	0.070	0.061
4	14	0.00146	8669	7787	1319136	1573541	0.0038	2.594	97.6	78.9	0.092	0.083
5	18	0.00130	10553	9755	1696032	1950437	0.0039	3.001	97.6	79.3	0.112	0.104
6	22	0.00125	12532	11685	2072924	2327333	0.0038	3.021	97.7	79.5	0.135	0.124
7	26	0.00117	14416	13575	2449625	2704224	0.0038	3.277	97.8	79.6	0.153	0.144
8	30	0.00108	16207	15437	2826721	3081125	0.0038	3.514	97.8	79.5	0.172	0.164
9	34	0.00106	18091	17269	3203617	3458022	0.0038	3.573	97.7	79.0	0.192	0.183
10	38	0.00107	19881	19097	3580513	3834918	0.0038	3.545	97.7	79.2	0.211	0.203
11	42	0.00099	21766	20905	3957409	4211814	0.0037	3.783	97.7	79.6	0.231	0.222
12	46	0.00107	23650	22696	4334305	4588710	0.0037	3.613	97.8	79.8	0.251	0.241
13	50	0.00099	25440	24475	4711201	4965606	0.0037	3.869	97.9	79.9	0.270	0.260
14	54	0.00090	27231	26251	5088097	5342502	0.0039	4.320	97.9	79.9	0.289	0.279
15	58	0.00097	29021	28023	5464993	5719398	0.0037	3.765	97.8	79.5	0.308	0.297
16	62	0.00098	30811	29821	5841889	6096294	0.0039	3.998	97.7	80.1	0.327	0.316
17	66	0.00082	32696	31627	6218785	6473190	0.0039	4.708	97.9	79.9	0.347	0.336
18	70	0.00083	34580	33595	6595681	6850086	0.0039	4.678	97.8	79.8	0.367	0.354
19	74	0.00085	36370	35168	6972577	7226982	0.0039	4.672	97.6	79.7	0.386	0.373
20	78	0.00080	38255	36945	7349473	7603878	0.0039	4.904	97.6	79.3	0.406	0.392
21	82	0.00075	40139	38711	7726370	7980774	0.0038	4.441	97.6	79.1	0.426	0.411
22	86	0.00084	41930	40503	8103266	8357671	0.0040	4.785	97.4	79.5	0.445	0.430
23	90	0.00079	43720	42289	8480162	8734567	0.0038	4.862	97.7	79.8	0.464	0.449
24	94	0.00064	45604	43944	8857058	9111463	0.0038	5.873	97.7	80.0	0.484	0.467

SKIN FRI COEFF AND VIRTUAL ORIGIN FROM CURVE FIT TO MOM TH MEASUREMENTS
 CURVE FIT THETA= 0.0066*(X-X0)** 0.9375 VIR ORIG(X0)= -2.697 INCHES

PL	X	IS	TH	MOM	TH	SHAPE	X-X0	MOM	TH	DIFF	CF2	RATIO	ROUGH
NO	IN	INCH	INCH	FACTOR	INCH	(FIT)	INCH	(FIT)	SMOOTH	RE	NO		
0	0	0.0117	0.0061	1.9244									
1	2	0.0302	0.0183	1.6531									
2	6	0.0785	0.0462	1.6987									
4	14	0.1678	0.0921	1.7132	16.70	0.0920	-0.0001	0.00137	0.00048	2.84	169.45		
6	22	0.2252	0.1326	1.6956	25.70	0.1328	0.0000	0.00124	0.00041	3.06	164.79		
9	34	0.3194	0.1920	1.6636	36.70	0.1926	0.0006	0.00112	0.00034	3.30	159.45		
12	46	0.4116	0.2514	1.6334	48.70	0.2518	-0.0004	0.00103	0.00030	3.48	155.54		
16	62	0.5331	0.3271	1.6246	64.70	0.3277	0.0005	0.00095	0.00020	947.87	91.52		
18	70	0.6061	0.3657	1.6574	72.70	0.3655	-0.0002	0.00091	0.00020	913.40	89.84		

STANTON RUN 5/19/73 NO BLOW V=242 FT/SEC
 VEL=242.4 FT/SEC T= 87.3 DEGF TO= 92.1 DEGF RHO=0.0724 LBS/FT3 P= 14.70 PSI
 TDB= 83.0 DEGF TWH= 68.0 DEGF PAMU= 29.87 IN HG VIR ORIG X0= -2.24 IN

PL	X	STN	MOM	ENTH	X	(X-X0)	F	B	TPL	TAIR	MOMTH	ENTH
NO	INCH	NO	REYNO	REYNO	REYNO	REYNO			DEGF	DEGF	INCH	INCH
1	2	0.00438	1517	1022	233419	494847	0.	0.	105.8	107.0	0.013	0.009
2	6	0.00359	3385	2881	700256	961685	0.	0.	105.7	110.5	0.029	0.025
3	10	0.00310	5018	4441	1167093	1428522	0.	0.	105.9	106.4	0.043	0.038
4	14	0.00286	6536	5831	1633930	1895359	0.	0.	106.0	106.7	0.056	0.050
5	18	0.00269	8053	7125	2100767	2362196	0.	0.	105.9	105.3	0.069	0.061
6	22	0.00253	9337	8344	2567604	2829033	0.	0.	105.8	103.3	0.080	0.071
7	26	0.00250	10737	9518	3034441	3295870	0.	0.	105.9	103.8	0.092	0.082
8	30	0.00234	11904	10648	3501279	3762707	0.	0.	105.8	104.4	0.102	0.091
9	34	0.00236	13188	11746	3968116	4229544	0.	0.	105.9	103.2	0.113	0.101
10	38	0.00230	14355	12834	4434953	4696382	0.	0.	105.9	102.0	0.123	0.110
11	42	0.00224	15522	13893	4901790	5163219	0.	0.	105.9	104.0	0.133	0.119
12	46	0.00222	16573	14933	5368627	5630056	0.	0.	105.9	104.9	0.142	0.128
13	50	0.00219	17857	15962	5835464	6096893	0.	0.	105.9	103.4	0.153	0.137
14	54	0.00213	19024	16970	6302301	6563730	0.	0.	105.8	104.7	0.163	0.145
15	58	0.00213	20191	17965	6769138	7030567	0.	0.	105.9	104.8	0.173	0.154
16	62	0.00215	21358	18966	7235976	7497404	0.	0.	105.8	103.8	0.183	0.163
17	66	0.00206	22525	19949	7702813	7964241	0.	0.	105.8	102.7	0.193	0.171
18	70	0.00206	23692	20915	8169650	8431079	0.	0.	105.8	103.5	0.203	0.179
19	74	0.00204	24742	21876	8636487	8897916	0.	0.	105.8	103.5	0.212	0.187
20	78	0.00199	25909	22818	9103324	9364753	0.	0.	105.8	101.8	0.222	0.196
21	82	0.00200	27077	23750	9570161	9831590	0.	0.	105.9	103.4	0.232	0.203
22	86	0.00200	28244	24682	10036998	10298427	0.	0.	105.8	106.0	0.242	0.211
23	90	0.00196	29294	25605	10503635	10765264	0.	0.	105.9	106.1	0.251	0.219
24	94	0.00202	30461	26533	10970271	11232101	0.	0.	105.8	106.8	0.261	0.227

SKIN FRI COEFF AND VIRTUAL ORIGIN FROM CURVE FIT TO MOM TH MEASUREMENTS
 CURVE FIT THETA= 0.0052*(X-X0)** 0.8565 VIR ORIG(X0)= -2.25 INCHES

PL	X	DIS	TH	MOM	TH	SHAPE	X-X0	MOM	TH	DIFF	CF2	CF2	RATIO	ROUGH
NO	IN	INCH	INCH	FACTOR	INCH	(FIT)	INCH	(FIT)	INCH	(FIT)	SMOOTH	RE	NO	
4	14	0.0902	0.0562	1.0057	16.23	0.0564	0.0003	0.00298	0.00139	2.14	200.04			
8	30	0.1574	0.1026	1.5343	32.23	0.1016	-0.0010	0.00270	0.00119	2.26	190.74			
12	46	0.2096	0.1422	1.4737	48.23	0.1434	0.0012	0.00255	0.00110	2.31	185.01			
16	62	0.2680	0.1837	1.4590	64.23	0.1833	-0.0004	0.00244	0.00103	2.37	181.25			
20	78	0.3240	0.2218	1.4608	80.23	0.2218	-0.0001	0.00237	0.00099	2.40	178.38			

STANTON RUN 8/24/73 V=242 FT/SEC F=0.001
 VEL=238.9 FT/SEC T= 77.5 DEGF TO= 82.2 DEGF RHO=0.0735 LBS/FT3 P= 14.60 PSI
 TDB= 78.0 DEGF TWH= 67.0 DEGF PAMU= 29.78 IN HG VIR ORIG X0= -0.61 IN

PL	X	STN	MOM	ENTH	X	(X-X0)	F	B	TPL	TAIR	MOMTH	ENTH
NO	INCH	NO	REYNO	REYNO	REYNO	REYNO			DEGF	DEGF	INCH	INCH
1	2	0.00380	1658	1136	236874	309120	0.0010	0.261	99.5	79.9	0.014	0.010
2	6	0.00300	3908	3216	710621	782867	0.0010	0.330	99.5	78.6	0.033	0.027
3	10	0.00264	5422	5016	1164368	1256615	0.0010	0.371	99.5	78.3	0.050	0.043
4	14	0.00238	7817	6670	1658116	1730362	0.0010	0.418	99.6	78.4	0.066	0.056
5	18	0.00230	9543	8250	2131663	2204194	0.0010	0.437	99.6	79.0	0.081	0.070
6	22	0.00221	11251	9794	2605610	2677857	0.0010	0.454	99.5	79.2	0.095	0.083
7	26	0.00217	12910	11307	3079357	3151604	0.0010	0.462	99.5	79.6	0.109	0.095
8	30	0.00207	14449	12781	3553105	3625351	0.0010	0.479	99.6	79.7	0.122	0.108
9	34	0.00203	16107	14218	4026652	4099099	0.0010	0.482	99.6	78.9	0.136	0.120
10	38	0.00195	17647	15630	4500599	4572846	0.0010	0.518	99.0	79.3	0.149	0.132
11	42	0.00191	19187	17025	4974347	5046593	0.0010	0.531	99.6	79.8	0.162	0.144
12	46	0.00193	20608	18415	5448094	5520341	0.0010	0.523	99.6	80.9	0.174	0.155
13	50	0.00190	22029	19796	5921641	5994088	0.0010	0.523	99.5	79.7	0.186	0.167
14	54	0.00186	23569	21160	6395589	6467835	0.0010	0.544	99.5	79.8	0.197	0.179
15	58	0.00178	24990	22501	6869336	6941582	0.0010	0.571	99.6	79.0	0.211	0.190
16	62	0.00178	26293	23825	7343083	7415330	0.0010	0.571	99.6	80.1	0.222	0.201
17	66	0.00180	27714	25155	7816830	7889077	0.0010	0.567	99.5	79.8	0.234	0.212
18	70	0.00178	29135	26483	8290578	8362824	0.0010	0.569	99.6	79.9	0.246	0.224
19	74	0.00177	30557	27804	8764325	8836571	0.0010	0.575	99.5	79.7	0.258	0.235
20	78	0.00171	31978	29106	9238072	9310319	0.0010	0.585	99.5	78.9	0.270	0.246
21	82	0.00168	33399	30385	9711619	9784066	0.0010	0.599	99.6	78.6	0.282	0.257
22	86	0.00164	34820	31694	10185567	10257813	0.0010	0.615	99.6	79.0	0.294	0.267
23	90	0.00166	36123	32911	10659314	10731561	0.0010	0.610	99.7	79.8	0.305	0.278
24	94	0.00136	37544	34098	11133061	11205308	0.0010	0.719	99.6	80.1	0.317	0.288

SKIN FRI COEFF AND VIRTUAL ORIGIN FROM CURVE FIT TO MOM TH MEASUREMENTS
 CURVE FIT THETA= 0.0069*(X-X0)** 0.8383 VIR ORIG(X0)= -0.612 INCHES

PL	X	DIS	TH	MOM	TH	SHAPE	X-X0	MOM	TH	DIFF	CF2	CF2	RATIO	ROUGH
NO	IN	INCH	INCH	FACTOR	INCH	(FIT)	INCH	(FIT)	INCH	(FIT)	SMOOTH	RE	NO	
2	6	0.0592	0.0339	1.7446	6.61	0.0338	-0.0001	0.00326	0.00124	2.64	207.14			
5	18	0.1336	0.0805	1.6592	18.61	0.0806	0.0001	0.00260	0.00094	2.76	184.46			
8	30	0.1923	0.1220	1.5771	30.61	0.1223	0.0004	0.00232	0.00082	2.82	174.69			
12	46	0.2606	0.1750	1.5236	46.61	0.1740	-0.0010	0.00210	0.00073	2.88	166.20			
16	62	0.3336	0.2221	1.5018	62.61	0.2229	0.0007	0.00195	0.00067	2.91	160.33			
20	78	0.4028	0.2699	1.4923	78.61	0.2697	-0.0002	0.00185	0.00063	2.94	155.84			

STANTON MUN 8/29/73 VE242 FT/SEC F=0.002
 VEL=236.2 FT/SEC T= 78.7 DEGF TO= 83.3 DEGF RHO=0.0733 LBS/FT3 P= 14.65 PSI
 TOB= 83.0 DEGF TMB= 68.0 DEGF PAMB= 29.76 IN HG VIR ORIG X0= -3.65 IN

PL	X	STN	HOM	ENTH	X	(X-X0)	F	B	TPL	TAIR	MOUTH	ENTH
NO	INCH	NO	KEYNO	KEYNO	KEYNO	KEYNO		DEGF	DEGF	INCH	INCH	
1	2	0.00333	1865	1248	233083	658459	0.0020	0.608	101.1	80.5	0.016	0.011
2	6	0.00262	4545	3582	699249	1124625	0.0020	0.775	101.0	80.0	0.039	0.031
3	10	0.00220	6759	5649	1165415	1590791	0.0020	0.918	100.9	79.4	0.058	0.048
4	14	0.00203	8974	7566	1631581	2056957	0.0020	0.979	100.9	79.7	0.077	0.065
5	18	0.00195	10555	9414	2097746	2523123	0.0020	1.010	101.0	80.1	0.094	0.081
6	22	0.00185	12820	11225	2563912	2989289	0.0020	1.086	101.1	80.4	0.110	0.096
7	26	0.00176	14684	13005	3030078	3455454	0.0020	1.150	100.9	80.5	0.126	0.112
8	30	0.00169	16316	14749	3496244	3921620	0.0020	1.192	100.9	80.5	0.140	0.127
9	34	0.00166	18180	16474	3962410	4387786	0.0020	1.229	100.9	79.9	0.156	0.141
10	38	0.00159	19929	18179	4428576	4853952	0.0020	1.279	101.0	80.1	0.171	0.156
11	42	0.00153	21677	19861	4894742	5320118	0.0021	1.356	100.9	80.6	0.186	0.170
12	46	0.00156	23308	21530	5360407	5786284	0.0020	1.279	101.1	81.2	0.200	0.185
13	50	0.00150	24940	23177	5827073	6252450	0.0020	1.334	100.9	80.6	0.214	0.199
14	54	0.00151	26571	24805	6293239	6718616	0.0020	1.308	100.9	80.5	0.228	0.213
15	58	0.00144	28320	26414	6759405	7184781	0.0020	1.373	101.0	80.0	0.243	0.227
16	62	0.00145	29951	28013	7225571	7650947	0.0020	1.371	101.1	80.8	0.257	0.240
17	66	0.00144	31649	29613	7691737	8117113	0.0020	1.390	100.9	80.8	0.272	0.254
18	70	0.00144	33331	31213	8157903	8583279	0.0020	1.390	101.0	80.8	0.286	0.268
19	74	0.00138	35079	32786	8624068	9049445	0.0019	1.403	101.0	80.6	0.301	0.281
20	78	0.00136	36711	34336	9090234	9515611	0.0020	1.458	100.9	80.1	0.315	0.295
21	82	0.00135	38459	35844	9556400	9981776	0.0020	1.486	101.0	79.8	0.330	0.308
22	86	0.00131	40090	37430	10025661	10447942	0.0020	1.506	101.1	80.3	0.344	0.321
23	90	0.00130	41722	38971	10488732	10914108	0.0020	1.536	101.0	80.8	0.358	0.334
24	94	0.00105	43470	40459	10954898	11380274	0.0020	1.893	101.1	81.1	0.373	0.347

SKIN FRI COEFF AND VIRTUAL ORIGIN FROM CURVE FIT TO MOM TAIL MEASUREMENTS
 CURVE FIT THETA= 0.0056*(X-X0)** 0.9166 *VIR ORI(X0)= -3.651 INCHES

PL	X	WIS	TH	MOM	TH	SHAPE	X-X0	MOM	TH	DIFF	CF2	CF2	RATIO	ROUGH
NO	IN	INCH	INCH	FACTOR	INCH	(FIT)	INCH	(FIT)	SMOOTH	RE NO				
0	0	0.0164	0.0036	4.5358										
4	14	0.1225	0.0771	1.5894	17.65	0.0773	0.0002	0.00201	0.00074	2.73	161.36			
8	30	0.2233	0.1401	1.5943	33.65	0.1346	-0.0004	0.00180	0.00058	3.08	152.70			
12	46	0.3038	0.1995	1.5475	44.65	0.1994	-0.0001	0.00168	0.00051	3.32	147.47			
16	62	0.3951	0.2569	1.5381	65.65	0.2576	0.0000	0.00160	0.00046	3.49	143.71			
20	78	0.4818	0.3150	1.5292	81.65	0.3146	-0.0004	0.00153	0.00042	3.65	140.76			

VELOCITY PROFILES WITH BLOWING AT 32 FT/SEC

F S VEL	34.95 FT/SEC	35.32 FT/SEC	34.59 FT/SEC	33.53 FT/SEC	32.88 FT/SEC
BLO FR	0.	0.001	0.002	0.004	0.008
STAT TLMP	76.40 DEG	74.80 DEG	75.10 DEG	68.10 DEG	75.80 DEG
STAT PRES	14.630 PSIA	14.800 PSIA	14.700 PSIA	14.600 PSIA	14.780 PSIA
PORT	8	6	4	3	5
DIST	14 INCH	14 INCH	10 INCH	14 INCH	2 INCH

Y-YTOP	V/VINF	Y-YTOP	V/VINF	Y-YTOP	V/VINF	Y-YTOP	V/VINF	Y-YTOP	V/VINF
0.	0.	0.	0.	0.	0.	0.	0.	0.	0.
0.011	0.412	0.011	0.399	0.011	0.411	0.011	0.360	0.011	0.312
0.012	0.418	0.013	0.413	0.013	0.433	0.012	0.370	0.016	0.341
0.013	0.434	0.015	0.432	0.015	0.457	0.013	0.381	0.026	0.375
0.014	0.438	0.020	0.465	0.017	0.470	0.014	0.386	0.046	0.457
0.015	0.444	0.025	0.496	0.020	0.497	0.015	0.400	0.066	0.445
0.016	0.452	0.030	0.519	0.025	0.519	0.016	0.405	0.091	0.542
0.017	0.460	0.035	0.537	0.030	0.546	0.017	0.415	0.116	0.573
0.018	0.468	0.040	0.553	0.035	0.565	0.018	0.423	0.141	0.602
0.019	0.475	0.045	0.562	0.040	0.579	0.019	0.428	0.166	0.630
0.021	0.486	0.051	0.568	0.045	0.593	0.020	0.433	0.216	0.608
0.023	0.502	0.065	0.604	0.055	0.619	0.022	0.442	0.296	0.727
0.025	0.512	0.075	0.623	0.065	0.636	0.024	0.454	0.366	0.812
0.027	0.521	0.090	0.646	0.075	0.651	0.026	0.463	0.466	0.840
0.032	0.538	0.115	0.678	0.090	0.679	0.028	0.473	0.566	0.931
0.037	0.558	0.140	0.701	0.115	0.719	0.032	0.495	0.666	0.996
0.042	0.579	0.165	0.733	0.140	0.748	0.038	0.509	0.766	0.991
0.047	0.593	0.190	0.757	0.165	0.777	0.048	0.548	0.866	1.000
0.051	0.611	0.215	0.777	0.190	0.804	0.058	0.565		
0.057	0.621	0.265	0.817	0.215	0.828	0.068	0.586		
0.067	0.648	0.315	0.861	0.265	0.873	0.078	0.608		
0.077	0.686	0.365	0.895	0.315	0.913	0.086	0.622		
0.087	0.706	0.415	0.924	0.365	0.943	0.098	0.641		
0.097	0.741	0.465	0.950	0.415	0.964	0.116	0.664		
0.107	0.763	0.565	0.981	0.465	0.981	0.143	0.696		
0.127	0.812	0.665	0.996	0.565	0.998	0.168	0.730		
0.152	0.860	0.765	1.000	0.665	1.000	0.193	0.757		
0.177	0.900					0.218	0.781		
0.202	0.931					0.243	0.806		
0.227	0.951					0.268	0.829		
0.277	0.976					0.293	0.854		
0.327	0.987					0.318	0.875		
0.377	0.995					0.368	0.911		
0.427	0.998					0.418	0.938		
0.477	0.999					0.468	0.960		
0.527	1.000					0.518	0.978		
						0.568	0.986		
						0.618	0.997		
						0.718	1.000		

VELOCITY PROFILES WITH BLOWING AT 90 FT/SEC

F S VEL	90.81FT/SEC	90.471/SEC	89.71FT/SEC	88.82FT/SEC	86.22FT/SEC
BLO FR	0.	0.001	0.002	0.004	0.008
STAT TLMP	76.5DEGF	77.0DEGF	75.0DEGF	76.4DEGF	76.3DEGF
STAT PRES	14.630PSIA	14.650PSIA	14.750PSIA	14.760PSIA	14.770PSIA
PORT	5	3	3	5	2
DIST	18INCH	10INCH	10INCH	10INCH	10INCH
Y-YTOP	V/VINF	Y-YTOP	V/VINF	Y-YTOP	V/VINF
0.	0.	0.	0.	0.	0.
0.011	0.446	0.011	0.458	0.011	0.429
0.013	0.450	0.013	0.468	0.013	0.437
0.015	0.462	0.015	0.481	0.015	0.452
0.017	0.468	0.017	0.494	0.017	0.464
0.020	0.482	0.019	0.505	0.019	0.474
0.025	0.501	0.021	0.517	0.021	0.484
0.030	0.523	0.026	0.538	0.023	0.496
0.035	0.537	0.031	0.560	0.025	0.505
0.040	0.552	0.036	0.576	0.027	0.514
0.045	0.564	0.041	0.593	0.032	0.534
0.055	0.588	0.046	0.605	0.037	0.550
0.065	0.610	0.051	0.621	0.042	0.566
0.075	0.629	0.061	0.644	0.047	0.580
0.090	0.655	0.071	0.669	0.052	0.591
0.115	0.697	0.081	0.692	0.057	0.606
0.140	0.734	0.091	0.710	0.067	0.631
0.165	0.771	0.111	0.748	0.077	0.651
0.190	0.802	0.136	0.793	0.087	0.671
0.215	0.833	0.161	0.830	0.097	0.690
0.265	0.888	0.186	0.866	0.107	0.710
0.315	0.934	0.211	0.896	0.117	0.727
0.365	0.971	0.236	0.925	0.127	0.743
0.415	0.992	0.286	0.969	0.147	0.775
0.465	1.000	0.336	0.990	0.172	0.812
		0.386	0.996	0.197	0.843
		0.436	1.000	0.222	0.876
				0.247	0.905
				0.272	0.931
				0.347	0.979
				0.397	0.992
				0.447	1.000

VELOCITY PROFILES WITH BLOWING AT 139 FT/SEC

F S VEL	139.71FT/SEC	137.631 T/SEC	136.68FT/SEC	135.26FT/SEC	
BLO FR	0.	0.001	0.002	0.004	
STAT TLMP	76.0DEGF	75.9DEGF	76.5DEGF	77.3DEGF	
STAT PRES	14.670PSIA	14.700PSIA	14.700PSIA	14.710PSIA	
PORT	3	3	3	5	
DIST	10INCH	10INCH	10INCH	10INCH	
Y-YTOP	V/VINF	Y-YTOP	V/VINF	Y-YTOP	V/VINF
0.	0.	0.	0.	0.	0.
0.011	0.434	0.011	0.426	0.011	0.410
0.013	0.454	0.013	0.444	0.013	0.419
0.015	0.469	0.015	0.455	0.015	0.426
0.017	0.480	0.017	0.466	0.017	0.445
0.019	0.491	0.022	0.495	0.019	0.460
0.021	0.500	0.027	0.516	0.021	0.467
0.026	0.522	0.032	0.535	0.026	0.488
0.031	0.544	0.037	0.552	0.031	0.507
0.036	0.564	0.047	0.586	0.036	0.528
0.041	0.578	0.057	0.612	0.041	0.547
0.051	0.607	0.067	0.636	0.051	0.577
0.061	0.634	0.077	0.660	0.061	0.603
0.086	0.693	0.092	0.692	0.071	0.629
0.111	0.747	0.117	0.739	0.081	0.651
0.136	0.795	0.142	0.785	0.091	0.674
0.161	0.839	0.167	0.826	0.111	0.714
0.211	0.917	0.192	0.861	0.136	0.759
0.261	0.972	0.217	0.896	0.161	0.792
0.311	0.996	0.267	0.952	0.186	0.824
0.361	0.999	0.317	0.985	0.211	0.855
0.461	1.000	0.367	0.998	0.261	0.912
		0.417	1.000	0.311	0.962
				0.361	0.998
				0.411	1.000

VELOCITY PROFILES WITH BLOWING AT 190 FT/SEC							
F S VEL	191.03 FT/SEC	190.82 FT/SEC	189.74 FT/SEC	190.43 FT/SEC			
BLO FR	0.	0.001	0.002	0.004			
STAT TEMP	78.10 DEG	76.60 DEG	77.30 DEG	78.00 DEG			
STAT PRES	14.620 PSIA	14.670 PSIA	14.670 PSIA	14.660 PSIA			
PORT	2	4	4	4			
DIST	10 INCH	14 INCH	14 INCH	14 INCH			
Y-YTOP	V/VINF	Y-YTOP	V/VINF	Y-YTOP	V/VINF	Y-YTOP	V/VINF
0.	0.	0.	0.	0.	0.	0.	0.
0.011	0.494	0.011	0.410	0.011	0.392	0.011	0.332
0.016	0.529	0.013	0.420	0.013	0.402	0.013	0.339
0.021	0.557	0.015	0.432	0.015	0.411	0.015	0.349
0.026	0.580	0.017	0.438	0.017	0.419	0.017	0.357
0.031	0.603	0.022	0.463	0.019	0.428	0.019	0.366
0.036	0.621	0.027	0.480	0.021	0.437	0.021	0.371
0.046	0.658	0.032	0.495	0.023	0.443	0.023	0.380
0.056	0.692	0.037	0.511	0.025	0.450	0.025	0.387
0.066	0.724	0.042	0.523	0.027	0.458	0.027	0.395
0.076	0.755	0.047	0.535	0.032	0.471	0.032	0.407
0.086	0.783	0.057	0.558	0.037	0.487	0.037	0.424
0.106	0.837	0.067	0.578	0.042	0.498	0.042	0.435
0.131	0.896	0.077	0.597	0.047	0.511	0.047	0.448
0.156	0.944	0.087	0.616	0.052	0.522	0.052	0.457
0.181	0.977	0.097	0.634	0.057	0.533	0.057	0.464
0.206	0.993	0.122	0.673	0.067	0.551	0.067	0.487
0.231	0.999	0.147	0.711	0.077	0.572	0.077	0.506
0.256	1.000	0.172	0.746	0.087	0.588	0.087	0.521
		0.197	0.779	0.097	0.603	0.097	0.538
		0.222	0.812	0.107	0.619	0.107	0.554
		0.272	0.870	0.132	0.654	0.132	0.585
		0.322	0.925	0.157	0.691	0.157	0.618
		0.372	0.964	0.182	0.724	0.182	0.648
		0.422	0.984	0.207	0.758	0.207	0.680
		0.522	1.000	0.232	0.788	0.232	0.708
				0.282	0.846	0.282	0.761
				0.332	0.897	0.332	0.814
				0.382	0.944	0.382	0.864
				0.432	0.977	0.432	0.909
				0.482	0.993	0.482	0.948
				0.582	1.000	0.582	0.990
						0.682	1.000

VELOCITY PROFILES WITH BLOWING AT 242 FT/SEC							
F S VEL	242.42 FT/SEC	238.95 FT/SEC	236.22 FT/SEC				
BLO FR	0.	0.001	0.002				
STAT TEMP	87.30 DEG	77.50 DEG	78.70 DEG				
STAT PRES	14.700 PSIA	14.660 PSIA	14.650 PSIA				
PORT	4	2	4				
DIST	2 INCH	2 INCH	2 INCH				
Y-YTOP	V/VINF	Y-YTOP	V/VINF	Y-YTOP	V/VINF		
0.	0.	0.	0.	0.	0.		
0.011	0.423	0.011	0.464	0.011	0.372		
0.013	0.431	0.016	0.498	0.013	0.372		
0.015	0.444	0.021	0.527	0.015	0.363		
0.020	0.471	0.026	0.569	0.017	0.369		
0.025	0.495	0.036	0.613	0.019	0.379		
0.036	0.515	0.046	0.649	0.021	0.389		
0.036	0.534	0.071	0.723	0.026	0.413		
0.045	0.564	0.096	0.784	0.031	0.437		
0.055	0.590	0.121	0.847	0.036	0.454		
0.065	0.612	0.146	0.900	0.041	0.471		
0.080	0.642	0.196	0.974	0.051	0.500		
0.105	0.687	0.246	0.998	0.061	0.524		
0.130	0.724	0.296	0.999	0.086	0.572		
0.155	0.766	0.346	1.000	0.111	0.613		
0.180	0.802			0.136	0.649		
0.205	0.835			0.161	0.681		
0.255	0.896			0.211	0.742		
0.305	0.946			0.261	0.802		
0.355	0.980			0.311	0.856		
0.405	0.995			0.361	0.906		
0.455	0.999			0.461	0.975		
0.555	1.000			0.561	0.997		
				0.661	0.999		
				0.761	1.000		

APPENDIX F

LISTING OF DATA REDUCTION PROGRAM

The following pages contain a source listing of the data reduction program used to reduce the Stanton number data. The program is written in Fortran IV and employs fixed-field input. Output includes the reduced data and a listing of the raw input data as well. Input requirements and card formats are documented with comment cards in the listing of the DATIN subroutine of the code.

```

C ST DATA REDUCTION PROGRAM FOR ROUGHNESS RIG STANTON NO & ENERGY BAL P.O.S
DIMENSION COND(24),RI(24),TCAST(24),TIN(24),BTIN(24),ELLST(15)
COMMON/DAI/TAIR,PSTAT,SG,PBOX,TPL(24),TCS(12),STR(24),CFM(24)
1,TAR(24),TCFM(24),EH(24),ES(24),KNEXT,MOMEC,XZERU,NST,FHUMT(24),
2,STQ(24),REXO(24),ITAB,TAMB(4),IOUT,IFR,IKHOR
COMMON/DAO/HEX(24),STN(24),BFE(24)
COMMON/HD/TAMBT(4),VAIR,TINF,TZFRH,RHOINF,PSI
COMMON/AMB/PAMB,TDB,TWB,UEHT(18),K1,IENBAL,VAH
COMMON/AFLU/XXX,SCFM
C CONDUCTION LOSS CONSTANTS, EVALUATE 8/25/73
DATA COND/.145,.180,.130,.090,.100,.280,.185,.190,.149,.150,.131,
1.155,.177,.172,.124,.121,.082,.160,.120,.125,.126,.105,.114,.147/
C SHUNT RESISTANCES, CALIBRATED 4/73
DATA RI/3.044,2.966,3.036,2.983,3.032,2.928,2.998,2.984,2.985,
12.984,2.990,2.984,2.986,2.969,2.965,2.967,3.015,2.980,2.957,2.984,
22.966,2.956,3.023,3.020/
C CONSTANTS FOR CORRECTION OF AIR INLET TEMP FOR CASTING TEMP MISMATCH
DATA ATIN/.30,.21,.16,.14,.30,.26,.30,.20,.29,.24,.38,.16,.47,.36,
1.27,.48,.25,.17,.36,.26,.18,.32,.20,.24/
DATA BTIN/.097,.150,.064,.194,.055,.037,.025,.058,.040,.060,.121,
1.076,.076,.040,.029,.078,.038,.097,.030,.000,.026,.043,.050,.020/
IKHOR=-1
24 CALL DATIN
C RH IS ABS HUMIDITY, LBS WATER/LB AIR
RH=.0196919-.000679526*TWB+.91667E-06*TWB**2-.000232*(TDB-TWB)
PRES=PAMB+.850,74/12.
DENCOR=1.-.0075*(TDB-60.)
IF((K1.GT.3).AND.(K1.LT.6))PSTAT=0.
PST=PSTAT/12.*62.3/DENCOR
IF((K1.EQ.3).OR.(K1.EQ.6))PBOX=0.
PUX=PBOX/12.*62.3/DENCOR
CP=0.241*(1+.9*RH)
C C1 IS A CONSTANT USED IN CALC OF ELECT POWER
C1=3.415/3600.*(144./148.)
PR4=0.71*0.4
DO 9 J=1,4
N=3*(J-1)+1
I=6*(J-1)+1
IF((K1.NE.3).AND.(K1.LT.6))CALL EMFT(TAMU(J),TAMBT(J),513)
IF((K1.EQ.3).OR.(K1.EQ.6))TAMBT(J)=TDB
CAS1=(TCS(N+1)+TCS(N))/2.
CAS2=(TCS(N+1)+TCS(N+2))/2.
CAS3=TCS(N)+(TCS(N)-CAS1)/2.
CALL EMFT(CAS3,TCAST(I),563)
CAS4=(TCS(N)+CAS1)/2.
CALL EMFT(CAS4,TCAST(I+1),563)
CAS5=(CAS1+TCS(N+1))/2.
CALL EMFT(CAS5,TCAST(I+2),563)
CAS6=(TCS(N+1)+CAS2)/2.
CALL EMFT(CAS6,TCAST(I+3),563)
CAS7=(CAS2+TCS(N+2))/2.
CALL EMFT(CAS7,TCAST(I+4),563)
CAS8=TCS(N+2)+(TCS(N+2)-CAS2)/2.
9 CALL EMFT(CAS8,TCAST(I+5),563)
C CALC OF FREE STREAM TEMP FROM IC READING
CALL EMFT(TAIR,TINF,563)
RHOINF=(PRES+PST)/(53.35*(TINF+459.6))*(1.-.26*RH)
IF((K1.GT.3).AND.(K1.LT.6))GO TO 12
RCF=.86
VAIR=SQRT(VAR=SG*32.17*62.46/(0.*RHOINF))
VELHD=VAIR*VAIR/(778.*64.34*CP)
C CORRECTION OF FREE STREAM TEMP FOR V-L HEAD
TZFRH=TINF+(1.-RCF)*VELHD
TINF=TINF-RCF*VELHD
RHOOLD=RHOINF
RHOINF=(PRES+PST)/(53.35*(TINF+459.6))*(1.-.26*RH)
PSI=(PRES+PST)/144.
VISINF=(11.0+.0175*TINF)/(1.86*RHOINF)
C CONSTANT FOR REYNOLDS NO CALC
VAIR=VAIR*SQRT(RHOOLD/RHOINF)
CONS=VAIR/VISINF
C CONSTANT FOR STANTON NO CALC
C12=0.5*CP*RHOINF*VAIR
12 IF((IOUT.EQ.0).AND.(IKHOR.LE.0))CALL HEAD
IF((IOUT.GT.0).AND.(IKHOR.LE.0))CALL HEAD2(IOUT,XZERU,512)
SUM=0.
FL=1./3.
FLG=1./6.
FLG=XZERU/12.
DO 6 N=1,24
C PLATE POWER CALCULATION
PHUEN=C1*ES(N)*EH(N)/RI(N)
CALL EMFT(TAIR(N),T,563)
CALL EMFT(TPL(N),T,563)
IF(K1.EQ.3)GO TO 501

```

```

C   CALC OF TRANS FLOW FROM FLO MEIER LME=K1=1 BLOW,K1=2 SUCK
CALL EMT(TCFM(N),TT,563)
RHO=(PRES+PHX)/(53.33*(TT+459.6))*(1.-.26*RH)
CALL FLOW(PAMB,TT,RH,RHO,K1,N,CFM(N),ACFM,PLFLO)
C   CORRECTION OF AIR TEMP FOR CAST TO AIR TEMP MISMATCH
IF((N.LE.9)TTAME=.75*TAMBT(1)+.25*TAMBT(2)
  IF((N.GT.9).AND.(N.LT.16))TTAME=(TAMBT(2)+TAMBT(3))/2.
  IF((N.GE.16)TTAME=.75*TAMBT(3)+.25*TAMBT(4)
  T1=TT+(TTAME-TT)*(1.-EXP(-1.175/ACFM))
  T2=(T1+TIN(N)-BTIN(N))*(TIN-ICAST(N))
C   RAD FROM FRONT OF PLATES
501 IF((IENBAL.EQ.1).AND.(K1.NE.3)) GO TO 41
  RCON=0.163
  TRADF4=((TZERO+459.6)/100.)**4
  GO TO 42
41 RCON=0.199
  TRADF4=((TDO+459.6)/100.)**4
42 GFRN=HCON+.1714*((TPLATE+459.6)/100.)**4-TRADF4/3600.
C   CONDUCTION LOSSES FROM PLATES, COND(I) FROM EXPLN.
  GCOND=COND(I)*(TPLATE-ICAST(N))/1000.
  TCA54=((ICAST(N)+459.6)/100.)**4
  TAIR4=((T+459.6)/100.)**4
  IF(K1.LT.3)GO TO 21
C   K1=3 NO TRANS
  TPL8=TPLATE+3600.*PRDEN/(40.*12.)
  TPL84=((TPL8+459.6)/100.)**4
  THC4=((TPL8+T)/2.+459.6)/100.)**4
C   RAD + COND FROM BACK, NO TRANS, HC AT AVG OF AIR AND PLATE BACK TEMP
  GBACK=.12.*.015*.5*(TPL8-T)
  GBACK=GBACK+.1714*(.0097*TPL84+.1718*THC4-.1455*ICAST4-.0360*TAIR4)
  GCOND=GCOND+GBACK/3600.
  ECOND=0.
  ACFM=0.
  SCF=0.
  AAA=0.
  PLFLO=0.
  T1=0.
  BLOF=0.
  BLL(N)=0.
  GO TO 23
21 FLAP=PLFLO*CP*3600./(40.*12.)
  IF(K1.LT.2)GO TO 22
C   K1=2 SUCKING
  TPL8=TPLATE+PRDEN/(PLFLO*CP)*(1.-EXP(-FLAP))
  TPL84=((TPL8+459.6)/100.)**4
C   RAD FROM BACK FOR SUCK, HC AT PLATE BACK TEMP
  GBACK=.1714*(.0097*TPL84+.1358*TAIR4-.1455*ICAST4)/3600.
  ECOND=CP*PLFLO*(TPL8-T1)
  GO TO 23
C   K1=1 BLOWING
22 TPL8=TPLATE+PRDEN/(PLFLO*CP)*(1.-EXP(-FLAP))
  TPL84=((TPL8+459.6)/100.)**4
C   RAD FROM BACK FOR BLOW, HC AT AIR TEMP
  GBACK=.1714*(.0097*TPL84+.1358*TAIR4-.1455*ICAST4)/3600.
  ECOND=CP*PLFLO*(TPLATE-T1)
23 IF((BACK.LT.0.) GBA=0.
  GCOND=GFRN+GBACK+GCOND
  GFRN=PRDEN*QLOS
  GCOND=HEAT-ECOND
  IF(IENBAL.EQ.1)GO TO 19
  IF((N.GT.1)STOL=STN(N-1)+BLOF
C   STATION NO CALC, BASED ON STAG TO WALL TEMP DIFF
  STN1=STN1/100.*(TPLATE-TZERO))
  IF(K1.EQ.3) GO TO 16
  HLOF=ALFMH*HLOF/160.*.5*AIR*HLOF1)
  BLL(N)=BLOF/STN(N)
16 IF((N.GT.1)GO TO 10
  E1=TH2.*(STN(N)+HLOF)
  SUMECONS=E1*TH/12.
  GO TO 3
10 E1=TH*(STN(N)+BLOF+STOL)*4.
  E1=TH*(E1+HLOF)/2.
  SUMECONS=SUMECONS+E1*TH/24.
  FLG=FLG+FL
3 FLG=FLG-PLCO
  IF(FLG.LT.0.)FLG=0.
  HEX(N)=FLG*CONS
  IF((PHOM.GT.0)GO TO 6
  IF((K1.NE.3).OR.(HEX(N).EQ.0.))GO TO 69
  ITAB=ITAB+1
  STOUTAB=STN(N)
  HEX(ITAB)=HEX(N)
69 INE=OFFMNT(N)*CONS/12.*0.5
  INEAT=CONS*FLG*0.5
  INEAT=HEX(N)+0.5
  INLENSUM=0.5

```

```

IFLG=FLG*12+0.5
IF (IREX(N).EQ.0.) GO TO 74
ST=0.295/(PR+REX(N)*0.2)
IF (K1+RE.3) ST=BLDF/(EXP(BLDF/ST)-1.)
STR(N)=ST/(1+PLATE*459.6)/(1+ZERO*459.6))*0.4
GO TO 75
74 ST=0.
STR(N)=0.
75 CONTINUE
IF (IOUT.GT.0) WRITE (6,4) (N, IFLG, STR(N), IREMO, IRELN, IREXX, IREXF, BLOF,
IREL(N), TPLATE, TFMONT(N), FTHTH
IF (IOUT.GT.1) PUNCH 4, N, IFLG, STR(N), IREMO, IRELN, IREXX, IREXF, BLOF,
IREL(N), TPLATE, TFMONT(N), FTHTH
4 FORMAT (13, 14, 3, 5, 2, 10, 2, 14, 7, 4, 5, 3, 2, 5, 1, 2, 5, 3)
IF (IOUT.EQ.0) WRITE (6,5) (N, STR(N), FTHTH, IRELN, FTMONT(N), IREMO, IFLG, IREXX,
IREXF, BLOF, IRELN, BLOF, IRELN, FTHTH, TPLATE, TFMONT, ECONV, QLOS, N
5 FORMAT (13, 9, 5, 3, 5, 3, 16, 5, 3, 16, 14, 18, 5, 2, 18, 5, 3, 5, 3, 4, 5, 1, 3, 5, 3
1, 14)
GO TO 6
19 PERCENT=T/GRAT*100.
STLR=QMT/(25.*5*CP*RHOFH*VAIR)*10000.
DECM=QMT/(CP*(1+PLATE-1)*0.75/60.)
IF (ERROR.GT.0) GO TO 6
IF (IOUT.EQ.0) WRITE (6,7) (N, GRAT, ECONV, QMT, PERC, XXX, SCFM, QLOS, TT, TP
ILATE, T, TCA, TIN) *OF NTH, QHACK, QCOMP, TIN, STLR
7 FORMAT (15, 3, 10, 6, 5, 3, 3, 7, 3, 4, 7, 1, 3, 5, 5, 5, 6, 1, 5, 2)
IF (IOUT.GT.0) WRITE (6,2) (N, PRDEN, ECONV, QLOS, QMT, PERC, STLR, ACM, TPL
ATE, TIN
IF (IOUT.GT.1) PUNCH 2, N, PRDEN, ECONV, QLOS, QMT, PERC, STLR, ACM, TPL
ATE, TIN
2 FORMAT (13, 5, 3, 5, 3, 5, 3, 5, 3, 7, 2, 5, 3, 2, 7, 1, 14)
6 CONTINUE
65 IF (IOUT.EQ.0) AND (ERROR.LE.0) CALL DATA1
C CHECK TO SEE IF ERROR ANALYSIS IS ASK FOR: IER=0: NO IER=1: YES
IF (IER.EQ.0) GO TO 104
13 CONTINUE
IF (ERROR.EQ.0) ST1=ST(1.)
IF (ERROR.GT.0) DELST=(ERROR)*ST1-ST(12)
IF (K1+RE.3) AND (ERROR.GT.0) GO TO 100
IF (K1+RE.3) AND (ERROR.LE.12) GO TO 100
GO TO 24
100 SUMR=0.
DO 101 I=1, ERROR
101 SUMR=SUMR+DELST(I)*DELST(I)
SUMR=SQRT(SUMR)
WRITE (6,11)
IF (ERROR.EQ.0) WRITE (6,10) (ST1, DELST(I), I=1, ERROR), SUMR
IF (ERROR.GT.0) WRITE (6,10) (ST1, DELST(I), I=1, ERROR), SUMR
102 FORMAT (7, 10, 1) 'UNCERTAINTY ANALYSIS SUMMARY FOR PLATE 12'
1 10X 'PLATE STANTON NUMBER =', E20.5//
2 10X ' (0.5 DEG TH) =', E20.5//
3 10X ' (0.1 MV TH) =', E20.5//
4 10X ' (0.02 AMP VAIR) =', E20.5//
5 10X ' (0.1 MV TPLATE) =', E20.5//
6 10X ' (0.1 MV TAIR) =', E20.5//
7 10X ' (0.01 VOLT EPL) =', E20.5//
8 10X ' (0.1 MV FSHORT) =', E20.5//
9 10X ' (0.1 MV TCAST) =', E20.5//
10 10X ' STANTON NUMBER ERROR =', E20.5//
103 FORMAT (7, 10, 1) 'UNCERTAINTY ANALYSIS SUMMARY FOR PLATE 12'
1 10X 'PLATE STANTON NUMBER =', E20.5//
2 10X ' (0.5 DEG TH) =', E20.5//
3 10X ' (0.1 MV TH) =', E20.5//
4 10X ' (0.02 AMP VAIR) =', E20.5//
5 10X ' (0.1 MV TPLATE) =', E20.5//
6 10X ' (0.1 MV TAIR) =', E20.5//
7 10X ' (0.01 VOLT EPL) =', E20.5//
8 10X ' (0.1 MV FSHORT) =', E20.5//
9 10X ' (0.1 MV TCAST) =', E20.5//
10 10X ' (0.1 MV FLOW) =', E20.5//
11 10X ' (0.05 MV FLOW) =', E20.5//
12 10X ' (0.1 MV TAIR) =', E20.5//
13 10X ' (0.1 AMP PROX) =', E20.5//
14 10X ' STANTON NUMBER ERROR =', E20.5//
104 IER=1
C CHECK FOR MORE CASES IN SEQUENCE: IEXT=1 GO BACK & READ SOME MORE
IF (IEXT.EQ.1) GO TO 24
WRITE (6,11)
11 FORMAT (11)
STOP
END
C DATA SUBROUTINE DATA1 FOR ST DATA REDUCTION PROGRAM
SUBROUTINE DATA1
C THIS SUBROUTINE READS IN DATA FROM THE ROUGHNESS RIG
COMMON/DA1/TAIR,PRDEN,SCFM,PLATE,TS(12),STR(24),CFM(24)

```

```

1. TAI(24),TCFM(24),EH(24),ES(24),KNEXT,MOMFC,XZLRU,NST,FHOMT(24),
2510(24),REXO(24),ITAB,TAMB(4),IOUT,IFR,IRHOR
COMMON/AMB/PAMB,TDB,TWB,DENT(18),K1,IENRAL,VAR
IRHOR=IRHOR+1
IF (IRHOR.EQ.0) GO TO 100
VARY INPUTS WITHIN UNCERTAINTY INTERVALS FOR ERROR ANALYSIS
IF (IRHOR.GT.1) GO TO 1
TUB=TUB+0.5
GO TO 54
1 IF (IRHOR.GT.2) GO TO 2
TUB=TUB-0.5
TAIR=TAIR+.01
GO TO 54
2 IF (IRHOR.GT.3) GO TO 3
TAIR=TAIR-.01
VAR=VAR+.002
GO TO 54
3 IF (IRHOR.GT.4) GO TO 4
VAR=VAR-.002
TPL(12)=TPL(12)+.01
GO TO 54
4 IF (IRHOR.GT.5) GO TO 5
TPL(12)=TPL(12)-.01
TAH(12)=TAH(12)+.01
GO TO 54
5 IF (IRHOR.GT.6) GO TO 6
TAH(12)=TAH(12)-.01
EH(12)=EH(12)+.001
GO TO 54
6 IF (IRHOR.GT.7) GO TO 7
EH(12)=EH(12)-.001
ES(12)=ES(12)+.01
GO TO 54
7 IF (IRHOR.GT.8) GO TO 8
ES(12)=ES(12)-.01
TCS(6)=TCS(6)+.01
GO TO 54
8 IF (IRHOR.GT.9) GO TO 9
TCS(6)=TCS(6)-.01
TCFM(12)=TCFM(12)+.01
GO TO 54
9 IF (IRHOR.GT.10) GO TO 10
TCFM(12)=TCFM(12)-.01
CFM(12)=CFM(12)+.025
GO TO 54
10 IF (IRHOR.GT.11) GO TO 11
CFM(12)=CFM(12)-.025
TAMB(3)=TAMB(3)+.01
GO TO 54
11 CONTINUE
TAMB(3)=TAMB(3)-.01
PBOX=PBOX+.1
GO TO 54
100 CONTINUE
C
C BEGIN HEAD1:G INPUT HERE, ALL INPUT FIXED FIELD FORMAT AS INDICATED BELOW
C HEAD INPUT: FIRST CARD HAS 72 COL OF TITLE AND COL 80 IS K1 INDICATOR
C IF K1=1 STANTON RUN WITH BLOWING
C IF K1=2 STANTON RUN WITH SUCTION
C IF K1=3 STANTON RUN WITHOUT TRANSPIRATION
C IF K1=4 BLOWING ENERGY BALANCE RUN
C IF K1=5 SUCTION ENERGY BALANCE RUN
C IF K1=6 NO FLOW ENERGY BALANCE RUN
C
C HEAD(5:25) DENT,K1
25 FORMAT(18A4,7X,I1)
IF (K1.LT.3) GO TO 61
ITAB=0
DU 57 I=1,24
SIR(I)=0.
SIU(I)=0.
57 REXO(I)=0.
C IF K1=1 OR 2: READ TDB,TWB,PAMB,TAIR,PSTAT,VAR,SG,PBOX, OF10 FORMAT
C 01 IF (K1.LT.3) READ(5:29) TDB,TWB,PAMB,TAIR,PSTAT,VAR,SG,PBOX
C IF K1=3 OR 6 READ TDB,TWB,PAMB,TAIR,PSTAT,VAR,SG, 7F10 FORMAT
C IF (K1.EQ.3).OR.(K1.EQ.6) READ(5:29) TDB,TWB,PAMB,TAIR,PSTAT,VAR,SG
C IF K1=4 OR 5 READ TDB,TWB,PAMB,TAIR,PBOX,VAR, OF10 FORMAT
C IF (K1.GT.3).AND.(K1.LT.6) READ(5:29) TDB,TWB,PAMB,TAIR,PBOX,VAR
C TDB=GET BULB TEMP IN DEGF
C TDB=DRY BULB TEMP IN DEGF
C PAMB=PAMB PRESSURE IN INCHES OF HG
C TAIR=FREE STREAM TEMP IN MV FOR STANTON RUNS AND AMB TEMP IN MV FOR
C ENERGY BALANCE RUNS
C PSTAT=TUNNEL-TO-AMB PRESSURE DIFFERENCE IN INCHES OF H2O
C VAR=FREE STREAM PITOT TUBE MANO READING IN INCHES OF FLUID OF SPECIFIC
C GRAVITY SG FOR STANTON RUNS, AND VEL TO BE USED IN STANTON NO ERROR

```

```

C      LEVEL FOR ENERGY BAL RUNS IN F1/SEC
C      SIZE MAIN FLUID FOR VAR READING
C      PBOOK=TRAN, HEADER BOX PRESSURE IN INCHES OF H2O
29 FORMAT(10.0)
DO 26 I=1,4
C      FOR K1=3 OR 6 READ TPL,TAR,THES, 4F10 FORMAT
IF((K1.EQ.3).OR.(K1.EQ.6))READ(5,27)TPL(I),TAR(I),THES(I),ES(I)
C      FOR K1=2,4,5 READ TPL,TAR,TCM,CFM,THES, 6F10 FORMAT
26 IF((K1.NE.3).AND.(K1.EQ.1))READ(5,27)TPL(I),TAR(I),TCM(I),CFM(I),
THES(I),ES(I)
C      TPL(I)=PLATE TEMP IN MV
C      TAR(I)=TRAP AIR TEMP IN MV
C      TCM(I)=FLOW METER TEMP IN MV
C      CFM(I)=FLOW METER SIGNAL IN MV
C      THES(I)=AIR VOLTAGE IN VOLTS
C      ES(I)=HUNT VOLTAGE IN MILLIVOLTS
C      FORMAT(6F10.0)
C      READ(5,TC(I)) CASING TEMPS IN MV, 6F10 FORMAT
READ(5,28)TC(I),I=1,12)
C      READ IN TAMB(I), 4H TEMPS IN MV FOR BLOWING RUNS ONLY, 4F10 FORMAT
IF((K1.NE.3).AND.(K1.EQ.1))READ(5,28)TAMB(I),I=1,4)
28 FORMAT(6F10.0)
DO 50 I=1,24
50 PBOOK(I)=0.
C      READ IN KNE,X1,MOMCK,X2,LOC,ST,ICUT,ILR, 2(11.9X)+1(10.3(9X,11) FORMAT
C      KNE,X1=1 FOR MORE CASES TO FOLLOW=0 IF LAST CASE
C      MOMCK=1 IF MOM THICKNESSES ARE TO BE READ IN TO CALC MOM THE KEY NO
C      X2,LOC= LOCATION OF TURN IN VIRTUAL ORIGIN FOR (X-X0) KEY NO
C      ST=1 IF NO BLOW STATION NUMBERS ARE TO BE USED TO CALC ST/ST0, IF THIS
C      OPTION IS USED A NO BLOW STATION NO RUN MUST BE EXECUTED FIRST
C      ICUT=1 FOR DETAILED OUTPUT, 2 FOR SHORT OUTPUT, 3 FOR SHORT OUT W/CARDS
C      ILR=1 IF STATION NO UNCERTAINTY OPTIN IS DESIRED, PLATE 12 ONLY
C      READ(5,31)KNE,X1,MOMCK,X2,LOC,ST,ICUT,ILR
31 FORMAT(11.9X+11.9X+11.0.9X+11.9X+11.9X+11)
IF(MOMCK.EQ.0) GO TO 54
C      READ IN PBOOK(I) MOMENTUM THE FOR EACH PLATE, 12F6 FORMAT
READ(5,53)PBOOK(I),I=1,24)
53 FORMAT(12F6.0)
54 CONTINUE
RETURN
END

C HEAD SUBROUTINE HEAD FOR ST DATA REDUCTION PROGRAM
SUBROUTINE HEAD
C      THIS SUBROUTINE PRINTS OUT OUTPUT READING
COMMON/HD/TAMF(4),VAIN,TIME,ZERO,RHOINH,PSI
COMMON/AMB/PAMB,TOD,TWO,DELTA(18),K1,ILR,JAL,VAR
WRITE(6,8)PRINT
8 FORMAT(1H,10A4)
IF((K1.EQ.3).AND.(K1.EQ.6)) GO TO 12
IF(K1.EQ.6)GO TO 43
WRITE(6,9)VAIN,TIME,ZERO
40 FORMAT(1H, ' STATION NUMBER AT FREE STREAM VEL=,F6.2,
1' F1/SEC TIME=,F6.1, DEG TIME=,F6.1, DEG')
TERMINAL=0
GO TO 40
43 WRITE(6,9)VAIN,TIME,ZERO
44 FORMAT(1H, ' NO TRAP, ENERGY BAL RUN AT FREE STREAM VEL=,F6.2,
1' F1/SEC TIME=,F6.1, DEG TIME=,F6.1, DEG')
TERMINAL=1
K1=3
46 WRITE(6,4)RHOINH,PSI,TOD,TWO,PAMB
4 FORMAT( ' RHOINH=,F6.4, LB/FT3 PRESINH=,F6.2, PSI
1' TOD=,F6.1, DEG TWO=,F6.1, DEG PAMB=,F6.2, ANG')
GO TO 14
12 WRITE(6,2)TIME,TOD,TWO,PAMB
2 FORMAT(1H, ' ENERGY BALANCE RUN TIME=,F6.1, DEG
1' TOD=,F6.1, DEG TWO=,F6.1, DEG PAMB=,F6.2, ANG')
TERMINAL=1
IF(K1.EQ.4) K1=1
IF(K1.EQ.5) K1=2
VAIN=VAR
14 WRITE(6,47)(TAMF(I),I=1,4)
47 FORMAT( ' TAMF=,F6.1, DEG TAM2=,F6.1, DEG TAM3=,F6.1,
1DEG TAM4=,F6.1, DEG')
IF(TERMINAL.EQ.0)WRITE(6,40)
40 FORMAT( ' PL STATION LENTH 1' H MONTH MOM X X X-X0
1X=AD 1 B TPL TCST TPL TAIR PL POWER E-CONV LOSS
2LS PL/2' NO NUMBER INCH REYN INCH REYN IN REYN INCH
SREYNO=,10A,DEG DEG DEG DEG DEG BTU/SEC BTU/SEC BTU/SEC NO')
IF(TERMINAL.EQ.1)WRITE(6,49)
49 FORMAT( ' PL PL POWER (NO CONV DIFF PERCENT EMFO FLOW
1DEFLD TFLOW TPL TAIN TCST GFRNT CHACK GCONU TPLB ST
2HCK/2' NO BTU/SEC BTU/SEC BTU/SEC BTU/SEC
3 CFM DEG DEG DEG DEG')

```

RETURN
END

C FLOW SUBROUTINE FLOW FOR ST DATA REDUCTION PROGRAM
SUBROUTINE FLOW(FAMH, FTH, HHO, K, H, LMF, ALF, M, PLF, LQ)
DIMENSION L(15,2,24), L1(5,2,24)
COMMON AFLO/XXX, LCFM

C FLOW METER CALIBRATION: UPDATED 8/24/73

DATA(L((I,J,K)), I=1:5, J=1:2, K=1:24)

1	76.5194, 76.92, 86.61, 84.6, 72.1, 6.5194, 4.7692, 2.8661, 1.846, .721 H/73- 1
1	5.4004, 5.362, 2.548, 1.759, .759, 5.4004, 4.362, 2.548, 1.759, .759 H/73- 2
2	5.5444, 5.442, 2.826, 1.790, .577, 5.5444, 4.842, 2.826, 1.790, .577 H/73- 3
3	7.1945, 5.000, 3.053, 2.117, .955, 4.4963, 3.963, 2.986, 1.115, .887 H/73- 4
4	6.5005, 5.320, 3.188, 2.194, 1.112, 6.1314, 4.650, 3.023, 1.424, 1.170 H/73- 5
5	5.8755, 5.675, 2.933, 1.940, .871, 5.7004, 4.715, 3.105, 1.674, .860 H/73- 6
6	4.4002, 4.857, 1.477, 1.573, 1.100, 4.426, 2.988, 1.496, 1.577, 1.204 H/73- 7
7	5.7444, 4.687, 2.763, 1.853, .813, 5.7814, 4.687, 3.033, 1.660, .872 H/73- 8
8	6.0444, 4.843, 2.942, 2.026, .831, 6.0444, 4.844, 2.943, 1.542, .867 H/73- 9
9	6.7385, 5.112, 2.946, 1.475, 1.004, 6.0624, 4.719, 3.810, 2.638, .982 H/73-10
A	6.3245, 5.046, 3.107, 2.151, 1.075, 6.1254, 4.850, 3.119, 1.677, .960 H/73-11
B	4.4203, 5.042, 2.057, 1.501, 1.165, 4.826, 3.141, 2.084, 1.661, 1.256 H/73-12

DATA(L((I,J,K)), I=1:5, J=1:2, K=13:24)

C	7.1903, 5.073, 2.334, 1.505, .654, 4.531, 3.204, 2.491, 1.059, .741 H/73-13
D	5.1302, 4.090, 1.440, 1.125, .838, 3.622, 2.044, 1.400, 1.094, .824 H/73-14
E	5.7002, 4.740, 1.772, 1.206, .957, 3.700, 2.670, 1.757, 1.170, .935 H/73-15
F	5.8962, 4.765, 1.915, 1.527, 1.194, 3.930, 2.673, 1.353, 1.448, 1.155 H/73-16
G	4.7663, 5.253, 2.263, 1.749, 1.404, 4.740, 3.214, 2.229, 1.782, 1.366 H/73-17
H	6.9484, 4.700, 3.080, 2.190, 1.056, 6.0004, 4.700, 3.080, 2.190, 1.056 H/73-18
I	5.9002, 4.673, 1.493, 1.242, 1.076, 4.096, 2.783, 1.880, 1.464, 1.103 H/73-19
J	4.2392, 4.944, 2.013, 1.611, 1.247, 4.477, 3.157, 2.157, 1.724, 1.323 H/73-20
K	5.7244, 4.965, 2.841, 1.724, .602, 5.8194, 4.519, 2.884, 1.543, .832 H/73-21
L	5.0552, 4.332, 1.568, 1.147, .942, 3.564, 2.420, 1.514, 1.282, .971 H/73-22
M	4.2262, 4.834, 1.909, 1.573, 1.232, 4.314, 2.913, 2.005, 1.509, 1.207 H/73-23
N	5.0444, 4.030, 2.521, 1.748, .806, 5.0694, 4.112, 2.684, 1.442, .863 H/73-24

DATA(L((I,J,K)), I=1:5, J=1:2, K=1:12)

1	.55, 1.48, 5.90, 15.00, 75.94, .55, 1.48, 5.90, 15.00, 75.94 H/73- 1
1	.64, 1.51, 6.27, 15.00, 73.03, .64, 1.51, 6.27, 15.00, 73.03 H/73- 2
2	.69, 1.56, 6.03, 15.00, 92.53, .69, 1.56, 6.03, 15.00, 92.53 H/73- 3
3	.59, 1.72, 6.14, 14.16, 67.26, 1.51, 2.02, 6.19, 17.86, 67.19 H/73- 4
4	.58, 1.47, 5.93, 14.87, 52.13, .58, 1.54, 6.06, 15.61, 46.98 H/73- 5
5	.62, 3.02, 5.96, 14.80, 80.69, .68, 1.64, 5.99, 23.92, 83.42 H/73- 6
6	1.32, 6.37, 14.95, 23.97, 41.90, 1.83, 6.10, 15.26, 24.58, 41.64 H/73- 7
7	.54, 1.46, 6.01, 14.59, 70.93, .54, 1.57, 6.10, 23.91, 80.52 H/73- 8
8	.62, 1.53, 6.17, 14.16, 73.39, .62, 1.53, 6.17, 24.36, 73.39 H/73- 9
9	.59, 1.56, 6.20, 13.90, 46.86, .60, 1.59, 3.16, 6.38, 47.55 H/73-10
A	.58, 1.64, 6.17, 14.90, 64.05, .62, 1.56, 5.99, 24.04, 64.22 H/73-11
B	1.74, 6.33, 14.73, 24.13, 41.82, 1.74, 6.02, 15.25, 24.12, 41.08 H/73-12

DATA(L((I,J,K)), I=1:5, J=1:2, K=13:24)

C	.63, 3.14, 6.19, 14.10, 67.35, .67, 3.17, 5.35, 24.34, 68.34 H/73-13
D	1.01, 6.10, 14.67, 23.86, 42.49, 1.82, 6.12, 14.11, 24.04, 41.72 H/73-14
E	.70, 1.89, 6.42, 15.06, 23.67, .70, 1.90, 6.30, 15.15, 24.08 H/73-15
F	1.88, 5.93, 14.85, 23.99, 41.05, 1.91, 6.40, 15.21, 23.88, 41.35 H/73-16
G	1.80, 6.06, 14.94, 24.26, 41.95, 1.82, 6.06, 15.05, 24.29, 41.94 H/73-17
H	.50, 1.56, 6.25, 14.80, 66.22, .50, 1.56, 6.25, 14.80, 66.22 H/73-18
I	2.73, 6.16, 12.13, 26.74, 39.95, 2.05, 6.33, 14.87, 24.37, 41.14 H/73-19
J	2.22, 6.24, 14.67, 23.00, 41.82, 2.22, 6.15, 15.32, 24.55, 41.49 H/73-20
K	.60, 1.42, 6.07, 18.00, 77.51, .60, 1.65, 6.30, 24.27, 77.16 H/73-21
L	1.97, 6.33, 14.77, 26.53, 41.59, 1.98, 6.17, 15.31, 24.12, 41.22 H/73-22
M	1.07, 6.13, 14.98, 23.89, 41.42, 1.09, 6.11, 15.25, 24.52, 42.07 H/73-23
N	.58, 1.60, 6.28, 14.40, 64.60, .58, 1.68, 5.98, 23.92, 65.11 H/73-24

XXX=EXP((T+459.6)/529.6)**.41*(1+.38*HH)

IF(XXX.GT.L(1,K,N))GO TO 60

IF(XXX.LT.L(5,K,N))GO TO 30

DO 20 I=2,5

IF(XXX.LT.L(I,K,N))GO TO 20

SCF=EXP(ALOG(5(I-1,K,N))+(ALOG(XXX)-ALOG(L(I-1,K,N)))+(ALOG(5(I

1,K,N))-ALOG(5(I-1,K,N)))/(ALOG(L(I,K,N))-ALOG(L(I-1,K,N))))

GO TO 500

20 CONTINUE

60 SCF=EXP(ALOG(5(I,K,N))+(ALOG(XXX)-ALOG(L(I,K,N)))+(ALOG(5(I

2,K,N))-ALOG(5(I,K,N)))/(ALOG(L(2,K,N))-ALOG(L(I,K,N))))

GO TO 500

30 SCF=EXP(ALOG(5(4,K,N))+(ALOG(XXX)-ALOG(L(4,K,N)))+(ALOG(5(I

5,K,N))-ALOG(5(4,K,N)))/(ALOG(L(5,K,N))-ALOG(L(4,K,N))))

50 ALF=SCF*.075/HHO

PLF=SCF*.075/60.

RETURN

END

C EMP SUBROUTINE EMP FOR ST DATA REDUCTION PROGRAM

SUBROUTINE EMP(EMP,TT,*)

DIMENSION L(40),T(40)

```

DATA L/0.50*0.60*0.70*0.80*0.85*0.90*0.95*1.00*1.05*1.10*1.15*1.20
1 .12*1.30*1.35*1.40*1.45*1.50*1.55*1.60*1.65*1.70*1.75*1.80
2 .18*1.90*1.95*2.00*2.05*2.10*2.15*2.20*2.25*2.30*2.35*2.40
3 .25*2.60*2.70*2.80/
DATA 1/ 49.86 53.34 56.93 64.46 62.22 63.97 65.72 67.49
1 69.24 70.98 72.70 74.42 76.14 77.84 79.63 81.35
2 83.08 84.79 86.52 88.24 89.97 91.69 93.42 95.15
3 96.87 98.54 100.32 102.03 103.76 105.48 107.20 108.93
4 110.64 112.34 114.06 115.76 117.48 119.18 122.59 125.97 129.37/
IF (EMP.GI.1.0) AND (EMP.LL.2.8) GO TO 1
WRITE (6,10) EMP
10 FORMAT(// '1 OUT OF EMP TABLES IN SUBROUTINE EMP T. EMP =',F10.3)
RETURN 1
1 IF (EMP.GI.1.0) GO TO 2
N1=1
N2=H
GO TO 5
2 IF (EMP.GI.1.5) GO TO 3
N1=H
N2=18
GO TO 5
3 IF (EMP.GI.2.0) GO TO 4
N1=18
N2=28
GO TO 5
4 N1=28
N2=40
5 GO 6 IF N1.N2
IF (EMP.LL.1) GO TO 7
6 CONTINUE
7 11=1(1-1)+(11-1(1-1))*(EMP-L(1-1))/(L(1)-L(1-1))
RETURN
END

C HEAD2 SUBROUTINE FOR ST DATA REDUCTION PROGRAM
SUBROUTINE HEAD2(IOUT,XZERO)
COMMON/H0/IAUT(4),VAIR,TINF,TZRO,RHOINF,PSI
COMMON/AMB/PAMB,TDB,TWB,DELTA(16),K1,ILNBAL,VAR
IF (K1.NE.6) GO TO 1
WRITE (6,10)
10 FORMAT(// 'THE OUTPUT ROUTINE REQUESTED CAN BE USED FOR STANTON RU
INS OR ENERGY BAL RUNS ONLY')
IOUT=0
RETURN 1
1 IF (K1.GT.3) GO TO 3
WRITE (6,8) DELTA,VAIR,TINF,TZRO,RHOINF,PSI,TDB,TWB,PAMB,XZERO
IF (IOUT.GE.1) PUNCH 5,DELTA,VAIR,TINF,TZRO,RHOINF,PSI,TDB,TWB,PAMB
1,XZERO
2 FORMAT(1H,18A4// ' VEL=',F5.1, ' FT/SEC T=',F5.1, ' DEGF TO=',F5.1
1, ' DEGF RHO=',F6.4, ' LBS/FT3 P=',F6.2, ' PSI TDB=',F5.1, ' DEGF
2 TWB=',F5.1, ' DEGF PAMB=',F6.2, ' IN HG VIR ORIG,XO=',F6.2, ' IN
3// ' PL X STN MOM ENTH X (X-XO) F B TPL
4 TAIR MOMTH ENTH// ' NO INCH NO REYNO REYNO REYNO REYNO*16
5X, 'DEGF DEGF INCH INCH')
5 FORMAT(1H,18A4// ' VEL=',F5.1, ' FT/SEC T=',F5.1, ' DEGF TO=',F5.1
1, ' DEGF RHO=',F6.4, ' LBS/FT3 P=',F6.2, ' PSI TDB=',F5.1, ' DEGF
2 TWB=',F5.1, ' DEGF PAMB=',F6.2, ' IN HG VIR ORIG,XO=',F6.2, ' IN
3// ' PL X STN MOM ENTH X (X-XO) F B TPL
4 TAIR MOMTH ENTH// ' NO INCH NO REYNO REYNO REYNO REYNO*16
5X, 'DEGF DEGF INCH INCH')
GO TO 4
3 CONTINUE
ILNBAL=1
IF (K1.EQ.4) K1=1
IF (K1.EQ.5) K1=2
VAIR=VAR
WRITE (6,7) DELTA,TDB,TWB,PAMB,VAIR
7 FORMAT(1H,18A4// ' TDB=',F5.1, ' DEGF TWB=',F5.1, ' DEGF PAMB=',F6
1.2, ' IN HG VEL(STN ERR)=',F6.1, ' FT/SEC// ' PL PL POWR E CONV
2 LOSSES DIFF PERCENT STN FLOW TPL TAIR PL// ' NO BT
3U/SEC BTU/SEC BTU/SEC BTU/SEC,10X, 'ERROR ACFM DEGF DEGF
4 NO')
IF (IOUT.GE.1) PUNCH 9,DELTA,TDB,TWB,PAMB,VAIR
9 FORMAT(1H,18A4// ' TDB=',F5.1, ' DEGF TWB=',F5.1, ' DEGF PAMB=',F6
1.2, ' IN HG VEL(STN ERR)=',F6.1, ' FT/SEC// ' PL PL POWR E CONV
2 LOSSES DIFF PERCENT STN FLOW TPL TAIR PL// ' NO BT
3U/SEC BTU/SEC BTU/SEC BTU/SEC,10X, 'ERROR ACFM DEGF DEGF
4 NO')
4 RETURN
END

C DATA1 SUBROUTINE DATA1 FOR ST DATA REDUCTION PROGRAM
SUBROUTINE DATA1
COMMON/DAI/TAIR,PSIAT,SG,POW,TPLE(24),TCE(12),STH(24),CFM(24)
1,TAH(24),ICFM(24),LEH(24),LCH(24),KHEX,MOMEX,XZLH,REH,1,MOMT(24),

```

```

250(24),HEX0(24),ITAB,TAMB(4),IOUT,IFH,INMR
COMMON/DAO/REX(24),STN(24),BEE(24)
COMMON/AMB/PAMB,TDB,TWB,DENT(16),K1,IENBAL,VAR
LIST OUT RAW INPUT DATA
C
IF((IENBAL.EQ.0).OR.(K1.EQ.3))GO TO 40
WRITE(6,17)TWB,TDB,PAMB,PBOX,TAIR,(TAMB(I),I=1,4)
17 FORMAT(1H, ' RAW INPUT DATA FOR ENERGY BALANCE RUN:/'
1 TWB=F6.1, DEGF TDB=F6.1, DEGF PAMB=F6.2, MV PBOX=F6.2,
2 P0.2, #H20 TAIR=F6.3, MV TAMB1=F6.3, MV TAMB2=F6.3,
3 MV TAMB3=F6.3, MV TAMB4=F6.3, MV
IF(K1.EQ.3)WRITE(6,8)
8 FORMAT(' PL NO T L(MV) TAR(MV) LH(VOLTS) EC(MV) CAST
1 TC TCS(MV) )
IF(K1.NE.3)WRITE(6,9)
9 FORMAT(' PL NO TPL(MV) TAR(MV) TCFM(MV) TFLO(MV) LH(VOL
1T) EC(MV) CAST TC TCS(MV) )
DO 2 N=1,24
IF(N.GT.12) GO TO 3
IF(K1.EQ.3)WRITE(6,32)N,TPL(N),TAR(N),EH(N),ES(N),N,TCS(N)
IF(K1.NE.3)WRITE(6,15)N,TPL(N),TAR(N),TCFM(N),CFM(N),EH(N),ES(N),N
1,TCS(N)
GO TO 2
3 IF(K1.EQ.3)WRITE(6,39)N,TPL(N),TAR(N),EH(N),ES(N)
IF(K1.NE.3)WRITE(6,40)N,TPL(N),TAR(N),TCFM(N),CFM(N),EH(N),ES(N)
2 CONTINUE
RETURN
50 IF(K1.NE.3) WRITE(6,51)TWB,TDB,PAMB,TAMB(1),TAMB(2),TAMB(3),TAMB(4
1),TAIR,VAR,PSTAT,PBOX,SG,XZERO
51 FORMAT(1H, ' RAW INPUT DATA FOR STATION NUMBER RUN:/'
1 TWB=F6.1, DEGF TDB=F6.1, DEGF PAMB=F6.2, #H20,
2 TAMB1=F6.3, MV TAMB2=F6.3, MV TAMB3=F6.3, MV TAMB4=F6.3,
3 MV, MV, TAIR=F6.3, MV VAIR=F6.3, #H20 PSTAT=F6.2, #H20
4 PBOX=F6.3, #H20 SPGR=F6.3, XZERO=F6.2, #H20
IF(K1.EQ.3).AND.(IENBAL.EQ.0)WRITE(6,54)
54 FORMAT(1H, ' RAW INPUT DATA FOR NO TRANS STATION NUMBER RUN:/'
IF(K1.EQ.3).AND.(IENBAL.EQ.1)WRITE(6,52)
52 FORMAT(1H, ' RAW INPUT DATA FOR NO TRANS ENERGY BAL RUN:/'
IF(K1.EQ.3) WRITE(6,55)TWB,TDB,PAMB,TAIR,VAR,PSTAT,PBOX,SG,XZERO
55 FORMAT(' TWB=F6.1, DEGF TDB=F6.1, DEGF PAMB=F6.2, #H20,
1 TAIR=F6.3, MV VAIR=F6.3, #H20 PSTAT=F6.2, #H20
2 PBOX=F6.3, #H20 SPGR=F6.3, XZERO=F6.2, #H20
53 IF(K1.EQ.3) WRITE(6,33)
33 FORMAT(' PL NO TPL(MV) TAR(MV) LH(VOLTS) LC(MV) CAST
1 TC TCS(MV) STS ST/STS )
IF(K1.NE.3) WRITE(6,34)
34 FORMAT(' PL NO TPL(MV) TAR(MV) TCFM(MV) IFLO(MV) LH(VOL
1T) EC(MV) CAST TC TCS(MV) STS ST/STS ST/STO LN
1(1+H)/B)
DO 13 N=1,24
IF(STR(N).GT.0.)STRAO=STN(N)/STR(N)
IF(STR(N).EQ.0.)STRAO=0.
IF(REX(N).LT.REX0(1))GO TO 70
IF(INST.EQ.0).OR.(K1.EQ.3))GO TO 58
DO 72 I=2,ITAB
IF(REX(N).LT.REX0(I))GO TO 71
72 CONTINUE
STOO=STO(ITAB)
GO TO 73
71 RATIO=(REX(N)-REX0(I-1))/(REX0(I)-REX0(I-1))
STOO=STO(I-1)+(STO(I)-STO(I-1))*RATIO
GO TO 73
70 STOO=STO(1)
73 STSTO=STN(N)/STOO
IF(HLE(N).GT.0.)FLNB=ALOG(BEE(N)+1.)/BEE(N)
IF(HLE(N).LE.0.)FLNB=0.0
IF(N.GT.12)GO TO 59
IF(K1.EQ.3)WRITE(6,35)N,TPL(N),TAR(N),EH(N),ES(N),N,TCS(N),STR(N),
1STRAO
32 FORMAT(110,2F10.3,F10.4,F10.3,110,F10.3,F10.5,3F10.2)
IF(K1.NE.3)WRITE(6,15)N,TPL(N),TAR(N),TCFM(N),CFM(N),LH(N),ES(N),N
1,TCS(N),STR(N),STRAO,STSTO,FLNB
15 FORMAT(110,4F10.3,F10.4,F10.3,110,F10.3,F10.5,3F10.3)
GO TO 13
59 IF(K1.EQ.3)WRITE(6,39)N,TPL(N),TAR(N),EH(N),ES(N),STR(N),STRAO
39 FORMAT(110,2F10.3,F10.4,F10.3,20X,F10.5,3F10.3)
IF(K1.NE.3)WRITE(6,40)N,TPL(N),TAR(N),TCFM(N),CFM(N),LH(N),ES(N),S
1T(N),STRAO,STSTO,FLNB
40 FORMAT(110,4F10.3,F10.4,F10.3,20X,F10.5,3F10.3)
GO TO 13
58 CONTINUE
IF(N.GT.12)GO TO 38
IF(K1.EQ.3)WRITE(6,32)N,TPL(N),TAR(N),EH(N),ES(N),N,TCS(N),STR(N),
1STRAO
IF(K1.NE.3)WRITE(6,15)N,TPL(N),TAR(N),TCFM(N),CFM(N),LH(N),ES(N),N
1,TCS(N),STR(N),STRAO
GO TO 13
38 IF(K1.EQ.3)WRITE(6,39)N,TPL(N),TAR(N),EH(N),ES(N),STR(N),STRAO
IF(K1.NE.3)WRITE(6,40)N,TPL(N),TAR(N),TCFM(N),CFM(N),LH(N),ES(N),S
1T(N),STRAO
13 CONTINUE
RETURN

```